

Cover Page



Universiteit Leiden



The handle <http://hdl.handle.net/1887/50189> holds various files of this Leiden University dissertation

Author: Andrews Mancilla, H.

Title: Shining Light on PAHs in Space

Issue Date: 2017-06-07

Shining Light on PAHs in Space

Shining Light on PAHs in Space

Proefschrift

ter verkrijging van
de graad van Doctor aan de Universiteit Leiden,
op gezag van Rector Magnificus prof. mr. C. J. J. M. Stolker,
volgens besluit van het College voor Promoties
te verdedigen op woensdag 7 juni 2017
klokke 10.00 uur

door

Heather Andrews Mancilla

geboren te Chuquicamata, Chile
in 1986

Promotiecommissie

Promotor: Prof. dr. A. G. G. M. Tielens
Co-promotor: Dr. Alessandra Candian

Overige leden: Prof. Els Peeters University of Western Ontario
Prof. Peter Sarre University of Nottingham
Prof. Takashi Onaka University of Tokyo
Prof. Harold Linnartz University of Leiden
Prof. dr. Paul van der Werf University of Leiden
Prof. dr. Huub Röttgering University of Leiden

Para mis padres: Mercedes y Carlos

Contents

1. Theoretical Framework	1
1.1. First is First: What are PAHs?	2
1.2. A Little Bit of History...	3
1.3. PAH Hypothesis	4
1.4. Photodissociation Regions	7
1.5. PAHs Through The Observation of PDRs	9
1.5.1. Charge	9
1.5.2. Composition-Hydrogenation	9
1.5.3. Size	12
1.5.4. Edge-Structure	12
1.6. Other Carriers	12
1.7. Current State of the Field	13
1.7.1. Infrared Spectra of PAHs	13
1.7.2. Emission Model	14
1.7.3. Photochemistry of PAHs	14
1.8. In This Thesis	15
1.8.1. The GrandPAHs	16
1.8.2. Formation of H ₂ in Clouds	17
1.8.3. Superhydrogenated PAHs and The 3.4 μ m Carrier	17
1.8.4. Deuterium Fractionation in the Local ISM	19
1.9. Outline of This Thesis	20
2. The GrandPAH hypothesis	25
2.1. Introduction	26
2.2. Observations	28
2.2.1. Selected PDRs	28
2.2.2. Data Collection and Reduction	29
2.2.3. Description of Removal of Continuum and Plateaus	30
2.3. Motivation	31
2.4. Method	32
2.4.1. Model Parameters	33
2.4.2. Database	34
2.5. Results	36
2.5.1. Base Run	36
2.5.2. Degeneracy	42
2.6. Discussion	45
2.6.1. Monte Carlo Experiment	46
2.6.2. Limitations	47

2.6.3. The Local Physical Environment	49
2.6.4. GrandPAH Hypothesis	50
2.6.5. GrandPAH Evolutionary Scenario	51
2.7. Summary and Conclusions	53
2.A. Features+Plateaus versus Features-Only Spectra	57
2.B. Tests on Model Parameters	60
2.B.1. Band Profile	60
2.B.2. FWHM	61
2.C. Base run fits to NGC 2023 and NGC 1333 spectra	63
2.D. PAHs used in the base run fit to NGC 7023	65
3. Hydrogenation and dehydrogenation of PAHs	67
3.1. Introduction	68
3.2. Physical–Chemical Processes	70
3.2.1. Environment	71
3.2.2. PDR Model	72
3.2.3. Molecular Characteristics	74
3.2.4. Processes	76
3.3. Model	84
3.4. Results	85
3.4.1. Abundances	85
3.4.2. H ₂ Formation	87
3.4.3. Spectral Variations	91
3.5. Discussion	93
3.5.1. Implications on the Origin of the 3.4 μm Feature	96
3.5.2. H ₂ Formation	98
3.6. Conclusions	100
3.A. Molecular Characteristics	103
3.A.1. Ionization potentials and electron affinities	103
3.A.2. IR intrinsic spectra	104
3.A.3. Electron attachment/recombination with electrons	106
3.B. Photodissociation Rates	106
3.C. Model	107
3.D. Fiducial Collision Rates	108
3.E. Relative Abundance Distribution of PAHs in NGC 7023	109
3.F. Spectral Variations	111
3.F.1. PAH emission spectra in the NW PDR of NGC 7023	111
3.F.2. PAH emission spectra for different $G_0/n(H)$ ratios at $G_0 = 10^3$	111
3.F.3. Intrinsic spectra of different hydrogenation states of neutral coronene, circumcoronene and circumcircumcoronene molecules	113
4. The Path to PAHDs	117
4.1. Introduction	118
4.2. Method	119
4.2.1. PAH Structure	119
4.2.2. Molecular Properties	120
4.2.3. Reactions with Deuterium	121
4.3. Results	124
4.3.1. Relative Abundance Distribution of PAHs	125
4.3.2. Deuterium Content in PAHs	127

4.4. Discussion	131
4.4.1. Deuterium fractionation of PAHs	131
4.4.2. Observations of interstellar PAHDs	132
4.4.3. PAHs and the gas phase abundance of D	133
4.5. Conclusions	134
5. Whipping IC63/IC59	137
5.1. Introduction	138
5.2. Data	139
5.2.1. Spitzer Data	139
5.2.2. Herschel	141
5.2.3. SOFIA Velocity Maps	143
5.3. Results	143
5.3.1. PAH Emission	143
5.3.2. Physical Conditions	147
5.3.3. [CII] Velocity Map of IC59	152
5.4. Discussion	154
5.4.1. Variability of PAH Emission	155
5.4.2. Heating Efficiency	156
5.4.3. Other Correlations	157
5.4.4. Morphology of IC59	159
5.5. Conclusion	160
Nederlandse Samenvatting	163
Curriculum Vitae	167
Acknowledgments	169

Theoretical Framework

“If we have made this our task, then there is no more rational procedure than the method of trial and error — of conjecture and refutation: of boldly proposing theories; of trying our best to show that these are erroneous; and of accepting them tentatively if our critical efforts are unsuccessful.”

– Karl Popper

Polycyclic aromatic hydrocarbons (PAHs) are now widely accepted to be the carriers of what were once called the Unidentified InfraRed (UIR) bands; emission bands observed in the mid-infrared spectra of a diverse type of astronomical sources subjected to stellar radiation. These molecules are thought to contain a significant amount of carbon (about 15% of the elemental carbon), which places them as the most abundant class of organic compounds in space. As such, they are an important part of the machinery that absorbs high-energy starlight and re-emits it at lower energies, contributing to the heating of the surrounding gas, and playing a crucial role in the ionization balance of interstellar clouds. Interestingly enough, these molecules have even been suggested as building blocks of life as we know it on Earth, as they can be a catalyst agent in the formation of RNA nucleobases, among other functions relevant to the development of organic matter. In this first chapter, we will set the theoretical framework of what this thesis is about. This thesis is particularly important for the research field of PAHs, as it integrates what we currently know from both, laboratory experiments and theoretical quantum calculations, and puts it all in an astronomical context. The questions we intend to answer in this thesis are the following: *how much of the current knowledge we have on PAHs actually applies in the interstellar medium? What is the link between their specific molecular properties and the astrophysical conditions under which they emit? And how does this determine their role in space?* Starting from how the PAH hypothesis was proposed almost simultaneously by independent scientific teams around the world, to the still pending questions in the field, we will explain where in this storyline, the research projects presented here come into play.

1.1. First is First: What are PAHs?

As their name specifies, *polycyclic aromatic hydrocarbons* (PAHs) refer to a family of planar organic molecules made out of carbon and hydrogen atoms (hence *hydrocarbons*), structured in multiple closed carbon rings (hence *polycyclic*), with the hydrogen atoms attached to the periphery, and whose main characteristic is to be extremely stable due to the ability of the electrons in the π orbitals to delocalize (hence *aromatic*; see Figure 1.1).

These molecules exist in our daily lives, as they are formed whenever and wherever carbon-based materials are burned (e.g., any combustion of fossil fuels, wooden fireplaces, even tobacco smoke). They are currently thoroughly studied in all branches of natural science, as they are considered to be extremely toxic and carcinogenic for terrestrial life. It is paradoxical then, that such dangerous compounds could be ubiquitous in space, and might have a crucial role in the evolution of our universe, and with it, of life as we know it.

In the following pages, we will first describe how their presence in space was inferred, and how the 'PAH hypothesis' was formulated (§1.2). In §1.3 to §1.5 a review will be given on what we know about interstellar PAHs, how they emit, and what PAH properties can be derived from astronomical observations. The concept of 'photodissociation regions' will be introduced (§1.4), as these are the regions where we focus our attention to, in order to study and model PAH emission. Other proposed carriers of the UIR bands will be briefly mentioned in §1.6. Sections 1.7 and 1.8 will then focus on the current state of the field regarding the subjects that are relevant for this thesis. At last, the outline of this thesis will be presented, stating the key questions that are explored in each chapter (§1.9).

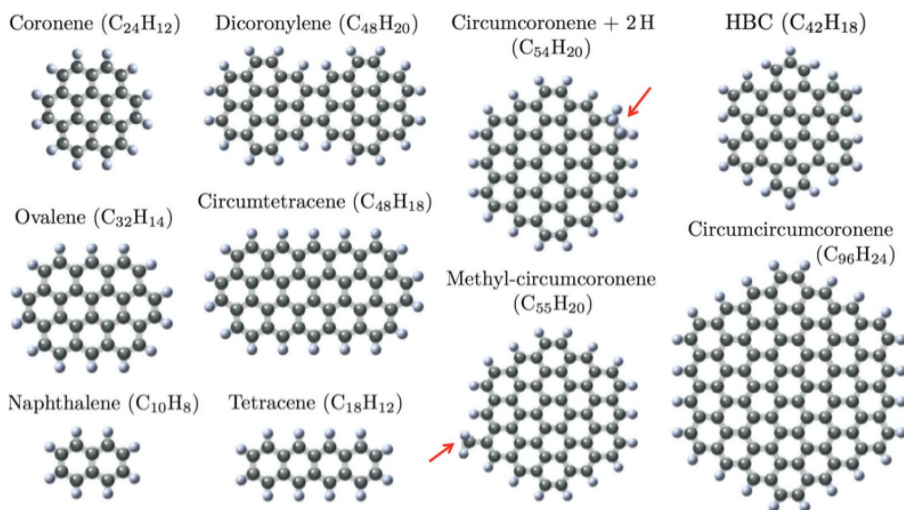


Figure 1.1: Examples of polycyclic aromatic hydrocarbons. Carbon atoms are depicted in grey, while hydrogen atoms are depicted in white. The molecule $C_{54}H_{20}$ corresponds to the circumcoronene molecule ($C_{54}H_{18}$) plus 2 additional hydrogen atoms (that lie perpendicular to the plane of the carbon core; indicated in red), turning each aromatic C-H bond into two aliphatic bonds. Such type of molecule is also referred to as a *superhydrogenated* PAH. The molecule $C_{55}H_{20}$ corresponds to circumcoronene plus a methyl group ($-CH_3$) attached to one of the edge C atoms (indicated in red). This type of PAH is also called a *methylated* PAH.

1.2. A Little Bit of History...

Before the 1950–1960s little was known about how astronomical objects (other than the Sun and the Moon) emitted at mid-infrared wavelengths. Even though infrared emission had been discovered at the beginning of the XIX century—thanks to the research performed by William Herschel—no major breakthroughs on the field of infrared (beyond-our-solar-system) astronomy had been achieved. It was not until the 1960s that infrared astronomy would make a huge leap into becoming what it is today. With the expected constant advent of technology, new telescopes and instruments opened a new spectral window to the rather ‘cool’ universe, which would naturally provide more questions than answers to the contemporary knowledge of astronomers.

The observation of astronomical objects at mid-infrared wavelengths ($3\text{--}13\mu\text{m}$) was pioneered in the 1970s. Little by little astronomers tried to understand the interaction between dust and starlight in different environments. Of particular interest was the discovery of broad bands in the emitted spectra of interstellar material. Gillett et al. (1973) detected very strong and broad emission in the mid-infrared spectrum of two planetary nebulae, BD+30°3639 and NGC 7027 (see also Gillett, Low & Stein 1967). The emission was broad but due to the instrumental spectral resolution, it was too soon to deduce whether there was a single feature, the blend of more than one feature, or just continuum emission. As time passed by, astronomers realized that a set of bands at 3.3 , 6.2 , 7.7 , 8.6 and $11.3\mu\text{m}$ was observed in the spectra of different planetary nebulae, H II regions, stellar objects, and even extragalactic sources (e.g., Grasdalen & Joyce 1976; Russell et al. 1977; Tokunaga & Young 1980; Aitken 1981; Sellgren 1981; Bregman et al. 1983). These bands became known as the Unidentified InfraRed (UIR) bands (see Figure 1.2).

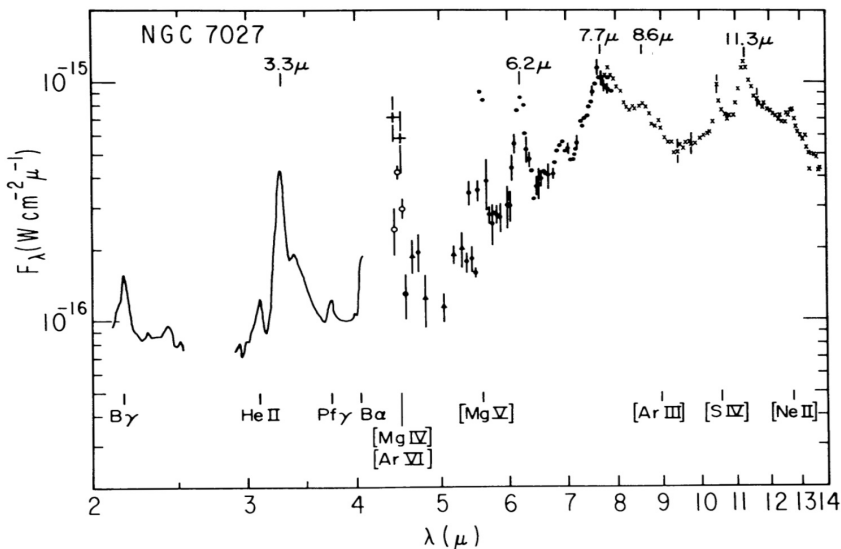


Figure 1.2: Mid-IR spectrum of the planetary nebula NGC7027. The $2\text{--}14\mu\text{m}$ spectrum has been taken from Russell et al. (1977). The spectrum gathers spectrophotometric data taken with the Kuiper Airborne Observatory (KAO) and with the University of Minnesota 1.5 m telescope on Mount Lemmon. This spectrum became the canonical one as it showed all the UIR bands known in the late 1970s.

Soon astronomers realized that the UIR bands appeared only in regions exposed to UV radiation. It was suggested then, that the excitation mechanism had to do with the absorption of UV photons. Two mechanisms of excitation were proposed: infrared fluorescence of molecules frozen on grain mantles (Allamandola et al. 1979), and equilibrium thermal emission of small ($\sim 100 \text{ \AA}$) grains (Dwek et al. 1980).

The work of Kris Sellgren in the early 80s gave further clues to this *long-standing mystery* (Sellgren et al. 1983, Sellgren 1984). By studying the $3.3 \mu\text{m}$ emission of reflection nebulae, Sellgren and coworkers inferred that the continuum emission would have to come from dust grains heated to $\sim 1000 \text{ K}$; a temperature way too high to be accounted for by equilibrium thermal emission from dust grains. They also noticed that even though the intensity of the continuum emission decreased with distance to the star, the derived temperature remained constant. Thus, it was suggested that the emission should come from the transient heating of very small dust grains of about 5 \AA in size. The carriers had to be molecules with a heat capacity small enough, so that they could be rapidly heated to very high temperatures after UV photon absorption (Sellgren 1984).

1.3. PAH Hypothesis

The mystery of identifying the carriers and the excitation mechanism that produced the UIR bands was partially solved with the publication of Léger & Puget (1984), who simultaneously with Allamandola et al. (1985) first proposed polycyclic aromatic hydrocarbons as the carriers of the bands.

Léger & Puget worked based on the premise of transient heating proposed by Sellgren (1984). The presence of PAHs in the interstellar medium (ISM) had already been suggested in the earlier work of Donn (1968), based on his analysis on interstellar extinction curves. Also, Duley & Williams (1981) proposed that the 3.3 and $11.3 \mu\text{m}$ bands were due to C-H aromatic bonds. Léger & Puget then proposed *planar aromatic carbonaceous molecules* as the carriers of the UIR bands: PAHs were the perfect candidate that had a heat capacity small enough to reach the expected high temperatures, without being internally destroyed or destroyed by sublimation, giving rise to an emission which would be independent from the distance to the star.

For its part, Allamandola and co-workers at NASA Ames Research Center showed that the infrared spectrum of a mixture of PAHs displayed features similar to the UIR bands (see left panels of Figure 1.3), as derived from a direct comparison between the Raman spectrum of automobile soot, and the $5\text{--}10 \mu\text{m}$ spectrum of the Orion bar. They also modelled the IR fluorescence from a small PAH, chrysene ($\text{C}_{18}\text{H}_{12}$), formally stating the excitation mechanism that we now accept to be the one producing the bands.

It would take almost a decade for the PAH hypothesis to be widely accepted among the ISM community though (see Donn et al. 1989). Since the excitation mechanism was IR fluorescence after UV absorption, to become formally accepted, the presence of PAHs in space was expected to leave a trace in both parts of the spectrum. In other words, electronic transitions in the UV spectrum had to match the vibrational transitions observed in the infrared.

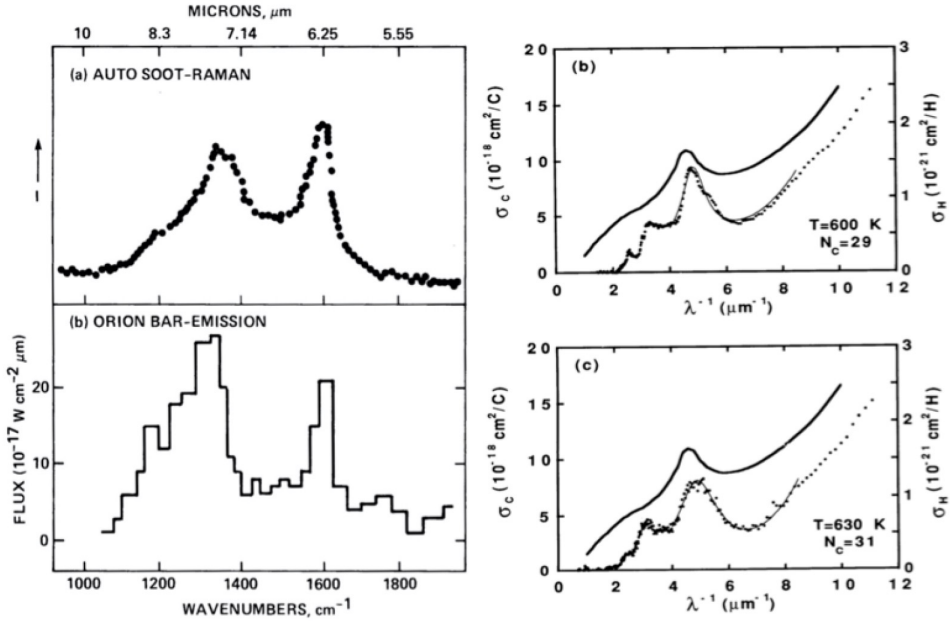


Figure 1.3: *Left panels:* Comparison of the IR Raman spectrum of automobile soot (*top panel*) and the IR spectrum of the Orion Bar (*bottom panel*). This figure has been taken from Allamandola et al. (1985). *Right panels:* Comparison of the absorption cross section of PAH mixtures per carbon atom (*dotted curve*) and the mean interstellar extinction curve derived by Savage & Mathis (1979) (*solid line*). This figure has been taken from Joblin et al. (1992).

Léger et al. (1989) discussed the PAH hypothesis regarding extinction curves, and showed that the UV absorption trace matched closely the overall shape of the UV absorption cross-section of PAHs: PAHs have a feature close to the 2175 Å bump and have the far-UV rise characteristic in interstellar extinction curves (see seminal works of Fitzpatrick & Massa 1986, 1988, 1990; see also Fitzpatrick & Massa 2005, 2007, 2009; Joblin et al. 1992; Li & Draine 2001; Salama 2007; Mulas et al. 2011; see also right panels of Figure 1.3). Accordingly, PAHs would also be proposed as responsible for the so-called Diffuse Interstellar Bands (DIBs; Léger & d'Hendecourt 1985): mysterious narrow features seen in the visible spectral region of the interstellar extinction curves towards background stars (e.g., Merrill 1934; Herbig 1975, 1995; Hobbs et al. 2010).

Subsequently, the PAH hypothesis was refined as different PAHs were being continuously detected in meteorite samples (e.g., Tingle et al. 1991; Kovalenko et al. 1992; Clemett et al. 1992, 1993; De Vries et al. 1993; McKay et al. 1996; Becker et al. 1997; Plows et al. 2003); and more experimental (e.g., Cook et al. 1993; Joblin et al. 1994, 1995), and theoretical spectra of PAH species (e.g., Langhoff 1996; Bauschlicher & Bakes 2000; Hudgins & Allamandola 2004; Mattioda et al. 2005) were obtained, compared and benchmarked. Also, astronomical observations of the PAH bands flourished thanks to the novel spectrometers and spectral imaging capabilities on board the Infrared Space Observatory (ISO), and the Spitzer Space Telescope. These facilities allowed for systematic studies on the mid-infrared emission of astronomical objects (e.g., Hony et al. 2001; Peeters et al. 2002; van Diedenhoven et al. 2004; Rapacioli et al. 2005; Berné et al. 2007; Sellgren et al. 2007; Smith et al.

2007; Galliano et al. 2008; Boersma et al. 2010; Boersma et al. 2014), and have provided (and are still providing) relevant information to test further the PAH hypothesis.

Nowadays we can summarize the PAH hypothesis as follows: the UIR bands we observe in the mid-infrared spectra of regions of dust and gas subjected to UV radiation, come from free-flying PAHs which get rapidly heated by absorbing (visible and) UV photons from their surroundings (Figure 1.4). Each absorption is followed by rapid non-radiative intramolecular processes, e.g., the respective timescales for internal conversion and intersystem crossing are of $\sim 10^{-12}$ s and 10^{-9} s respectively. These processes relax each molecule to its electronic ground state, but leave it vibrationally excited. As PAHs relax further, they emit IR radiation from their vibrational C-C and C-H modes giving rise to the UIR bands (Figure 1.4). The bands we observe then belong to a mixture of PAHs present in the ISM, and not to an individual species.

Interstellar PAHs are expected to have intermediate-to-large sizes (i.e., above 50 carbon atoms), since smaller species are expected to be rapidly destroyed in intense UV fields. The fractional PAH abundance has been estimated to be of about 10^{-7} for intermediate-to-large species (Habart et al. 2004; Tielens 2008). Due to their relatively low ionization potentials ($\sim 4\text{--}7$ eV), they are expected to be mostly in neutral and positively ionized states. Depending on the radiation field under which they emit, they can get ionized, photodissociate, recombine with electrons, react with surrounding atoms through collisions, etc. Therefore, their emission spectra will depend on the radiation field to which they are subjected to, the emission process, and their molecular properties as determined from their photo-chemical evolution. It is precisely this symbiosis what we tackle in this thesis, and we do so by studying PAH emission in the photodissociation regions around stars.

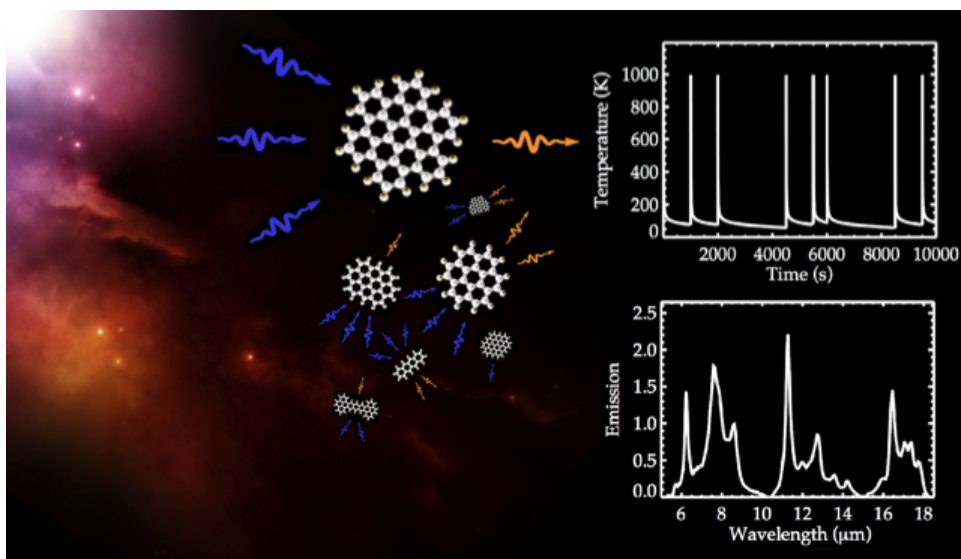


Figure 1.4: Schematic representation of the emission of PAHs in clouds under the influence of UV stellar radiation. When exposed to UV radiation (depicted in purple) PAHs get rapidly heated to high temperatures, and relax through their respective vibrational modes, emitting energy in the IR (orange) giving rise to the emission features also known as UIR bands.

1.4. Photodissociation Regions

Photodissociation regions (PDRs) are the best astronomical laboratories to study PAH emission. They are the UV illuminated surfaces of molecular clouds, where the PAH emission is found to be the strongest (see Figure 1.5). These are regions where the (photo) chemistry is driven by the incident UV radiation that hits the cloud (Hollenbach & Tielens 1999). The physical conditions in a PDR depend then on the intensity of the UV field and the total density. The incident UV radiation is primarily absorbed by PAHs and dust grains, which then re-emit it as IR radiation. PAHs contribute to the heating of the gas in the cloud through the photoelectric effect. Far UV pumping of H_2 is also an important heating mechanism at the edge of the cloud. The gas cools via fine structure lines, mainly $[\text{CII}] 158 \mu\text{m}$ and $[\text{OI}] 63 \mu\text{m}$. Deeper in the clouds ion-neutral chemistry is driven by cosmic ray ionization. Observationally then PDRs are bright in PAH emission, far-IR atomic fine structure lines, pure rotational lines of H_2 and (low-J) CO; UV pumped ro-vibrational transitions of H_2 , and mid/far-IR continuum emission associated with warm dust.

Figure 1.6 shows the mid-IR spectra of the PDRs in the Orion bar and NGC 7027. Aside from atomic and H_2 emission lines, we see the PAH bands very clearly. PAHs as aromatic hydrocarbons have very well known vibrations associated to their structure: the $3.3 \mu\text{m}$ band corresponds to the relaxation of aromatic C-H stretching modes; the $5 \mu\text{m}$ region is due to combination modes; the $6.2 \mu\text{m}$ band corresponds to aromatic C-C stretching modes;

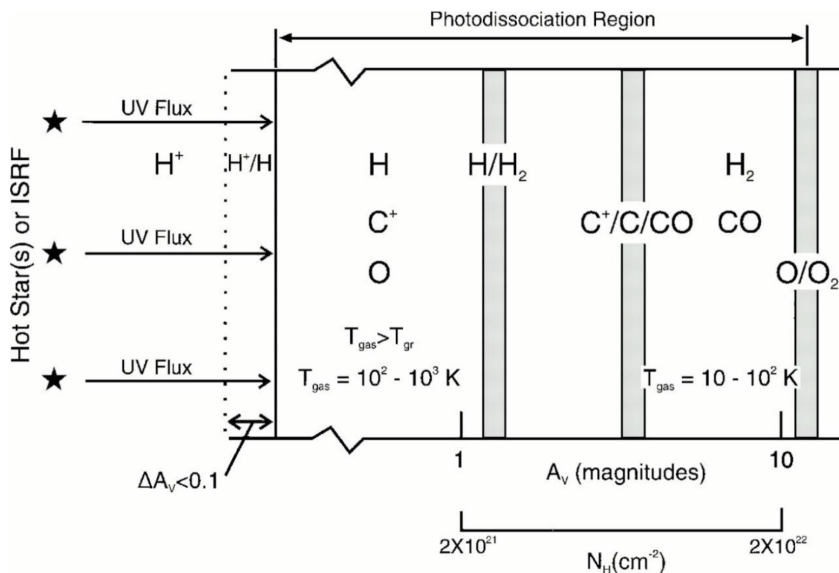


Figure 1.5: Structure of a prototypical PDR. At the surface of the cloud, UV stellar radiation ($< 13.6 \text{ eV}$) keeps the atomic material mostly ionized. The conversion from neutral hydrogen to molecular hydrogen H_2 occurs deeper into the cloud. Going into the PDR, the material goes from being mostly atomic into a molecular regime (conversion from CII to CI to CO). The gas temperature decreases as the extinction A_v increases, reaching similar values to the dust temperature.

the $7.7\mu\text{m}$ band comes from C-C stretching modes and C-H in-plane bending modes; the $8\text{--}9\mu\text{m}$ region corresponds to C-H in-plane wagging modes; the $11\text{--}15\mu\text{m}$ region on the other hand appears to be more sensitive to the edge structure of PAHs, where the 11.3 and $12.6\mu\text{m}$ bands correspond to C-H out of plane bending modes of peripheral rings with 1 and 3 hydrogen atoms respectively (e.g., Allamandola et al. 1989; see Tielens 2008 for a more updated review).

Throughout this past decade, Spitzer observations have allowed the detection of other spectral features at 15.9 , 16.4 , 17.0 , 17.4 and $17.8\mu\text{m}$, which have also been ascribed to PAHs (Moutou et al. 2000; Sellgren et al. 2007). These bands have been associated to PAH edge structure, bending motions of the carbon core, and size (Boersma et al. 2010; Ricca et al. 2010, 2012; Peeters et al. 2012). However no clear consensus has been reached yet, as some of the features have also been linked to fullerenes (i.e., molecules of only carbon in the form of a hollow sphere; Sellgren et al. 2010; Bernard-Salas et al. 2012).

Together with the PAH bands, the mid-infrared spectra of PDRs also show broader emission underneath the bands, e.g., below the $3\mu\text{m}$ complex, at $\sim 6\text{--}9\mu\text{m}$, $11\text{--}15\mu\text{m}$ and $15\text{--}20\mu\text{m}$ (e.g., van Kerckhoven et al. 2000; Sellgren et al. 2007). These broad features are referred to as the *plateaus*. Currently, there is a debate on the origin of this emission: plateaus may be considered as the blending of the 'tails' of PAH bands (implying a PAH origin; see Bregman et al. 1989; Sellgren et al. 2007; Galliano et al. 2008), or they may arise from a different carrier that somehow co-exists with PAHs (Boersma et al. 2010; Bernard-Salas et al. 2012; García Hernández et al. 2012; Peeters et al. 2017).

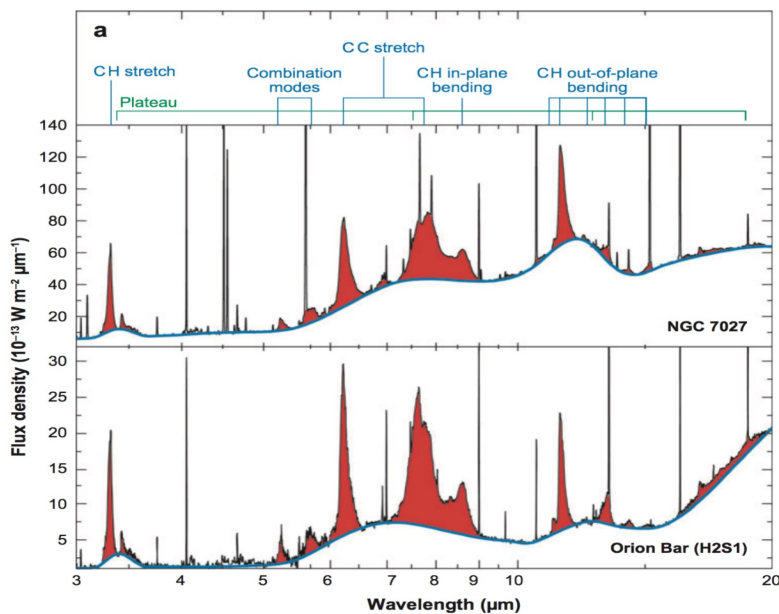


Figure 1.6: The mid-infrared spectra of the PDRs in the Orion Bar and in NGC7027. This figure has been taken from Tielens (2008) (adapted from Peeters et al. 2002). The top panel indicates the vibrational modes of PAHs.

1.5. PAHs Through The Observation of PDRs

Spectral mapping of PDRs, as well as spectral comparison of large samples of sources, provide a powerful tool to study the characteristics of interstellar PAHs. Techniques like principal component analysis (Rapacioli et al. 2005) and blind-signal separation (Berné et al. 2007; Rosenberg et al. 2011), have been applied to analyze the mid-infrared spectrum of different PDRs, where the observed emission is decomposed into independent components. By jointly studying the spatial distribution of such components, together with the analysis of the vibrational spectra of PAHs, some links can be made between the general properties of the emitting PAH population and the relative strength of some PAH bands (see also Pilleri et al. 2012, 2015).

In order to exemplify this, in the following paragraphs we present the relations that (through both theory and experiments) have been found to arise with PAH a) charge, b) composition, c) size and d) edge-structure (Figures 1.7 and 1.8). Based on these relations and the observation of PDRs, astronomers have been able to characterize the population of emitting PAHs. The upcoming discussion is based on the PAH IR spectra as seen in *absorption*, so keep in mind that in order to compare both, these spectra and the observations *directly*, an emission model has to be applied to the intrinsic PAH spectra.

1.5.1. Charge

When comparing the IR spectra of a given PAH in different charge states (see top panel of Figure 1.7), we notice the C-C modes are intrinsically stronger in cationic species, while C-H modes are stronger in neutral species (e.g., Langhoff 1996; Allamandola et al. 1999; Bauschlicher et al. 2008). Correspondingly, the ratio between the 6.2 and 11.3 μm bands has been linked to the ionization conditions in the astronomical environments under which PAHs emit, and its ratio is currently used as a measure of the level of ionization of PAHs (Hony et al. 2001; Peeters et al. 2002; Bregman & Temi 2005; Galliano et al. 2008; Berné et al. 2007; Boersma et al. 2013; Boersma et al. 2016). This in turn has important effects on the heating of the gas in a PDR, as the photoelectric effect on PAHs is less efficient in positively ionized species (Tielens 2005).

1.5.2. Composition-Hydrogenation

After UV absorption a PAH can also dissociate and fragment depending on how much energy is absorbed, and on how such energy is distributed within the available decay channels of the molecule. The bottom panel of Figure 1.7 shows how the spectra of a small compact PAH such as coronene ($\text{C}_{24}\text{H}_{12}$) varies with variable hydrogen content. We see that the PAH with 1 hydrogen atom per peripheral carbon atom (i.e., $\text{C}_{24}\text{H}_{12}$) has intrinsically strong C-H modes compared to the carbon cluster analogue C_{24} which is, as expected, devoid of C-H stretches. Once there are aliphatic groups attached to the molecule (e.g., 2 hydrogen atoms per peripheral carbon atom, $\text{C}_{24}\text{H}_{24}$) we see that new features arise, especially in the 3 μm region. However, as also PAHs with methyl ($-\text{CH}_3$) groups attached show additional bands at similar wavelengths (see more in Chapter 3 of this thesis), this spectral region is still rather puzzling to explain in astronomical observations.

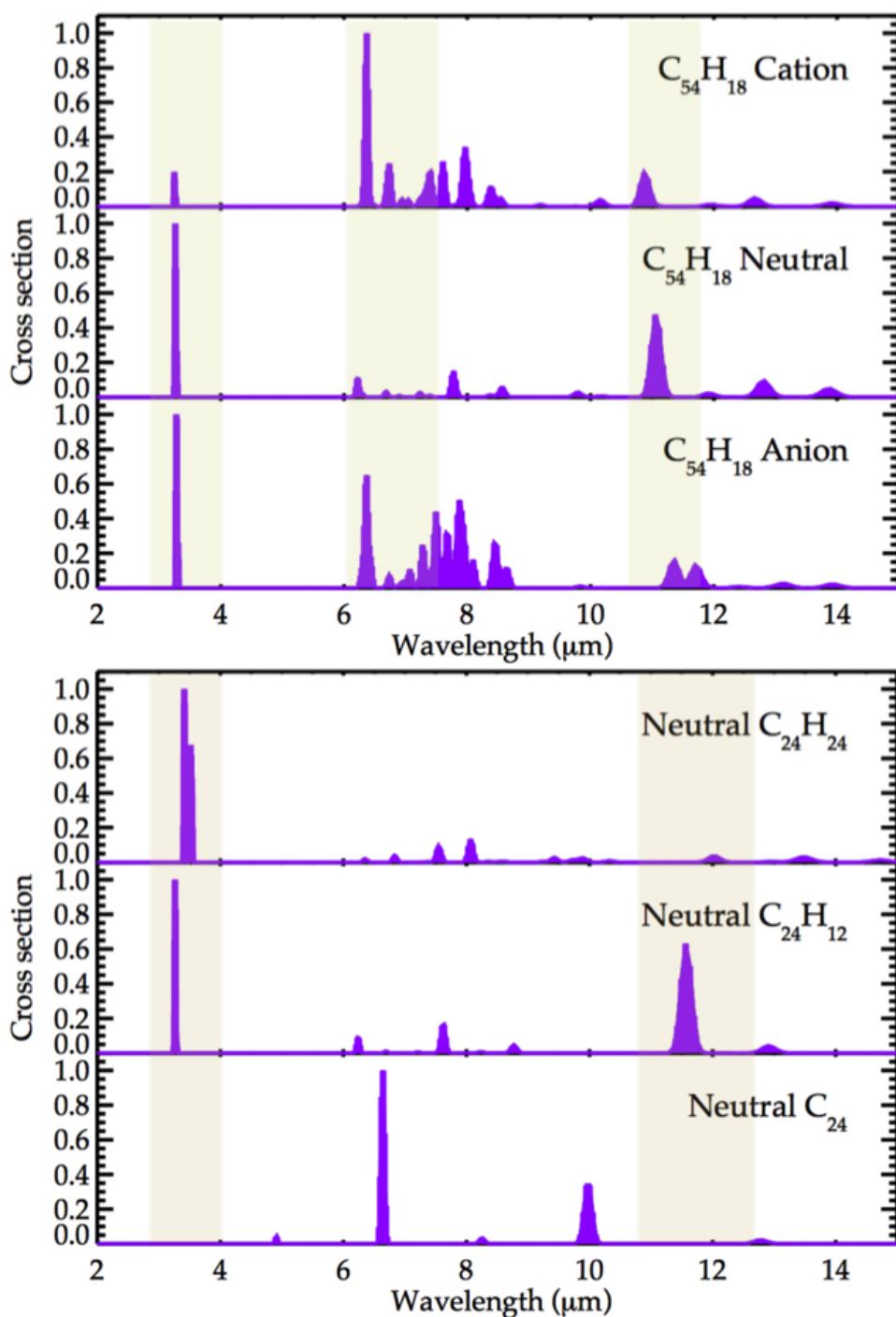


Figure 1.7: Comparison of IR cross sections of PAHs showing how charge state and hydrogenation level affect their intrinsic modes. All spectra have been retrieved from the NASA Ames PAH IR Spectroscopic Database, which contains hundreds of theoretical spectra of different PAHs (further insight on this database will be found in Chapter 2). All IR cross sections have been normalized to the peak intensity of its most prominent feature.

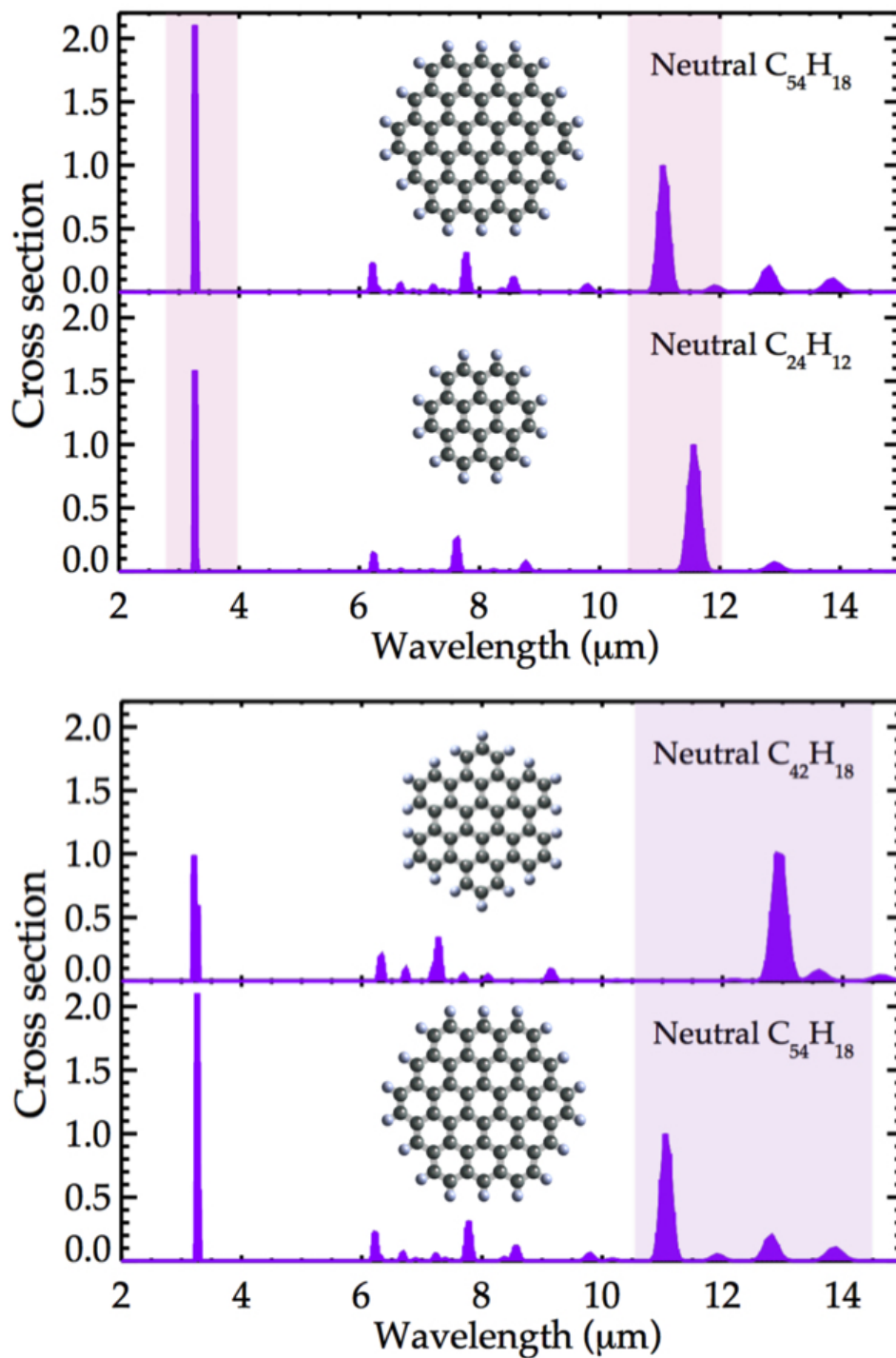


Figure 1.8: Comparison of IR cross sections of PAHs showing how size (i.e., number of carbon atoms) and edge-structure affect their intrinsic modes. Unlike Figure 1.7, the normalization is based on the peak of the most intense feature at long wavelengths ($> 10 \mu\text{m}$).

Aside the hydrogenation level of PAHs, these molecules can also have other elements and/or functional groups, which modify their transitions (Hudgins, Bauschlicher & Allamandola 2005; Bauschlicher et al. 2008). For example, nitrogenated PAHs (also called PAHNs) have been invoked to explain shifts of the $6.2\mu\text{m}$ band observed in some astronomical environments (Peeters et al. 2002), which otherwise cannot be explained by 'normal' (i.e., only hydrogen atoms aside carbon) PAHs (Hudgins, Bauschlicher & Allamandola 2005).

1.5.3. Size

Differences in PAH size (i.e., number of carbon atoms) also affect their IR cross sections. The top panel of Figure 1.8 shows an example comparing PAHs of increasing size from 24 to 54 carbon atoms. Even though the edge-structure is slightly modified, we see a variation in the relative strength of the 3.3 and $11.3\mu\text{m}$ features (Allamandola et al. 1989; Ricca et al. 2012; see also Chapter 3). In *emission*, small PAHs can excite more easily the $3\mu\text{m}$ region, as they get more heated than the larger molecules, and therefore we expect the $3.3/11.3$ ratio to decrease with increasing PAH size within a given charge state (see Chapter 3). Recently, this ratio was used as an indicator of the PAH size distribution in the reflection nebulae NGC7023 using new data from the Stratospheric Observatory For Infrared Astronomy, SOFIA (Croiset et al. 2016). However caution must be taken when using the $3.3/11.3$ as a tracer of PAH size, as other aspects of PAHs can affect this ratio as well (see more in Chapter 3). Also the $3\mu\text{m}$ region is very sensitive to how the PAH emission spectra is modelled, as it can be highly affected by anharmonicities and combination modes; something theoretical calculations are currently investigating (Mackie et al. 2015; Maltseva et al. 2016; Candian & Mackie 2017). More insights will also come up in time as the James Webb Space Telescope (JWST) will provide spectroscopic observations of the $3\mu\text{m}$ region, a spectral region not covered by Spitzer data.

1.5.4. Edge-Structure

Lastly, as we mentioned before, the $11\text{--}15\mu\text{m}$ region is more sensitive towards the molecular structure of PAHs (e.g., Hony et al. 2001; Bauschlicher et al. 2008). The bottom panel of Figure 1.8 shows that in molecules with more edge-structure (e.g., $\text{C}_{42}\text{H}_{18}$), bands in the long-wavelength region become intrinsically stronger (Boersma et al. 2010). In fact we see that the $11.3\mu\text{m}$ band disappears as no solo-rings (i.e., peripheral rings that can only attach 1 hydrogen atom) are present in $\text{C}_{42}\text{H}_{18}$ (see also the top panel of Figure 1.8, where increasing the size of the molecule adds solo-rings to the edges). This supports the motion that most interstellar PAHs must be compact, as the $11.3\mu\text{m}$ band is almost always present in the IR spectra of astronomical objects. The bands at 12.6 , 13.5 and $14.0\mu\text{m}$ then have been ascribed to different edge-structures, and the $12.6/11.3$ ratio has been used as a tracer of molecular structure of PAHs in astronomical sources (Bauschlicher et al. 2008; Tielens 2008; Candian, Sarre & Tielens 2014).

1.6. Other Carriers

Even though the PAH hypothesis is relatively well-established among the community, other carriers have been proposed as well (although these have not been extensively explored as PAHs have). These are mainly amorphous solids with a mix of aromatic/aliphatic compounds, among which there is the hydrogenated amorphous carbon HAC (Jones et

al. 1990; Buss et al. 1990; Gadallah et al. 2012), quenched carbonaceous composites (QCC; Sakata et al. 1987, 1990), soot (Hu & Duley 2008), coal or kerogen (Papoular et al. 1989), and more recently, Mixed Aromatic/Aliphatic Organic Nanoparticles (MAONs; Kwok & Zhang 2011, 2013). Most of these propose that the UIR bands arise from the excitation of small thermally-isolated aromatic units within or attached to the bulk materials.

The proposal of such carriers is mainly based on two arguments: the missing link to the UV spectral region (see Salama 2007 and Pino et al. 2011 for reviews on the electronic spectra of PAHs and the DIBs discussion), and the missing individual identification of PAHs (Ali-Haïmoud 2013). However both subjects are challenging as experiments are technique-limited (Pino et al. 2011), and astronomical observations rely either on *i*) the far-IR spectral region where carbon-skeleton modes are intrinsically weak, or may be simply hampered by the strong continuum from larger dust grains, or *ii*) rely on rotational spectroscopy, which is limited to PAHs with a dipole moment (e.g., bowl-shaped, PAHNS, among others).

1.7. Current State of the Field

In the following paragraphs we will first give an overview of the contemporary research performed on PAHs, focusing the attention on the topics relevant for this thesis.

1.7.1. Infrared Spectra of PAHs

Laboratory and theoretical studies have altogether allowed a better assessment of the bands and PAH emission process (see Oomens et al. 2003 and 2006 for reviews on experiments, and see Pauzat 2011 and Candian & Mackie 2017 for reviews on theoretical calculations). Nowadays, hundreds of intrinsic IR PAH (theoretical and experimental) spectra are available to the community, and databases such as the NASA Ames PAH IR Spectroscopic Database¹ (Bauschlicher et al. 2010; Boersma et al. 2014) and the Cagliari PAH Database² (Mallocci et al. 2007) currently offer an opportunity to study PAH emission in a systematic manner, and even compare it to space observations. Such resources are now starting to be used to analyze astronomical spectra (Cami 2011; Rosenberg et al. 2011; Boersma et al. 2014; Andrews et al. 2015, Chapter 2). Care must be taken though, as the previously mentioned databases are not complete (i.e., do not have all PAH classes well-represented), and thus a good handling of their biases and caveats is mandatory before interpreting the results.

The feedback between theoretical computations and laboratory studies is relevant when analyzing PAH properties. Laboratory studies in gas-phase are currently limited to mostly small (less than 50 carbon atoms) cationic and radical species (e.g., Joblin et al. 1994, 1995; Oomens et al. 2000, 2003, 2006; Bakker et al. 2011). While the bulk of the experimental spectra of (cationic) PAHs was obtained through matrix isolation spectroscopy throughout the 90s and early 2000s (see Joblin et al. 1994 for an analysis on possible matrix effects), at present the leading technique in the field is the infrared multiphoton dissociation spectroscopy (IRMPD) using a free electron laser (Oomens et al. 2000; Lorenz et al. 2007). This technique gives the IR spectra of gas-phase PAHs, however it has been mostly used for small cationic species (Oomens et al. 2006). Even though positively ionized species are indeed

¹<http://www.astrochem.org/pahdb>

²<http://astrochemistry.iaa-cagliari.inaf.it/database/>

important—as they are expected to be the dominant population in warm ionizing regions—neutral species are also relevant and experimental studies are unfortunately scarce (Cook et al. 1996, 1998; Piest et al. 2001; Mattioda et al. 2009). The other limitation regarding PAH size is also given by the commercial unavailability of pure PAHs with more than 42 carbon atoms, which forces most experiments to be performed on smaller species.

For its part, quantum chemistry calculations within the framework of Density Functional Theory (DFT), while extensively used to predict spectral properties of PAHs, still have some issues. Most calculations have been performed on small species, since larger systems are computationally demanding. Symmetry breaking artifacts in open-shell molecules are still problematic, as they produce abnormally large intensities and a significant shift of the bands (Pauzat 2011; Bauschlicher 2016). Theoretical calculations require experiments for benchmarking non-standard systems (e.g., partially hydrogenated PAHs; Ricca et al. 2011; Bauschlicher & Ricca 2013). Also more experiments are required to find the proper scale factors to bring the theoretical harmonic frequencies into agreement with the experiments³.

1.7.2. Emission Model

In order to compare theoretical (absorption) spectra of PAHs to astronomical spectra, a model of the emission process has to be assumed (Schutte et al. 1993; Cook & Saykally 1998; Pech et al. 2002; Mulas et al. 2006). Such a model requires PAH molecular properties like the UV absorption cross-section, and the IR vibrational transitions. Putting aside the fact that the UV absorption cross-sections have been calculated only for few small species (up to the size of circumovalene $C_{66}H_{20}$) and are limited in accuracy to ± 0.3 eV (Mallocci et al. 2007), some important assumptions have to be made. Several parameters need to be assumed since they are not well understood by theorists, such as the profile, width and shift of the bands (Pech et al. 2002; Joblin et al. 1995). The profile and width of the bands reflect intra/inter-mode anharmonicities coupled with the non-radiative vibrational redistribution process of the absorbed energy (e.g., Pech et al. 2002). The shift of the bands also arises from anharmonic effects throughout the emission process. Joblin et al. (1995) is still the only experimental evaluation of the shift induced on vibrational modes as a function of internal energy, performed on a handful of neutral PAHs. On the other hand, theoretical studies are now flourishing on the subject of anharmonicities, and we expect lots of interesting results in the upcoming future (Calvo et al. 2011; Mackie et al. 2015; Maltseva et al. 2016).

1.7.3. Photochemistry of PAHs

Other still pending issues involve not only finding a viable route of formation of PAHs in the envelopes of asymptotic giant branch stars (Latter 1991; Frenklach & Feigelson 1989; Cherchneff, Barker & Tielens 1992; Sloan et al. 2007; Lau et al. 2016), but also the photochemistry that guides their evolution (Jochims et al. 1994; Le Page et al. 2001; 2003; Bakes et al. 2001; Montillaud et al. 2013; Berné et al. 2015). Focusing on the latter, the photochemistry of PAHs is extremely important to better assess the role of PAHs in the ISM. Based on theoretical and experimental results, astrophysical models can be applied to interpret the spectral variations observed within astronomical objects.

³<http://cccbdb.nist.gov/vibscalejust.asp>

Ionization of PAHs has been extensively investigated since the 90s, in terms of both photoionization yields, and the calculation of ionization potentials and electron affinities for some PAH molecules (e.g., Verstraete et al. 1990; Jochims et al. 1996, 1997; Duncan et al. 1999; Mallocci et al. 2007). Hydrogen, carbon and acetylene losses are currently under investigation, as well as isomerization of PAHs (Stockett et al. 2015; Zhen et al. 2015; Bouwman et al. 2016). Regarding kinetic parameters, the time-dependent mass spectrometry experiments on small cations performed by Ling and co-workers in the 90s (e.g., Ling et al. 1995) are still unique in their field, and unfortunately similar experiments have still not been carried out on larger species. What it is now mostly studied instead, is the energetic competition between ionization and photodissociation in PAHs (e.g., mass spectrometry experiments; see Reitsma et al. 2014; Zhen et al. 2014, 2015). PAHs appear to lose their hydrogens in pairs independently of their edge structure (work in progress at Sackler Laboratory). Exposure of PAH cations to synchrotron radiation of 8–40 eV, suggests PAHs of different sizes (24–42 carbon atoms) undergo different relaxation channels after photon absorption; with small PAHs being rapidly destroyed, while larger species go through several ionization steps before starting to lose any hydrogen atom (Zhen et al. 2014, 2015).

Few models then have been developed in order to incorporate the studied photochemistry into an astronomical context. Most of the kinetic models consider either generic properties for the PAHs (Allain et al. 1996; Le Page et al. 2001, 2003), and/or limit their analysis to the study of the abundance of PAH species (i.e., Montillaud et al. 2013). The astrophysical modelling of the PAH emission obtained from using specific molecular properties was first performed by Bakes et al. (2001), who focused only on the charge distribution of the species and its effect on the emitted spectra. Chapter 3 of this book constitutes the first attempt to model PAH emission from specific molecules under realistic astrophysical conditions, using the properties specific to each molecule.

1.8. In This Thesis

We have seen the PAH field evolves from the constant interaction between experimentalists, theorists, modellers and observers. While laboratory research and quantum chemical calculations together set up the molecular properties of PAH species, astronomers on the other hand, retrieve as much information as possible from the space observations. Nowadays, the PAH field is advanced enough to start implementing all these results into astronomical models, in order to study PAHs from a molecular groundwork. In this regard, the research projects presented in this thesis do precisely that. They constitute a first attempt to gather the vast current knowledge available on specific PAH molecules (not using generic properties), and put it in an astrophysical context, and with it, target some of the key subjects of the field such as: the existence of the so-called *grandPAHs* in space (§1.8.1); the role of PAHs in the formation of H₂ in PDRs (§1.8.2); the abundance of *superhydrogenated* PAHs and their contribution as a carrier of the 3.4 μ m band observed in PDRs (§1.8.3); and the deuterium fractionation in PAHs, and their consequent role in explaining the observed deuterium abundance in the local ISM (§1.8.4).

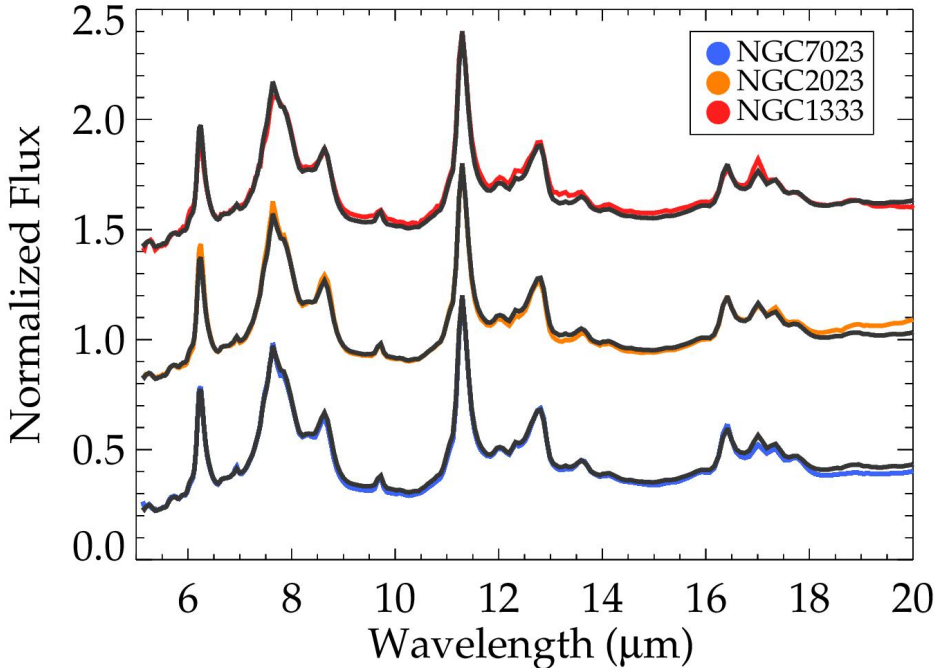


Figure 1.9: Comparison of the spectra taken at the brightest mid-IR spot of three different nebulae: NGC7023, NGC2023 and NGC1333. The spectra have been taken with the InfraRed Spectrograph (IRS) on board the Spitzer Space Telescope. All spectra have been normalized to the peak intensity of the $11.3\mu\text{m}$ band. The average of the three normalized spectra is plotted in black. As clear from the Figure, despite the infinite possibility of PAH mixtures in the ISM, the mid-IR spectra at the brightest spots of different PDRs is remarkably similar (Werner et al. 2004, 2009). This has led the community to wonder about the possibility of having a unique mixture of the most stable PAHs emitting at these 'extreme' spots. Chapter 2 of this thesis is the first attempt to explore the grandPAH hypothesis by using the available PAH spectra of the NASA Ames PAH IR Spectroscopic Database.

1.8.1. The GrandPAHs

Tielens (2013) first formally proposed the concept of *grandPAHs*, as a set of the most stable PAH species that are able to survive the harsh conditions of the ISM. The idea of having a sort-of unique mixture of PAHs emitting in the most extreme regions of the ISM, was motivated by the relatively similar PAH emission detected in different interstellar sources, specially at $15\text{--}20\mu\text{m}$ which is the region expected to trace the more specific structure of PAHs (Boersma et al. 2010, Ricca et al 2010; see Figure 1.9). Since their proposition, the concept of grandPAHs has been mentioned in some works (e.g., Ali-Haïmoud 2014; Peeters et al. 2017). However it has not been explored in any way. Chapter 2 constitutes the first attempt to do this. Given the current availability of PAH spectra thanks to the NASA Ames PAH IR Spectroscopic Database, we have now an actual tool to explore how feasible it is to have grandPAHs in space. If present, their relevance would be extremely helpful in simplifying the picture for the scientific community, as only a handful of species would be important to understand what happens with the carbonaceous material in PDRs.

1.8.2. Formation of H₂ in Clouds

Molecular hydrogen is the most abundant molecule in space. It plays an important role in the thermal balance and chemistry of the ISM. However, the formation of molecular hydrogen in interstellar clouds has been puzzling astronomers since the early 70s. As molecular hydrogen cannot be formed effectively in gas-phase reactions (Gould & Salpeter 1963; Duley & Williams 1984), it has long been suggested that molecular hydrogen can instead be formed through surface reactions on dust grains (Hollenbach & Salpeter 1970, 1971). The main formation mechanism proposed, considered that a hydrogen atom could first be adsorbed on a dust grain, diffuse throughout its surface, eventually interact with another hydrogen atom, and form an H₂ molecule, which would be desorbed into space. Following this scenario, assuming an efficiency formation of H₂ close to unity, can lead to a rate of $\sim 10^{-17}$ cm³/s, in agreement with the observed estimates for diffuse clouds (Jura 1975). However later observations of PDRs led to rates a factor of 10 higher, which could not be explained by such mechanism (Habart et al. 2003, 2004). Throughout the years, theoretical and experimental studies of H₂ formation on dust grains have shown that different mechanisms work at different dust temperatures (Duley 1996; Pirronello et al. 1997, 1999; Katz et al. 1999; Cazaux & Tielens 2002, 2004; Cuppen & Herbst 2005; Le Petit et al. 2009; Le Bourlot et al. 2012; Bron et al. 2014). Langmuir-Hinshelwood reactions —where two physisorbed mobile hydrogen atoms interact on the surface, and desorb as H₂— appears to be efficient only at grain temperatures below 20 K (Pirronello et al. 1997, 1999). Eley-Rideal reactions on the other hand —where a free hydrogen atom interacts with an already chemisorbed hydrogen atom, and desorb as H₂— has been found to be efficient at much higher temperatures (e.g., Duley 1996, Le Bourlot et al. 2012). PAHs have been invoked to be effective at temperatures where larger dust grains are not (Le Bourlot et al. 2012; Bron et al. 2014). Indeed correlations between H₂ and PAH emission in PDRs have been observed (e.g., Habart et al. 2003, 2004). More recently, experiments on the bombardment of PAHs with deuterium atoms have shown that H₂ can be formed through Eley-Rideal abstraction processes (Thrower et al. 2011; Mennella et al. 2012; see Figure 1.10). Theoretical calculations also support these results (Rauls & Horn aker 2008). In Chapter 3 we will address this issue from the PAH perspective using a kinetic model. This will naturally allow an analysis on the formation of H₂ on PAHs, as derived from the resulting abundance distribution of 3 specific PAH molecules of different (astrophysically-relevant) sizes.

1.8.3. Superhydrogenated PAHs and The 3.4 μm Carrier

Among the observed PAH bands in the mid-IR spectra towards PDRs, aside the main band at 3.3 μm there are weak features that appear in the 3 μm region at 3.4, 3.47, 3.51 and 3.56 μm (see Figure 1.11; Joblin et al. 1996; Pilleri et al. 2015). Their carrier is still unknown (Joblin et al. 1996; Onaka et al. 2014; Pilleri et al. 2015). These could be hot bands of the 3.3 μm mode (Barker et al. 1987), the C-H stretching modes of aliphatic side groups attached to PAHs such as methyl functional groups (Duley & Williams 1981; Li & Draine 2012; Yang et al. 2013, 2016; Sadjadi et al. 2015), or they could be due to PAHs with extra hydrogens (i.e., *superhydrogenated* species; Bernstein et al. 1996; Sandford et al. 2013). The question mark on the carrier of the 3.4 μm band is a recurrent topic in the field. As the knowledge on the photochemistry of PAHs increases, the physics behind superhydrogenated species can be better understood. In Chapter 3 we will study the hydrogenation of specific PAHs with different sizes, and therefore we will naturally tackle the question whether superhydrogenated species can be the solely carriers of the 3.4 μm band.

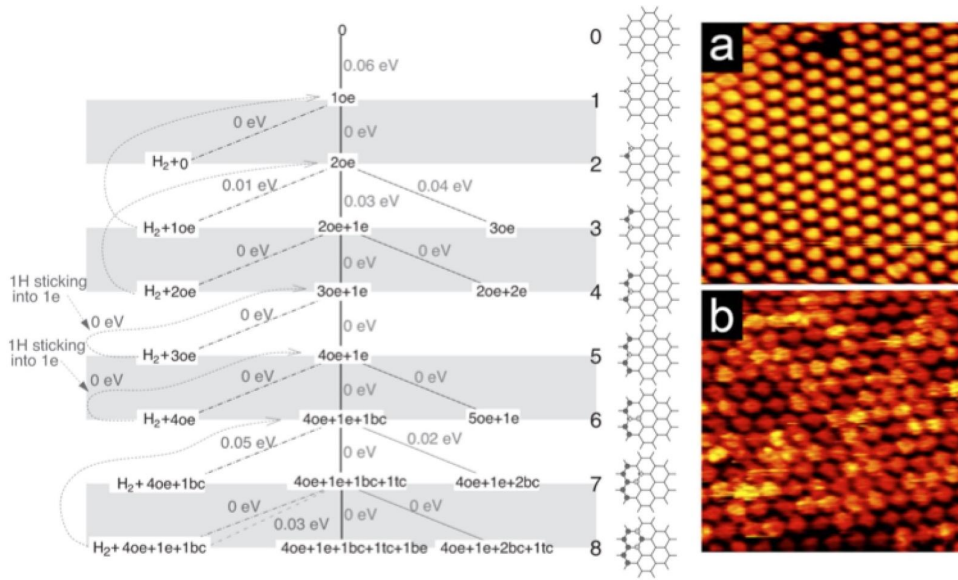


Figure 1.10: Theoretical and experimental results on the formation of H_2 in PAHs. The figures have been taken from Thrower et al. (2011). The right panels correspond to scanning tunneling microscopic images of a monolayer of coronene molecules before (a) and after (b) deuterium bombardment. The left panel shows the DFT calculations on the H_2 formation on coronene presented in Rauls & Horn aker (2008). The central line shows the most energetically favourable route of hydrogenation and H_2 abstraction. For example: starting from the top to bottom, the first hydrogen is attached to an outer edge (oe) of the coronene molecule with a reaction barrier of 0.06 eV; the addition of a second H atom is barrier-less for the adjacent outer edge position; abstraction of H_2 from these positions are essentially barrier-less (there is only a 0.01 eV barrier for the abstraction of one of the two extra H atoms). In general we see that once 1 H atom is added, the following additions require very small barriers (if any). The abstractions of H_2 are also mostly barrier-less processes.

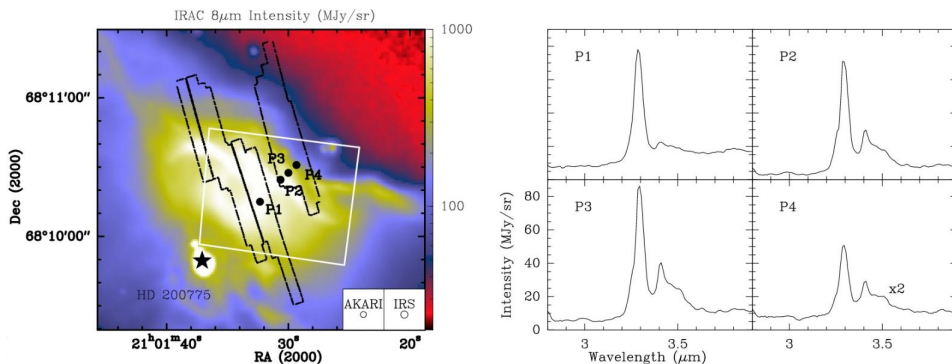


Figure 1.11: Observations of the $3\mu m$ complex from the north-western PDR of NGC 7023. The spectra have been taken with the AKARI satellite. This figure has been taken from Pilleri et al. (2015).

1.8.4. Deuterium Fractionation in the Local ISM

The abundance of deuterium relative to hydrogen (D/H) is an important value that helps constrain the baryonic content in the Universe, since its evolution with cosmic time is expected to steadily decrease as deuterium is heavily processed in stars (Mazzitelli & Moretti 1980; Linsky et al. 2006; Linsky 2010; Tosi et al. 2010). Recent estimates of the primordial (D/H) ratio have led to values of $\sim 2.5 \times 10^{-5}$ (Srianand et al. 2010; Coc et al. 2015; Cooke & Pettini 2016). For its part, the local (D/H) ratio shows a wide range of values between $0.5\text{--}2.2 \times 10^{-5}$ in the galactic disk, with a value of 1.6×10^{-5} within the Local Bubble (Wood et al. 2004; Linsky et al. 2006; Linsky 2010; see Figure 1.12). This variation in the local ISM is very confusing as it cannot be explained by current models of chemical galactic evolution. In order to explain such variation, infall of unprocessed gas in the galaxy and deuterium depletion onto dust grains have been proposed (Jura 1982; Draine 2004; Prochaska et al. 2005; Romano et al. 2006; Linsky et al. 2006). The latter is strongly supported as correlations between the gas-phase (D/H) ratio and the depletion of refractory metals have been found in different lines-of-sight (Linsky et al. 2006). PAHs then, as an important part of the dust population, have been proposed as important reservoirs of deuterium in space (Tielens 1997; Millar et al. 2000; Draine 2006). Evidence for the presence of deuterated PAHs is motivated by the detection of bands in the $4\mu\text{m}$ spectral region of PDRs (Peeters et al. 2004; Onaka et al. 2014; Doney et al. 2016), which is where C-D stretching modes are expected to be found. Indeed, the IR spectra of few deuterated PAHs show bands at wavelengths coinciding with the observations (Hudgins et al. 2004; Buragohain et al. 2015, 2016). Also the energy difference between C-H and C-D bonds is expected to favour deuteration of PAHs. We address this issue in Chapter 4 within the kinetic model presented in Chapter 3, in order to explore how the (D/H) in PAHs varies with astrophysical conditions.

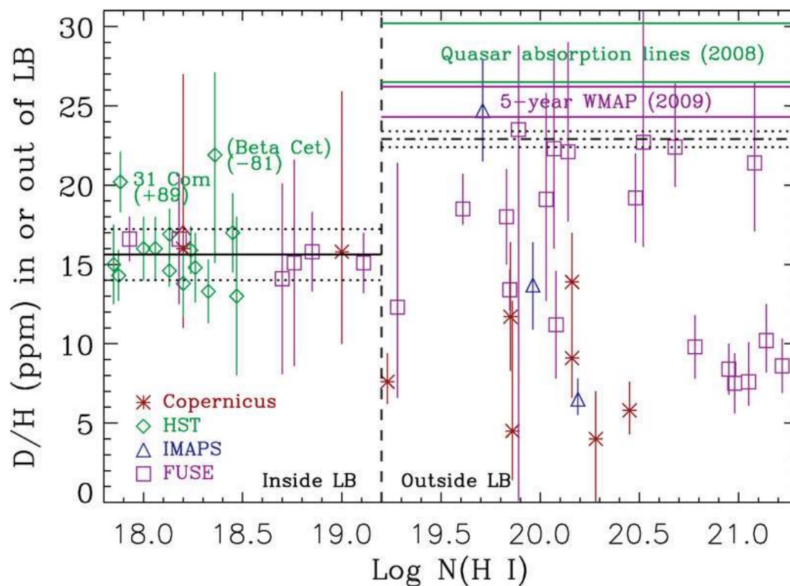


Figure 1.12: Measurements of the (D/H) ratio within and outside the Local Bubble (LB). The upper right corner shows the range of cosmic (D/H) values as derived from quasar absorption lines and from the cosmic microwave background signal. This figure has been taken from Linsky (2010).

1.9. Outline of This Thesis

Chapter 2 As previously mentioned, in this chapter we explore the existence of grandPAHs in the ISM. We do this by using the available data on different PAH species compiled in the NASA Ames PAH IR Spectroscopic Database. The motivation arises from the analysis of the mid-IR spectra of three well-studied nebulae: NGC 7023, NGC 2023 and NGC 1333. The spectra correspond to the brightest spots of PAH emission within the respective PDRs (see Figure 1.9). The PAH emission looks strikingly similar even though these are different lines-of-sight, there are different physical conditions, and all objects present large variations of the PAH emission within themselves. Having all this in mind, the question of whether there could be remarkably similar PAH mixtures emitting at these spots naturally arises. In this way, we call upon the concept of *grandPAHs* proposed in Tielens (2013): a set of the most stable PAH species that are able to survive the intense processing in the ISM, and as such, dominates the PAH population in space. We tackle this proposition for the first time ever, and we also do it in a novelty way by using the available IR spectra of hundreds of PAHs compiled in the NASA Ames PAH IR Spectroscopic Database mentioned earlier. In fact, this is the first work that has made use of this database to fit the observations modelling consistently the emission spectrum of each PAH considering the radiation field under which they emit. In this way, we point out and deal with the uncertainties involved in modelling the PAH emission process, keeping also in mind the caveats when fitting astronomical spectra using a database like the NASA Ames one (see also Boersma et al. 2013).

Chapter 3 There are different techniques by which the properties of PAHs can be linked to astrophysical conditions. Usually this is done using as a start point the space observations. In Chapter 3 we go the other way around, linking the astrophysical conditions to PAH properties but starting from the PAHs themselves. In this project we take 3 individual PAH molecules of astrophysically-relevant PAH sizes (24, 54 and 96 carbon atoms), and we model their emission under PDR-like physical conditions, using their specific properties as derived from theory and experiments. The 3 PAHs are expected to be very stable species due to their compact structure. In the model we take into account the most relevant photo/chemical reactions, using the latest data available for each molecule. This work constitutes then the first astronomical kinetic model built to analyze the PAH emission from specific molecules, considering their resulting ionization and hydrogenation distributions. Together with this, we also address the role of PAHs in the formation of molecular hydrogen in PDRs, and the abundance of superhydrogenated species (and together with that, the discussion on the carrier of the $3.4\mu\text{m}$ band: can PAHs with extra hydrogen atoms be the carriers of the observed $3.4\mu\text{m}$ band?).

Chapter 4 Using the kinetic model from Chapter 3, here we address the key question of whether the deuterium abundance in PAHs can contribute to the deuterium fractionation problem observed in the local ISM. We aim to answer the specific questions of how sensitive the (D/H) ratio in PAHs is relative to astrophysical conditions, and together with that, elucidate in which way PAHs can contribute to the deuterium fractionation problem mentioned in section 1.8.4. This is the first time that these questions are approached considering specific PAH properties. We consider this to be a first modelling attempt, and we encourage further studies as more experimental and theoretical research on the reactivity of deuterated PAHs come along.

Chapter 5 At last, all previous chapters have considered PDRs as the best laboratories to study PAH emission, as these are regions driven by UV radiation, where the material transitions from the more diffuse ionized medium close to the star, to the molecular domain. This chapter will focus on the famous pair of nebulae IC63-IC59 in the vicinity of the star γ Cas. We perform a global characterization of both nebulae from an observational perspective, using not only Spitzer and Herschel data, but also high-resolution velocity maps from SOFIA. Our aim here is to study the PDRs associated to these clouds, and derive the physical conditions under which PAHs emit.

Bibliography

- Aitken, D. K. 1981, in *Infrared Astronomy*, IAU Symp. Nr 97, eds. C. G. Wynn-Williams, D. P. Cruikshank, Reidel, Dordrecht, p.207
- Ali-Haimoud, Y. 2013, *Advances in Astronomy*, 2013, 462697
- Ali-Haimoud, Y. 2014, *MNRAS*, 437, 2728
- Allain, T., Leach, S., & Sedlmayr, E. 1996, *A&A*, 305, 602
- Allamandola, L. J., Greenberg, J. M., & Norman, C. A. 1979, *Astr. Ap.*, 77, 66
- Allamandola, L. J., Tielens, A. G. G. M., & Barker, J. R. 1985, *ApJL*, 290, L25
- Allamandola, L. J., Tielens, A. G. G. M., & Barker, J. R. 1989, *ApJS*, 71, 733
- Allamandola, L. J., Hudgins, D. M., & Sandford, S. A. 1999, *ApJ*, 511, L115
- Andrews, H., Boersma, C., Werner, M. W., et al. 2015, *ApJ*, 807, 99
- Bakes, E. L. O., Tielens, A. G. G. M., Bauschlicher, C.W., 2001, *ApJ*, 556, 501
- Bakker, J. M., Redlich, B., van der Meer, A. F. G., & Oomens, J. 2011, *ApJ*, 741, 74
- Barker, J. R., Allamandola, L. J., & Tielens, A. G. G. M. 1987, *ApJ*, 315, L61
- Bauschlicher, C.W., & Bakes, E.L.O. 2000, *Chem. Phys.*, 262, 285
- Bauschlicher, C. W., Peeters, E., Allamandola, L. J. 2008, *ApJ*, 678, 316
- Bauschlicher, C. W., Boersma, C., Ricca, A., et al. 2010, *ApJS*, 189, 341
- Bauschlicher, C. W., & Ricca, A. 2013, *Chem. Phys. Lett.*, 566, 1
- Bauschlicher, C. W. 2016, *CPL*, 665, 100
- Becker, L., Glavin, D. P., & Bada, J. L. 1997, *GeCoA*, 61, 475
- Bernard-Salas, J., Cami, J., Peeters, E., Jones, A. P., Micelotta, E. R., & Groenewegen, M. A. T. 2012, *ApJ*, 757, 41
- Bérne, O., Joblin, C., Deville, Y., Smith, J. D., Rapacioli, M., et al. 2007, *A&A*, 469, 575
- Berné, O., Montillaud, J., Joblin, C. 2015, *A&A*, 577, A133
- Bernstein, M. P., Sandford, S. A., & Allamandola, L. J. 1996, *ApJ*, 472, L127
- Boersma, C., Bauschlicher, C. W., Allamandola, L. J., et al. 2010, *A&A*, 511, A32
- Boersma, C., Bregman, J. D., & Allamandola, L. J. 2013, *ApJ*, 769, 117
- Boersma, C. et al., 2014, *ApJS*, 211, 8
- Boersma, C., Bregman, J., & Allamandola, L. J. 2016, *ApJ*, 832, 51
- Bouwman, J., J. de Haasa, A., & Oomens, J. 2016, *Chem. Commun.*, 52, 2636
- Bregman, J. D., Dinerstein, H. L., Goebel, J. H., Lester, D. F., & Witteborn, F. C. 1983, *ApJ*, 274, 666
- Bregman, J. D., Allamandola, L. J., Witteborn, F. C., Tielens, A. G. G. M., & Geballe, T. R. 1989, *ApJ*, 344, 791
- Bregman, J. D., & Temi, P. 2005, *ApJ*, 621, 831
- Bron, E., Le Bourlot, J., & Le Petit, F. 2014, *A&A*, 569, A100
- Buragohain, M., Pathak, A., Sarre, P., Onaka, T., & Sakon, I. 2015, *MNRAS*, 454, 193
- Buragohain, M., Pathak, A., Sarre, P., Onaka, T., & Sakon, I. 2016, *P&SS*, 133, 97
- Buss, R. H., Jr., Cohen, M., Tielens, A. G. G. M., Werner, M. W., Bregman, J. D., Witteborn, F. C., Rank, D., & Sandford, S. A. 1990, *ApJ*, 365, 23
- Calvo, F., Basire, M., & Parneix, P. 2011, *JPCA*, 115, 8845
- Cami, J. 2011, in *EAS Publications Series*, Vol. 46, PAHs and the Universe, ed. C. Joblin & A. G. G. M. Tielens (Cambridge: Cambridge Univ. Press), 117
- Candian, A., Sarre, P. J., & Tielens, A. G. G. M. 2014, *ApJ*, 791, 10
- Candian, A., & Mackie, C. J. 2017, *Int. J. Quantum Chem.* 117, 146
- Cazaux, S., & Tielens, A. G. G. M. 2002, *ApJ*, 575, 29
- Cazaux, S., & Tielens, A. G. G. M. 2004, *ApJ*, 604, 222
- Cherchneff, I., Barker, J. R., & Tielens, A. G. G. M. 1992, *ApJ*, 401, 269
- Clemett, S. J., Maechling, C. R., Zare, R. N., & Alexander, C. M. 1992, *LPI*, 23, 233
- Clemett, S. J., Maechling, C. R., Zare, R. N., Swan, P. D., & Walker, R. M. 1993, *LPI*, 24, 309

- Coc, A., Petitjean, P., Uzan, J.-P., Vangioni, E., Descouvemont, P., Iliadis, C., & Longland, R. 2015, *Phys. Rev. D*, 92, 123526
- Cook, D. J., Schlemmer, S., Harrison, J. A., Wurfel, B. E., Chapman, W., Moore, C. B., & Saykally, R. J. 1993, abstract in the 48th Symposium on Molecular Spectroscopy, Ohio state University
- Cook, D. J., Schlemmer, S., Balucani, N., Wagner, D. R., Steiner, B., & Saykally, R. J. 1996, *Natur*, 380, 227
- Cook, D. J., & Saykally, R. J. 1998, *ApJ*, 493, 793
- Cooke, R., & Pettini, M. 2016, *MNRAS*, 455, 1512–1521
- Croiset, B. A., Candian, A., Berné, O., & Tielens, A.G.G.M. 2016, *A&A*, DOI: 10.1051/0004-6361/201527714
- Cuppen, H. M., & Herbst, E. 2005, *MNRAS*, 361, 565
- De Vries, M. S., Reihls, K., Wendt, H. R., Golden, W. G., Hunziker, H. E., Fleming, R., Peterson, & E., Chang, S. 1993, *GeCoA*, 57, 933
- Donej, K. D., Candian, A., Mori, T., Onaka, T., & Tielens, A. G. G. M. 2016, *A&A*, 586, A65
- Donn, B. 1968, *ApJL*, 152, L129
- Donn, B., Allen, J., & Khanna, R. 1989, in *Interstellar Dust*, IAU Symp., 135, 181
- Draine, B.T. 2004, in *Origin and Evolution of the Elements*, ed. A. McWilliams & M. Rauch (Cambridge: Cambridge Univ. Press), p. 320
- Draine, B. T. 2006, *ASPC*, 348, 58
- Duley, W. W. 1996, *MNRAS*, 279, 591
- Duley, W. W., & Williams, D. A. 1981, *MNRAS*, 196, 269
- Duley, W. W., & Williams, D. A. 1984, *Interstellar Chemistry*. Academic Press, London, p. 121
- Duncan, M. A., Knight, A. M., Negishi, Y., et al. 1999, *Chem. Phys. Lett.*, 309, 49
- Duek, E., Sellgren, K., Soifer, B. T., & Werner, M. W. 1980, *ApJ*, 238, 140
- Fitzpatrick, E. L., & Massa, D. 1986, *ApJ*, 307, 286
- Fitzpatrick, E. L., & Massa, D. 1988, *ApJ*, 328, 734
- Fitzpatrick, E. L., & Massa, D. 1990, *ApJ*, 72, 163
- Fitzpatrick, E. L., & Massa, D. 2005, *ApJ*, 130, 1127
- Fitzpatrick, E. L., & Massa, D. 2007, *ApJ*, 663, 320
- Fitzpatrick, E. L., & Massa D. 2009, *ApJ*, 699, 1209
- Frenklach, M., & Feigelson, E. D. 1989, *ApJ*, 341, 372
- García-Hernández, D. A., Villaver, E., García-Lario, P., Acosta-Pulido, J. A., Machado, A., Stanghellini, L., Shaw, R. A., Cataldo, F. 2012, *ApJ*, 760, 107
- Gadallah, K. A. K., Mutschke, H., & Jager, C. 2012, *A&A*, 544, 107
- Galliano, F., Madden, S. C., Tielens, A. G. G. M., Peters, E., & Jones, A. P. 2008, *ApJ*, 679, 310
- Gillett, F. C., Low, F. J., & Stein, W. A. 1967, *ApJL*, 149, L97
- Gillett, F. C., Forrest, W. J., & Merrill, K. M. 1973, *ApJ*, 183, 87
- Gould, R. J., & Salpeter, E. E. 1963, *ApJ*, 138, 393
- Grasdalen, G. L., & Joyce, R. R. 1976, *ApJ*, 205, L11
- Habart, E., Boulanger, F., Verstraete, L., et al. 2003, *A&A*, 397, 623
- Habart, E., Natta, A., & Krugel, E. 2004, *A&A*, 427, 179
- Habart, E., Boulanger, F., Verstraete, L., Walmsley, C. M., & Pineau des Forêts, G. 2004, *A&A*, 414, 531
- Herbig, G. H. 1975, *ApJ*, 196, 129
- Herbig, G. H. 1995, *ARA&A*, 33, 19
- Hobbs., L.M., York, D.G., Thorburn, J.A., et al. 2010, *A New Atlas of the Diffuse Interstellar Bands: HD 183143*, 65th International Symposium On Molecular Spectroscopy
- Hollenbach, D., & Salpeter, E. E. 1970, *J. Chem. Phys.*, 53, 79
- Hollenbach, D., & Salpeter, E. E. 1971, *ApJ*, 163, 155
- Hollenbach, D., & Tielens, A. G. G. M. 1999, *RvMP*, 71, 173
- Hony, S., Van Kerckhoven, C., Peeters, E., et al. 2001, *A&A*, 370, 1030
- Hu, A., & Duley, W. W. 2008, *ApJ*, 677, 153
- Hudgins, D. M., & Allamandola, L. J. 2004, *ASPC*, 309, 665
- Hudgins, D. M., Bauschlicher, C. W., & Sandford, S. A. 2004, *ApJ*, 614, 770
- Hudgins, D. M., Bauschlicher, C. W., & Allamandola, L. J. 2005, *ApJ*, 632, 316
- Joblin, C., Léger, A., & Martin, P. 1992, *ApJ*, 393, L79
- Joblin, C., d'Hendecourt, L., Léger, A., & Defourneau, D. 1994, *A&A*, 281, 923
- Joblin, C., Boissel, P., Léger, A., d'Hendecourt, L., & Defourneau, D. 1995, *A&A*, 299, 835
- Joblin, C., Tielens, A. G. G. M., Allamandola, L. J., & Geballe, T. R. 1996, *ApJ*, 458, 610
- Jochims, H. W., Rühl, E., Baumgartel, H., Tobita, S., & Leach, S. 1994, *ApJ*, 420, 307
- Jochims, H. W., Rühl, E., Baumgartel, H., & Leach, S. 1996, *A&A*, 314, 1003
- Jochims, H. W., Rühl, E., Baumgartel, H., Tobita, S., & Leach, S. 1997, *IJMSI*, 167/168, 35
- Jones, A. P., Duley, W. W., & Williams, D. A. 1990, *QJRAS*, 31, 567

- Jura, M. 1975, *ApJ*, 197, 575
- Jura, M. 1982, in *Advances in UV Astronomy: 4 Years of IUE Research*, ed. Y. Kondo, J. M. Mead, & R. D. Chapman (NASA CP 2238: Greenbelt, MD: NSAS), 54
- Katz, N., Furman, I., Biham, O., Pirronello, V., & Vidali, G. 1999, *ApJ*, 522, 305
- Kovalenko, L. J., Maechling, C. R., Clemett, S. J., Philipoz, J. M., Zare, R. N., & Alexander, C. M. O. 1992, *Anal. Chem.*, 64, 682
- Kwok, S., & Zhang, Y. 2011, *Natur*, 479, 80
- Kwok, S., & Zhang, Y. 2013, *ApJ*, 771, 5K
- Langhoff, S. R. 1996, *J. Phys. Chem*, 100, 2819
- Latter, W. B. 1991, *ApJ*, 377, 187
- Lau, R. M., Werner, M., Sahai, R., & Ressler, M. E. 2016, *ApJ*, 833, 115
- Léger, A., & Puget, J. 1984, *A&A*, 137, L5
- Léger, A., Verstraete, L., d'Hendecourt, L., et al. 1989, in *IAU Symp. 135, Interstellar Dust*, ed. L. J. Allamandola & A. G. G. M. Tielens (Dordrecht: Kluwer), 173
- Léger, A., & d'Hendecourt, L. 1985, *A&A*, 146, 81
- Le Bourlot, J., Le Petit, F., Pinto, C., Roue, E., & Roy, F. 2012, *A&A*, 541, A76
- Le Page, V., Snow, T. P., & Bierbaum, V. M. 2001, *ApJSS*, 132, 233
- Le Page, V., Snow, T. P., & Bierbaum, V. M. 2003, *AJ*, 584, 316
- Le Petit, F., Barzel, B., Biham, O., Roueff, E., & Le Bourlot, J. 2009, *A&A*, 505, 1153
- Li, A., & Draine, B. T. 2012, *ApJ*, 760, 35
- Ling, Y., Gotkis, Y., & Lifshitz, C. 1995, *Eur. J. Mass Spectrom.*, 1, 41
- Linsky, J. L., Draine, B. T., Moos, H. W., et al. 2006, *ApJ*, 647, 1106
- Linsky, J. L. 2010, *IAUS*, 268, 53
- Lorenz, U. J., Lemaire, J., Maitre, P., Crestoni, M. E., Fornarini, S., & Dopfer, O. 2007, *IJMS*, 267, 43
- Mackie, C. J., Candian, A., Huang, X., Maltseva, E., Petrigani, A., Oomens, J., Buma, W. J., Lee, T. J., & Tielens, A. G. G. M. 2015, *JChPh*, 143, 4314
- Mallici, G., Joblin, C., & Mulas, G. 2007, *Chem. Phys.*, 332, 353
- Maltseva, E., Petrigani, A., Candian, A., Mackie, C. J., Huang, X., Lee, T. J., Tielens, A. G. G. M., Oomens, J., & Buma, W. J. 2016, *ApJ*, 820, 81
- Mattioda, A. L., Hudgins, D. M., Bauschlicher, C. W., & Allamandola, L. J. 2005, *AdSpR*, 36, 156
- Mattioda, A. L., Ricca, A., Tucker, J., Bauschlicher, C. W. Jr., & Allamandola, L. J. 2009, *AJ*, 137, 4054
- Mazzitelli, I. & Moretti, M. 1980, *ApJ*, 235, 955
- McKay, D. S., Gibson, E. K., Thomas-Keprta, K. L., Vali, H., Romanek, C. S., Clemett, S. J., Chiller, X. D. F., Maechling, C. R., & Zare, R. N. 1996. Search for past life on Mars: Possible relic biogenic activity in martian meteorite ALH 84001. *Science*, 273, 924
- Mennella, V., Hornekær, L., Throer, J., & Accolla, M. 2012, *ApJ*, 745, L2
- Merrill, P.W. 1934, *PASP*, 46, 206
- Miller, T. J., Roberts, H., Markwick, A. J., & Charnley, S. B. 2000, *Philos. Trans. R. Soc. London A*, 358, 2535
- Montillaud, J., Joblin, C., & Toubanc, D. 2013, *A&A*, 552, A15
- Moutou, C., Verstraete, L., Léger, A., Sellgren, K., & Schmidt, W. 2000, *A&A*, 354, 17
- Mulas, G., Mallici, G., Joblin, C., & Toubanc, D. 2006, *A&A*, 446, 537
- Mulas, G., Mallici, G., Joblin, C., & Cecchi-Pestellini, C. 2011, *EAS*, 46, 327
- Onaka, T., et al. 2014, *ApJ*, 780, 114
- Oomens, J., van Roij, A. J. A., Meijer, G., & von Helden, G. 2000, *ApJ*, 542, 404
- Oomens, J., Tielens, A. G. G. M., Sartakov, B. G., von Helden, G., & Meijer, G. 2003, *ApJ*, 591, 968
- Oomens, J., Sartakov, B. G., Meijer, G., & von Helden, G. 2006, *IJMS*, 254, 1
- Papoular, R., Conrad, J., Giuliano, M., Kister, J., & Mille, G. 1989, *A&A*, 217, 204
- Pauzat, F. 2011, *EAS*, 46, 75
- Pech, C., Joblin, C., & Boissel, P. 2002, *A&A*, 388, 639
- Peeters, E., Hony, S., Van Kerckhoven, C., et al. 2002, *A&A*, 390, 1089
- Peeters, E., Allamandola, L. J., Bauschlicher, Jr., C. W., et al. 2004, *ApJ*, 604, 252
- Peeters, E., Tielens, A. G. G. M., Allamandola, L. J., & Wolfire, M. G. 2012, *ApJ*, 747, 44
- Peeters, E., Bauschlicher, C. W., Allamandola, L. J., Tielens, A. G. G. M., Ricca, A., & Wolfire, M. G. 2017, *ApJ*, 836, 198
- Piest, J. A., Oomens, J., Bakker, J., von Helden, G., & Meijer, G. 2001, *AcSpA*, 57, 717
- Pilleri, P., Montillaud, J., Berné, O., & Joblin, C. 2012, *A&A*, 542, A69
- Pilleri, P., Joblin, C., Boulanger, F., & Onaka, T. 2015, *A&A*, 577, A16
- Pino, T., Carpentier, Y., Féraud, G., Friha, H., Kokkin, D. L., Troy, T. P., Chalygavi, N., Bréchnignac, Ph., & Schmidt, T. W. 2011, *EAS*, 46, 355
- Pirronello, V., Biham, O., Liu, C., Shen, L., & Vidali, G. 1997, *ApJ*, 483, L131
- Pirronello, V., Liu, C., Roser, J. E., & Vidali, G. 1999, *A&A*, 344, 681

- Ploufs, F. L., Elsila, J. E., Zare, R. N., & Buseck, P. R. 2003, *GeCoA*, 67, 1429
- Prochaska, J. X., Tripp, T. M., & Howk, J. C. 2005, *ApJ*, 620, L39
- Rapacioli, M., Joblin, C., & Boissel, P. 2005, *A&A*, 429, 193
- Rauls, E., & Hornekaer, L. 2008, *ApJ*, 679, 531
- Reitsma, G., Boschman, L., Deuzeman, M.J., González-Magaña, O., Hoekstra, S., Cazaux, S., Hoekstra, R., & Schlathölter, T. 2014, *Phys. Rev. Lett.*, 113, 053002
- Ricca, A., Bauschlicher, C. W., Jr., Mattioda, A. L., Boersma, C., & Allamandola, L. J. 2010, *ApJ*, 709, 42
- Ricca, A., Bauschlicher, C. W., Jr., & Allamandola, L. J. 2011, *ApJ*, 729, 94
- Ricca, A., Bauschlicher, C. W., Jr., Boersma, C., Tielens, A. G. G. M., & Allamandola, L. J. 2012, *ApJ*, 754, 75
- Romano, D., Tosi, M., Chiappini, C., & Matteucci, F. 2006, *MNRAS*, 369, 295
- Rosenberg, M. J. F., Berné, O., Boersma, C., Allamandola, L. J., & Tielens, A. G. G. M. 2011, *A&A*, 532, A128
- Russel, R. W., Soifer, B. T., & Willner, S. P. 1977, *ApJL*, 217, L149
- Sadjadi, S., Zhang, Y., & Kwok, S. 2015, *ApJ*, 801, 34
- Sakata, A., Wada, S., Onaka, T., & Tokunaga, A. T. 1987, *ApJ*, 320, 63
- Sakata, A., Wada, S., Onaka, T., & Tokunaga, A. T. 1990, *ApJ*, 353, 543
- Salama, F. 2007, in *Molecules in Space and Laboratory*, ed. J. L. Lemaire & F. Combes (Paris: S. Diana), 51
- Sandford, S. A., Bernstein, M. P., & Materese, C. K. 2013, *ApJS*, 205, 8
- Savage, B. D., & Mathis, J. S. 1979, *ARA&A*, 17, 73
- Schutte, W. A., Tielens, A. G. G. M., & Allamandola, L. J. 1993, *ApJ*, 415, 397
- Sellgren, K. 1981, *ApJ*, 245, 138
- Sellgren, K., Werner, M. W., & Dinerstein, H. L. 1983, *ApJL*, 271, L13
- Sellgren, K. 1984, *ApJ*, 277, 623
- Sellgren, K., Uchida, K. I., & Werner, M. W. 2007, *ApJ*, 659, 1338
- Sellgren, K., Werner, M. W., Ingalls, J. G., et al. 2010, *ApJ*, 722, L54
- Sloan, G. C., Jura, M., Duley, W. W., Kraemer, K. E., Bernard-Salas, J., et al. 2007, *ApJ*, 664, 1144
- Smith, J. D. T., Draine, B. T., Dale, D. A., Moustakas, J., Kennicutt, R. C. Jr, et al. 2007, *ApJ*, 656, 770
- Srianand, R., Gupta, N., Petitjean, P., Noterdaeme, P. & Ledoux, C. 2010, *MNRAS*, 405, 1888
- Stockett, M. H., Gatchell, M., de Ruette, N., Giacomozzi, L., Chen, T., et al. 2015, *IJMS*, 392, 58
- Throuer, J. D., Nilsson, L., Jørgensen, B., et al. 2011, in *PAHs and the Universe*, ed. C. Joblin & A. G. G. M. Tielens (EAS Pub. Ser. 46; Les Ulis: EDP), 453
- Tielens, A. G. G. M. 1997, in *AIP Conf. Proc. 402, Astrophysical Implications of the Laboratory Study of Presolar Materials*, ed. T. H. Bernatowicz & E. K. Zinner (New York: AIP), 523
- Tielens, A. G. G. M. 2005, *The Physics and Chemistry of the Interstellar Medium* (Cambridge: Cambridge Univ. Press)
- Tielens, A. G. G. M. 2008, *ARA&A*, 46, 289
- Tielens, A. G. G. M. 2013, *Rev. Mod. Phys.*, 85, 1021
- Tingle, T. N., Becker, C. H. & Malhotra, R. 1991, *Metic*, 26, 117
- Tokunaga, A. T., & Young, E. T. 1980, *ApJL*, 237, L93
- Tosi, M. 2010, in *Proc. IAU Symp. 268, Light Elements in the Universe*, ed. C. Charbonnel, M. Tosi, F. Primas & C. Chiappini (Cambridge: Cambridge Univ. Press), 153
- Van Diedenhoven, B., Peeters, E., Van Kerckhoven, C., et al. 2004, *ApJ*, 611, 928
- Van Kerckhoven, C., Hony, S., Peeters, E., Tielens, A. G. G. M., Allamandola, L. J., Hudgins, D. M., et al. 2000, *A&A*, 357, 1013
- Verstraete, L., Leger, A., d'Hendecourt, L., Defourneau, D., & Dutuit, O. 1990, *A&A*, 237, 436
- Werner, M. W., Uchida, K. I., Sellgren, K., et al. 2004, *ApJS*, 154, 309
- Werner, M. W., Sellgren, K., & Livingston, J. 2009, *AAS Meeting Abstracts*, 213, #412.15
- Wood, B. E., Linsky, J. L., Hébrard, G., Williger, G. M., Moos, H. W., & Blair, W. P. 2004, *ApJ*, 609, 838
- Yang, X. J., Glaser, R., Li, A., & Zhong, J. X. 2013, *ApJ*, 776, 110
- Yang, X. J., Li, A., Glaser, R., & Zhong, J. X. 2016, *ApJ*, 825, 22
- Zhen, J., Castellanos, P., Paardekooper, D. M., Linnartz, H., & Tielens, A. G. G. M. 2014, *ApJ*, 797, 30
- Zhen, J., Castellanos, P., Paardekooper, D. M., Ligterink, N., Linnartz, H., Nahon, L., Joblin, C., & Tielens, A. G. G. M. 2015, *ApJ*, 804, 7

PAH Emission at the Bright Locations of PDRs: the GrandPAH hypothesis

The PAH emission observed in the Spitzer-IRS spectra of bright mid-IR locations of three well known reflection nebulae NGC 7023, NGC 2023 and NGC 1333 were analyzed. Each of these objects shows large variations in PAH band ratios when studied through spectral mapping. Nevertheless, the mid-IR spectra at these bright spots show a remarkably similar PAH emission spectrum. We used the NASA Ames PAH IR Spectroscopic Database to fit the observations and analyze the derived PAH populations. Our results show that PAH emission spectra in the 5–15 μm range appear to be rather insensitive to variations of the radiation field. Similar PAH populations of neutral small-to-medium sized PAHs ($\sim 50\%$), with ionized species contributing in slightly less than 50%, provide very good fits. Analyzing the degeneracy of the results shows that spectroscopic details place strong constraints on the PAH population. Subtle (but intrinsic) variations in the emission properties of individual PAHs lead to observable differences in the resulting spectra. On top of this, we found that variations of $< 30\%$ in the PAH abundances would lead to noticeable spectral differences between the three PDRs. Therefore **PAH populations must be remarkably similar at these different lines-of-sight**. To account for this, **we suggest the concept of grandPAHs as a unique mixture of the most stable PAHs emitting at these spots**. This unique mixture would be a result of intense processing in the ISM. Using NGC 7023 as an example, the grandPAHs refer to the robust PAH population that results from the processing of PAHs at the border limit between the PDR and the molecular cloud where, due to the UV radiation that destroys the PAH population, the abundance of PAHs starts decreasing as we move towards the star.

H. Andrews, C. Boersma, M. W. Werner, J. Livingston, L. J. Allamandola & A. G. G. M. Tielens
ApJ, Volume 807, Issue 1, article id. 99, 24 pp. (2015)

2.1. Introduction

When observing the mid-IR spectra of gaseous and dusty regions in the sky, we can distinguish strong emission bands at 3.3, 6.2, 7.7, 11.3 and 12.7 μm , perched on emission plateaus at 7.0, 11.0 and 17.0 μm . In addition, many weak features can be observed at 8.6, 11.0, 12.0, 13.5, 14.0, 14.2, 15.9, 16.4, 17.4 and 17.8 μm . The carriers of these bands are nowadays accepted to be a class of organic molecules called polycyclic aromatic hydrocarbons (PAHs) (Léger & Puget 1984; Allamandola et al. 1985).

PAHs consist of hexagonal aromatic carbon rings with hydrogen atoms attached at the periphery. When exposed to high energy photons (up to 13.6 eV) PAHs get electronically excited; they increase their temperature considerably (reaching up to ~ 1000 K); rapidly redistribute the absorbed energy among all available vibrational states; and relax, either by fragmenting or emitting IR photons through a fluorescence process.

Observational studies of PAHs have recently flourished with the available data from both Spitzer and Herschel space telescopes on UV illuminated environments such as photodissociation regions (PDRs). PDRs are the UV illuminated surfaces of molecular clouds, where the chemical reactions taking place are driven by the high energy UV photons that penetrate largely neutral atomic gas (Hollenbach & Tielens 1999). PDRs are bright in — among others— atomic fine structure lines of [OI] and [CII]; pure rotational lines of H_2 and (low-J) CO; UV pumped ro-vibrational transitions of H_2 ; PAH emission features, and mid/far-IR continuum emission associated with warm dust.

Much focus has been directed to the study of PDRs in reflection nebulae (RNe) as these are relatively benign, quiescent, extended regions (Young Owl et al. 2002), that allow us to observe more clearly the footprint of PAHs (e.g., Bregman & Temi 2005; Sellgren et al. 2007; Peeters et al. 2012). Spectral mapping of RNe, as well as spectral comparison of large samples of sources, provide a powerful tool to study the characteristics of interstellar PAHs. The variations observed between the C-C (6–9 μm region) and the C-H modes (10–15 μm) are generally attributed to variations in the degree of ionization of the emitting PAHs (e.g., Allamandola et al. 1999; Peeters et al. 2002; Galliano et al. 2008; and references therein). In contrast, variations among the C-H out-of-plane modes (11.3 and 12.7 μm bands) as well as variations between the 7.6, 7.8 and 8.6 μm bands are thought to result from variations in the molecular structure of the emitting PAH family (e.g., Hony et al. 2001; Peeters et al. 2012; Ricca et al. 2011; Ricca et al. 2012).

Laboratory studies and quantum chemical calculations have determined the IR spectra of a large number of PAH species. These have been compiled in The NASA Ames PAH IR Spectroscopic Database (PAHdb¹; Bauschlicher et al. 2010; Boersma et al. 2014). The latest version (v2.00) contains 700 theoretically calculated and 75 experimental spectra of PAHs of different sizes ($N_c = 6\text{--}384$ carbon atoms), ionization states, composition (including nitrogenated species) and structure (e.g., different hydrogen adjacency ratios). PAHdb also provides a suite of IDL scripts (AmesPAHdbIDLSuite) that allows users to handle the database in a practical and easy way (Boersma et al. 2014). Several works have used the AmesPAHdbIDLSuite to fit observational data (e.g., Cami 2011; Rosenberg et al. 2011; Boersma et al. 2013), and proved how insightful this approach is.

¹<http://www.astrochem.org/pahdb>

Table 2.1: Brightest mid-IR Locations of the PDRs Studied in this Work.

Object	RA (J2000.0)	DEC (J2000.0)	$F_{11.3\mu\text{m}}^a$	Observation Date	Position Angles
NGC7023 NW	21 01 32.5	+68 10 25.7	2.21	2004-08-29	66.13
NGC2023	05 41 41.0	-02 15 41.7	1.21	2004-10-04	178.43
NGC1333	03 29 20.7	+31 24 33.0	0.32	2005-02-06	-15.31

^a Peak flux of the $11.3\mu\text{m}$ feature after continuum subtraction, in Jy units.

In this work, we analyze the mid-IR spectra of the PDRs of three well-studied RNe: NGC7023, NGC2023 and NGC1333. We carefully selected bright spots of PAH emission in the PDRs, that probe the transition of the molecular clouds to the cavities surrounding the stars. The spectra were obtained with the Spitzer Infrared Spectrograph (IRS; Houck et al. 2004). Long slit spectra were obtained along rims particularly bright in the mid-IR (Werner et al. 2004), and the spectra of the pixels of interest were extracted from the long slit data. Our focus is on the PAH emission, and so we use PAHdb to fit the astronomical spectra and analyze the derived PAH populations. We are particularly interested in these spectra, since they look strikingly similar in terms of PAH emission, considering that these are different objects and all present large variations of the PAH emission within themselves. Werner et al. (2009) originally pointed out the similarity of the slit spectra in these three nebulae. Here we study the similarity in the PAH emission from PAHdb standpoint, and we propose the *grandPAHs* as a plausible explanation to the results derived from PAHdb.

The concept of *grandPAHs* has been defined in Tielens (2013) as a set of the most stable PAH species that are able to survive the intense processing in the ISM, and as such, dominates the PAH population in space. This was proposed in order to explain the relatively constant $15\text{--}18\mu\text{m}$ emission band patterns, and the overall homogeneity of PAH emission observed in different interstellar sources. Even though the *grandPAHs* have been mentioned in several works (e.g., Berné et al. 2009; Ali-Haïmoud 2014), up until now this hypothesis has not been explored in any way. This is the first attempt to do this. The simple geometry and well-determined physical conditions in the three RNe studied here, offer a great opportunity to examine the *grandPAH* hypothesis, using our current knowledge on PAH emission spectra through the use of PAHdb.

The outline of this work is the following: section 2.2 presents the data of the RNe studied in this work. In section 2.3 we present the motivation of this work. Section 2.4 discusses PAHdb and the assumptions we consider before performing the fits. The results are presented in section 2.5, while the implications of our results are discussed in section 2.6. In this last section we explore the concept of *grandPAHs* and propose a new interpretation about their role in the evolution of carbonaceous material in RNe.

2.2. Observations

2.2.1. Selected PDRs

NGC7023 This is a well-studied RN illuminated by the Herbig Be star HD200775. Our study focuses on the brightest mid-IR spot located in the North-West PDR (NW), 45" from the exciting star (see Table 2.1). NGC7023 NW is often considered as the prototype of a PDR since it has an edge-on structure, which shows a clear stratification of the emitting region. The star has created a low density cavity which is surrounded by a dense molecular cloud. The cavity wall is lined by a thin HI layer (Fuente et al. 1998). The fullerene abundance increases rapidly into the cavity while the PAH abundance decreases from the PDR front towards the star (Sellgren et al. 2010; Pilleri et al. 2012; Berné & Tielens 2012). Table 2.2 lists the physical parameters taken from the literature determined for this location. Analysis of the observed far-IR continuum intensity yields an incident UV field of $G_0 = 2600$ Habing field units in the NW PDR (Chokshi et al. 1988). This is in agreement with the stellar flux at the projected distance (Alecian et al. 2008). Okada et al. (2013) reported a larger value of $G_0 = 7700$ from integrating the total IR emission from 3–100 μm . However this assumes spherical symmetry and it is presented as an upper limit. The gas density n_H and temperature T_{gas} listed in Table 2.2 have been estimated from the observed line intensities of [OI]63 μm and [CII]158 μm (Young Owl et al. 2002; Chokshi et al. 1988). The derived gas density in the PDR is in good agreement with the HI observations (Fuente et al. 1998).

NGC2023 This RN located in Orion, just below the Horsehead nebula, is illuminated by the B1.5V star HD37903, at a distance of 350 pc (Mookerjee et al. 2009; Sheffer et al. 2011). Our position is located 39" east of the star, and it is the brightest spot along one of the brightest rims observed at 8 μm (Peeters et al. 2012). The physical parameters considered for this position have been taken from the work of Steiman-Cameron et al. (1997). They determined T_{gas} , n_H and G_0 for a position 42" south-east of the star (position P4 in their paper). This is the closest one to ours, and it falls along the clumpy rim where the peak of the mid-IR continuum (and cooling line emission) is observed. The value of $G_0 = 15000$ for P4 was obtained from the FIR continuum. Using this value and considering a dilution that goes as the square of the projected distance to the star, we get $G_0 = 17400$ for our position. The estimates of the gas density and temperature were derived using the cooling lines. However a comparison with PDR models shows there is a better agreement when assuming a clumpy structure of density 10^5 cm^{-3} and temperature of 750 K; and thus here we adopt these values instead (Table 2.2).

NGC1333 This is a highly active star forming region in the Perseus molecular cloud. Here we study the brightest mid-IR spot as observed at 8 μm , which is in the nebula illuminated by the late B star BD+30°549. This is not where the far IR peak is, which is in the nebula illuminated by SVS-3. The parameters listed in Table 2.2 have been taken from Young Owl et al. (2002). They derived physical conditions for the nebulae where our brightest spot is, based on far-IR observations with Kuiper Airborne Observatory (KAO). According to the far-IR dust continuum emission they derived $G_0 = 4800$. The gas density and temperatures were obtained from comparing the cooling lines ratio with the models of Tielens & Hollenbach (1985).

Table 2.2: Physical Conditions in Different PDRs Taken From the Literature

Property	NGC 7023 NW	NGC 2023	NGC 1333
Central Star	HD 200775	HD 37903	BD+30°549
Star Type	B2.5 Ve ^a	B1.5 V ^e	B9V ^f
Star Temperature (K)	17000 ^a	23000 ^d	14000 ^f
Distance from Star (")	45	39	27
G ₀	2600 ^b	15000 ^d	4800 ^f
Dust Temperature (K)	50 ^c	50 ^d	45 ^f
Gas Temperature (K)	200 ^c	750 ^d	690 ^f
Gas density (cm ⁻³)	4×10 ^{3c}	10 ^{5d}	2×10 ^{4f}
Ionization Parameter* γ	6.5×10 ⁴	3.4×10 ⁴	4.5×10 ⁴

^a Rogers et al. (1995); ^b Pilleri et al. (2012); ^c Chokshi et al. (1988); ^d Steiman-Cameron et al. (1997); ^e de Boer (1983); ^f Young Owl et al. (2002).

* The ionization parameter is defined as $\gamma \equiv G_0 \sqrt{T_{\text{gas}}}/n_e$, where the electron density has been calculated assuming that all free electrons come from singly ionized carbon, using the diffuse ISM gas-phase carbon abundance of 1.4×10^{-4} (Cardelli et al. 1996).

2.2.2. Data Collection and Reduction

The spectra of the three nebulae were obtained as part of Spitzer GTO Program #19, PI M. Werner. The observation dates and positions observed are shown in Table 2.1 (note however, that the IRS spectra of NGC 7023 shown in Werner et al. (2004) were obtained under a separate Early Release Observation program; the NGC 7023 data shown here were obtained somewhat later in the mission and with a different slit position angle). Spectra were obtained for each nebula using both the 1st and 2nd order slits of the IRS short-low module (Houck et al. 2004). First order runs from 7.4 to 14 μm , and second order from 5.2 to 7.7 μm . Each IRS slit is 58" long in the spatial dimension and 3.6" wide in the dispersion direction. The extension of the spectra to 15 μm was scaled from a Spitzer long-low spectrum. For a given slit, spectra are obtained first with the telescope at a nominal position, and next with the telescope nodded half the slit length but along the slit, so that the two slit positions overlap. The RNe are bright enough that we chose to analyze data from only one of the slit positions. The on sky integration time for the spectra analyzed here is 44 sec.

The data reduction is carried out by downloading the calibrated two dimensional image frames and ancillary data from the Spitzer archive at IRSA. The reduction was done using Cornell University SMART data reduction program², which coadds the separate frames into a final image from which spectra at particular positions along the slit can be extracted. It is also possible to obtain a total spectrum summed along the slit. For this program, we extracted the spectrum of a region 4 pixels in length and two pixels wide (in the dispersion direction) centered at the position listed in Table 2.1 for each nebula. Thus the field of view is a rectangle 3.6"×7.2" in size. For each nebula, Table 2.1 gives the position angle of the

²<http://isc.astro.cornell.edu/IRS/SmartRelease>

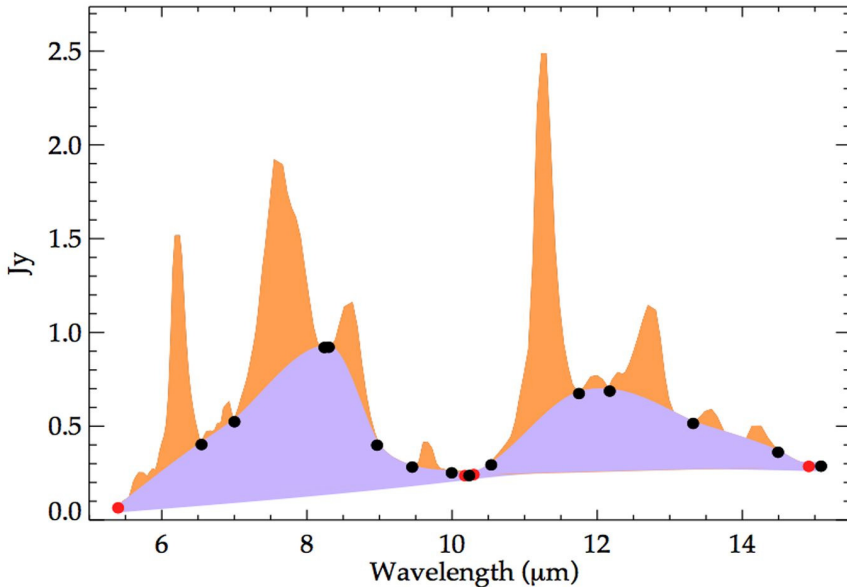


Figure 2.1: Schematic of Spline Decomposition Procedure. The spectrum corresponds to the brightest location in the NW PDR of NGC7023. Red dots indicate the *anchor points* used to define the dust continuum. Black dots indicate *anchor points* used to define the emission from the first (6–10 μm) and second (10–15 μm) plateaus. The purple area then shows the plateau emission, while the orange area depicts the emission lines and PAH bands. See 2.2.3 for details.

slit, which is the orientation of the long side of the $3.6'' \times 7.2''$ field of view. The spectra were extracted separately for the two orders and matched at the boundary ($7 \mu\text{m}$) where they overlap spectrally for a few tenths of a micron. Because of the brightness of the source and the fact that a baseline was extracted from the spectra before the analysis was begun, we did not do a sky subtraction. The uncertainties in the inferred flux are dominated by possible systematic rather than by statistical errors. To obtain an estimate, we have compared the independent measurements in the two nodes of the spectrum of NGC1333, which is the faintest of the sources. We find that the two spectra agree to well within 5% on average. On this basis, we estimate that the one-sigma uncertainty in our measurements is no more than 3% per data point.

2.2.3. Description of Removal of Continuum and Plateaus

There are different ways of decomposing and retrieving the PAH band strengths from the mid-IR spectra of astronomical objects. The methods depend basically on whether plateaus are considered as an inherent part of the narrow PAH bands (Sellgren et al. 2007; Smith et al. 2007) or as a separate component which may or may not be related to PAHs. As described in Boersma et al. (2012) and Peeters et al. (2012) the 10–15 and 15–18 μm plateaus vary independently from most of the narrower PAH bands. Therefore we consider plateaus and features separately, using spline functions to describe the plateaus, while PAH bands are described through Gaussian profiles. It is important to mention that extensive analysis on the variation of the PAH band ratios has shown that general trends are the same irrespective of the method used (Galliano et al. 2008).

Figure 2.1 presents a schematic of a spectrum analyzed using our decomposition method. The procedure was carried out as follows: first the continuum underneath the plateaus and PAH bands is removed by fitting a *continuum spline*, using as anchor points the local minima at 5.5, 10.3, 10.5 and 15.0 μm (see red dots in Figure 2.1). These are referred to as the *Features+Plateaus* spectra, since they contain both the PAH bands and the underlying plateaus.

A *plateau spline* was then fitted to the *Features+Plateaus* spectra to distinguish the plateaus (see purple area in Figure 2.1) from the individual PAH bands and emission lines (see orange area in Figure 2.1). Each *plateau spline* was defined by anchor points at around 5.5, 6.6, 7.2, 8.1, 8.4, 8.8, 9.4, 9.9 and 10.3 μm for the features rising above the *first plateau* between 6–10 μm ; and at 10.3, 10.5, 11.8, 12.2, 13.2, 14.5 and 15.0 μm for the features of the *second plateau* at 10–15 μm (see black dots in Figure 2.1). This set of anchor points isolate the emission lines and PAH bands. These spectra are referred to as the *Features-Only* spectra.

In order to quantify the integrated intensities for later use, once the *plateau splines* were subtracted from the spectra, the narrow emission lines and PAH bands were fitted using multi-gaussian profiles. In order to do this, we used the least squares curve fitting routine MPFITFUN on IDL, which uses the Levenberg-Marquardt algorithm to minimize the χ^2 (Markwardt 2009).

The narrow emission lines of H₂ S(6)–S(2) were then subtracted from both *Features+Plateaus* and *Features-Only* spectra, in order to isolate the emission coming from PAH features and plateaus. The spectra were finally rebinned on a wavenumber grid with a spacing of 5 cm^{-1} following Boersma et al. (2013). Given the uncertainty in the band profile of PAHs and the unknown nature of plateau carriers (and their possible relation with PAHs), throughout this work all results will be presented for *Features+Plateaus* spectra. The fits to *Features-Only* spectra lead to very similar results and can be found in Appendix 2.A, together with a comparison to the *Features+Plateaus* spectra. Although most of the work in this paper is done with normalized spectra, we also give in Table 2.1 the flux (in Jy) at the peak of the 11.3 μm PAH feature above the baseline of the *Features+Plateaus* spectrum. This establishes a flux scale for each spectrum, which will permit future analysis to determine the abundance of the various PAH species along the observed line of sight.

2.3. Motivation

Figure 2.2 presents the *Features+Plateaus* spectra before removing the H₂ lines. The top panel shows the normalized spectra, while the bottom panel shows the difference between each normalized spectrum with the average of all three.

Inspection of Figure 2.2 reveals that the spectra are very similar to the smallest details; not just in terms of the presence of the same aromatic IR bands, but also the PAH band ratios. The differences with respect to the average are less than 10%, with the largest differences in the peak flux and band profile of the 6.2 and 7.7 μm features. We note that the spectra along the full slit —aligned with bright rims— are all very similar to those of the hot spots. This contrasts with the fact that large spectral variations have been observed across these nebulae (e.g., Berné et al. 2009; Rosenberg et al. 2011). *It is important to note that this similarity is not affected by whether plateaus are taken into account or not.*

This impressive spectroscopic similarity poses an important question. Why do the mid-IR spectra of these bright locations of the PDRs in these RNe resemble each other to such a high degree? All the more, when taking into account the different physical conditions and histories of the exciting stars (see Table 2.2). To gain insight into the PAH populations and physical conditions that might give rise to the same PAH spectrum, we use PAHdb to decompose the PAH emission into contributing PAH subclasses, namely: size, charge, composition and hydrogen adjacency (structure); and use an appropriate PAH emission model.

2.4. Method

The spectra shown in Figure 2.2 were analyzed using version 2.00 of PAHdb which comprises 700 theoretically computed PAH spectra. In order to perform the fit, we used the AmesPAHdbIDL Suite provided by PAHdb. The fitting routine in this case uses a non-negative least-square approach that solves $Ax = b$ (where A is the matrix of PAH spectra

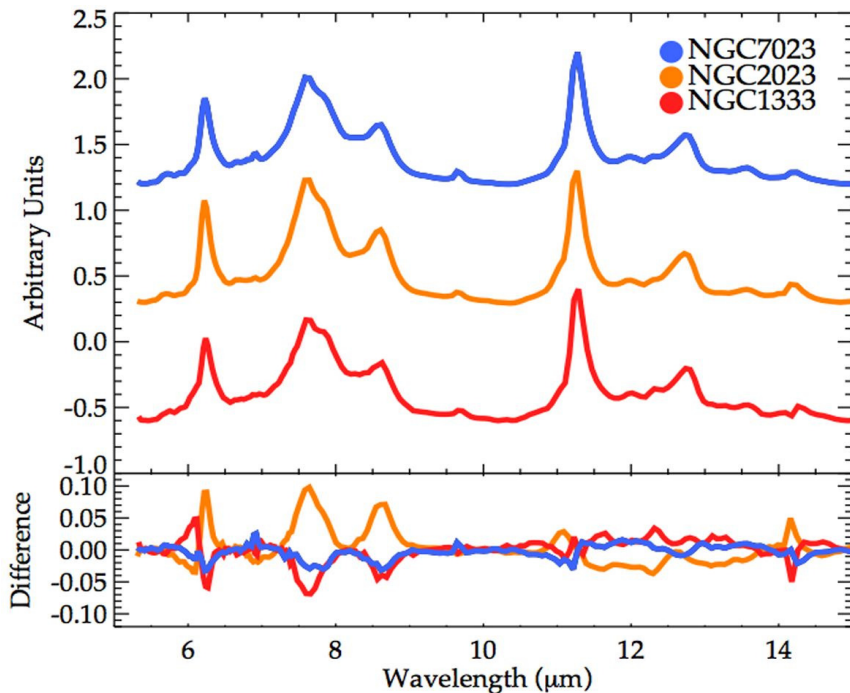


Figure 2.2: *Features+Plateaus* spectra of the brightest locations in NGC7023, NGC2023 and NGC1333 before removing the H_2 lines. The *top panel* shows the normalized spectra plotted on an arbitrary scale for comparison. The *bottom panel* shows the difference between each normalized spectrum with the average of all three spectra using the same color scheme. As clear from this figure, all spectra look remarkably the same. In terms of PAH emission only, the largest differences between the individual spectra with the average are only a few percent, with the largest deviations associated with the profile of the 6.2 and 7.7 μm features (<10%). The spectra also differ only slightly in the H_2 emission lines, as it can be observed from the lines H_2 S(5) 6.9 μm , S(3) 9.7 μm , and S(2) 12.3 μm .

and b is the observed spectrum), by minimizing the Euclidian norm while forcing all coefficients x to remain non-negative (Lawson & Hanson 1974). The suite also provides useful routines to model the emission of PAHs upon the absorption of a single photon. Here we have extended these routines to take more physical detail into account, admitting the entire spectrum of photons emitted by a star instead of considering a single photon energy.

2.4.1. Model Parameters

When using the PAH absorption spectra in PAHdb to fit astronomical spectra, we have to take the following into account: 1) the radiation field that excites the mixture of PAHs; 2) the stepwise nature of the emission process; 3) the profile and full-width-at-half-maximum (FWHM) of the emitted bands; and 4) the shift of the bands arising from anharmonic effects.

Radiation Field: PAHs emit in the mid-IR after absorption of UV-vis photons. For the regions studied here, we can assume single photon events (Tielens 2005). In the Ames-PAHdbIDLSuite, PAHs absorb a photon of an energy equal to the average photon energy emitted by the star. This is computed from considering the stellar spectrum together with the PAH absorption cross sections (from Li & Draine 2001). However, a more complete approach—though more time consuming—is to consider the entire spectrum of photons emitted by the star. Here we use this approach using Kurucz stellar atmosphere models to describe the emission of each star according to the parameters given in Table 2.2. We assume a solar metallicity model, and a surface gravity of $\log(g) = 4$ for all three stars (Kurucz 1993). We consider each PAH absorbs photons of energies up to $E_{max} = 13.6$ eV.

Emission Model: Prior to absorbing an exciting photon, each PAH is assumed to be in its ground electronic (and vibrational) state at a temperature considered to be that of the cosmic microwave background $T_{ini} = 2.73$ K. We note however, that the emission spectrum does not depend strongly on the assumed initial temperature. In the environments studied here collisional excitation and multiphoton events are unimportant compared to single UV photon excitations.

After photon absorption, a PAH attains a maximum temperature $T_{max}(E)$ that depends on the energy absorbed, and the heat capacity of the PAH in question, $C_v(T)$. This heat capacity and the consequent cooling rate dT/dt are here calculated using the so-called thermal approximation (e.g., Schutte et al. 1993; Bakes et al. 2001) just as considered in PAHdb. In this approximation, the emission from a given vibrational mode is calculated as the average emission of an oscillator connected to a thermal bath at T . Thus the Boltzmann equation is used to describe the excitation process, and both $C_v(T)$ and dT/dt are calculated using the frequencies, $\bar{\nu}_i$, of all the vibrational modes of each PAH. The maximum temperature attained is then calculated from:

$$\int_{T_{ini}}^{T_{max}(E)} C_v(T) dT = E \quad (2.1)$$

In order to model the relaxation process we consider the temperature probability distribution function $G(T)$ from Bakes et al. (2001), which considers the emission process as a Poisson process, leading to an exponential distribution of the cooling times (see also Aannestad & Kenyon 1979; Purcell 1976) given by:

$$G(T, E) = \frac{\bar{r}}{dT/dt} \exp(-\bar{r}\tau_{min}(T, E)) \quad (2.2)$$

Where \bar{r} corresponds to the average photon absorption rate, and τ_{min} corresponds to the minimum amount of time the PAH spends at a temperature T after reaching $T_{max}(E)$. Since we consider that PAHs can absorb photons of different energies $E = h\nu$, the $G(T)$ function has to be integrated over the photon spectrum under consideration. This depends on both the stellar spectrum F_ν and the absorption cross section of each PAH $\sigma_{abs}(\nu)$, which here is taken from Li & Draine (2001). The relaxation process then lasts until each PAH returns to its initial temperature T_{ini} . The emission from a given mode I_i then can be described as:

$$I_i = 4\pi \int \sigma_{\bar{\nu}_i} B(\bar{\nu}_i, T) \tilde{G}(T) dT \quad (2.3)$$

Where $\tilde{G}(T)$ is $G(T, E)$ averaged over the photon energies:

$$\tilde{G}(T) = \frac{1}{\bar{r}} \int G(T, E) n(E) dE \quad (2.4)$$

Here $\sigma_{\bar{\nu}_i}$ corresponds to the integrated infrared cross section of mode i , and $n(E)$ corresponds to the number of photons of energy E absorbed by the PAH.

Band Profile and FWHM: The PAH band profile reflects intra/intermode anharmonicities coupled with the non-radiative vibrational redistribution process (e.g., Pech et al. 2002). As these processes are not well-understood, the profile to be adopted is uncertain. Typically either Lorentzian or Gaussian profiles are assumed. As the vibrational modes in a PAH are strongly coupled, Lorentzian oscillators do not provide a good description for the intrinsic profiles of these bands (Barker et al. 1987; Pech et al. 2002). Depending on the anharmonicity of the modes involved, the profiles may develop a strong red-shaded wing. If the emission bands arise from a broad mixture of related species, we can consider that the PAH species contributing to each band emit as oscillators randomly distributed around a mean, which leads to Gaussian band profiles. In terms of the width of the bands, we consider the same FWHM for all bands to be 15 cm^{-1} . This choice is based on experiments on small PAHs that have shown that, for short wavelength bands ($\lambda < 15 \mu\text{m}$), typical widths range between $10\text{--}30 \text{ cm}^{-1}$ depending on the band in question. The instrumental FWHM of IRS low resolution spectra expected at these wavelengths is roughly 5 to 20 cm^{-1} , sufficiently similar for this work. See the Appendix for a further discussion on the band profile assumed in this study.

Band Shifts: Anharmonic effects induce a small redshift of the band positions. Experiments have only been performed on small PAHs (e.g., Joblin et al. 1995), and since what happens for larger PAHs is unknown, we consider a uniform shift for all bands of 15 cm^{-1} as a first approximation (Cook & Saykally 1998; Pech et al. 2002; Boersma et al. 2013).

2.4.2. Database

Once the description of the emission process had been defined, decisions were made regarding the pool of PAHs to be considered in the fits. On this matter it is important to keep the characteristics of PAHdb in mind. These have been extensively discussed in Boersma et al. (2013). Here we summarize the relevant points as follows:

i) The database contains a large number of small PAHs with $N_c < 20$. Such small PAHs are assumed to be destroyed in the radiation fields considered here. Consequently, all species with less than 20 carbon atoms are removed from the initial pool of PAHs prior to the fit of the astronomical spectra.

ii) Regarding charge, one expects neutral and positively ionized PAHs to dominate the PAH population in PDRs where the ionization parameter $\gamma \equiv G_0 \sqrt{T_{\text{gas}}}/n_e > 10^4$. Most of the PAHs in the database are cations and neutrals, with only 12% of the entire database being singly ionized anions. While this would seem to be consistent with the expected population in the emission zone, fits can still result in high anionic abundances. This is because PAH anion bands are redshifted compared to the bands of their neutral/cationic counterparts. In effect, the fitting procedure uses anions to account for anharmonic redshifts of the bands.

iii) Concerning heteroatomic species, we only include PAHs that contain nitrogen atoms (PANHs). N-substitution has been suggested as one way of shifting the emission in the 6–6.5 μm region to the observed position of the 6.2 μm band (Hudgins et al. 2005). Given that there are still doubts about their formation process, in a way, PANHs may be viewed as representatives of any class of PAHs in which the C-C modes are shifted to 6.2 μm , e.g., pyramidal carbon or aliphatic structures (Galué 2014; Pino et al. 2008). Other heteroatomic PAHs are expected to be less stable, and thus we do not include them in the fits.

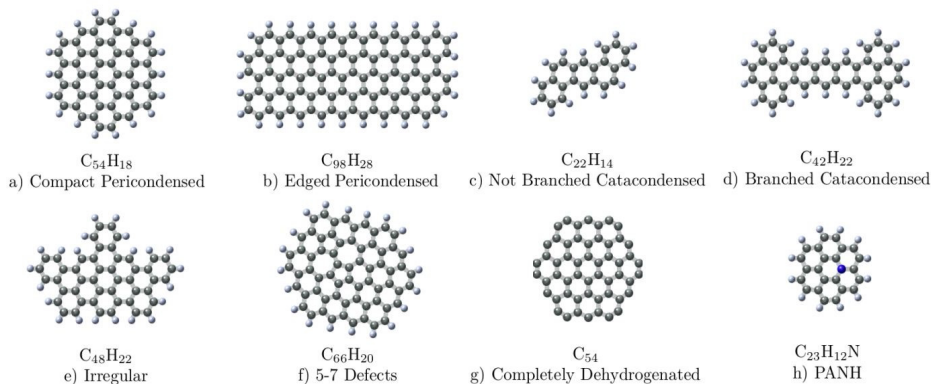


Figure 2.3: Structure classification of PAHs as typified by one characteristic PAH (see text for details). a) Compact Pericondensed PAHs: These are PAHs with a compact core of carbon atoms with 12 duo-hydrogens and solo-hydrogens at the periphery. b) Pericondensed PAHs With Edges: These are pericondensed PAHs with edges containing trios. c) Not Branched Catacondensed PAHs: these are linear PAHs showing either only 8 quartets and solos (extremely linear) or admitting also duos (i.e., corners). d) Branched Catacondensed PAHs: these are linear PAHs containing trios (having branches). e) Irregular PAHs: these are PAHs whose shape do not follow any of the other classifications. They are mostly pericondensed PAHs with sharp edges (admitting trios and/or quartets). f) PAHs having the 5–7 fused ring defects. These are compact pericondensed PAHs. Their abundance contribution is already considered in the output values of the contribution of pericondensed PAHs listed in Table 2.4. g) Completely Dehydrogenated PAHs: These are PAHs with all hydrogens removed. h) Nitrogenated PAHs (PANHs): the nitrogen atom is always replacing one carbon atom from the core of the PAH.

iv) Lastly, PAHdb is dominated by pericondensed and symmetric PAHs. Stability studies have long shown that pericondensed and symmetric PAHs are in general more stable (in terms of chemical reactivity and fragmentation) than catacondensed PAHs (e.g., Stein 1978; Crauford et al. 1985; Ricca et al. 2011). This is due to the difference in the electronic density distribution and resonance energies of PAHs having different structures. Figure 2.3 shows the structure classification considered in this work. We have distinguished two types of *pericondensed* PAHs: *compact* (only solos and 12 duo-hydrogens at the periphery) and with *edges* (admitting trio-hydrogens). Likewise, we also distinguish between two types of *catacondensed* (linear) PAHs: *branched* (admitting trios) and *not branched* (8 quartets and solos and/or duos). Those that do not fall in any of these categories are considered as having *irregular* structure. We also recognize that PAHdb lacks enough large pericondensed PAHs with edge structure (i.e., trio and quartet-hydrogens). Since these are the PAHs necessary to properly describe the 15–20 μm region (Boersma et al. 2010; Ricca et al. 2010), we restrict our fits to the 5–15 μm range only. While we do not include the 15–18 μm region in our fitting procedure, we will come back to this spectral range in the discussion.

In view of the above, we have restricted the entire pool of (initially 700) PAHs available in PAHdb to include medium-to-large PAHs (i.e. $N_c > 20$); pure (carbon-and-hydrogen) PAHs and PANHs; and PAHs having no CH_2/CH_X side groups (since these species are also expected to be underrepresented in PAHdb). This results in an initial pool containing 292 PAHs. The results derived from using this condition are presented in the next section and are referred to as the *base run* results. It is important to mention that all these PAHs are expected to have ionization potentials $\text{IP} < 13.6$ eV, following the $\text{IP} \propto (Z + 0.5) \times N_c^{-1/2}$ dependence described in Tielens (2005), where Z is the ionization state of the PAH.

2.5. Results

The results are presented for *Features+Plateaus* spectra and only refer to NGC7023, since—as the spectra are similar to a very high degree—the fits for all three spectra lead to the same results. The results for the other two RNe and the *Features-Only* spectra can be found in the Appendix 2.A.

First the *base run* results are presented. This is then followed by an exploration of the degeneracy in the fit, which provides insight into the allowed variation in both, the actual contributing PAH species and PAH subclasses.

2.5.1. Base Run

The fit to the NGC7023 *Features+Plateaus* spectrum is shown in Figure 2.4. Table 2.3 lists all PAHs that make up the fit, together with their relative abundances, a brief description of their structure class, and whether the PAH is a radical or not. This set of PAHs comprises the *base run* fit to NGC7023. Their structures are shown in the Appendix. Table 2.4 summarizes the breakdown of the fits to all PDR spectra in terms of size, ionization states, composition, and structure. The average photon energy has been derived convolving the stellar emission, with the absorption cross section of the PAHs. We have admitted in our fits dehydrogenated PAHs, and PAHs with Stone-Wales (five and seven fused rings) defects, referred to here as PAHs with *SW defects* (Stone & Wales 1986; Ricca et al. 2011). Their contribution is included in that of pericondensed PAHs.

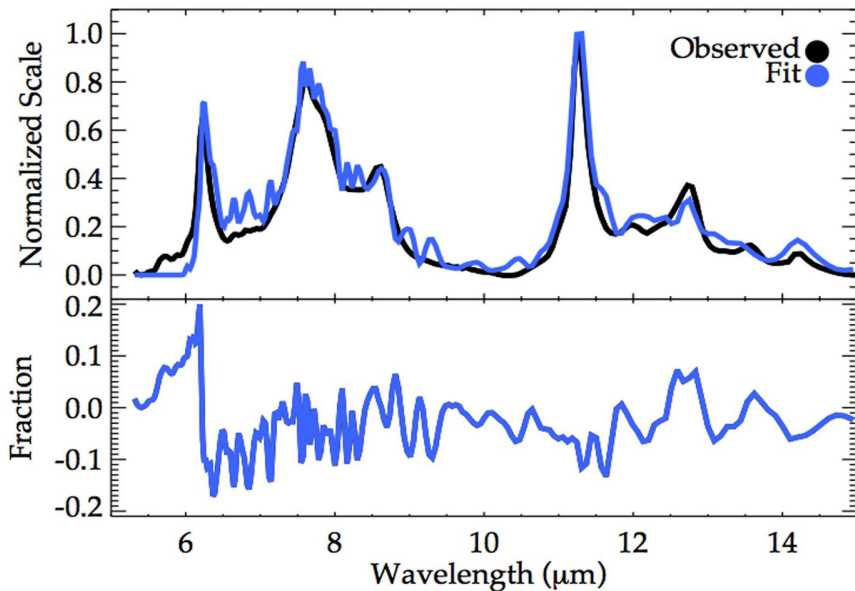


Figure 2.4: *Base run* fit to the *Features+Plateaus* spectrum of the brightest location in NW PDR of NGC 7023. The spectra are shown in normalized scale. The figure also shows the difference between both normalized spectra. Out of a pool of 292 PAHs, this fit requires only 33. Table 2.3 lists the PAHs used in this fit. The results of the *base run* for NGC 2023 and NGC 1333 can be found in the Appendix.

As observed from Figure 2.4 there are regions that are not well-reproduced by the fit. However these *problematic regions* do contain valuable information. The region at $\lambda < 6\mu\text{m}$ is dominated by the emission from combination bands and overtones that are not included in the database (Boersma et al. 2009). The residual at $6.2\mu\text{m}$ is usually attributed to the incompleteness of the database, related possibly to PANHs, pyramidal carbon or aliphatic groups (Hudgins et al. 2005; Galu e 2014; Pino et al. 2008). The spectra available in PAHdb also do not fit well the weakest features, such as the $13.5\mu\text{m}$. This is because the database lacks the necessary variation in edge structure to reproduce the weak bands properly, while simultaneously satisfying all constraints posed by the dominant features between $5\text{--}15\mu\text{m}$.

Perusal of Table 2.4 shows that the best fits to all three RNe spectra produce very similar results. In fact, the PAH population derived for all three PDRs is practically the same down to the derived abundances of the contributing species. Around 88% of the PAHs used to fit NGC 2023 are also used to fit the spectrum of NGC 7023, and they make up 98% of the total abundance of PAHs in the fit to NGC 2023. Similarly, the fit to NGC 1333 shares 88% of its PAHs with NGC 7023, contributing 94% to the total abundance of PAHs in the fit. Thus, all three fits essentially rely on the same set of PAHs.

The fact that we get very similar results highlights the similarity of the astronomical spectra, and the insensitivity of PAH emission spectra relative to the exciting radiation field. The three RNe studied here have different illuminating stars with effective temperatures ranging from $T_{eff} = 14000$ to 23000 K. As a test run, we studied the effect of the radiation field on the emission spectrum of the *base run* PAHs, using Kurucz stellar atmosphere

Table 2.3: Base-run PAHs Derived From Fit to NGC7023 Features+Plateaus Spectrum. See 2.5.1 for details.

Uid ^a	Formula	Abundance (%)	n _{solo}	n _{duo}	n _{trio}	n _{quartet}	Structure ^b	R/NR ^c
128	C ₃₆ H ₁₆	16.0	2	8	6	0	Irregular	NR
605	C ₆₆ H ₂₀ ⁻	14.4	8	12	0	0	5-7 Ring defects	R
620	C ₄₂ H ₁₆	9.3	4	12	0	0	Pericondensed	NR
226	C ₂₃ H ₁₂ N	6.6	0	12	0	0	Pericondensed	R
600	C ₆₆ H ₂₀	5.5	7	10	3	0	5-7 Ring defects, with edges	NR
157	C ₄₂ H ₂₂	4.8	6	4	12	0	Catacondensed, branched	R
11	C ₃₂ H ₁₄	4.5	2	12	0	0	Pericondensed	R
636	C ₄₈ H ₁₈ ⁺	4.3	6	12	0	0	Pericondensed	R
255	C ₅₂ H ₁₈ N ₂ ⁺	3.3	6	12	0	0	Pericondensed	NR
243	C ₃₁ H ₁₄ N ₂ ⁺	3.2	2	12	0	0	Pericondensed	NR
592	C ₃₂ H ₁₄ ⁺	3.0	2	12	0	0	5-7 Ring defects	R
284	C ₂₂ H ₁₂	2.6	0	6	6	0	Irregular	NR
704	C ₅₄	2.4	0	0	0	0	100% Dehydrogenated, pericondensed	R
229	C ₂₃ H ₁₂ N	2.2	0	12	0	0	Pericondensed	R
31	C ₂₄ H ₁₂ ⁺	1.9	0	12	0	0	Pericondensed	R
308	C ₂₂ H ₁₄ ⁺	1.7	6	0	0	8	Catacondensed, not branched	R
639	C ₉₀ H ₂₄ ⁺	1.7	12	12	0	0	Pericondensed	R
301	C ₂₂ H ₁₄	1.7	2	4	0	8	Catacondensed, not branched	NR
307	C ₂₂ H ₁₄	1.7	6	0	0	8	Catacondensed, not branched	NR
158	C ₄₂ H ₂₂ ⁺	1.6	6	4	12	0	Catacondensed, branched	R
544	C ₃₂ H ₁₈ ⁺	1.3	4	0	6	8	Catacondensed, branched	R
601	C ₆₆ H ₂₀	1.0	7	10	3	0	5-7 Ring defects, with edges	R
632	C ₁₂₈ H ₂₈ ⁺	0.9	16	12	0	0	Pericondensed	R
167	C ₁₁₂ H ₂₆ ⁺	0.8	14	12	0	0	Pericondensed	R
181	C ₁₀₂ H ₂₆ ⁺	0.7	12	8	6	0	Pericondensed, with edges	R
591	C ₃₂ H ₁₄	0.6	2	12	0	0	5-7 Ring defects	NR
543	C ₃₆ H ₂₀	0.6	6	0	6	8	Catacondensed, branched	R
624	C ₁₇₀ H ₃₂	0.5	20	12	0	0	Pericondensed	R
707	C ₆₆ ⁺	0.5	0	0	0	0	100% Dehydrogenated, pericondensed	R
626	C ₄₀ H ₁₆ ⁺	0.4	4	12	0	0	Pericondensed	R
257	C ₅₂ H ₁₈ N ₂ ⁺	0.4	6	12	0	0	Pericondensed	NR
614	C ₁₅₀ H ₃₀	<0.1	18	12	0	0	Pericondensed	R
228	C ₂₃ H ₁₂ N ⁺	<0.1	0	12	0	0	Pericondensed	NR

^a Unique identifier for each PAH in PAHdb. ^b The structures of these PAHs can be found in the Appendix. ^c R stands for radical species, NR stands for non-radical species.

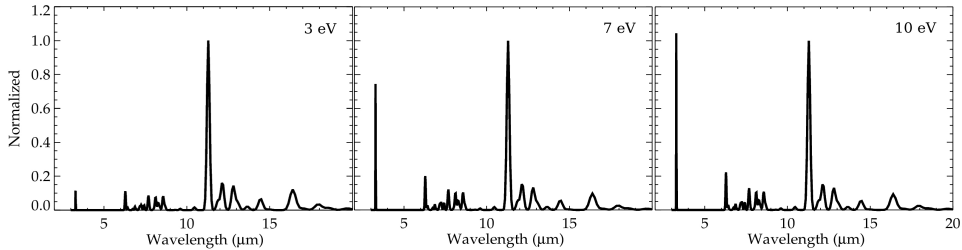


Figure 2.5: Computed emission spectrum of circumpyrene (the most abundant PAH in all *base run* fits) after absorbing a 3, 7 and 10 eV photon. These values correspond to the average photon energies absorbed by PAHs in fields illuminated by stars at $T_{eff} = 4000, 17000$ and 35000 K respectively. The emission spectra are shown normalized to the $11.3\mu\text{m}$ band to illustrate how the relative band intensities vary with increasing (absorbed) photon energy.

models of main sequence stars with effective temperatures varying from 4 000 to 35 000 K. We then coadded their spectra using the original relative abundances listed in Table 2.3. The resulting spectra show little if any band intensity variations. The reason for this is illustrated with the spectra given in Figure 2.5. The computed emission spectrum of circumpyrene (one of the most abundant PAH in all *base run* fits) after absorbing a 3, 7 and 10 eV photon is shown in the left, middle and right panels respectively. These energies correspond to the average photon energies absorbed by PAHs in fields illuminated by stars at $T_{eff} = 4\,000$, 17 000 and 35 000 K respectively. We see that, using our emission model, the relative intensity of the $3.3\mu\text{m}$ band to the other bands is the only ratio that is very sensitive to the effective temperature of the illuminating star. Unfortunately this band is not probed with IRS data, and in PAHdb its intensity can be 50% off (Langhoff 1996). We would like to emphasize then the importance of measuring the $3.3\mu\text{m}$ band with the same aperture along the same line-of-sight as the longer wavelength spectrum, in order to get further information on the PAH population (see also Li & Draine 2001).

Concerning the relative abundance distribution of PAHs, the fitting procedure relies on a wide range of PAHs. The *base run* contains no single PAH with an abundance greater than 16%. The PAHs that contribute the most are the irregular-shaped closed shell 3,4,5,6,7,8,12,13-tetrabenzoperopyrene $\text{C}_{36}\text{H}_{16}$ (uid = 128), the *SW defect* radical of circumovalene $\text{C}_{66}\text{H}_{20}^-$ (uid = 605), and the non radical circumpyrene $\text{C}_{42}\text{H}_{16}$ (uid = 620), which—as a side note—is the most abundant PAH in the fits to *Features-Only* spectra (see Appendix 2.A). The abundances of these PAHs are between 9–16%. In fact, most of the PAHs contribute in small abundances < 5%.

The fit to NGC7023 is initially set using the 23 most abundant PAHs, which constitute 95% of the fit. The remaining 10 are used to fill in the gaps of the profile of the $7.7\mu\text{m}$ band and to fit the $8.6\mu\text{m}$ feature. Using the first 25 most abundant PAHs—which contribute 96.8% (uid = 128–181 in Table 2.3)—the fit is completely set. The remaining 8 PAHs are used only to fill in minor details in the 6–9 μm range, since their spectra is mainly dominated by a few features in that wavelength region. We can affirm then, that the first 25 most abundant PAHs listed in Table 2.3 are in fact the important ones. Out of these, 8 are non-radical and contribute 43% to the total abundance of the fit. The last 8 PAHs only contribute 3.2%, and as such do not have a large effect on the ratios listed in Table 2.4.

Inspection of Table 2.4 shows that the mixture of *base-run* PAHs is mostly composed of small PAHs ($20 < N_c < 50$), adding up to a contribution of 68% versus the 32% abundance from large PAHs. Figure 2.6 shows the *base run* PAH size distribution in terms of the number of carbon atoms. Even though the PAHdb lacks large PAHs, the 7 PAHs having $50 < N_c < 70$ in the *base run* contribute 25% to the total abundance of PAHs in the fit. This is on average comparable to the abundance per PAH contributed by the smaller species. This may be pointing out the importance of medium sized PAHs having $50 < N_c < 70$. Larger PAHs contribute 7%, where the largest PAH used in the fit is $\text{C}_{170}\text{H}_{32}^-$ —at only 0.5% abundance—and is used to fill the profile of the $7.7\mu\text{m}$ band due to its strong emission at $7.9\mu\text{m}$.

In terms of charge, the *base-run* set has neutral PAHs contributing 48% to the total abundance. *Base run* cationic species consist of mostly singly charged PAHs (3 dications contribute at a 5.6% level, while trications do not show up in any of the fits). The total input from cations is 26%, equal to that of anionic species. As mentioned above, anions are likely

Table 2.4: Results Derived From the Base Run Fit to the Features+Plateaus Spectra of NGC 7023, NGC 2023 and NGC 1333. See 2.5.1 for details.

	NGC 7023 NW	NGC 2023	NGC 1333
Fit			
Average Photon Energy (eV)	7.0	8.1	6.2
Euclidian Norm*	2.1	1.4	0.3
Number of PAHs Used	33	31	36
Size**			
$x_{N_c < 50}/x_{N_c > 50}$	2.12	1.74	2.06
Ionization State**			
$x_{\text{PAH}^+}/x_{\text{PAH}^0}$	0.42	0.45	0.38
$x_{\text{PAH}^{+/+}}/x_{\text{PAH}^0}$	0.53	0.61	0.49
$x_{\text{PAH}^-}/x_{\text{PAH}^0}$	0.53	0.59	0.51
Composition**			
$x_{\text{PANH}}/x_{\text{PAH}}$	0.19	0.19	0.20
Structure			
$n_{\text{duo}}/n_{\text{solo}}$	2.16	1.96	2.32
$n_{\text{trio}}/n_{\text{duo}}$	0.24	0.22	0.23
$n_{\text{quartet}}/n_{\text{solo}}$	0.13	0.14	0.05
Shape (%)			
Compact Pericondensed (incl. 5–7)	58.0	60.5	60.8
Pericondensed With Edges (incl. 5–7)	9.9	7.8	12.6
Unbranched Catacondensed	5.0	5.4	1.7
Branched Catacondensed	8.2	9.9	6.7
Total contribution from PAHs with SW Defects	24.6	25.5	27.3
Total contribution Pericondensed	67.8	68.3	73.4
Total contribution Catacondensed	13.3	15.3	8.4
Total contribution Irregular	16.0	13.2	15.8
Total contribution Completely Dehydrogenated	2.9	3.2	2.4

* The Euclidian Norm is defined as the square root of the residual sum of squares between the observed spectrum and the corresponding fit. ** All ratios are expressed in terms of the abundances of each species x . PAHs with $N_c < 50$ carbon atoms are considered to be small, while PAHs with $N_c > 50$ carbon atoms are considered to be large PAHs. In terms of ionization states, PAH^0 refers to neutral species; $\text{PAH}^{+/+}$ refers to all positively ionized PAHs; PAH^+ refers to only singly positively ionized PAHs; and PAH^- refers to anionic species (PAHdb only contains singly negatively ionized PAHs). In terms of composition, $x_{\text{PANH}}/x_{\text{PAH}}$ refers to the abundance ratio of nitrogenated species relative to pure (carbon and hydrogen) PAHs. Hydrogen adjacency ratios are given in terms of solo (n_{solo}), duo (n_{duo}), trio (n_{trio}) and quartet hydrogens (n_{quartet}), i.e. number of adjacent hydrogens attached to the same aromatic ring.

very overestimated because they are used to fill in for anharmonic red wings. Among the anions, the largest contribution from an anion is given by the second most abundant PAH: the PAH with *SW defects*, $\text{C}_{66}\text{H}_{20}^-$. This class of PAHs is used to fit the plateaus underneath the PAH bands (presumably because the *SW defect* only slightly perturbs the vibrational modes), and also to fit the $6.2\ \mu\text{m}$ band (see more in the Appendix). If we perform the *base run* fit without considering any PAH with *SW defects*, we do get good quality fits where the contribution from Stone-Wales PAHs is replaced by increasing the fraction of PANHs (from 19% to 43% compared to pure PAHs) and small cationic species of slightly more irregular

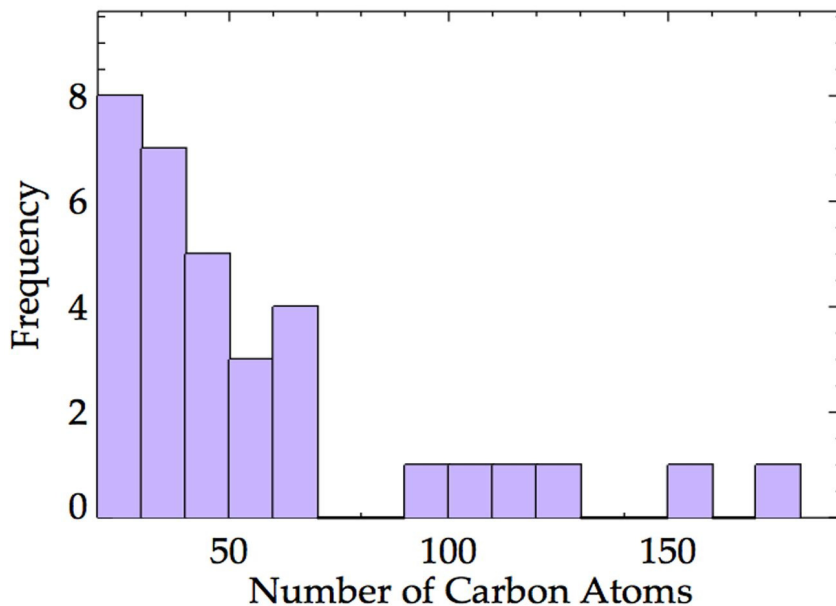


Figure 2.6: *Base run* PAH size distribution. Small PAHs having $20 < N_c < 50$ carbon atoms contribute 68% to the total abundance of PAHs in the fit to NGC 7023. Among the large PAHs, those having $50 < N_c < 70$ carbon atoms contribute 25%, while larger PAHs contribute 7% (see also Table 2.3).

structures (from $x_{\text{PAH}^{+}/+}/x_{\text{PAH}^0} = 0.53$ to 0.80). The contribution from anions is then only 10%. In fact, if we perform the fits without allowing any anions, we get similar results (e.g., PANHs contribute 30% and $x_{\text{PAH}^{+}/+}/x_{\text{PAH}^0} = 0.99$) without diminishing the quality of the fit. Thus the 26% contribution from anionic species should be considered as an upper limit.

Other minor inputs include completely dehydrogenated PAHs, which contribute only 3%. The spectra of completely dehydrogenated PAHs have, in general, very few salient features, and as such their spectra are used to fill in gaps at specific wavelengths in the 6–9 μm region.

Concerning the structure of *base-run* PAHs, Table 2.4 shows the PAHs are mostly compact and pericondensed in shape. Catacondensed PAHs contribute at a $\sim 10\%$ level to the total abundance of PAHs in the *base run*, while irregular-shaped PAHs contribute at 15–20% level. The actual structure of the irregular-shaped PAHs is that of pericondensed PAHs with sharp edges and bay regions (e.g., see Figure 2.3). There are only 37 catacondensed PAHs in the initial pool of 292 PAHs. Test runs show that the observed spectra cannot be fitted well using only catacondensed PAHs, as the species included in the database lack strong 6.2 and 11.3 μm bands, a general characteristic of catacondensed species. In general, catacondensed PAHs will have weak solo out-of-plane C-H bending modes compared to duo and trio out-of-plane modes and hence, even if the database were more complete in terms of catacondensed PAHs, they would not be selected as an important component of the interstellar PAH family contributing to these spectra (Hony et al. 2001).

2.5.2. Degeneracy

The *base run* fit is subjected to a certain degree of degeneracy as classes rather than specific molecules are probed. To examine this degeneracy further, we proceeded to fit iteratively the observed spectrum of NGC 7023 using the *base run* condition, but removing all PAHs used in the previous fit each time. The fitting procedure was then allowed to use any of the PAHs remaining after each iteration that satisfied the criteria defined in 2.4. The results are summarized in Figure 2.7 in terms of the total number of different PAHs used in the fits, and the variation of ratios after each iteration. Figure 2.8 shows the first 4 fits. Here we clearly see that the fit gets significantly worse after 2 iterations, and the ratios vary considerably from one iteration to the other. Up until now, it has been recognized that random mixtures of PAHs can reproduce the general shape of the PAH emission spectra observed in different astronomical objects (Rosenberg et al. 2014). Here our exercise shows that even though completely different sets of PAHs can indeed produce the general shape of the PAH emission spectra, they cannot reproduce the spectrum in detail.

Naturally, the number of different sets that could reproduce the observed spectrum at a given level of detail is related to the incompleteness of PAHdb. Despite this, our results highlight that there is a preferred set of PAHs. The fitting procedure chooses the PAHs with bands at the precise, observed wavelengths. Once it runs out of these PAHs, it tries to reproduce the peak positions by combining different PAH spectra. This point is already reached at the first iteration, which reflects the intrinsic, subtle variations in the PAH spectra.

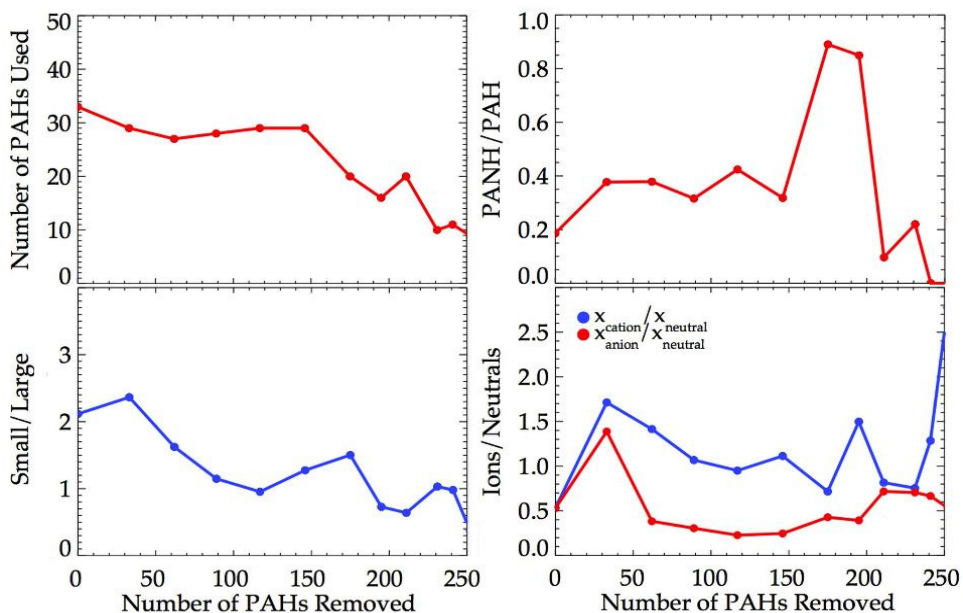


Figure 2.7: Results derived from the fits to the spectrum of NGC 7023 after sequentially removing all chosen PAHs after each iteration. The variation of composition, size and charge ratios are shown together with the number of PAHs used and removed after each iteration. The results are shown only for the first 10 iterations (241 PAHs removed from the initial pool). As shown from these plots, as we remove more PAHs, the ratios vary considerably from one iteration to the other.

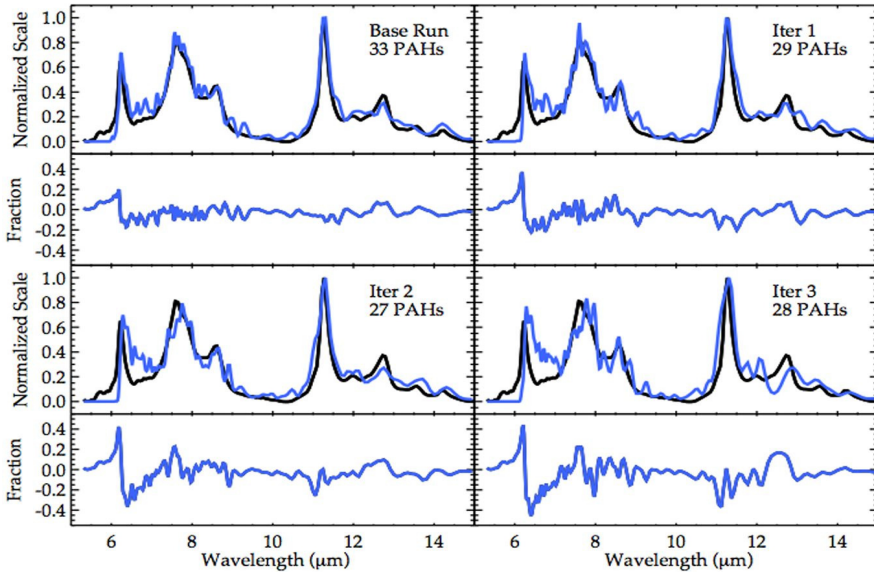


Figure 2.8: Fits to the spectrum of NGC7023 obtained after sequentially removing the entire set of PAHs used in the previous iteration. The first fit corresponds to the actual *base run*. All spectra have been normalized to the peak intensity of the $11.3\mu\text{m}$ feature. The observed spectrum is shown in black, while the fits are shown in blue. Also shown is the difference between each normalized fit and the observed normalized spectrum. Out of a pool of 292-33 PAHs, the first iteration uses 29 and the Euclidian norm is already increased by $\sim 40\%$ (right top panel). The second and third iterations are shown in the bottom panels. The third iteration is still able to reproduce the overall shape of the observed spectrum, but fails in the details. At the third iteration the Euclidian norm has already exceeded that obtained in the *base run* by more than a 100%.

We can study the robustness of this last statement by performing the same exercise, but removing only the most abundant PAH each time. Figure 2.9 shows the number of PAHs used in each fit, and the contribution from *base-run* PAHs that are used after each iteration. As observed from both panels, the fits always use *base-run* PAHs to some degree. Also the fitting procedure uses a relatively steady number of PAHs to fit the spectrum, and the abundance of the most relevant PAH is at a 10% level for all runs.

Regarding the quality of the fits, Figure 2.10 shows the *base run* together with the fits after the removal of 10, 20 and 30 PAHs. As we remove an increasing number of PAHs, the fit has more trouble in reproducing the observations in detail, e.g., *problematic regions* get worse, and the fits have more difficulty reproducing the position and profile of the main PAH bands. The Euclidian norm increases by 23, 31 and 50% when we remove 10, 20 and 30 PAHs, respectively. Although this is a rather gradual variation, the Euclidian norm increases more rapidly from the 20th iteration on. Figure 2.11 shows how the size, charge, structure and composition ratios vary throughout the first 30 iterations. From these values we can estimate average ratios for the first 20 fits. These are shown in Table 2.5 and appear to be consistent with the values presented in Table 2.4. Standard deviations represent variations of less than 30% for most ratios. The ratios that vary $> 30\%$ correspond to the fraction of PANHs relative to pure carbon PAHs, number fraction of quartet to solo-hydrogens, and the contribution of unbranched catacondensed PAHs.

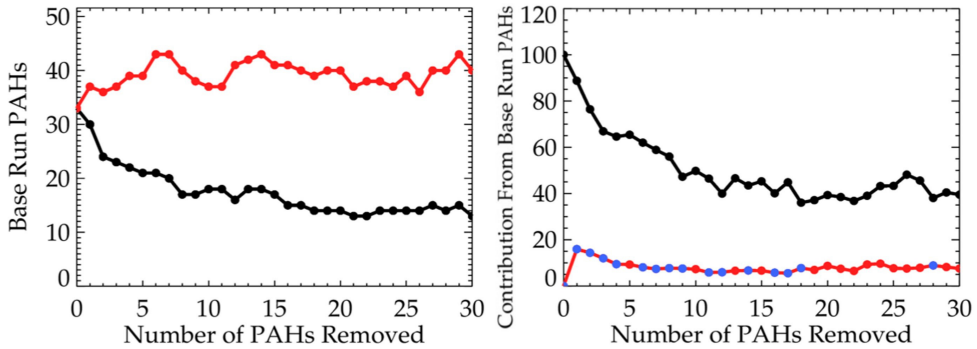


Figure 2.9: *Left panel.* Total number of different PAHs used in the fit to the *Features+Plateaus* spectrum of NGC 7023 after each iteration (in red). The black dots refer to the number of PAHs from the initial *base run* that are used in each iteration, e.g., the 0^{th} iteration corresponds to the actual *base run* fit where the 33 PAHs listed in Table 2.3 are used. *Right panel.* Contribution in relative abundance of the PAHs from the initial *base run* that are used after each iteration (in black), e.g., at the 0^{th} iteration *base-run* PAHs contribute in a 100% to the fit. Red dots refer to the most abundant PAH from the previous iteration that is removed each time. Blue dots indicate whenever the most relevant PAH removed was a *base-run* one, e.g., the first PAH removed is the most abundant one in the *base run* contributing in 16.0% as shown in Table 2.3.

From Figure 2.9 we notice that, as we remove the most abundant PAHs of each fit—which are most of the time *base-run* PAHs (see blue dots in Figure 2.9)—the fitting procedure uses different subsets of the remaining *base-run* PAHs to constitute the bulk of the fits. Each removed PAH is not replaced by another single new PAH, but by increasing the abundance of *base-run* PAHs, and adding a lower abundance of new PAHs to fill in the details of the spectrum. Figure 2.12 shows the coadded spectra of the *base-run* PAHs that have been removed in the first 20 iterations at their initial abundances derived in the *base run*. These 14 PAHs contributed a 68.4% abundance to the *base run* fit. These PAHs are mainly responsible for the strongest bands in the observed spectrum (e.g, $11.3\mu\text{m}$ band).

Table 2.5: Average Size, Charge, Structure and Composition Ratios for the First 20 Iterations

Small/Large	$x_{\text{cation}}/x_{\text{neutral}}$	$x_{\text{anion}}/x_{\text{neutral}}$	$x_{\text{PANH}}/x_{\text{PAH}}$	$n_{\text{duo}}/n_{\text{solo}}$	$n_{\text{trio}}/n_{\text{duo}}$	$n_{\text{quartet}}/n_{\text{solo}}$
1.93 ± 0.53	0.97 ± 0.28	0.48 ± 0.12	0.25 ± 0.08	2.01 ± 0.21	0.23 ± 0.05	0.31 ± 0.13
Structure (Average contributions in %) ^a						
Compact	With Edges	5–7	Branched	Unbranched	Irregular	Dehydrogenated
53.98 ± 4.37	11.06 ± 4.46	15.58 ± 4.24	11.83 ± 1.77	9.63 ± 4.09	8.85 ± 4.98	4.65 ± 0.65

^a See Figure 2.3 for the definitions of these structures.

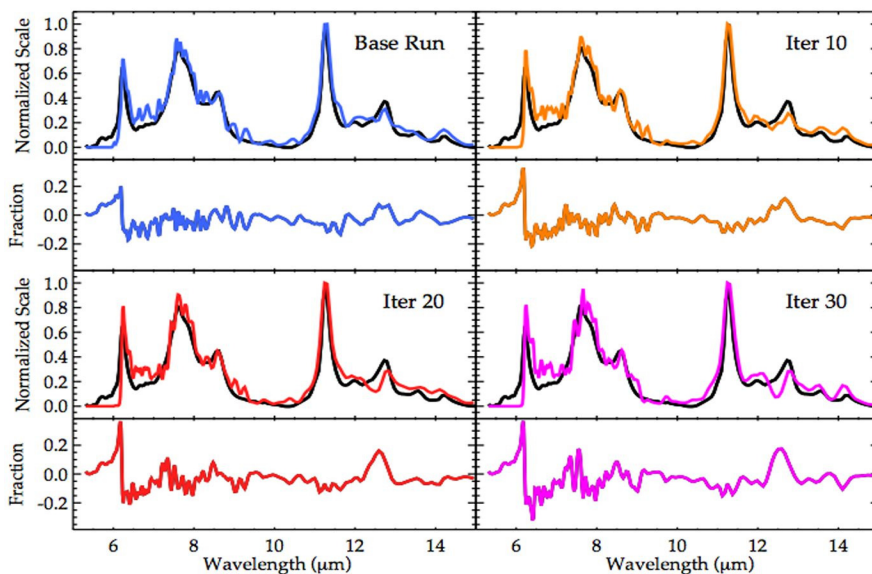


Figure 2.10: Fits to the spectrum of NGC7023 after removing 10, 20 and 30 PAHs compared to the *base run*. All spectra have been normalized to the peak intensity of the $11.3\ \mu\text{m}$ feature. The observed spectrum is shown in black, while the *base run* is shown in blue and the fits after the removal of 10, 20 and 30 PAHs are shown in the colors of each panel. Also shown is the difference between each normalized fit and the observed normalized spectrum. This figure shows that the quality of the fits decreases as we remove a larger number of PAHs, showing problems in matching band peak positions and the *problematic regions* explained in 2.5.1.

On the other hand, the 14 *base-run* PAHs used at the 20th iteration contributed only 27.7% to the *base run* fit, but at the 20th iteration they make up almost 40% of the total abundance of PAHs in the fit. In this iteration, the removed PAHs are replaced by comparable species. However, those do not reproduce the observed C-H out-of-plane bending bands to the same degree, as the quality of the fit at the 20th iteration is less than that for the *base run*.

In summary, *base-run* PAHs appear to be the preferred set in order to reproduce the observations in detail. Nevertheless, as long as we are not concerned with a very detailed fit, the spectra of the PAHs in PAHdb are highly degenerate as, up to a point, any single PAH can be replaced—although not by a single other PAH—and the resulting spectrum is similar. However, it is not possible to produce identical fits.

2.6. Discussion

The results showed that, within the limits of the database, the *base-run* PAHs are the preferred set of PAHs to match the observations. Going back to the observations themselves, it is important to determine if variation in the distribution of relative abundances of *base-run* PAHs (see Table 2.3) can account for the observed differences between the three RNe. To address this question, we first performed a Monte Carlo experiment. This is then followed by a discussion on the effects of the incompleteness of the database, and the

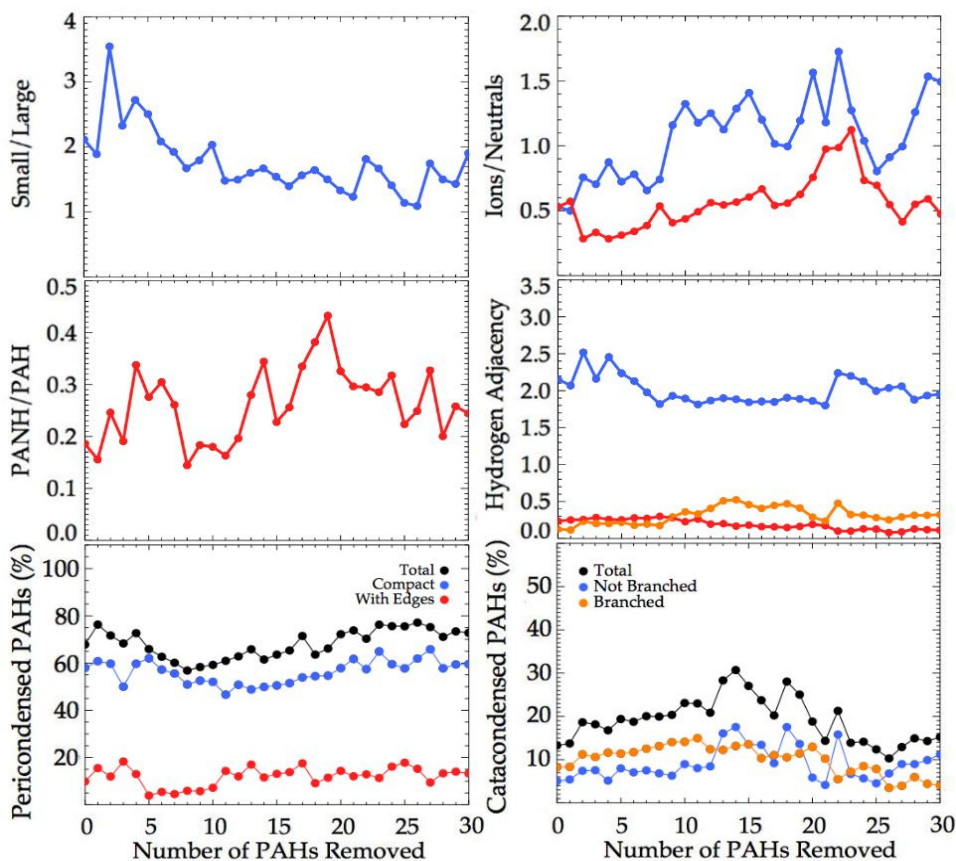


Figure 2.11: Size, Charge, Structure and Composition Ratios derived from the fits to the spectrum of NGC 7023. The results are shown only for the first 30 iterations. *Top* and *middle panels* show the ratios in terms of abundances. The bottom panels refer to the abundance contribution of PAHs classified according to their structure. The *left panel* shows the contribution from pericondensed PAHs (including PAHs with 5–7 ring SW defects), while the *right panel* shows the contribution from catacondensed PAHs. Irregular-shaped PAHs are not shown in these plots but tend to contribute at the 15% level, being mostly pericondensed in shape with few sharp edges.

limitations of the applied emission model on our results. Next the *grandPAH* hypothesis is outlined and, lastly, the concept of *grandPAHs* is applied to the spatial evolution of PAHs within NGC 7023.

2.6.1. Monte Carlo Experiment

We performed a Monte Carlo analysis on the relative abundances of the *base-run* PAHs derived from the fit to the spectrum of NGC 7023. Each PAH relative abundance was varied according to a Gaussian distribution of 5 000 random numbers around a mean given by the relative abundance derived from the *base-run* (listed in Table 2.3). The width of each Gaussian distribution represented the variation of the relative abundances as a certain percentage of the mean. All resultant spectra were then averaged (Figure 2.13).

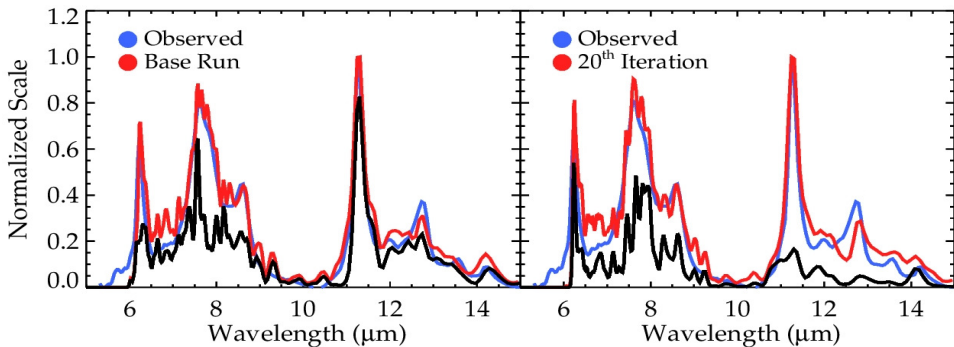


Figure 2.12: *Left panel.* Coadded spectra of the 14 *base-run* PAHs that have been removed by the time we perform the 20th iteration (black curve). The spectra have been coadded using their respective contributions to the *base-run* fit. Also shown are the observed spectrum of NGC7023 plotted in blue, and the *base run* fit which is shown in red. The removed *base-run* PAHs contribute greatly to the observed flux of the most salient bands, especially in the 10–15 μm region. *Right panel.* Spectra of the 14 *base-run* PAHs used in the 20th iteration. The spectra have been stacked according to their contribution to the fit at the 20th iteration (black curve). Also shown are the observed spectrum of NGC7023 plotted in blue, and the fit at the 20th iteration in red. As observed here, the coadded spectra fill in the strong bands at 5–9 μm , while the new PAHs are used to fit the long wavelength region which is not properly fitted as illustrated in Figure 2.10.

The results show that only a modest variation on the *base-run* relative abundances is enough to account for the small differences observed between the spectra of the three PDRs. The relative abundances of *base-run* PAHs can change up to 20% to account for the small differences observed between NGC 1333 and NGC7023, and around 30% to explain the differences between NGC 2023 and NGC1333.

We recognize that the derived percentage variation allowed depends largely on the quality of the fit in the *problematic regions* (see section 2.5.1) and hence, these variations are uncertain. However, we stress that the variation in the abundances allowed by the observed differences between the three RNe spectra are significantly less than the variations in the abundances of the PAHs in the *base run* (i.e., ranging from 16 to 3% for the first 10 PAHs in the *base run*), and this we consider a robust result. Taking this into account, it is even more striking to have such similar PAH emission at the studied locations of the three PDRs.

2.6.2. Limitations

Given that we focused on studying the fits at a detailed level, it is important to explore what determines how much detail we can go into when analyzing our results. Here several things come into play: the spectroscopic resolution of the Spitzer-IRS SL data, the completeness of PAHdb, and the calculation of PAH emission spectra. The resolution of our observed spectra does not allow one to discriminate between the A, B, C classifications of the 6.2 μm feature, and smears out the details in the 7.7 μm feature. We have already discussed the completeness of PAHdb in terms of the *problematic regions* in the fits. Concerning the PAH emission spectra, the FWHM and shift of the bands, the assumed band profile, and the emission model play a determinant role when studying the results of the fits.

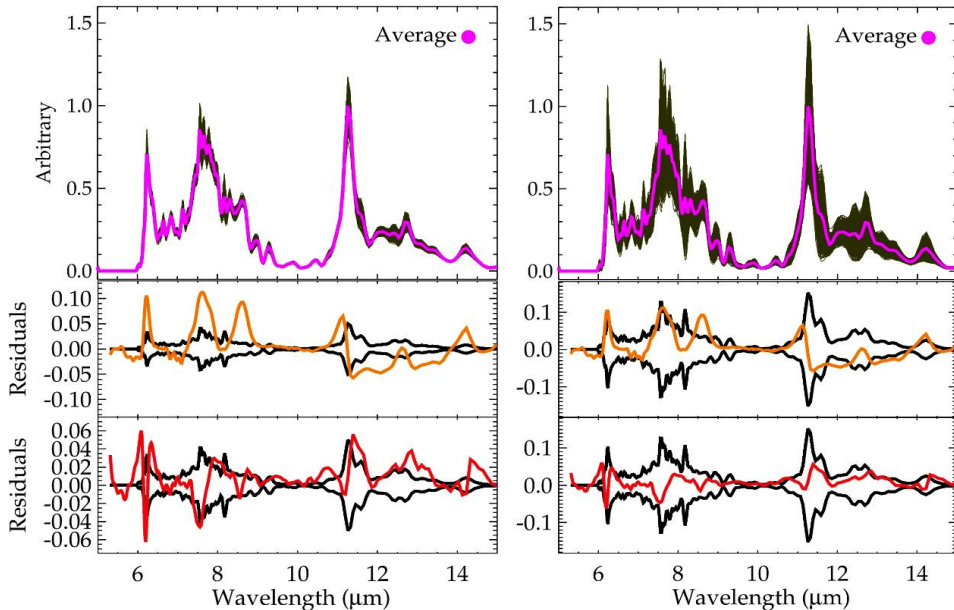


Figure 2.13: Monte Carlo analysis varying *base-run* relative abundances. *Top panels*: Average spectra obtained by varying the *base-run* relative abundances up to 10% (*left panel*) and 30% (*right panel*). *Bottom panels*: Comparison between the standard deviation of the averaged spectrum ($\pm 1\sigma$ shown in black) and the observed differences between the spectrum of NGC 7023 and that of NGC 2023 (shown in orange) and NGC 1333 (shown in red). Variations of 20–30% are enough to account for the observed differences between the spectra of the 3 PDRs.

Both the widening and shift of the bands are temperature, mode and molecule specific (Joblin et al. 1995; Pech et al. 2002; Oomens et al. 2003). Regarding the width of the bands, experiments have only been performed on a handful of small PAHs, and thus a constant value is assumed as a first approximation. Throughout this work we have adopted a $\text{FWHM} = 15 \text{ cm}^{-1}$ using Gaussian profiles for all bands. Adopting the wavelength dependent FWHM of the bands as proposed in Bauschlicher et al. (2008) (see Appendix for details), we find that both the quality of the fit and the class ratios are actually similar to those of the *base run*. The main difference is that by using different band widths, the fit uses more PAHs than in the *base run* (44 PAHs against 33). It increases the fraction of nitrogenated PAHs (from 19% to 26%) and cationic species ($x_{\text{PAH}^{+}}/x_{\text{PAH}^0} = 0.53$ to 0.84), by decreasing the contribution from neutrals and anions to 41% and 24%, respectively. Still the PAHs that contribute the most are *base-run* ones (30 out of the 44 PAHs), making up for 85% of the total abundance of PAHs in the fit. The largest contribution from one of the new PAHs is of 3.5% only. The shift of the bands are related to anharmonicities which are currently not well-understood and thus, we have used a single value as a first approximation. A further analysis on this is beyond the scope of this work.

As explained in 2.4.1 we assumed Gaussian profiles for all bands. Using Lorentzian profiles instead (see Appendix), we again obtain results quite similar to the original *base run* fit, e.g., the most abundant species are the same for both fits. The largest difference is also in the number of PAHs used to fit the spectrum. When using Lorentzian profiles only

26 PAHs are required for a good fit, which relates to the fact that with a Lorentzian profile, the same PAHs that produce the narrow features also produce much of the plateaus, given the extensive wings of Lorentzian profiles.

With respect to the PAH emission model, the only physical condition we have taken into account is the strength of the radiation field as emitted by the exciting star. Our approach does not consider ionization balance, and we have not used any constraint regarding reactions of formation/destruction of PAHs when fitting the observed spectra. A further analysis on these is encouraged and will be treated in a future work.

2.6.3. The Local Physical Environment

Given the similarity in the PAH emission spectra, we expect physical conditions also to be similar at these spots. Indeed all spectra show a similar 6.2/11.3 ratio. This ratio is known to be driven by ionization. Inspection of Table 2.2 shows the ionization parameter γ for NGC 7023 is 6.5×10^4 . Using the upper limit for G_0 published in Okada et al. (2013), γ increases by a factor of 3. NGC 2023 on the other hand has a γ value of 3.4×10^4 . The interclump medium in this case has a γ which is a factor 4 larger. However we expect that the PDR emission is dominated by the clump. The ionization parameter for NGC 1333 is between that of NGC 7023 and NGC 2023, 4.5×10^4 , but overall we see that the ionization parameter varies within a factor of 2 between the three PDRs, which is expected to fall within the uncertainties in the estimated parameters. This agrees with the fact that all fits lead to similar $x_{\text{PAH}^{+}}/x_{\text{PAH}^0}$ ratios, where neutral PAHs dominate the spectra contributing $\sim 50\%$, while the input from cationic species accounts for 25% of the total abundance of PAHs in the fits (or even larger given that the contribution from anionic species should be considered as an upper limit). Even though we did not take ionization balance into account, our results agree with theoretical calculations for circumcoronene (Tielens 2005). According to this, a variation of a factor of 2 in γ would be translated in a factor of 1.4 in the ionization fraction, and for γ values of a few 10^4 , we should indeed expect neutral and cationic species to be dominant, with a negligible contribution ($< 10\%$) from anions and doubly cationic species.

Aside from ionization, the chemical state of the PAH population is also a reflection of the local physical conditions, and of the history. We can discuss the chemical state of PAHs in terms of the 12.7/11.3 and 8.6/6.2 ratios. The 12.7/11.3 is often considered a measure of the molecular edge structure, while the 8.6/6.2 ratio is an indicator of the size of compact symmetric PAHs (Ricca et al. 2012). Both ratios vary widely within each source. However they are very similar at the bright spots studied here. Even the much weaker 12.0, 13.5 and $14.2 \mu\text{m}$ bands (which measure the presence of duo/trio modes) have the same intensity among the three locations. Likewise, while all (cationic) pericondensed PAHs show strong bands in the 7.6– $8.0 \mu\text{m}$ range, the $8.6 \mu\text{m}$ band is characteristic for highly condensed, symmetric PAHs such as the pyrene, coronene or ovalene family (Bauschlicher et al. 2009; Ricca et al. 2012).

In addition, even though we did not analyze the 15– $18 \mu\text{m}$ emission with PAHdb, we would like to point out the similarity between all three spectra as observed from Figure 2.14. This similarity is not only in terms of the presence of features, but also their relative intensities. The spectra only differ in the H_2 $17.0 \mu\text{m}$ line emission, which is still $< 20\%$. The 15– $18 \mu\text{m}$ wavelength range is expected to be related to C-skeletal modes and/or the

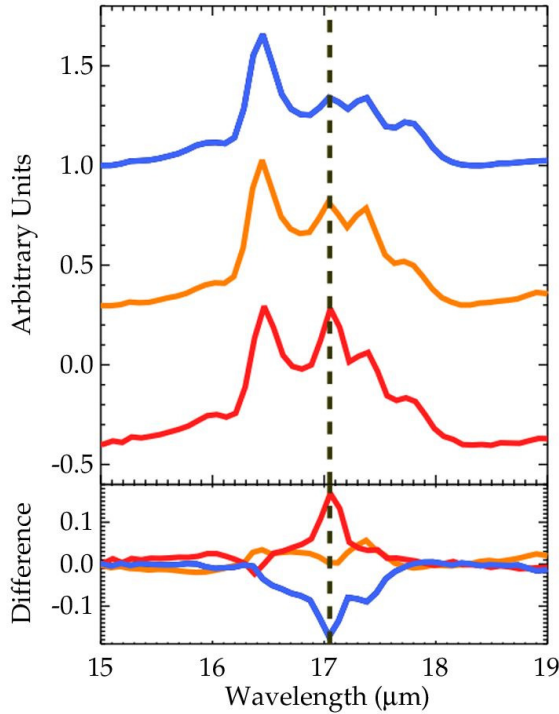


Figure 2.14: Continuum-subtracted 15–19 μm spectra of the brightest locations in NGC 7023, NGC 2023 and NGC 1333 (*top panel*). The *bottom panel* shows the difference between each normalized spectrum with the average of all three spectra using the same color scheme. For this wavelength range the continuum has been defined fitting a spline function to the anchor points listed in 2.2.3 plus an anchor point at 18.0 μm . Just as in the short wavelength region (Figure 2.2), the spectra show the same bands and very similar relative intensities. The largest difference is observed in the H_2 S(1) 17.0 μm line, where the spectra differ by about 20% (dashed line).

edge structure of PAHs, and therefore it is to some extent molecule specific. Inspection of PAHdb shows PAH spectra have a wide variety of features and relative intensities in this wavelength range. However in the spots studied here, we see a remarkable similar emission from only few bands.

Hence, these examples illustrate clearly that the emitting PAH families have to be fairly similar in order to produce such highly similar spectra observed at these different locations.

2.6.4. GrandPAH Hypothesis

The prevalence of a single preferred subset of PAHs leads one to conjecture about the idea of a possible set of *grandPAHs*. As mentioned in the introduction, the concept of *grandPAHs* has been defined in the literature as a set of the most stable PAH species that can survive in the harsh conditions of the ISM (Tielens 2013). Here we now can examine the *grandPAH* hypothesis in more detail, and refine the concept for the case of RNe.

Our concept of *grandPAHs* relies on the following six points:

1) The spectroscopic similarity between the three observed spectra, even in the smallest details (Figures 2.2 and 2.14).

2) The initial *base run* fits showed the same PAH subclass breakdown for the three spectra, revealing an insensitivity of the PAH emission to the shape of the radiation field (Table 2.4).

3) The degeneracy study that removed iteratively the whole fitted set, clearly showed that the set of *base-run* PAHs is the preferred set in order to reproduce the observations in detail (2.5.2).

4) The degeneracy study that removed iteratively the most abundant PAH also showed the same preferred set of *base-run* PAHs. It also hinted at the large diversity in PAH spectra available in PAHdb (2.5.2). For example, there it was shown that the most abundant PAHs are mainly chosen for having an intense $11.3\mu\text{m}$ band, that can fit the observed one with only 1.4 cm^{-1} difference in peak positions. As more of these PAHs are removed from the pool, the fitting procedure finds it more difficult to fit this band, and we notice that—very rapidly—there are no more PAHs (either alone or a combination of them) that can fit the band in detail.

5) The Monte-Carlo analysis showed that subtle variations in the abundance distribution of the preferred set of PAHs can explain the observed minor variations between the three observed spectra (2.6.1).

6) Estimates of the ionization parameter at the three locations show they are similar, varying by only a factor of 2 (2.6.3).

Points 1–4 indicate that, within the limits of the database and Spitzer spectral resolution, there is one set of PAHs that explains the observations best. Point 5 shows that the subtle variations between the three spectra can be explained with only the one set of PAHs. Lastly, point 6 supports the fact that the local physical environment would be driving the PAH population to the *grandPAHs*.

It is important to emphasize that we are not saying the *base-run* set of PAHs is the actual *grandPAH* family. Instead, we are stating that the available data implies that a limited number of compact, highly symmetric PAHs dominate the interstellar PAH family at the brightest spots of RNe, and that they share the *base run* characteristics (e.g., the ratios shown in Table 2.4).

2.6.5. GrandPAH Evolutionary Scenario

Since NGC7023 NW is an edge-on PDR, and the PAH emission has been extensively studied throughout the entire nebula, we can take NGC7023 as a reference to analyze what is happening at these bright spots.

The position studied in this work is located along the brightest rim of NGC7023, $40''$ north-west of the exciting star. Our location falls in the peak emission of the filament observed in Extended Red Emission, and it also coincides with the bulk of the [CII] emission

(Berné et al. 2008). Regarding molecular hydrogen, the peak of the PAH emission is slightly offset from where the H_2 peak is observed, being closer to the star and at the limit where the ortho-to-para ratio R_{OP} decreases from the LTE value (Fleming et al. 2010; Sellgren et al. 2010). In fact the spectrum of the brightest spot does not show strong H_2 emission lines in the mid-IR range. Interestingly, this holds for all three PDRs (Figure 2.2).

Berné et al. (2007) performed a blind signal separation analysis on the spectral data cube of NGC 7023. Their analysis revealed that NGC 7023 shows a stratified structure where the PAH emission closer to the star is dominated by cationic species, while the PAH emission further away from the star is dominated by neutral PAHs. They also reported a third signal whose emission dominates deeper into the cold molecular cloud, and that they assigned to very-small-grains (VSG). This VSG emission disappears as the PAH emission dominated by neutral species becomes more important in the PDR front (see also Sellgren et al. 2010; Rosenberg et al. 2011). This was interpreted as a transformation process where VSGs are photo-evaporated, releasing free flying PAHs into space as they get destroyed due to the incoming UV radiation. According to this scheme, when VSGs are destroyed they release mostly neutral PAHs, and those PAHs close enough to the star become ionized/destroyed as a result of the intense radiation. Indeed in their maps, the location of the brightest mid-IR spot falls right at the peak of the signal dominated by neutral PAHs, neighboring the border where the VSG abundance decreases considerably, while the emission from neutral PAHs starts dominating the spectra, as we leave the molecular cloud going into the PDR region. Their suggestion that PAH emission is dominated by neutral PAHs agrees with our derived ratios as listed in Table 2.4. According to Berné & Tielens (2012) the brightest spot of the PDR is located where the abundance of PAHs starts decreasing, right at the edge of the transition zone between the beginning of the molecular cloud and the PDR. Boersma et al. (2013) shows that this is also where the relative contributions from the different PAH subclasses making up the PAH mixture start to change.

Within the interpretation given by Berné et al. (2007) and Berné & Tielens (2012), the brightest location of the PDR would be the place where the intense processing of the PAHs starts; where PAHs are being released from the VSGs, ice mantles and other PAH reservoirs inhabiting the dense molecular cloud. The free flying PAHs will quickly lock into the ionization balance since this process is much more quickly established than the evaporation timescale of PAH clusters in PDRs. The released PAHs should also be (or should be further processed into) mainly small-to-medium size PAHs (30–50 carbon atoms), pericondensed in shape. The last figure of this chapter (page number 54) schematically shows where *grandPAHs* fall within the evolution of carbonaceous material in a RN such as NGC 7023. The figure shows the transformation the PAH population goes through from the molecular cloud (right side) to the region closest to the star (left side) based on what is known from NGC 7023. The bottom panel corresponds to a composite image of NGC 7023 from the star to the NW PDR. The three-color image has been built from combining PACS $70\mu\text{m}$ (red), $6.2\mu\text{m}$ (green; image courtesy O. Berné) and MIPS $24\mu\text{m}$ (blue) images, and shows the brightest spot studied in our work (edge between the *PDR* and the *molecular cloud*).

In NGC 7023 it has been observed that there is a flow of material from the molecular cloud to the PDR, through the PDR front, into the cavity (Fuente et al. 1998). As the material flows through the molecular cloud to its surface and through the PDR front into the cavity, PAH clusters/VSGs and PAHs are exposed to a stronger radiation field, which induces a pronounced chemical evolution. Initially this will lead to a slow evaporation of PAHs from

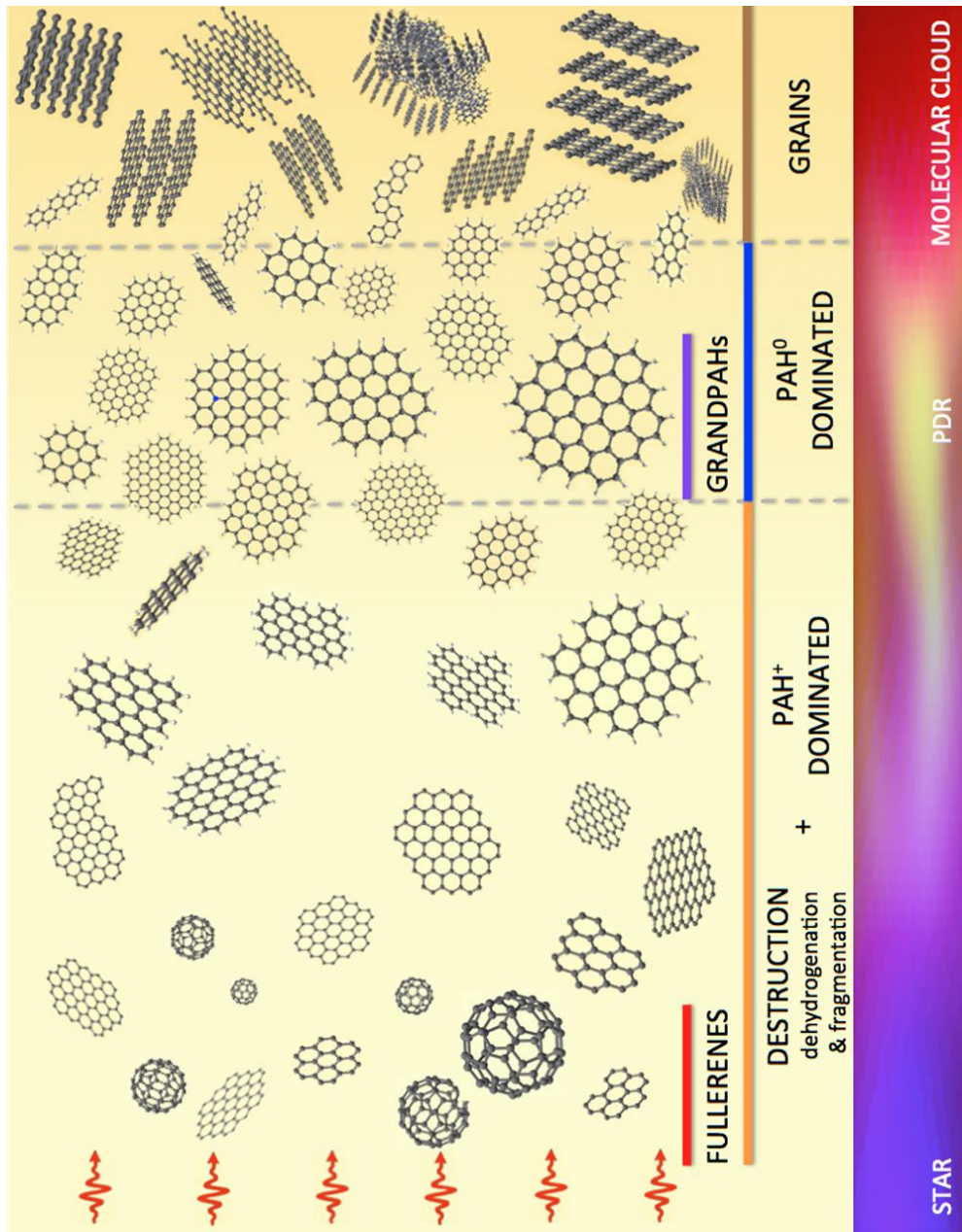
PAH clusters/VSGs (right side of the figure). These PAHs are freed when they meet the radiation from the star for the first time. These newly freed PAHs will be further processed and become the population of *grandPAHs*: a unique mixture of the most stable PAHs. Initially this population would be dominated by neutral PAHs, of small-to-medium sizes and compact pericondensed structure. Those *grandPAHs* that get close enough to the star will then become ionized, dehydrogenated and eventually destroyed. Under an even stronger UV radiation field (the closest region to the star) these ionized and fragmented PAHs will end up in the most stable forms of fullerenes.

We surmise then that at the brightest spots of RNe, the PAHs are first exposed to the strong radiation field of the illuminating stars, and this converts the members of the PAH family to the most stable PAH species, where side groups as well as dangling rings are photochemically eroded. We have seen that G_0 , T_{gas} and n_H vary between the three nebulae: G_0 varies by a factor of 5–6, T_{gas} varies by a factor of 3–4, and n_H varies from 4000 to 10^5 cm^{-3} . However the ionization parameter varies by only a factor of 2. Thus, it is tempting to link the chemical variations to γ and/or G_0/n_H . This last variable has been identified as the driving force for the PAH-to-fullerene conversion (Berné & Tielens 2012), and it has also been suggested to determine the hydrogenation state of PAHs as long as multiphoton events are not important (Montillaud et al. 2013). Thus, it may also play a role in the PAH-to-*grandPAH* family conversion, as hydrogen has a much lower binding energy, and experiments show hydrogen loss occurs much more rapidly than C_2H_2 or C_2 loss (Ekern et al. 1998). In this view, the change in the ionization balance and the chemical conversion of PAHs to *grandPAHs* are both linked to G_0/n_H . This may be the underlying cause as to why the spectra of the bright spots studied here are so similar in their ionization and chemical character.

2.7. Summary and Conclusions

We analyzed the PAH emission observed in the Spitzer-IRS spectra of the brightest PDRs of three well-known different reflection nebulae: NGC 7023, NGC 2023 and NGC 1333. These locations are the brightest spots within the rims that delineate transition zones of the molecular cloud and the surroundings, as observed in the mid-IR. The three nebulae are illuminated by different stars; and overall the intensity of the UV radiation field, together with the gas density and temperature are known to be different between them. In terms of PAH emission, each one of them show variations in relative ratios and appearance of features when studied through spectral mapping. Despite all this, the mid-IR spectra at the brightest spots studied here show practically the same PAH emission.

In order to tackle this issue, we used the theoretical PAH spectra comprised within The NASA Ames PAH IR Spectroscopic Database, to fit the observations and analyze the derived PAH populations. The results of the fits led to remarkably similar PAH populations for all three spectra, representing a mixture of mostly neutral small PAHs contributing in $\sim 50\%$, while cationic and anionic species contribute 25% abundance each. Such input from anionic species is known to be overestimated since —given the PAHs within the database— anionic species are systematically used to reproduce the observed shift of PAH bands relative to the theoretical estimates. Contributions from nitrogenated and Stone-Wales species are $\lesssim 25\%$, and should also be taken cautiously given the characteristics and incompleteness of the database.



The analysis on the degeneracy of the results showed that the properties of this set of PAHs are, indeed, necessary to reproduce the details of the observed PAH emission. In this sense, we conclude that not any random mixture of PAHs can fit the observations *in detail*. Furthermore, small variations in relative abundances can indeed produce differences in the spectra that are larger than what we observe between NGC 7023, NGC 2023 and NGC 1333. Thus, together with the fact that the three spectra show extremely similar ratios that are known to be related to the ionization and chemical state of the PAH population, we propose that PAH populations must be remarkably similar at these different lines-of-sight. As an explanation, we considered the concept of the *grandPAHs* as a unique mixture of PAHs that dominates the emission at the brightest spot of all three PDRs. Such a set of PAHs would be the result of extensive processing that takes place at these locations, and that does not depend on the histories nor the initial mixture of PAHs present in these nebulae. Even though this concept of *grandPAHs* has been presented in the literature before, our work constitutes the first attempt to test and draw specific conclusions regarding this hypothesis, given the current state of the PAH field.

We would like to emphasize that the set of PAHs derived from the fit is not the actual *grandPAH* family. Instead, our results point towards a limited number of compact (highly symmetric) PAHs dominating the interstellar PAH family at the brightest spots of the RNe studied here. We also propose that the *grandPAHs* would indeed share the properties and characteristics of the set of PAHs derived from our fits.

We recognize that the degree of degeneracy of our results depends on both Spitzer spectral resolution and how complete the database is. Perhaps, the more complete the database, the greater the degeneracy we would likely obtain. However the analysis on these three PDRs indicates that there is a preferred set of structures and sizes. Unfortunately we cannot assess their uniqueness, chemically, unless we put more constraints or study more spectra. PAH relative band intensities in the 5–15 μm region appear to be largely insensitive to variations of the radiation field, which is the only parameter we are considering when calculating each PAH emission spectrum. These uncertainties can be significantly tightened by the availability of fully resolved, complete 2.5–20 μm spectra.

We finally propose that the *grandPAH* population in RNe is the outcome of the intense processing of carbonaceous material at the transition interface between the PDR and the cold molecular cloud, where the PAH population (initially in the molecular cloud) faces the strong stellar radiation field for the first time. Further processing of the *grandPAH* population in regions closer to the exciting star would produce a large population of cationic species and irregular PAH structures, that under even more extreme conditions would stabilize into fullerene forms.

Acknowledgements

Studies of interstellar PAHs at Leiden Observatory are supported through advanced ERC grant 246976 from the European Research Council, through a grant by the Dutch Science Agency, NWO, as part of the Dutch Astrochemistry Network, and through the Spinoza premie from the Dutch Science Agency, NWO. This work is based [in part] on observations made with the Spitzer Space Telescope, which is operated by the Jet Propulsion Laboratory, California Institute of Technology under a contract with NASA. CB and

LA gratefully acknowledge support from NASA's "Carbon in the Galaxy" consortium grant (NNH10ZDA001N) and NASA's Astrobiology; Astronomy and Physics Research and Analysis (APRA; NNX07AH02G) and Spitzer Space Telescope Support programs (50082). CB is grateful for an appointment at NASA's Ames Research Center through San José State University Research Foundation (NNX14AG80A).

Bibliography

- Aannestad, P. A., & Kenyon, S. J. 1979, *ApJ*, 230, 771
 Alecian, E., Catala, C., Wade, G. A., et al. 2008, *MNRAS*, 385, 391
 Ali-Haïmoud, Y. 2014, *MNRAS*, 437, 272
 Allamandola, L. J., Tielens, A. G. G. M., & Barker, J. R. 1985, *ApJ*, 290, L25–L28
 Allamandola, L. J., Hudgins, D. M., & Sandford, S. A. 1999, *ApJ*, 511, L115
 Bakes E.L.O., Tielens A.G.G.M., Bauschlicher, Jr. C.W., 2001, *ApJ*, 556, 501
 Barker, J. R., Allamandola, L. J., & Tielens, A. G. G. M. 1987, *ApJ*, 315, L61
 Bauschlicher, C. W., Peeters, E., & Allamandola, L. J. 2008, *ApJ*, 678, 316
 Bauschlicher, C. W., Peeters, E., & Allamandola, L. J. 2009, *ApJ*, 697, 311
 Bauschlicher, C. W., Boersma, C., Ricca, A., et al. 2010, *ApJS*, 189, 341
 Berné, O., Joblin, C., Deville, Y., et al. 2007, *A&A*, 469, 575
 Berné, O., Joblin, C., Rapacioli, M., et al. 2008, *A&A*, 479, L41
 Berné, O., Joblin, C., Mulas, G., Tielens, A. G. G. M., & Goicoechea, J. R. 2009, arXiv:0910.4069
 Berné, O. & Tielens, A. G. G. M. 2012, *Proc. of the National Academy of Science of the United States*, 109, 401
 Boersma, C., Mattioda, A. L., Bauschlicher, C. W., et al. 2009, *ApJ*, 690, 1208
 Boersma, C., Bauschlicher, C. W., Allamandola, L. J., et al. 2010, *A&A*, 511, A32
 Boersma, C., Rubin, R. H., & Allamandola, L. J. 2012, *ApJ*, 753, 168
 Boersma, C., Bregman, J. D., & Allamandola, L. J. 2013, *ApJ*, 769, 117
 Boersma C. et al., 2014, *ApJS*, 211, 8
 Bregman, J., & Temi, P. 2005, *ApJ*, 621, 831
 Cami, J. 2011, in *EAS Publications Series*, Vol. 46, PAHs and the Universe, ed. C. Joblin & A. G. G. M. Tielens (Cambridge: Cambridge Univ. Press), 117
 Cardelli, J. A., Meyer, D. M., Jura, M., & Savage, B. D. 1996, *ApJ*, 467, 334
 Chokshi, A., Tielens, A. G. G. M., Werner, M. W., & Castelaz, M. W. 1988, *ApJ*, 334, 803
 Cook, D. J., & Saykally, R. J. 1998, *ApJ*, 493, 793
 Crawford, M., Tielens, A., & Allamandola, L. 1985, *ApJ*, 293, L45
 de Boer, K. S. 1983, *A&A*, 125, 258
 Ekern, S. P., Marshall, A. G., Szczepanski, J., & Vala, M. 1998, *J. Phys. Chem.*, 102, 3498
 Fleming, B., France, K., Lupu, R. E., & McCandliss, S. R. 2010, *ApJ*, 725, 159
 Fuente A., Martín-Pintado J., Rodríguez-Franco A., Moriarty-Schieven G.D., 1998, *A&A* 339, 575
 Galliano, F., Madden, S. C., Tielens, A. G. G. M., Peeters, E., & Jones, A. P. 2008, *ApJ*, 679, 310
 Galué, H. A. 2014, *Chem. Sci.*, DOI: 10.1039/C4SC00890A
 Hollenbach, D. R., Tielens, A. G. G. M. 1999, *Rev. Mod. Phys.*, 71, 173
 Hony, S., van Kerckhoven, C., Peeters, E., et al. 2001, *A&A*, 370, 1030
 Houck, J.R., Roellig, T.L., van Cleve, J., et al. 2004, *ApJS*, 154, 18
 Hudgins, D. M., Bauschlicher, C. W., & Allamandola, L. J. 2005, *ApJ*, 632, 316
 Joblin, C., Boissel, P., Léger, A., d'Hendecourt, L., & Defourneau, D. 1995, *A&A*, 299, 835
 Kurucz, R. L. 1993, *VizieR Online Data Catalog*, 6039, 0
 Langhoff, S. R. 1996, *J. Phys. Chem.*, 100, 2819
 Lawson, C. L., & Hanson, R. J. 1974, *Solving Least Squares Problems* (Prentice-Hall Series in Automatic Computation; Englewood Cliffs, NJ: Prentice-Hall)
 Léger, A. & Puget, J. L. 1984, *A&A*, 137, L5–L8
 Li A., Draine B. T., 2001, *ApJ*, 550, L213
 Markwardt, C. B. 2009, in *Astronomical Society of the Pacific Conference Series*, Vol. 411, *Astronomical Data Analysis Software and Systems XVIII*, ed. D. A. Bohlender, D. Durand, & P. Dowler, 251
 Montillaud, J., Joblin, C., Toubanc, D. 2013, *A&A*, 552, A15
 Mookerjee, B., Sandell, G., Jarrett, T. H., & McMullin, J. P. 2009, *A&A*, 507, 1485
 Okada, Y., Pilleri, P., Berné, O., et al. 2013, *A&A*, 553, A2
 Oomens, J., Tielens, A. G. G. M., Sartakov, B. G., von Helden, G., & Meijer, G. 2003, *ApJ*, 591, 968
 Pech, C., Joblin, C., & Boissel, P. 2002, *A&A*, 388, 639
 Peeters, E., Hony, S., Van Kerckhoven, C., Tielens, A. G. G. M., Allamandola, L. J., Hudgins, D. M., &

- Bauschlicher, C. W. 2002, A&A, 390, 1089
- Peeters, E., Tielens, A.G.G.M, Allamandola, L.J., & Wolfire, M.G. 2012, ApJ, 747, 44
- Pillari, P., Montillaud, J., Berné, O., & Joblin, C. 2012, A&A, 542, A69
- Pino, T., Dartois, E., Cao, A.-T., et al. 2008, A&A, 490, 665
- Purcell, E. M. 1976, ApJ, 206, 685
- Ricca, A., Bauschlicher, C. W., Jr., Mattioda, A. L., Boersma, C., & Allamandola, L. J. 2010, ApJ, 709, 42
- Ricca, A., Bauschlicher, C. W., Jr., & Allamandola, L. J. 2011, ApJ, 729, 94
- Ricca, A., Bauschlicher, C. W., Jr., Boersma, C., Tielens, A. G. G. M., & Allamandola, L. J. 2012, ApJ, 754, 75
- Rogers, C., Heyer, M. H., & Dewdney, P. E. 1995, ApJ, 442, 694
- Rosenberg, M. J. F., Berné, O., Boersma, C., Allamandola, L. J., & Tielens, A. G. G. M. 2011, A&A, 532, A128
- Rosenberg, M. J. F., Berné, O., Boersma, C. 2014, A&A, 566, 4
- Schutte, W. A., Tielens, A. G. G. M., & Allamandola, L. J. 1993, ApJ, 415, 397
- Sellgren, K., Uchida, K. I., & Werner, M. W. 2007, ApJ, 659, 1338
- Sellgren, K., Werner, M. W., Ingalls, J. G., et al. 2010, ApJ, 722, L54
- Sheffer, Y., Wolfire, M., Hollenbach, D. J., Kaufman, M. J., & Cordier, M. 2011, ApJ, 741, 45
- Smith, J. D. T., Draine, B. T., Dale, D. A., et al. 2007, ApJ, 656, 770
- Steiman-Cameron, T. Y., Haas, M. R., Tielens, A. G. G. M., & Burton, M. G. 1997, ApJ, 478, 261
- Stein, S. E. 1978, J. Phys. Chem., 82, 566
- Stone, A. J., & Wales, D. J. 1986, Chem. Phys. Lett., 128, 501
- Tielens, A. G. G. M., & Hollenbach, D. 1985, ApJ, 291, 722
- Tielens, A. G. G. M. 2005, The Physics and Chemistry of the Interstellar Medium (Cambridge: Cambridge Univ. Press)
- Tielens, A. G. G. M. 2013, Rev. Mod. Phys., 85, 1021
- Werner, M. W., Uchida, K. I., Sellgren, K., et al. 2004, ApJS, 154, 309
- Werner, M. W., Sellgren, K., & Livingston, J. 2009, AAS Meeting Abstracts, 213, #412.15
- Whitesides, R., & Frenklach, M. 2010, J. Phys. Chem. A., 114, 689
- Young Owl, R. C., Meixner, M. M., Fong, D., Haas, M. R., Rudolph, A. L., & Tielens, A. G. G. M. 2002, ApJ, 578, 885
- Yu, H., & Nyman, G. 2012, ApJ, 751, 3

2.A. Features+Plateaus versus Features-Only Spectra

As mentioned in 2.4, both the nature of the plateau carriers, and the intrinsic profile of PAH bands are unknown. Because of this we decided to base our results on *Features+Plateaus* spectra only. Here we briefly explore the results for *Features-Only* spectra.

Figure 2.15 shows the fit to the *Features-Only* spectrum of NGC7023 using the *base run* condition presented in §2.4. The residuals of the fits in the *problematic regions* described in §2.5.1 are at a similar level as the differences shown in Figure 2.4 of the main text. The excess at ~ 7 and $8\mu\text{m}$ are partly related to the *problematic regions* inherent to the fits, and partly to the fact that when performing the spline decomposition we are also removing the emission that is attributed to the wings of the PAH bands, whose intrinsic profile is unknown.

Regardless of the quality of the fits, we can get useful information about the properties of the underlying PAH population. Table 2.6 lists the PAHs used in the fit. We see that the fitting procedure uses less PAHs than to fit the *Features+Plateaus* spectra (e.g., 25 against 33 in the case of NGC7023). Out of the 25 PAHs used in the fit, 16 are also used in the fit to the *Features+Plateaus* spectrum of NGC7023. These PAHs contribute in 68% and 60% to the total abundance of PAHs in the *Features-Only* and *Features+Plateaus* spectra, respectively.

Table 2.7 shows the class ratios of the sets of PAHs derived from the fits to the *Features-Only* spectra of NGC7023, NGC2023 and NGC1333. Overall most ratios are consistent with the values derived for *Features+Plateaus* spectra. There is however an increase in the cation fraction, while the anionic fraction relative to neutrals decreases in $> 50\%$. Part of this change is related to the fact that

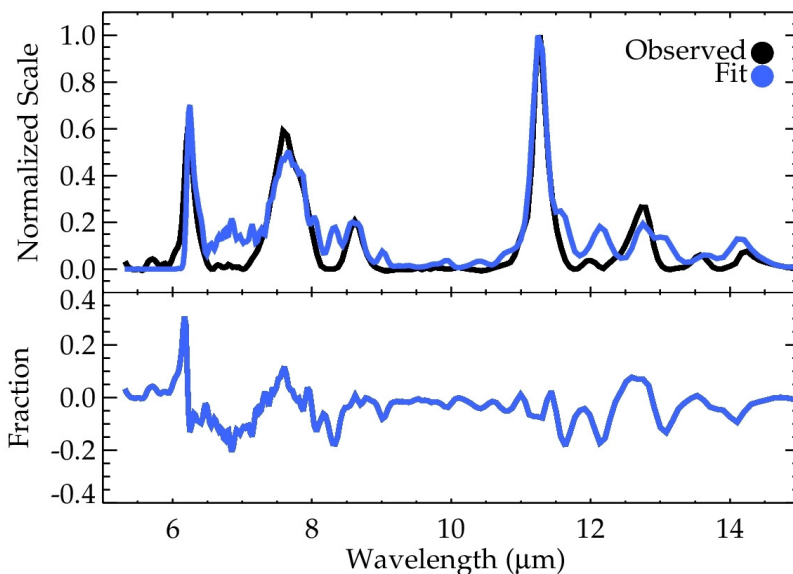


Figure 2.15: Base run fit to the *Features-Only* spectrum of the brightest location in NGC7023. The spectra are shown in normalized scale. The figure also shows the difference between both normalized spectra. For NGC7023 out of a pool of 292 PAHs, the fit ends up using 25 PAHs. Table 2.6 lists the PAHs used in this fit.

Table 2.6: Base-run PAHs derived from fit to NGC7023 *Features-Only* spectrum

Uid	Formula	Abundance (%)	n_{solo}	n_{duo}	n_{trio}	n_{quartet}	Structure
620	C ₄₂ H ₁₆	14.5	4	12	0	0	Pericondensed
228	C ₂₃ H ₁₂ N ⁺	13.0	0	12	0	0	Pericondensed
37	C ₅₄ H ₁₈	11.8	6	12	0	0	Pericondensed
11	C ₃₂ H ₁₄ ⁻	7.0	2	12	0	0	Pericondensed
154	C ₃₆ H ₁₆	6.0	2	8	6	0	Irregular
157	C ₄₂ H ₂₂ ⁻	5.6	6	4	12	0	Catacondensed, branched
233	C ₂₃ H ₁₂ N ⁺	5.4	0	12	0	0	Pericondensed
255	C ₅₂ H ₁₈ N ₂ ⁺²	4.9	6	12	0	0	Pericondensed
704	C ₅₄	4.7	0	0	0	0	100% Dehydrogenated, pericondensed
636	C ₄₈ H ₁₈ ⁺	4.0	6	12	0	0	Pericondensed
31	C ₂₄ H ₁₂ ⁺²	3.7	0	12	0	0	Pericondensed
549	C ₂₄ H ₁₄ ⁺	2.8	0	0	6	8	Catacondensed, branched
601	C ₆₆ H ₂₀ ⁺	2.7	7	10	3	0	5-7 Ring defects
226	C ₂₃ H ₁₂ N	2.1	0	12	0	0	Pericondensed
307	C ₂₂ H ₁₄	1.9	6	0	0	8	Catacondensed, not branched
568	C ₉₈ H ₂₈ ⁺	1.8	14	8	6	0	Pericondensed
306	C ₂₂ H ₁₄ ⁺	1.6	2	4	6	0	Catacondensed, not branched
108	C ₉₆ H ₂₄	1.4	12	12	0	0	Pericondensed
128	C ₃₆ H ₁₆	1.1	2	8	6	0	Irregular
234	C ₅₃ H ₁₈ N ⁺	1.0	6	12	0	0	Pericondensed
544	C ₃₂ H ₁₈ ⁺	0.9	4	0	6	8	Catacondensed, branched
639	C ₉₀ H ₂₄ ⁺	0.8	12	12	0	0	Pericondensed
167	C ₁₁₂ H ₂₆ ⁻	0.7	14	12	0	0	Pericondensed
627	C ₄₀ H ₁₆ ⁻²⁶	0.7	4	12	0	0	Pericondensed
632	C ₁₂₈ H ₂₈	<0.1	16	12	0	0	Pericondensed

Table 2.7: Results Derived From the Base Run on Features–Only Spectra

	NGC 7023 NW	NGC 2023	NGC 1333
Fit			
Euclidian Norm*	2.3	1.6	0.3
Number of PAHs Used	25	25	27
Size**			
$x_{N_c < 50} / x_{N_c > 50}$	2.35	2.18	2.19
Ionization State**			
x_{PAH^+} / x_{PAH^0}	0.79	0.94	0.79
$x_{PAH^{+/+}} / x_{PAH^0}$	0.98	1.20	0.97
x_{PAH^-} / x_{PAH^0}	0.32	0.41	0.27
Composition**			
x_{PANH} / x_{PAH}	0.36	0.35	0.44
Structure			
n_{duo} / n_{solo}	2.79	2.52	3.00
n_{trio} / n_{duo}	0.15	0.17	0.13
$n_{quartet} / n_{solo}$	0.16	0.19	0.12
Shape (%)			
Compact Pericondensed (incl. 5–7)	72.9	70.7	79.0
Pericondensed With Edges (incl. 5–7)	2.7	3.9	10.5
Not Branched Catacondensed	3.4	4.4	2.3
Branched Catacondensed	9.2	11.4	4.1
Total contribution from PAHs with Defects	2.7	3.5	1.3
Total contribution Pericondensed	75.6	74.6	89.6
Total contribution Catacondensed	12.6	15.8	6.3
Total contribution Irregular	7.1	4.9	0.1
Total contribution Completely Dehydrogenated	4.7	4.8	4.0

* The Euclidian Norm is defined as the square root of the residual sum of squares between the observed spectrum and the corresponding fit. ** All ratios are expressed in terms of the abundances of each species x . PAHs with $N_c < 50$ carbon atoms are considered to be small, while PAHs with $N_c > 50$ carbon atoms are considered to be large PAHs. In terms of ionization states, PAH⁰ refers to neutral species; PAH^{+ / + +} refers to all positively ionized PAHs; PAH⁺ refers to only singly positively ionized PAHs; and PAH⁻ refers to anionic species (PAHdb only contains singly negatively ionized PAHs). In terms of composition, x_{PANH} / x_{PAH} refers to the abundance ratio of nitrogenated species relative to pure (carbon and hydrogen) PAHs. Hydrogen adjacency ratios are given in terms of the number of solo (n_{solo}), duo (n_{duo}), trio (n_{trio}) and quartet hydrogens ($n_{quartet}$), i.e. number of adjacent hydrogens attached to the same aromatic ring.

now PAHs with 5–7 ring *SW defects* contribute in only ~3% to the total abundance. Recent studies have concluded that PAHs having *SW defects* may be important members of the family of interstellar PAHs (Ricca et al. 2011; Yu & Nyman 2012). In principle, these PAHs appear to be important in the growth of edged-graphene structures, based on high temperature combustion models. These models are expected to resemble the physical conditions under which PAHs are presumably formed in the external envelopes of AGB stars (Whitesides & Frenklach 2010; Ricca et al. 2011). In terms of their mid-IR spectra, PAHs with *SW defects* show more bands than their non-defected analogues and, most importantly, they show C-C stretching bands at systematically different wavelengths around 6.2 μm . This has been used as an argument in favor of the presence of PAHs with *SW defects* in space, as it could potentially explain the observed differences in this band position between the A-B-C classes established in Peeters et al. (2002).

Table 2.8: New PAHs Used to Fit NGC 7023 Features+Plateaus spectrum Without Admitting PAHs With SW Defects

Uid	Formula	Abundance (%)	n _{solo}	n _{duo}	n _{trio}	n _{quartet}	Structure
306	C ₂₂ H ₁₄ ⁺	5.7	2	4	0	8	Catacondensed, not branched
568	C ₉₈ H ₂₈ ⁺	2.3	14	8	6	0	Pericondensed, with edges
550	C ₂₄ H ₁₄ ⁺	2.1	0	0	6	8	Catacondensed, branched
115	C ₆₆ H ₂₀	1.7	8	12	0	0	Pericondensed
233	C ₂₃ H ₁₂ N ⁺	1.4	0	12	0	0	Pericondensed
242	C ₃₁ H ₁₄ N ⁺	1.4	2	12	0	0	Pericondensed
173	C ₉₀ H ₃₀ ⁻	1.0	18	12	0	0	Irregular
642	C ₁₄₄ H ₃₀	1.0	18	12	0	0	Pericondensed
535	C ₃₂ H ₁₈	0.8	4	0	6	8	Catacondensed, branched
171	C ₉₀ H ₃₀	0.6	18	12	0	0	Irregular
313	C ₂₁ H ₁₃ N ⁺	0.4	6	0	0	8	Catacondensed, not branched

Figure 2.16 shows the normalized spectrum of the *SW defect* PAH of circumovalene anion C₆₆H₂₀⁻ after absorbing a 7 eV photon. This PAH appears to be the second most abundant PAH in all *base run* fits to *Features+Plateaus* spectra, and in this figure we can clearly see why. It has several bands in the 6–9 μm region, and as such, the fitting procedure uses it to fit the plateaus. Once plateaus are removed, the contribution from PAHs with *SW defects* become negligible compared to the input from the other classes. In fact when performing the *base run* fit to *Features+Plateaus* spectra but removing all PAHs with *SW defects* from the initial pool (590 < uid < 609), we obtain good quality fits, where the abundance input from Stone-Wales PAHs is replaced by increasing the fraction of small cationic species containing slightly more irregular structures (quartet and trio-hydrogens). Interestingly we realize that PAHs with *SW defects* (especially C₆₆H₂₀⁻) are also used to account for the 6.2 μm band. For NGC 7023 *Features+Plateaus* spectrum the new fit uses 33 PAHs, from which 11 PAHs are not *base-run* ones. These 11 new PAHs contribute in 18.5% abundance (see Table 2.8). Stone-Wales PAHs then are replaced by generally increasing the abundance of small cationic original *base-run* PAHs ($x_{Nc<50}/x_{Nc>50} = 5.06$; $x_{PAH+/++}/x_{PAH0} = 0.80$; $x_{PAH-}/x_{PAH0} = 0.20$); but also by adding new nitrogenated species, increasing their contribution to 44% compared to the 19% input derived from the fit admitting PAHs with *SW defects*. This refers to the need to reproduce the 6.2 μm feature once Stone-Wales PAHs are removed from the fit. We can affirm then that given the current state of PAHdb, both PAHns and 5–7 ring defected species are, by default, used to fit the 6.2 μm feature. Therefore both contributions should be taken cautiously until our knowledge on PAH formation/destruction processes can give us further clues on which species are indeed expected to be more abundant in the ISM.

2.B. Tests on Model Parameters

2.B.1. Band Profile

All results shown in this work have been obtained from considering that PAH bands can be described by Gaussian profiles. Here we test how the *base run* results vary when considering Lorentzian profiles instead. In this case we are also considering a constant FWHM of 15 wavenumbers for each band, in order to only test the effect of changing the band profiles.

Comparing the results of the fits derived from using Gaussian profiles against Lorentzian ones, we see that the quality of both fits is quite similar (Euclidian norm of 2.0) just as the level of the

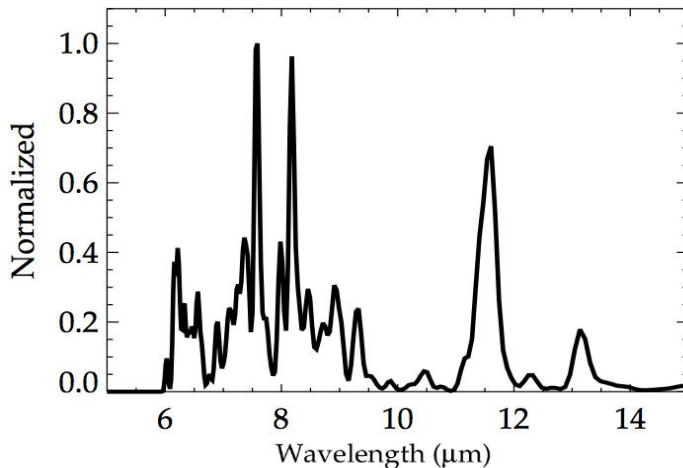


Figure 2.16: Emission spectrum of the SW *defect* PAH of $C_{66}H_{20}$ in the radiation field of NGC7023. The spectrum is shown in normalized scale. This PAH is the second most abundant PAH in all *base-run* fits of *Features+Plateaus* spectra. However when fitting *Features-Only* spectra, this PAH is not longer used in the fits. In fact the contribution of PAHs with 5–7 ring SW *defects* decreases to negligible levels for all three PDR spectra when compared to other species.

residuals (see Figure 2.17). The largest difference is in the number of different PAHs used in the fit, which in this case is lower (only 26 PAHs) than that of the *base run* using Gaussian profiles. This reflects the fact that Lorentzian profiles appear to fit better some PAH bands that otherwise have to be fitted with more than one Gaussian (Smith et al. 2007).

In terms of the PAHs themselves, out of the 26 PAHs used in this new fit, 21 of them correspond to original *base-run* PAHs. These 21 *base-run* PAHs contribute 95% to the total abundance of the PAHs in the new fit. Hence class ratios remain the same between both runs (ratios change in $<10\%$). The only ratio that does change is the $n_{\text{quartet}}/n_{\text{solo}}$ hydrogen adjacency ratio which decreases in $\sim 70\%$ its value from the one listed in Table 2.4 of the main text. This is because 3 out of the 5 PAHs with quartet hydrogens present in the *base-run* set are no longer used in this new fit. Interestingly all of these are catacondensed branched PAHs.

2.B.2. FWHM

Here we test what happens when we change the FWHM of the bands according to Bauschlicher et al. (2008). This approach considers a FWHM of 30 wavenumbers for bands at $\lambda < 9\mu\text{m}$; a FWHM of 10 wavenumbers for bands at $\lambda > 10\mu\text{m}$; and a FWHM that scales linearly from 30 to 10 wavenumbers in the 9–10 μm region.

The result of the fit is shown in Figure 2.18. The fit resembles that of the *base run*, which considers a constant FWHM for all bands. In terms of classes, there is a small increase in the cation/neutral fraction. The input from cations is now of 35% to the total abundance, against 26% in the original *base run*. Neutral species are still dominating the mixture then with an abundance contribution of 42% (against 48% in the *base run*).

In terms of the fit itself, we see the quality is similar. The new fit uses more PAHs: 44 compared to 33 in the original *base run*. Out of these 44 PAHs, 29 are *base-run* ones, and they contribute in $\sim 81\%$ to the total abundance of PAHs in the fit.

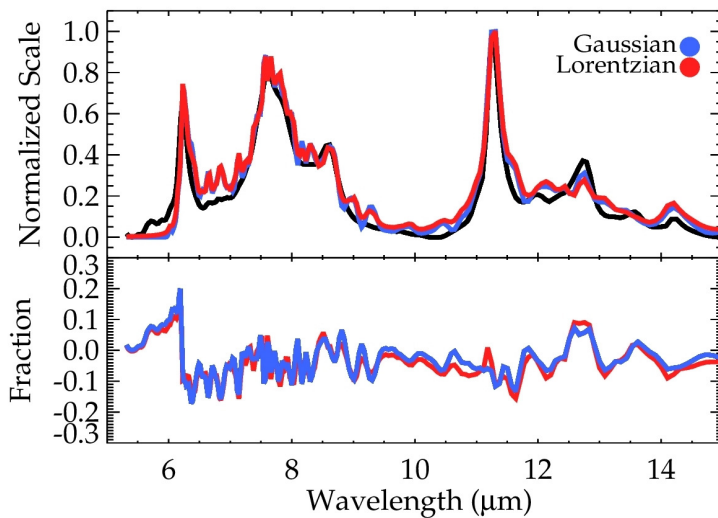


Figure 2.17: Base run fit to the *Features+Plateaus* spectrum of the brightest location in NGC7023 using Lorentzians to describe the profile of PAH bands (red curve). The *base run* fit using Gaussian profiles is also shown for a comparison (blue curve). The spectra are shown in normalized scale. The figure also shows the difference between both normalized spectra. For NGC7023 out of a pool of 292 PAHs, the fit ends up using 26 PAHs.

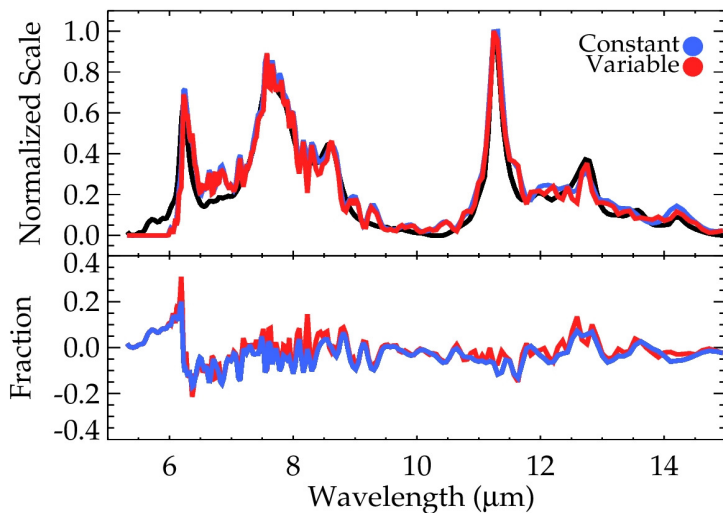


Figure 2.18: Base run fit to the *Features+Plateaus* spectrum of the brightest location in NGC7023 using variable FWHM depending on the wavelength range of the bands following Bauschlicher et al. (2008) (shown in red). The fit using a constant FWHM = 15 cm^{-1} is shown in blue for a comparison. The figure also shows the difference between both normalized spectra. For NGC7023 out of a pool of 292 PAHs, the fit ends up using 44 PAHs, against the 33 used when considering a constant FWHM.

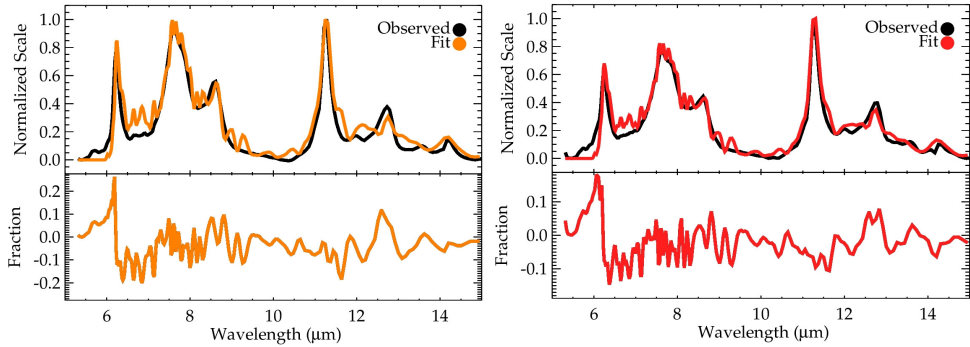


Figure 2.19: Base run fit to the *Features+Plateaus* spectrum of the brightest location in NGC 2023 (left) and NGC 1333 (right). The spectra are shown in normalized scale. The figure also shows the difference between both normalized spectra. For NGC 2023 out of a pool of 292 PAHs, the fit ends up using 31 PAHs (see Table 2.9). For NGC 1333, the fit ends up using 36 PAHs (see Table 2.10).

2.C. Base run fits to NGC 2023 and NGC 1333 spectra

Table 2.9: Base run PAHs derived from fit to NGC 2023 *Features+Plateaus* spectrum

Uid	Formula	Abundance (%)	n_{solo}	n_{duo}	n_{trio}	n_{quartet}	Shape
605	$\text{C}_{66}\text{H}_{70}^-$	15.2	8	12	0	0	5–7 Ring defects
128	$\text{C}_{36}\text{H}_{16}$	13.0	2	8	6	0	Irregular
620	$\text{C}_{42}\text{H}_{16}$	8.9	4	12	0	0	Pericondensed
226	$\text{C}_{23}\text{H}_{12}\text{N}$	6.4	0	12	0	0	Pericondensed
157	$\text{C}_{42}\text{H}_{22}^-$	5.1	6	4	12	0	Catacondensed, branched
636	$\text{C}_{48}\text{H}_{18}^+$	5.0	6	12	0	0	Pericondensed
600	$\text{C}_{66}\text{H}_{20}$	5.0	7	10	3	0	5–7 Ring defects, with edges
255	$\text{C}_{52}\text{H}_{18}\text{N}_2^{+2}$	4.9	6	12	0	0	Pericondensed
307	$\text{C}_{22}\text{H}_{14}$	4.5	6	0	0	8	Catacondensed, not branched
11	$\text{C}_{32}\text{H}_{14}^-$	4.2	2	12	0	0	Pericondensed
229	$\text{C}_{23}\text{H}_{12}\text{N}$	3.6	0	12	0	0	Pericondensed
704	C_{54}	3.2	0	0	0	0	100% Dehydrogenated, pericondensed
592	$\text{C}_{32}\text{H}_{14}^+$	3.0	2	12	0	0	5–7 Ring defects
601	$\text{C}_{66}\text{H}_{30}^+$	2.3	7	10	3	0	5–7 Ring defects, with edges
639	$\text{C}_{90}\text{H}_{24}^+$	2.2	12	12	0	0	Pericondensed
31	$\text{C}_{24}\text{H}_{12}^{+2}$	2.1	0	12	0	0	Pericondensed
158	$\text{C}_{42}\text{H}_{22}^+$	2.1	6	4	12	0	Catacondensed, branched
544	$\text{C}_{32}\text{H}_{18}^+$	2.0	4	0	6	8	Catacondensed, branched
243	$\text{C}_{31}\text{H}_{14}\text{N}^+$	1.1	2	12	0	0	Pericondensed
632	$\text{C}_{128}\text{H}_{28}^+$	0.9	16	12	0	0	Pericondensed
308	$\text{C}_{22}\text{H}_{14}^+$	0.9	6	0	0	8	Catacondensed, not branched
614	$\text{C}_{150}\text{H}_{30}$	0.7	18	12	0	0	Pericondensed
543	$\text{C}_{36}\text{H}_{20}$	0.7	6	0	6	8	Catacondensed, branched
626	$\text{C}_{40}\text{H}_{16}^+$	0.7	4	12	0	0	Pericondensed
37	$\text{C}_{34}\text{H}_{18}$	0.5	0	12	0	0	Pericondensed
181	$\text{C}_{102}\text{H}_{26}^+$	0.5	12	8	6	0	Pericondensed, with edges
114	$\text{C}_{96}\text{H}_{24}^-$	0.3	12	12	0	0	Pericondensed
624	$\text{C}_{170}\text{H}_{32}$	0.3	20	12	0	0	Pericondensed
108	$\text{C}_{96}\text{H}_{24}$	0.2	12	12	0	0	Pericondensed
167	$\text{C}_{112}\text{H}_{26}^-$	0.2	14	12	0	0	Pericondensed
171	$\text{C}_{90}\text{H}_{30}$	<0.1	18	12	0	0	Irregular

Table 2.10: Base run PAHs derived from fit to NGC 1333 Features+Plateaus spectrum

Uid	Formula	Abundance (%)	n _{solo}	n _{duo}	n _{trio}	n _{quartet}	Shape
128	C ₃₆ H ₁₆	15.2	2	8	6	0	Irregular
605	C ₆₆ H ₂₀ ⁻	14.2	8	12	0	0	5-7 Ring defects
620	C ₄₂ H ₁₆	8.8	4	12	0	0	Pericondensed
226	C ₂₃ H ₁₂ N	6.7	0	12	0	0	Pericondensed
600	C ₆₆ H ₂₀	6.2	7	10	3	0	5-7 Ring defects, with edges
11	C ₃₂ H ₁₄ ⁻	4.4	2	12	0	0	Pericondensed
636	C ₄₈ H ₁₈	4.0	6	12	0	0	Pericondensed
157	C ₄₂ H ₂₂	3.8	6	4	12	0	Catacondensed, branched
255	C ₅₂ H ₁₈ N ₂ ⁺²	3.5	6	12	0	0	Pericondensed
243	C ₃₁ H ₁₄ N ⁺	3.2	2	12	0	0	Pericondensed
592	C ₃₂ H ₁₄ ⁺	3.2	2	12	0	0	5-7 Ring defects
591	C ₃₂ H ₁₄	2.8	2	12	0	0	5-7 Ring defects
154	C ₃₆ H ₁₆	2.4	2	8	6	0	Pericondensed, with edges
284	C ₂₂ H ₁₂	2.4	0	6	6	0	Irregular
229	C ₂₃ H ₁₂ N	2.1	0	12	0	0	Pericondensed
158	C ₄₂ H ₂₂	1.9	6	4	12	0	Catacondensed, branched
704	C ₅₄	1.9	0	0	0	0	100% Dehydrogenated, pericondensed
639	C ₉₀ H ₂₄ ⁺	1.7	12	12	0	0	Pericondensed
31	C ₂₄ H ₁₂ ⁺²	1.2	0	12	0	0	Pericondensed
632	C ₁₂₈ H ₂₈ ⁻	1.0	16	12	0	0	Pericondensed
543	C ₃₆ H ₂₀	1.0	6	0	6	8	Catacondensed, branched
29	C ₂₄ H ₁₂ ⁻	1.0	0	12	0	0	Pericondensed
601	C ₆₆ H ₂₀ ⁺	0.9	7	10	3	0	5-7 Ring defects, with edges
305	C ₂₂ H ₁₄	0.8	2	4	0	8	Catacondensed, not branched
308	C ₂₂ H ₁₄ ⁺	0.8	6	0	0	8	Catacondensed, not branched
181	C ₁₀₂ H ₂₆ ⁺	0.7	12	8	6	0	Pericondensed, with edges
257	C ₅₂ H ₁₈ N ₂ ⁺²	0.7	6	12	0	0	Pericondensed
624	C ₁₇₀ H ₃₂	0.7	20	12	0	0	Pericondensed
134	C ₄₂ H ₁₈	0.6	0	6	12	0	Irregular
626	C ₄₀ H ₁₆ ⁺	0.6	4	12	0	0	Pericondensed
707	C ₆₆ ⁺	0.5	0	0	0	0	100% Dehydrogenated, pericondensed
167	C ₁₁₂ H ₂₆ ⁻	0.5	14	12	0	0	Pericondensed
228	C ₂₃ H ₁₂ N ⁺	0.3	0	12	0	0	Pericondensed
701	C ₉₆ H ₂₂ ⁻	0.2	12	10	0	0	Pericondensed, partially dehydrogenated
544	C ₃₂ H ₁₈ ⁺	0.1	4	0	6	8	Catacondensed, branched
614	C ₁₅₀ H ₃₀	<0.1	18	12	0	0	Pericondensed

2.D. PAHs used in the base run fit to NGC7023

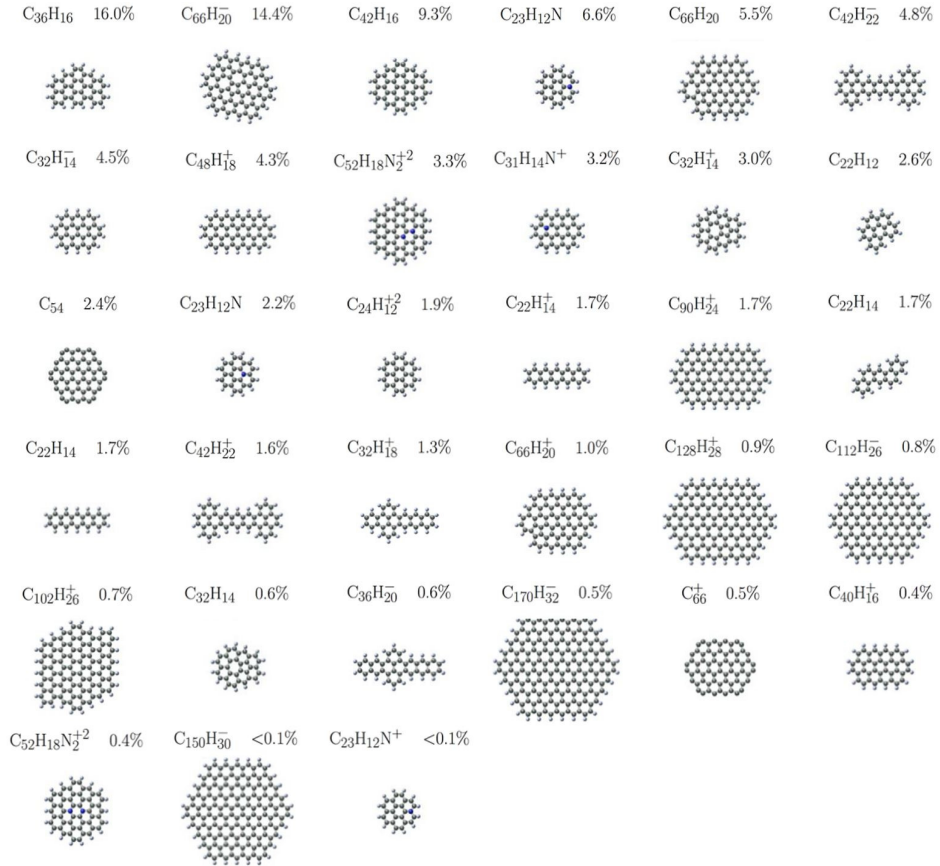


Figure 2.20: Base-run PAHs used in the fit to the *Features+Plateaus* spectrum of the brightest location in NGC 7023. The formulae and relative abundances of each PAH are shown in the figure.

Hydrogenation and dehydrogenation of interstellar PAHs: Spectral characteristics and H₂ formation

We have modelled the abundance distribution and IR emission of the first 3 members of the coronene family in the north-west photodissociation region of the well-studied reflection nebulae NGC 7023. Our aim was 3-fold: *i*) analyze the distribution of abundances; *ii*) examine the spectral footprints from the hydrogenation state of PAHs; and *iii*) assess the role of PAHs in the formation of H₂ in photodissociation regions. To model the physical conditions inside the cloud, we used the Meudon PDR Code, and we gave this as input to our kinetic model. We used specific molecular properties for each PAH, based on the latest data available at the present time. We considered the loss of an H atom or an H₂ molecule as multiphoton processes, and we worked under the premise that PAHs with extra H atoms can form H₂ through an Eley-Rideal abstraction mechanism. In terms of abundances, we can distinguish clear differences with PAH size. The smallest PAH, coronene (C₂₄H₁₂), is found to be easily destroyed down to the complete loss of all of its H atoms. The largest species circumcircumcoronene (C₉₆H₂₄), is found in its normal hydrogenated state. The intermediate size molecule, circumcoronene (C₅₄H₁₈), shows an intermediate behaviour with respect to the other two, where partial dehydrogenation is observed inside the cloud. Regarding spectral variations, we find that the emission spectra in NGC 7023 are dominated by the variation in the ionization of the dominant hydrogenation state of each species at each point inside the cloud. It is difficult to “catch” the effect of dehydrogenation in the emitted PAH spectra since, for any conditions, only PAHs within a narrow size range will be susceptible to dehydrogenation, being quickly stripped off of all H atoms (and may isomerize to cages or fullerenes). The 3 μm region is the most sensitive one towards the hydrogenation level of PAHs. Based on our results, we conclude that **PAHs with extra H atoms are not the carriers of the 3.4 μm band observed in NGC 7023**, since these species are only found in very benign environments. Finally, concerning the role of PAHs in the formation of H₂ in photodissociation regions, we find that **H₂ abstraction from PAHs with extra H atoms is an inefficient process compared to grains**. Instead, we propose that photodissociation of PAHs of small-to-intermediate sizes could contribute to H₂ formation in PDR surfaces, but they cannot account by themselves for the inferred high H₂ formation rates in these regions.

3.1. Introduction

Polycyclic aromatic hydrocarbons (PAHs) are a set of molecules consisting of hexagonal aromatic carbon rings, with hydrogen atoms attached at the periphery. Upon absorption of high energy photons they get electronically excited, rapidly redistribute the absorbed energy among all available vibrational states, and relax, either by fragmenting or emitting IR photons through a fluorescence process (Léger & Puget 1984; Allamandola et al. 1989). Their presence in space is now widely accepted as being the carriers of the strong emission bands at 3.3, 6.2, 7.7, 11.3 and 12.7 μm , observed in the mid-IR spectra of UV-rich environments such as photodissociation regions (PDRs). PDRs are then considered to be the best laboratories to study PAH emission since they are the UV illuminated surfaces of molecular clouds, where the PAH emission is found to be the strongest.

Observational studies on PDRs using the ISO and Spitzer space telescopes have examined the emission of PAHs in the mid-IR range (among others Bregman et al. 1989; Berné et al. 2007; Joblin et al. 2010; Boersma et al. 2012). The combination of these studies with theoretical calculations on the IR emission of different PAH species, has allowed a characterization of the emission of PAHs as a whole (Rapacioli et al. 2005; Berné et al. 2007; Rosenberg et al. 2011; Boersma et al. 2013; Boersma et al. 2014; Boersma et al. 2015; Andrews et al. 2015). Hundreds of theoretical (and experimental) spectra of PAHs have been compiled in the NASA Ames PAH IR Spectroscopic Database (PAHdb¹; Bauschlicher et al. 2010; Boersma et al. 2014) and the Cagliari PAH Database² (Mallocci et al. 2007). The use of such databases has provided great insight on how different classes of PAHs can leave particular footprints in the emission at mid-IR wavelengths. In this regard, spectral variations due to changes in the ionization state of PAH molecules have been well characterized (e.g., Rosenberg et al. 2011; Boersma et al. 2014). Indeed, PAH band ratios such as the 6.2/11.3, 7.7/11.3 and 11.0/11.3 are now used as tracers of the ionization state of the emitting population of PAHs (Galliano et al. 2008; Fleming et al. 2010; Boersma et al. 2014). Likewise, astronomical models have long pointed out the potential importance of hydrogenation for the IR emission spectra (Schutte et al. 1993). Specifically, the 3.4 μm band has been interpreted as due to PAHs with extra H atoms—the so-called, *superhydrogenated PAHs* (Schutte et al. 1993)—in the emitting zones (Sandford et al. 2013; Bernstein et al. 1996) but other explanations for this band have also been put forward, e.g., methylated PAHs and overtones of the 3.3 μm CH stretching mode (Barker et al. 1987; Geballe et al. 1989; Joblin et al. 1996). Observationally, the ratio of the 3.4 to the 3.3 μm band is known to vary with distance to the illuminating star (Joblin et al. 1996; Pilleri et al. 2015) and this may provide a test for these assignments.

Over the years, even more sophisticated models have been developed to calculate the IR emission spectra, and to aid in the interpretation of the observed spectral variations. Bakes et al. (2001) developed a model to describe the PAH emission under the physical conditions in the Orion bar, using the latest available data (at that time) on symmetric condensed PAHs up to 54 carbon atoms. That work was the first attempt to study the emission of specific PAH molecules, focusing on the spectral variations produced by changes in the charge distribution of the species. However in PDR environments, PAHs are expected to undergo not only changes in their charge states, but also experience further processing due to the interaction with high energy photons. Allain et al. (1996) developed a kinetic model that

¹<http://www.astrochem.org/pahdb>

²<http://astrochemistry.oa-cagliari.inaf.it/database/>

considered photodissociation of PAHs. They used generic estimates for the rates of direct H-loss, H₂-loss and acetylene-loss, and found that small PAHs (< 50 carbon atoms) would be destroyed in highly UV illuminated environments. Based on the available experimental data at that time, Le Page et al. (2001) and (2003) modelled the ionization and hydrogenation of generic PAHs (up to 200 carbon atoms) in diffuse clouds in terms of abundances only. Montillaud et al. (2013) built a kinetic model for 4 PAHs up to the size of circumcoronene (96 carbon atoms), and modelled the spatial abundance evolution of these species in the north-west NW PDR of NGC 7023. They only considered neutral and cationic species, and hydrogenation states ranging from the pure carbon clusters up to the parent molecule plus 1 extra hydrogen atom. Their novelty was to admit multiphoton events to describe the photodissociation rates. They showed that multiphoton events can cause the fragmentation of large species, that otherwise would never fragment due to large energies required for such processing.

PAH processing can also leave its impression on the environment. In particular, it has been suggested that the H₂ formation rate may be affected by the presence of PAHs, as observations of PDRs have revealed H₂ formation rates of up to 10⁻¹⁶ cm³/s (Habart et al. 2004), that well exceeds the accepted value for diffuse clouds (3×10⁻¹⁷ cm³/s; Jura(1975); Gry et al. 2002). For the diffuse medium, H₂ is generally thought to form through surface reactions on dust grains (Hollenbach & Salpeter 1971). Detailed studies have shown that different routes for H₂ formation on dust grains are effective in different temperature ranges (e.g., Cuppen & Herbst 2005; Le Bourlot et al. 2012; Bron et al. 2014). While Langmuir Hinselwood reactions – where two physisorbed mobile H atoms interact and desorb as H₂ – have been found to be efficient on grains at temperatures below 20 K (e.g., Pirronello et al. 1997; Pirronello et al. 1999; Katz et al. 1999), surface reactions involving chemisorbed H atoms in an Eley-Rideal fashion – where a free H atom interacts with a chemisorbed H atom, and desorb as H₂ – have been found to be efficient at higher temperatures (e.g., Duley 1996; Habart et al. 2004; Le Bourlot et al. 2012). Surface reactions on PAHs have been proposed as an effective alternative at intermediate temperatures. This is also supported by observational correlations between H₂ and PAH emission in PDRs (Habart et al. 2003; Habart et al. 2004). Experimental and theoretical studies on neutral PAHs with extra H atoms suggest PAHs could effectively form H₂ through Eley-Rideal abstractions (Bauschlicher 1998; Rauls & Hornekær 2008; Thrower et al. 2011; Mennella et al. 2012). At the same time, PAHs could also contribute to the H₂ budget through photodissociation, where H₂-loss competes with H-loss, the main fragmentation channel after photon excitation (e.g., Jochims et al. 1994; Ling et al. 1995). Boschman et al. (2015) built a kinetic model based on the coronene molecule (24 carbon atoms), to study the role of PAHs in the formation of H₂ in PDRs. They found that a small PAH like coronene would not form H₂ through surface reactions, but mainly through direct loss (i.e., photodissociation). It is of interest then to compare these processes in order to assess the role of PAHs in the formation of H₂ in PDRs, and describe how these contributions depend on PAH size.

In this work, we model the abundance distribution of PAHs under the physical conditions expected in a prototypical PDR as the NW PDR of NGC 7023. Our aim is to study the variations in the hydrogenation and ionization state of each species, not only in terms of abundances, but also in terms of their emitted spectra. Extending on previous studies, we are able to make use of the greater availability of theoretical and experimental data on specific PAH species. We focus on the study of PAHs of different sizes that are expected to be relevant in the ISM. Thus, here we intend to extend the work of Bakes et al. (2001)

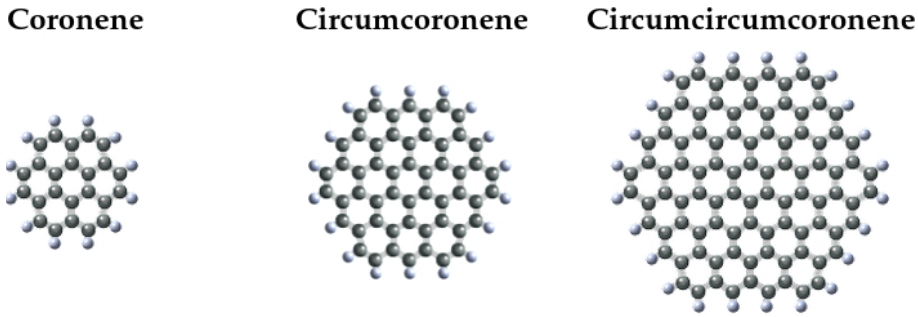


Figure 3.1: PAHs studied in this work. From left to right: coronene ($C_{24}H_{12}$), circumcoronene ($C_{54}H_{18}$) and circumcircumcoronene ($C_{96}H_{24}$). The carbon cores are depicted in grey, while H atoms are depicted in white.

by modelling the PAH emission, taking into account also the hydrogenation degree of each species. We expect then to be able to discern the spectral footprint of the hydrogenation of PAHs. In particular, we would like to assess whether it is feasible for superhydrogenated species to be present in PDRs, and be the carriers for the $3.4\mu\text{m}$ band whose origin is still unknown (Bernstein et al. 1996; Sandford et al. 2013). Together with this, we will explore the effectiveness of H_2 formation on PAHs. For this, we justify our assumptions on the works of Throuer and coworkers, that have proposed H_2 abstraction from superhydrogenated PAHs as a feasible pathway for H_2 formation (Rauls & Hornekær 2008; Throuer et al. 2011). Here, we will explore this process for PAHs bigger than coronene, and we will establish how photoprocessing of PAHs can contribute to the formation of H_2 in highly UV irradiated environments such as PDRs.

The present work is organized as follows: sections 3.2 and 3.3 present a general description of all the processes admitted in the model, and how the equations are implemented. The results are presented in section 3.4 in terms of the variations in the ionization state and hydrogenation state of the PAHs (§ 3.4.1), the H_2 formation rate from PAHs (§ 3.4.2), and the spectral variations observed in their emission (§ 3.4.3). The discussion of our results and its implications on the PAH population in the NW PDR of NGC 7023 are presented in 3.5.

3.2. Physical–Chemical Processes

We consider 3 molecules of increasing size within the *coronene family*: coronene ($C_{24}H_{12}$), circumcoronene ($C_{54}H_{18}$), and circumcircumcoronene ($C_{96}H_{24}$). We chose these molecules since this so-called *coronene family* is one of the best studied (experimentally and theoretically) set of PAHs. Circumcoronene and circumcircumcoronene consist of a coronene core surrounded by one and two rings of hexagons respectively (see Figure 3.1). Because of their similarity in molecular structure, their physical and spectroscopic properties show a global trend (Ricca et al. 2012). The sizes of these three species span the range of astrophysical relevant PAHs (Allamandola et al. 1989; Croiset et al. 2016). Also, given their compact structure, the *coronene family* is expected to be among the most stable PAHs in the ISM (Ricca et al. 2012).

PAHs in our model absorb photon energies up to $E_{\max} = 13.6$ eV, as expected in PDRs. All possible ionization states (given this threshold energy) are admitted in our model. In terms of hydrogenation state, we refer to the *parent molecule* as the molecule with a number of hydrogen atoms N_{H} equal to N_{H}^0 , where N_{H}^0 corresponds to 12 for coronene, 18 for circumcoronene, and 24 for circumcircumcoronene. Parent molecules will also be referred to as the molecule in the *normal hydrogenated* state. All molecules with $N_{\text{H}} < N_{\text{H}}^0$ are referred to as *dehydrogenated* derivatives; while molecules with extra hydrogen atoms $N_{\text{H}} > N_{\text{H}}^0$ are denominated as molecules in *superhydrogenated* states (Schutte et al. 1993). Throughout this work we consider that the hydrogenation state of each molecule can go from being completely dehydrogenated ($N_{\text{H}} = 0$) to having up to 4 additional H atoms ($N_{\text{H}} = N_{\text{H}}^0 + 4$). A discussion on this choice will be given later in the paper (see § 3.5). In the following, we will describe all the parameters and assumptions regarding the processes considered in our model.

3.2.1. Environment

We analyze the PAH abundance and emission spectra in the environment of the northwest NW PDR of the well-studied reflection nebula NGC 7023 (RA (J2000.0): 21 01 32.3; DEC (J2000.0): +68 10 25.4). Figure 3.2 shows the region studied in this work. The NW PDR of NGC 7023 is located $\sim 45''$ from the exciting binary system HD 200775 (Alecian et al. 2008), and it is the brightest one in the mid-IR extending to about $60''$ (Werner et al. 2004). It is often considered as a prototype of a PDR due to its edge-on structure, which shows a clear stratification of the emitting region (Pilleri et al. 2012). The star has created a

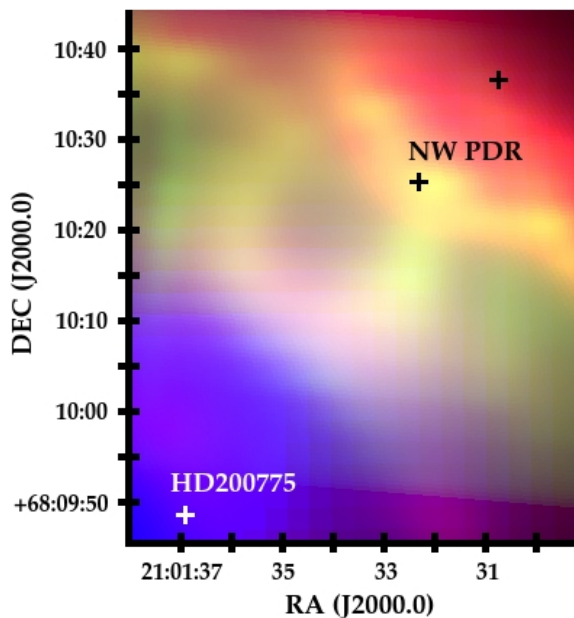


Figure 3.2: Composite image of the NW PDR of NGC 7023. The three-color image combines the PACS $70\ \mu\text{m}$ (red), PAH emission at $6.2\ \mu\text{m}$ (green, image courtesy of O. Berné), and MIPS $24\ \mu\text{m}$ (blue) images. The white cross indicates the position of the star HD 200775, while the black crosses indicate the reference extension of the NW PDR (at $45''$ and $60''$ away from the star).

Table 3.1: Input parameters for modelling the NW PDR of NGC7023 using the Meudon PDR Code.

Property	Values
Initial density n_{H} (cm^{-3})	2×10^4
UV Field G_0 (Habing units)	2600
Cosmic rays ionization rate (s^{-1})	5×10^{-17}
Pressure (cm^{-3} K)	7×10^6
R_V	5.56
$N_{\text{H}}/E(B - V)$	5.8×10^{21}
Grains to gas mass ratio	0.01
Grains distribution index	3.5
Grains minimum radius (cm)	3×10^{-7}
Grains maximum radius (cm)	3×10^{-5}

low-density cavity that is surrounded by a dense molecular cloud apparent in ^{12}CO , ^{13}CO , CO^+ and other species (Fuente et al. 1998; Fuente et al. 2003). The cavity edge is lined by a layer of HI (Fuente et al. 1998). The molecular cloud surface is traced by fluorescent H_2 emission and by bright Extended Red Emission (Lemaire et al. 1996; Witt et al. 2006). Spitzer/IRS observations have revealed the presence of C_{60} in this nebula (Sellgren et al. 2010; Berné & Tielens 2012; Berné et al. 2015). While the PAH abundance decreases rapidly into the cavity, the fullerene abundance actually increases (Berné & Tielens 2012). The average size of the PAHs at the PDR front is smaller than the sizes of PAHs deeper in the PDR, as well as the PAHs in the cavity (Croiset et al. 2016). All of these effects have been attributed to photoprocessing of PAHs, driving dehydrogenation, graphene formation and isomerization to cages and fullerenes (Berné & Tielens 2012; Berné et al. 2015).

3.2.2. PDR Model

In order to model the physical conditions within the PDR region we use the Meudon PDR Code (version 1.4.4; Le Petit et al. 2006; Le Bourlot et al. 2012). This code has been widely used to describe the NW PDR region (see Joblin et al. 2010; Montillaud et al. 2013; Bernard-Salas et al. 2015; among others). It calculates the steady state structure, solving the radiation transfer equation and the thermal and chemical balance as a function of depth in each plane-parallel slab of the cloud.

Table 3.1 lists the input parameters we adopted from the literature. We consider an isobaric model following Montillaud et al. (2013). As suggested by the Meudon PDR Code guide, we consider a cloud of finite size ($A_{V_{\text{max}}} = 5$) being illuminated by the stellar radiation on one side, and a radiation field of standard intensity on the other side. Analysis of the observed far-IR continuum intensity yields an incident UV field of $G_0 = 2600$ Habing units in the region of interest (Chokshi et al. 1988; Pilleri et al. 2012). We consider the flux of a binary star with both components modelled with a Kurucz stellar spectrum of 15000 K each (Kurucz 1993; Pilleri et al. 2012). Young Owl et al. (2002) estimated a gas density of $4 \times 10^3 \text{ cm}^{-3}$ from the observed line intensities of $[\text{O I}]63 \mu\text{m}$ and $[\text{C II}]158 \mu\text{m}$, which is in good agreement with HI observations from Fuente et al. (1998). More recent observations of the cooling lines with Herschel have led to slightly higher density estimates of the region (10^4 cm^{-3} ; Bernard-Salas et al. 2015). SPIRE observations of the CO rotational lines, plus

an analysis of the dust continuum emission show the inhomogeneous structure of the NW PDR of NGC 7023, leading to density estimates as high as 10^5 cm^{-3} in the filaments and at large distances from the PDR front (Köhler et al. 2014). Here, we adopt a value of $2 \times 10^4 \text{ cm}^{-3}$ as the initial density (Pilleri et al. 2012).

Figure 3.3 shows the calculated physical conditions. At the surface of the cloud, hydrogen is mainly in atomic form, and the temperature of the gas is a few hundred K. The conversion from HI to H₂ occurs at an extinction of $A_V = 0.9$. The density of the gas increases towards high A_V reaching $\sim 10^5 \text{ cm}^{-3}$, while the gas temperature decreases, reaching values comparable to the dust temperature ($T_{\text{gas}} \sim 60 \text{ K}$). Going into the PDR, the abundance of electrons decreases slightly due to neutralization reactions with atomic species, but from $A_V = 0.4$ onwards, the electron abundance follows closely that of ionized carbon. Carbon is mostly in ionized form. The conversion from CII to CI occurs at an $A_V \sim 4$. The CO abundance increases with depth reaching a maximum at $A_V \sim 4.5$, from where it starts dissociating due to photons penetrating from the other side of the cloud.

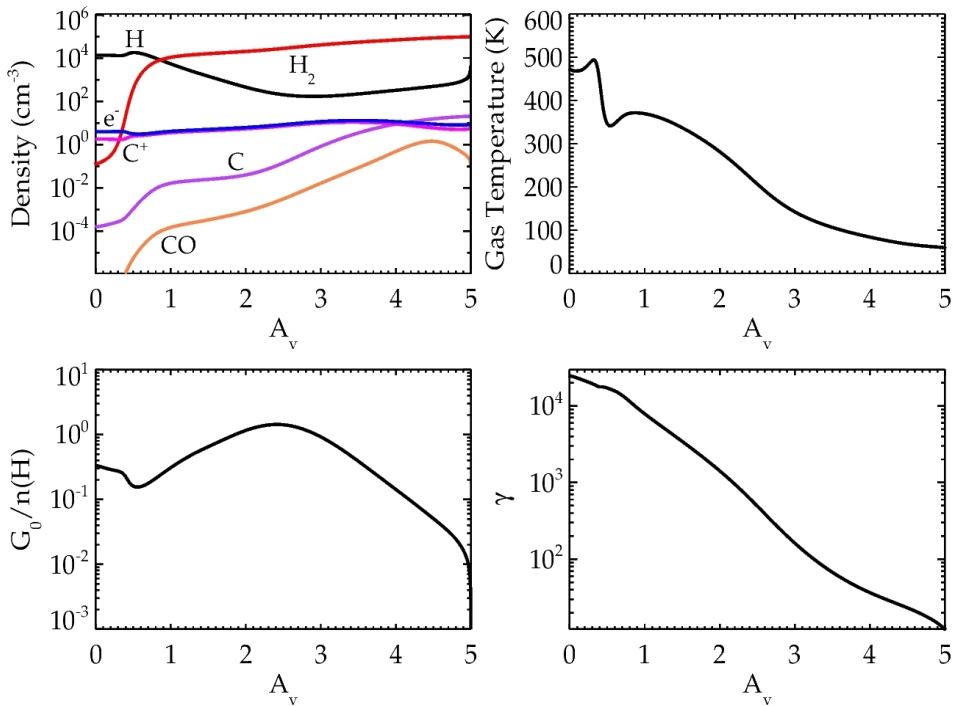


Figure 3.3: Physical conditions in the NW PDR of NGC 7023. The *top panels* show the variation of the densities and gas temperature inside the cloud. The HI to H₂ transition occurs at an $A_V \sim 0.9$, while the CII-CI transition occurs deeper in the cloud at an $A_V \sim 4$. The *bottom panels* show the physical parameters relevant for PAH hydrogenation and ionization evolution. The hydrogenation of PAHs is expected to be controlled by the ratio between the UV field intensity G_0 and the density of atomic hydrogen, which in our case only varies by about 2 orders of magnitude throughout the cloud. The ionization state of the PAH population on the other hand depends on the so-called ionization parameter, $\gamma \equiv G_0 \sqrt{T_{\text{gas}}} / n(e)$, which measures the ratio between ionization and electron recombination of the PAH species.

The physics of PAHs in PDRs is controlled by two parameters: the ionization parameter, $\gamma \equiv G_0 \sqrt{T_{\text{gas}}}/n(e)$, which controls the ionization balance of PAHs (Bakes & Tielens 1994), and the hydrogenation parameter, $G_0/n(H)$, which sets their level of dehydrogenation (Tielens 2005). The variation of these parameters in the NW PDR of NGC 7023 is shown in Figure 3.3. The ionization parameter decreases by several orders of magnitude into the PDR due to the attenuation of the UV radiation field, coupled with the relatively constant electron density for this isobaric model. In contrast, the variations in the hydrogenation parameter are more modest, but also show a more complex behaviour as the UV field and the hydrogen abundance decrease inwards but not in lockstep. Starting at the surface of the cloud, as A_V increases, $G_0/n(H)$ decreases due to the rapid attenuation of the radiation field compared to the density, which stays relatively constant until the HI to H₂ transition occurs. Once this point is reached, the decrease in the atomic hydrogen density translates into an increase of $G_0/n(H)$ to a maximum value of 1.43 at an $A_V \sim 2.4$. After this point, $G_0/n(H)$ rapidly decreases as the UV field attenuates while the hydrogen density hardly changes.

3.2.3. Molecular Characteristics

When absorbing a UV photon, PAHs in our model can either ionize or dissociate through the loss of an H atom or an H₂ molecule, as long as the absorbed energy is large enough to open these channels and win over IR relaxation. It is important to mention that we do not consider C nor C₂H₂-losses, as the kinetics of these processes are rather uncertain. Experiments have shown that, even for small PAHs, H-loss dominates over C-loss (Jochims et al. 1994). For PAHs larger than some 30 C atoms, UV photolysis proceeds by stripping off all H atoms before C-loss sets in (Zhen et al. 2014 a,b; Castellanos et al. in prep). This separates photo fragmentation into two processes where in the first step, the H-coverage of PAHs is set by a balance of UV driven H-loss and hydrogenation reactions, controlled by the hydrogenation parameter, $G_0/n(H)$. Only when all H atoms are lost, will C-loss commence and this will occur close to the star. In our analysis, we have ignored this second step. The separation of photolysis into two distinct steps simplifies the model analysis considerably, as only a limited number of species needs to be followed.

Since the internal energies required for fragmentation of large PAHs to be competitive with IR relaxation are very high (e.g., 15 eV for C₅₄H₁₈), we consider photodissociation as a multiphoton process where PAHs can absorb more than one photon before fully cooling down. Details on how we describe the photodissociation rates are given in § 3.2.4.

Superhydrogenated species are allowed to form H₂ through Eley-Rideal abstraction. We also consider attachment/recombination with electrons and H-addition reactions. H₂-addition is not considered as experimental data indicates that such reactions are not important in PDRs.

In the following we will describe the molecular characteristics we consider in order to calculate the kinetic rates for all the processes taken into account in our work. The mathematical formulation of each rate will be given in § 3.2.4.

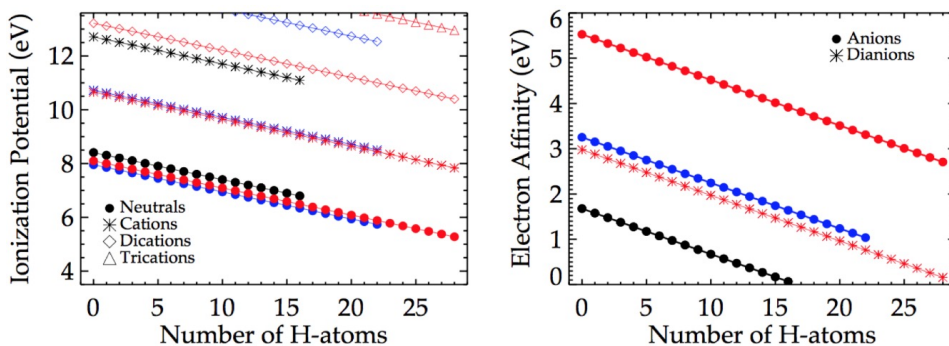


Figure 3.4: Ionization potentials and electron affinities assumed in our model. Energies for coronene, circumcoronene and circumcircumcoronene derivatives are shown in black, blue and red, respectively. Given that PAHs in our model can absorb photon energies up to 13.6 eV, the highest charge state for coronene derivatives is the doubly charged one ($Z = 2$). Circumcoronene derivatives can be doubly ionized, and only those having more than 12 H atoms can be triply ionized ($Z = 3$). Circumcircumcoronene derivatives on the other hand can be triply ionized, and those having more than 22 H atoms can be found in the +4 charge state. Given the uncertainty in the electron affinities for highly negative charge states ($Z < -1$), we do not take into account that the more dehydrogenated molecules could also exist in these highly negative states (e.g., $Z = -2$ for circumcoronene derivatives).

Ionization Potentials and Electron Affinities

We use specific ionization potentials (IP) and electron affinities (EA) for each of the molecules considered. Given the photon energies available (< 13.6 eV), we have to consider multiple cationic states. For coronene and circumcoronene we only have to consider the anionic state ($Z = -1$) but for circumcircumcoronene we have to consider dianions as well ($Z = -2$). For the normally hydrogenated species, we have taken estimates from experiments when available (Tobita et al. 1994). If no experimental values were available, we then adopted results from quantum theory (Mallocci et al. 2007; Mallocci et al. 2008), or estimates based upon conducting disk behaviour (Bakes & Tielens 1994). See more details in Appendix 3.A.

For dehydrogenated PAHs, we have followed Mallocci et al. (2008) who calculated the IPs for the *even* dehydrogenated states of coronene, i.e., $C_{24}H_{2n}$ where $n = 0-6$. Based on their estimated change of IP with hydrogenation level of the PAH, ΔIP , we assume that for each PAH in charge state Z , and with N_H number of H atoms, the following relation applies:

$$IP(Z, N_H) = IP(Z, N_H^0) + \Delta IP \times (N_H^0 - N_H), \quad (3.1)$$

where $IP(Z, N_H^0)$ is the IP of the parent molecule in charge state Z , and ΔIP is constant (about 0.1 eV approximately; see Figure 3.4). We adopt this for all hydrogenation states allowed (see more in Appendix 3.A).

Regarding EAs, the first EA of $C_{24}H_{12}$ is 0.47 eV, as derived from both theory and experiments (Duncan et al. 1999; Mallocci et al. 2007). An et al. (2008) reports an EA of 1.89 eV for C_{24} , which agrees with the ~ 0.1 eV variation per dehydrogenation derived from the IPs. Therefore, we also consider the relation given by equation 3.1 for the EAs (Figure 3.4).

Ionization Yield & UV Absorption Cross Sections

We adopt the ionization yield, Y_{ion} , derived from experiments on small PAHs from Jochims et al. (1996, 1997). These experiments show that Y_{ion} scales linearly with energy, until it reaches unity for energies above $\sim(\text{IP} + 9.2)$ eV. This describes well the ionization yield measured for coronene (Verstraete et al. 1990), supporting the fact that the variation of the ionization yield with energy appears to be rather independent of the size of the PAH.

We have adopted the UV absorption cross sections, σ_{UV} , from the Cagliari PAH database for $\text{C}_{24}\text{H}_{12}$ and $\text{C}_{54}\text{H}_{18}$ (Mallocci et al. 2007). For $\text{C}_{96}\text{H}_{24}$ no information is available in the literature, and so we adopt the UV cross sections of $\text{C}_{54}\text{H}_{18}$ scaled by the number of carbon atoms of circumcoronene.

For the *even* dehydrogenated states of coronene, we use the DFT results from Mallocci et al. (2008). For the other species we use the UV absorption cross section of the molecule with the closest number of H atoms within the same ionization state. We expect this to be a good approximation, based on the analysis of Mallocci et al. (2008). Even though the overall shape varies somewhat with dehydrogenation, when calculating the average photon energy absorbed in a given stellar radiation field, the absorbed average energy varies by less than 1 eV for the different hydrogenation states, being slightly higher for dehydrogenated states. Thus, we expect that this assumption will have little impact on our calculations.

IR Cross Sections and Density of States

IR cross sections, $\sigma_{\bar{\nu}_i}$, and frequencies, $\bar{\nu}_i$ were collected either from the NASA Ames PAH Database (PAHdb) (Bauschlicher et al. 2010; Boersma et al. 2014), or from our own *ab initio* DFT calculations, using B3LYP/4-31G (Becke 1993; Stephens et al. 1994) on Gaussian 09 (Frisch et al. 2009). In the case of dehydrogenated PAHs, several isomers with various multiplicities were calculated. To facilitate our analysis, here we always report the vibrational spectrum of the most stable isomer. Following Langhoff (1996) the vibrational frequencies were scaled by 0.958, except for the modes involving CC triple bonds. Bauschlicher & Ricca (2013) showed that B3LYP/4-31G failed to reproduce the stretching modes of the triple CC bond in C_6H_4 . In order to compensate for this, a specific scaling factor of 0.9097 was used. This was obtained by direct comparison of the calculated frequency for the triple CC bond stretching mode of C_6H_4 , with the experimental result published in Radziszewski et al. (1992).

Tables summarizing the set of molecules for which IR spectra are available can be found in Appendix 3.A. For the molecules for which we have the intrinsic spectra, density of vibrational states are calculated explicitly using the Beyer-Swinehart counting algorithm (Beyer & Swinehart 1973; Stein & Rabinovitch 1973). Whenever this data is not available, we consider the spectra of the molecule with the closest number of H atoms within the same ionization state.

3.2.4. Processes

In this section we specify the processes for each molecule, and we describe how we calculate each rate using the parameters described in § 3.2.3.

Photoionization

The photoionization rate, k_{ion} , for a molecule in a given ionization state, Z , and with N_H H atoms is given by:

$$k_{ion}(Z, N_H) = \int_{IP(Z, N_H)}^{E_{max}} \sigma_{UV}(Z, N_H, E) Y_{ion}(Z, N_H, E) n(E) dE, \quad (3.2)$$

where $\sigma_{UV}(Z, N_H)$ is the UV absorption cross section of the molecule, $Y_{ion}(Z, N_H)$ is the ionization yield, and $n(E)$ corresponds to the flux of photons.

Electron Attachment/Recombination with Electrons

We have adopted electron attachment and recombination rates based on the collisional rates described in Bakes & Tielens (1994), which are in good agreement with experiments for small PAHs (see Appendix 3.A for details).

For the coronene anion formation our estimate gives a value of $\sim 3 \times 10^{-10}$ cm³/s, which is slightly smaller than the rate coefficient determined by Denifl et al. (2005). With respect to the measured rates for small cationic PAHs, the experimental values are smaller than our formalism would predict, but they seem to be approaching our adopted conducting disk values with increasing size (Tielens 2008).

Note that electron recombination is an excitation process and can lead to fragmentation if the dissociative channel is energetically accessible (Tobita et al. 1992; Denifl et al. 2005). Therefore, we explored direct H-loss and H₂-loss as possible pathways for relaxation after recombination with an electron. However, we found that these channels are, in general, not relevant for the molecules considered. Only for coronene derivatives we find that dissociative recombination can be important for superhydrogenated cations. However, as we will see in § 3.4, these are not relevant derivatives of coronene.

Photodissociation Channels

As mentioned before, we consider dissociation and IR emission as possible relaxation channels after the absorption of non-ionizing photons. We calculate the IR emission rate explicitly using either the IR cross sections of the respective molecule if available, or the IR cross sections from the molecule with the closest number of H atoms, within the same ionization state. Table 3.2 shows the adopted parameters for each photodissociation process. The explanation of each choice is given below.

H-loss For coronene and its dehydrogenated states ($N_H \leq 12$), we will use the activation energies and entropies derived for pyrene cation from the time-dependent mass spectrometry experiments of Ling et al. (1995); that is, activation energies of 4.6 and 4.1 eV, and entropies of 44.8 and 55.6 J/K/mol, for PAHs with an even and odd number of H atoms, respectively (see Table 3.2).

These values compare well with our theoretically determined dissociation energies for the coronene cation ($Z = 1$) and its dehydrogenated states (4.9 and 3.9 eV respectively), as well as with Reitsma et al. (2014) for the first 6 H-losses (4.7 and 4.1 eV respectively). Theoretical analysis also shows that the CH interaction is a rather local process, and thus, its energetics remain relatively constant with increasing degree of dehydrogenation of the

molecule: considering *even* and *odd* dehydrogenated states separately, only small variations of ~ 0.02 eV are obtained (Candian et al. in prep). Calculations also predict little difference (< 0.4 eV) in the energies between neutral and positively ionized coronene (Paris et al. 2014); and also between their respective neutral and positively ionized dehydrogenated states (Candian et al. in prep). Concerning anionic species, the energy for the first H-loss from coronene anion is about 4.1 eV according to DFT calculations (Candian et al. in prep), much less than the 4.9 eV obtained for the other ionization states of coronene. However, calculations on anions require a different level of theory which may add a systematic difference with respect to the values obtained for the other ionization states. Keeping this in mind, we will assume the same energies and entropies for all ionization states.

For $C_{54}H_{18}$ and $C_{96}H_{24}$, and their respective dehydrogenated states ($N_H \leq N_H^0$), we must take into account their edge structure in order to define how these molecules fragment (see Figure 3.1). While coronene has a carbon core with 12 H atoms attached in pairs to 6 different rings (i.e., 6 duo rings), $C_{54}H_{18}$ has 12 H atoms attached in pairs to 6 separate rings (6 duo rings), and 6 H atoms attached to the other 6 peripheral rings (6 solo rings). Circumcircumcoronene has similarly 6 duo rings and 12 solo rings. Given these structures, we will consider that these molecules first lose all the duo H-atoms in the same fashion as the H-losses in coronene. Once the duo H-atoms are gone, then they start losing the solo H-atoms. This assumption is based on theoretical calculations that predict higher binding energies for solo H-atoms than duo H-atoms (Castellanos et al. in prep).

Table 3.2: Dissociation parameters considered in our work.

Normal-to-dehydrogenated states ($N_H \leq N_H^0$)							
H-Loss				H ₂ -Loss			
	Ion. State	E_{act} (eV)	ΔS (J/K/mol)		Ion. State	E_{act} (eV)	ΔS (J/K/mol)
Even N_H	All	4.6	44.8	Even N_H	All	3.52	-53.1
Odd N_H	All	4.1	55.6	$N_H > N_{solo}$			
Superhydrogenated states ($N_H > N_H^0$)							
H-Loss							
	Ion. State	E_{act} (eV)	ΔS (J/K/mol)				
Extra H atom in a duo ring	$Z < 0$	1.4	55.6				
	$Z = 0$	1.4	55.6				
	$Z > 0$	1.55	55.6				

The upper table shows the activation energies, E_{act} , and change in entropy, ΔS , for the normal-to-dehydrogenated states ($N_H \leq N_H^0$), while the bottom table shows the dissociation parameters for the superhydrogenated states ($N_H > N_H^0$). N_{solo} corresponds to the number of solo H atoms of each molecule, i.e., 0 for coronene, 6 for circumcoronene and 12 for circumcircumcoronene. Dissociation parameters for normal-to-dehydrogenated molecules are taken from Ling et al. (1995). The activation energies considered for the H-loss from superhydrogenated molecules are taken from the theoretical work of Bauschlicher & Ricca (2014).

For the loss of the extra hydrogen atoms (i.e., $N_{\text{H}} > N_{\text{H}}^0$) we adopt the theoretically derived values from Bauschlicher & Ricca (2014) for the binding energies of the extra H-atom for the $\text{C}_{96}\text{H}_{25}$ anion, neutral and cation molecule. We will assume extra H atoms always stick to duo positions, even for $\text{C}_{54}\text{H}_{18}$ and $\text{C}_{96}\text{H}_{24}$ derivatives that also have solo rings available for attachment. The binding energies of an extra H-atom in a duo position are of 1.4 eV for the anion, 1.4 eV for the neutral and 1.55 eV for the cation. The respective energies for the attachment to a solo position are of 2.2, 1.8 and 2.3 eV. These small differences do not have an impact on the derived rates. Given the lack of data, we will use an activation entropy of 55.6 J/K/mol, as assumed for PAHs with an odd number of H atoms (Ling et al. 1995).

H₂-loss The loss of H₂ will be considered for normal-to-dehydrogenated molecules, while H₂-loss from superhydrogenated molecules will be considered as an abstraction process through an Eley-Rideal mechanism. Test runs show that for superhydrogenated molecules, H₂ abstraction by H is more important than H₂-loss through photoexcitation. According to DFT calculations (Castellanos et al. in prep), the activation energies for the H₂-loss from a duo and a solo position are of 3.89 and 2.2 eV, respectively. Assuming a change in entropy of -53.1 J/K/mol (Ling et al. 1995), we get that superhydrogenated molecules will preferably lose their extra H atom after UV photon absorption, rather than an H₂ molecule, and that superhydrogenated isomers with free C atoms are not relevant species. Thus, we do not consider direct H₂-loss from superhydrogenated molecules.

Regarding normal-to-dehydrogenated molecules, due to the lack of experimental data on large PAHs, we will use the activation energy and entropy obtained for pyrene cation from the experiments of Ling et al. (1995); that is, an activation energy of 3.52 eV, and an activation entropy of -53.1 J/K/mol. This energy is small compared to the theoretical calculations for the first H₂-losses from coronene cation, which give energies of ~5.0 eV (Reitsma et al. 2014; Paris et al. 2014). However DFT calculations are known to overestimate energies, and so we chose to use the experimental values.

A theoretical study on coronene and its positively ionized states shows that H₂-loss from 2 H atoms within the same ring has a lower dissociation energy than the H₂-loss from 2 H atoms from different rings (Paris et al. 2014). Thus, we will assume that the H₂-loss comes from 2 H atoms in a duo ring. In the case of coronene derivatives, this indicates that direct H₂-loss will be considered only for the molecules with an even number of H-atoms. Dehydrogenated coronene derivatives with an odd number of H-atoms will only lose the (more loosely bound) H atom left in the ring.

In the case of $\text{C}_{54}\text{H}_{18}$ and $\text{C}_{96}\text{H}_{24}$ derivatives (which have solo and duo rings), the H₂ molecule will also be assumed to form from 2 H atoms from the same ring (a duo ring). In other words, direct H₂-loss will only be considered for molecules having an even number of H atoms until only solo H atoms remain in the molecule. These solo H atoms will be lost 1 by 1 using the activation energies and entropies discussed before (see Table 3.2).

Dissociation Rates In order to obtain the multiphoton dissociation rates, we first calculate each rate constant according to the Rice-Rampsberger-Kassel-Marcus (RRKM) theory in the Arrhenius form, using the parameters described above (Tielens 2005).

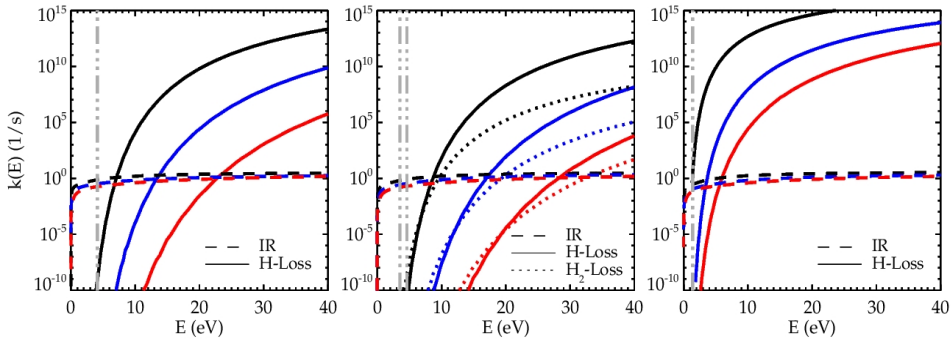


Figure 3.5: Comparison of IR emission and photodissociation rates as a function of internal energy of the PAH. The rates determined for coronene derivatives are shown in black, while the rates for circumcoronene and circumcircumcoronene are shown in blue and red respectively, following the color scheme of Figure 3.4. The grey vertical lines show the activation energies assumed listed in Table 3.2. The *left panel* shows the rates for the first dehydrogenated state of each parent molecule in their neutral state ($C_{24}H_{11}^0$, $C_{54}H_{17}^0$ and $C_{96}H_{23}^0$), in order to exemplify the rates for molecules with an odd number of H atoms. The *middle panel* shows the rates for the parent neutral molecules, illustrating the H and H_2 -loss rates for PAHs with an even number of H atoms. The *right panel* shows the rates for the first superhydrogenated state of the neutral molecules (i.e., $C_{24}H_{13}^0$, $C_{54}H_{19}^0$, and $C_{96}H_{25}^0$) for which no direct H_2 -loss is considered. IR emission rates as a function of internal energy, $k_{IR}(E)$, have been calculated using the IR cross sections of each molecule whenever available. For $C_{24}H_{11}^0$ and $C_{96}H_{23}^0$ we have assumed the intrinsic frequencies of the parent molecules.

IR emission rates, $k_{IR}(Z, N_H, E)$, were calculated using the so-called thermal approximation (e.g., Schutte et al. 1993; Bakes et al. 2001). In this approximation, the emission from a given vibrational mode corresponds to the average emission of an oscillator connected to a thermal bath at temperature T . The inverse timescale of IR emission is then given by:

$$k_{IR}(Z, N_H, E) = 4\pi \sum_i \sigma_{IR_i} \frac{B(\bar{\nu}_i, T(E))}{E}, \quad (3.3)$$

where $B(\bar{\nu}_i, T(E))$ is the Planck function, and σ_{IR_i} is the IR cross section of mode i at frequency $\bar{\nu}_i$. The $T(E)$ relation is derived from the heat capacity $C_v(T)$ calculated for each molecule (Bakes et al. 2001). Figure 3.5 compares the calculated IR emission and dissociation rates. H_2 -loss dominates over H-loss only at low internal energies, where IR emission dominates over both dissociation processes. At an internal energy of 9 eV, H-loss becomes faster than IR emission for neutral coronene. This transition occurs at 17 eV and ~ 28 eV for $C_{54}H_{18}^0$ and $C_{96}H_{24}^0$ respectively, way above the Lyman limit. The same behaviour is observed for the other ionization states, where the crossing point between the H-loss rate and IR relaxation occurs at slightly higher energies (up to 2 eV) due to the faster IR emission rates of ions compared to those of neutrals. For dehydrogenated states with an odd number of H-atoms, for which we have assumed a smaller activation energy, the crossing point occurs at energies 3–5 eV smaller than for the molecules with an even number of H-atoms, but this is still above the Lyman limit for the larger molecules. For superhydrogenated states, on the other hand, the transition occurs at much lower energies, all below 13.6 eV. Comparing our estimates with Montillaud et al. (2013) for the parent molecules, we get that the H-loss rates as a function of internal energy of the PAH are fairly similar: the curves of Figure 3.5 are slightly steeper, leading to smaller rates than theirs at lower energies (near the crossing

points), but similar at higher energies. Clearly for superhydrogenated molecules, our rates are significantly larger than theirs given that we assume low energies compared to their 3.2 eV dissociation energy for H-loss from $\text{N}_{\text{H}}^0 + 1$ molecule (their maximum hydrogenation state). Montillaud et al. (2013) also compares their rates to the values used in Berné & Tielens (2012) and Le Page et al. (2001). Somewhat different rates are obtained due to the different adopted binding energies (3.3 eV for the H-loss in Berné & Tielens 2012, and 4.8 eV in Le Page et al. 2001) and pre-exponential factors ($3 \times 10^{16} \text{ s}^{-1}$ in both studies). For coronene, the H-loss rates of Montillaud et al. (2013) are higher than the ones in Le Page et al. (2001). Compared to Berné & Tielens (2012), the crossing points occur at slightly different energies, but due to the steeper change of the rates of Montillaud et al. (2013), their rates are higher at energies above 11 eV.

Assuming that the cooling of a PAH can be described as a Poisson process, we can estimate the temperature probability function of the PAH in a given radiation field following Bakes et al. (2001) (see also Purcell 1976; Aannestad & Kenyon 1979). The temperature probability function for a PAH exposed to photons of energy E , $G(T, E)$, is then given by:

$$G(T, E)dE = \frac{\bar{r}}{dT/dt} \exp(-\bar{r} \tau_{\min}(T, E))dE, \quad (3.4)$$

with \bar{r} the photon absorption rate, dT/dt the cooling rate, and τ_{\min} the minimum amount of time the PAH requires to cool from a maximum temperature $T_{\max}(E)$ to T , after absorbing a photon of energy E . Since the PAH is absorbing photons in a stellar radiation field $n(E)$, expression 3.4 must be averaged over the distribution of photon energies:

$$\tilde{G}(T) = \frac{1}{\bar{r}} \int G(T, E) n(E) dE, \quad (3.5)$$

so that $\tilde{G}(T) dT$ corresponds to the probability of finding the PAH at a temperature between T and $T + dT$ given a single photon event. When considering multiphoton events, we must calculate the temperature probability function for n photon events, $G_n(T)$, in an iterative fashion:

$$G_n(T) = \int G_{n-1}(T_i, T') G(T', T) dT', \quad (3.6)$$

where we are essentially calculating the probability for a PAH to be at temperature T given that $n - 1$ photon events take the PAH to a temperature T' starting from an initial temperature T_i , and an additional photon event takes the PAH from T' to a temperature T .

We start by calculating $G_1(T)$ considering an initial temperature T_i . In order to make sure the probability distribution is well defined (i.e., integral over T gives unity), we choose a proper initial temperature T_i and a temperature grid for each molecule, based on where the peak of the distribution is expected to be, i.e., the temperature T_{peak} at which $dT/dt = \bar{r}$. This procedure also helps in decreasing the time it takes for the calculations to run. At each step we check that $T_i > 0$ K and that the integral $\int G_1(T) dT \sim 1$ to within a few percent. Once $G_1(T)$ is obtained following Bakes et al. (2001), we estimate the H-loss, H_2 -loss and IR emission rates for each PAH (Z, N_{H}) in a given hydrogenation and ionization state as:

$$k_i = \int k_i(T) G_n(T) dT. \quad (3.7)$$

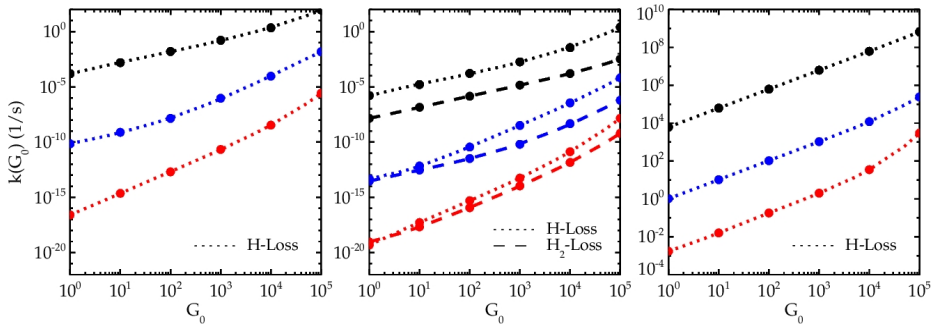


Figure 3.6: Variation of the photodissociation rates with respect to the intensity of the UV field, G_0 . The rates are shown for the same molecules as in Figure 3.5, following the same color scheme. For the smallest molecule (black curves) the rates scale linearly with G_0 at the range of interest for NGC 7023 ($G_0 \leq 2600$) indicating single photon events occurrence for coronene derivatives. For the larger molecules, multiphoton events are important. Even though H-loss is the dominant dissociation channel, at low G_0 values, H_2 -loss can become a competitive process for the larger circumcoronene and circumcircumcoronene species.

Once convergence is reached between successive iterations, we calculate the probability for each reaction i as:

$$P_i = \frac{k_i}{k_{tot}}, \quad (3.8)$$

where: $k_{tot} = k_{H,Loss} + k_{H_2,Loss} + k_{IR}$. We perform this calculation for each PAH (Z, N_H) for different intensities of the radiation field, i.e., varying G_0 between 1 and 10^6 . Figure 3.6 shows $k_{H,Loss}(G_0)$ and $k_{H_2,Loss}(G_0)$ as a function of G_0 for the molecules presented in Figure 3.5. Fits to some of these curves can be found in the Appendix 3.B. The variation of both rates scales linearly with G_0 for coronene up to very high G_0 values, meaning this PAH dissociates through single photon events in our range of interest. Larger molecules need more photons to dissociate (Montillaud et al. 2013): H-loss for $C_{54}H_{18}^0$ is already a 2 photons event at $G_0 < 10$, while at the edge of the NGC 7023 NW PDR, it is expected to be a 3 photons event. $C_{96}H_{24}^0$ on the other hand, needs ≥ 3 photons depending on the G_0 considered (at $G_0 > 10^5$ it becomes a 4 photons event). As H_2 -loss occurs at low internal energies of the PAH, it scales linearly with UV field intensity in highly shielded environments, becoming a competitive process with respect to the direct H-loss for the larger molecules ($N_C > 54$).

The final rate of dissociation for each process is given by the rate of photon absorptions times the probability for each channel to occur given by expression 3.8.

Electronic Relaxation As an aside, we note that for small neutral species, electronic fluorescence and phosphorescence can play a role as a de-excitation process. However, for coronene, mean fluorescence and phosphorescence yields are of only 0.2 and 0.1, respectively (Dawson & Kropp 1969). Because of smaller energy gaps, fluorescence and phosphorescence for large species is unimportant (Pino et al. 2011). For ions, internal conversion will be even more important as the energy gaps involved are smaller (cf. Pino et al. 2011). Delayed fluorescence —also sometimes called Poincaré fluorescence, where the excited species revisits the S_1 (or T_1) state (Léger et al. 1988)— is measured to be unimportant for

coronene as it only accounts for a small fraction of the total radiationless de-activation of triplet coronene (Kropp & Dawson 1967). While delayed fluorescence cannot compete with IR relaxation for low levels of excitation, at high internal energies it does become more important. As fragmentation, particularly for the large species, requires high levels of internal energy, delayed fluorescence may play more of a role. Following Berné et al. (2015), and adopting a binding energy of 4.6 eV and an energy gap of 2.1 eV (Fusaro 2012), we have examined the possible effect of electronic relaxation on the H-loss rate of large PAHs. As an example, for circumcoronene, at an internal energy of 25 eV the H-loss rate is calculated to be $5 \times 10^4 \text{ s}^{-1}$, which should be compared to the electronic relaxation rate of $\sim 0.5 \text{ s}^{-1}$ and the IR relaxation rate of $\sim 1 \text{ s}^{-1}$. Likewise for circumcircumcoronene at an internal energy of 37 eV, the H-loss rate is 10^3 s^{-1} , the electronic relaxation rate is $\sim 1 \text{ s}^{-1}$ and the IR rate is $\sim 1 \text{ s}^{-1}$. Hence we have chosen to ignore electronic fluorescence.

Reactivity with Hydrogen

For cationic species we will consider the works of Le Page et al. (1997) and Betts et al. (2006). These studies have experimentally determined rate coefficients for the first and second hydrogenation of small cationic PAHs ($N_C \leq 24$). The rates for all PAHs agreed within the uncertainties with the rate derived for coronene, $1.4 \pm 0.7 \times 10^{-10} \text{ cm}^3/\text{s}$.

More recent experiments on the hydrogenation of coronene cation reveal that only coronene cations with an odd number of H-atoms are detected through mass spectrometry (Boschman et al. 2012; Reitsma et al. 2014). Transition states calculations predict a small (0.01 eV) barrier for the first hydrogenation to a duo ring, and a barrier of 0.03 eV for the second one within the same ring (Cazaux et al. 2016). Further H-additions have different barriers depending on both, the radical nature of the reactants and the deformation in the carbon structure of the PAH. Low barriers are typically of the order of 0.01 eV, while large barriers are typically of the order of 0.03 eV. As a reference, a 0.01 eV barrier leads to a rate similar as the one derived by Le Page and coworkers assuming the geometrical cross section of coronene (35.7 \AA^2). Given the lack of data on the hydrogenation of dehydrogenated states, we will adopt the rate of $1.4 \times 10^{-10} \text{ cm}^3/\text{s}$ for all hydrogenation steps of all positively ionized species, irrespective of the barriers.

For neutral species we will consider the work of Rauls & Hornekær (2008) on the hydrogenation of neutral coronene. This work predicts a barrier of 0.06 eV for the first hydrogenation; no barrier for the second; a 0.03 or 0.04 eV barrier for the third extra H atom depending on whether the H atom is attached to an inner or outer edge of the molecule; and no barriers for additional hydrogenations up to 8 extra H atoms. Considering the geometrical cross section of coronene, a 0.06 eV barrier leads to rates of the order of $10^{-10} \text{ cm}^3/\text{s}$ at the temperature range of relevance (few hundred K). Given the lack of data on the larger molecules we decide to use the geometrical cross sections of each molecule together with the barriers given in Rauls & Hornekær (2008) for all neutral species in normally-to-superhydrogenated states. For the dehydrogenated molecules we do not consider any barrier, and we adopt a 7% efficiency as found for cations by Demarais et al. (2014).

Regarding anionic species, Demarais et al. (2012) performed experiments on the reactivity of deprotonated small PAH anions with H atoms, and found that hydrogenation occurs through associative detachment (i.e., formation of the neutral parent molecule and the release of an electron). For the largest PAH they studied, $C_{14}H_7^-$, they found a reaction

rate of $(7.8 \pm 0.2) \times 10^{-10} \text{ cm}^3/\text{s}$ and report that, although energetically feasible, the pure association reaction ($\text{C}_{14}\text{H}_9^- + \text{H} \rightarrow \text{C}_{14}\text{H}_{10}^-$) is not observed. Thus, we will consider the associative detachment pathway as the H-addition process for all negatively ionized species considered in our work ($Z < 0$). In their study, the reaction rate decreases slightly with increasing size of the PAH. However given their small sample (benzene, naphthalene and anthracene), and the lack of data on larger PAHs, we will adopt the rate determined for anthracene for all our anionic molecules.

It is important to mention that no H_2 -addition reactions will be considered for any of the molecules since the few experiments that have been carried out on small cationic PAHs have detected little, if not any, reactivity with H_2 , at least not above a detection threshold of $5 \times 10^{-13} \text{ cm}^3/\text{s}$ (Le Page et al. 1997; Demarais et al. 2012).

H_2 abstraction

H_2 abstraction from superhydrogenated neutral coronene has been observed in desorption experiments on coronene bombarded with deuterium atoms (Thrower et al. 2011). This has also been analyzed from a theoretical perspective in the work of Rauls & Hornekær (2008). They predict that the H_2 abstraction (occurring at the outer edge) from $\text{C}_{24}\text{H}_{13}^0$ is a barrier-less process, while the abstraction from $\text{C}_{24}\text{H}_{14}^0$ has a small barrier of 0.01 eV. Further abstractions occur in barrier-less processes. Bauschlicher & Bakes (2001) also predict no barriers for H_2 abstraction from $\text{C}_{24}\text{H}_{13}^-$ and $\text{C}_{54}\text{H}_{19}^-$. Experiments on deuteration of coronene films taken at 300 K suggest abstraction cross sections of 0.06 \AA^2 (Mennella et al. 2012). Considering this cross section for all abstractions, σ_{er} , then the Eley-Rideal rate is given by:

$$k_{er} = \sigma_{er} \left(\frac{8 k_B T_{gas}}{\pi m_H} \right)^{1/2} n(H), \quad (3.9)$$

which translates to a rate:

$$k_{er} = 8.7 \times 10^{-13} \sqrt{\frac{T_{gas}}{100}} n(H). \quad (3.10)$$

3.3. Model

Once the physical conditions and all processes are defined for each PAH, we proceed to establish the kinetic equation for the abundance of each PAH considered in the model (see Appendix 3.C). We solve the system of equations assuming steady state i.e., $d[\text{PAH}(Z, N_H)]/dt = 0$. Once the distribution of PAH abundances were obtained for each species, we calculate the emission spectra following Bakes et al. (2001), i.e., using the temperature probability function described in the previous section. In order to analyze the emission band ratios, we consider an intrinsic shift of the bands of 15 cm^{-1} , and Gaussian line profiles with a FWHM of 15 cm^{-1} for all spectra (see Boersma et al. 2013). The results regarding the spectral variations will be presented in § 3.4.3.

3.4. Results

Here we present the results of our work in terms of the distribution of abundances (§ 3.4.1), the H_2 formation rates (§ 3.4.2), and the spectral variations expected from the derived distribution of PAH species (§ 3.4.3).

3.4.1. Abundances

In agreement with Montillaud et al. (2013) and Boschman et al. (2015), the hydrogenation of PAHs varies strongly with PAH size and depth into the PDR (see Appendix 3.E). While coronene is mostly dehydrogenated throughout most of the cloud—only at an A_V around 4.2 do the first hydrogenated states appear—, circumcoronene does not show any dehydrogenation under the same physical conditions. The medium-sized PAH, circumcoronene, shows an intermediate behaviour compared to the other 2 species, with small traces ($\lesssim 20\%$) of singly- and di-dehydrogenated states at the surface. The dehydrogenated fraction first decreases with depth in the PDR and then increases again slightly around an A_V of 1.7 (see Figure 3.7).

We also note that both circumcoronene and circumcircumcoronene molecules, show small amounts of superhydrogenated species deep in the cloud ($A_V > 4$) due to the increase in the atomic H density resulting from UV photons penetrating from the backside of the cloud (this also leads to the appearance of the first hydrogenated states of coronene; see Appendix 3.E). In contrast, Montillaud et al. (2013) reported that circumcircumcoronene is superhydrogenated ($N_H^0 + 1$) throughout the entire cloud. The difference mainly lies in the dissociation parameters we have assumed for the superhydrogenated species (Bauschlicher & Ricca 2014). The low activation energies we have adopted make UV driven H-loss the main dehydrogenation process for superhydrogenated circumcircumcoronene derivatives (e.g., rates of $\sim 10^{-3} \text{ s}^{-1}$ at $A_V = 0$). Test runs of $\pm 0.4 \text{ eV}$ in the activation energies presented in Table 3.2 for the superhydrogenated species, do not have an impact on this aspect.

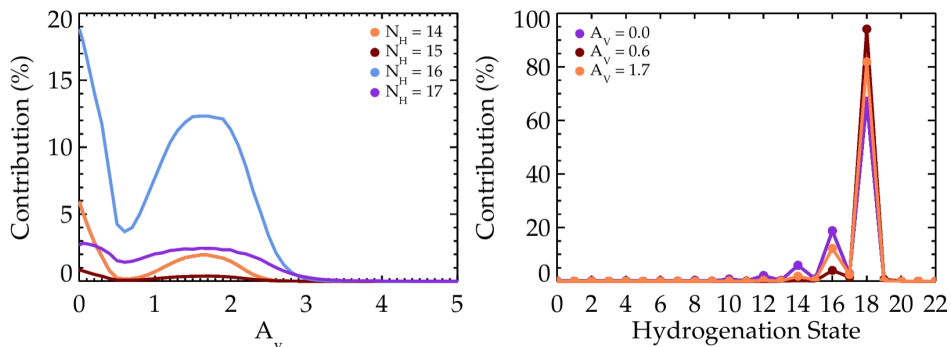


Figure 3.7: *Left Panel:* Relative contribution of dehydrogenated states of circumcoronene as a function of depth into the cloud, A_V . The contributions consider all ionization states at which the molecules are present. The curves are shown for the first 4 dehydrogenated states of the parent molecule ($N_H = 17-4$). Other partially dehydrogenated states contribute in smaller fractions. *Right Panel:* Distribution of circumcoronene derivatives at different A_V values where partially dehydrogenated species are observed.

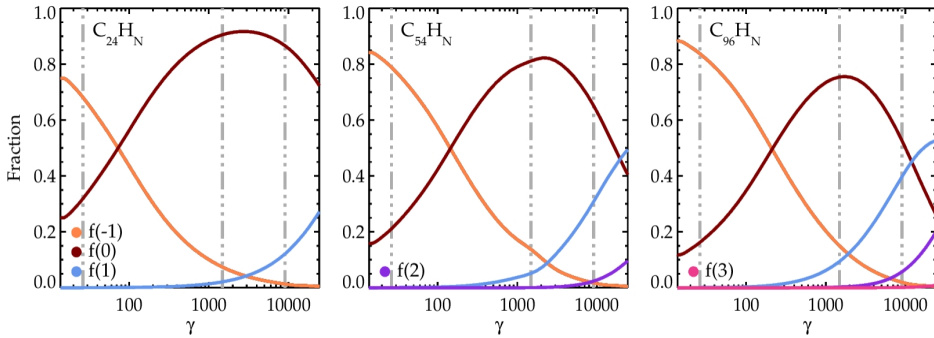


Figure 3.8: Charge distribution of the PAHs considered in our study. The contribution from each ionization state is shown as a function of the ionization parameter $\gamma \equiv G_0 \sqrt{T_{\text{gas}}}/n(e)$ for coronene (left panel), circumcoronene (middle panel) and circumcircumcoronene (right panel) derivatives. The color scheme is the same for all panels. Dashed grey lines are at $A_V = 1, 2$ and 4 . As observed from the panels, the main charge states throughout the cloud are the neutrals ($Z = 0$), anions ($Z = -1$) and cations ($Z = 1$). Higher positively charged states are only present in minor levels at the surface of the NW PDR of NGC 7023. Higher anionic states ($Z < -1$) are not observed.

Regarding ionization, we see that the larger the molecule, the higher the contribution from positively ionized species at the surface of the cloud. In the case of coronene derivatives, we find that neutrals contribute $\sim 73\%$ to the total abundance of PAHs at an $A_V = 0$, while cations contribute $\sim 27\%$. The radiation field intensity is not strong enough to produce dications for this species. For the larger molecules in our sample, the neutral-to-cation ratio inverts with respect to coronene. Positively charged circumcoronene derivatives contribute 59% , while neutrals contribute 41% . In the case of circumcircumcoronene, we see higher ionization states than for the smaller species. Here the percentage considering cations and dications adds up to $\sim 74\%$, while it is 26% for the neutrals. Higher positively ionized species, $Z > 2$, contribute at negligible levels ($< 1\%$). Figure 3.8 shows the charge distribution variation with respect to the ionization parameter $\gamma \equiv G_0 \sqrt{T_{\text{gas}}}/n(e)$ for the 3 species considered in our work. As the UV field intensity decreases, neutrals and anions become the dominant charge states. This appearance of anions occurs at lower A_V values as the size of the parent molecule increases: a 10% contribution from anions is expected at a $\gamma = 2.2 \times 10^3$, 2×10^3 and 10^3 for $C_{96}H_{24}$, $C_{54}H_{18}$, and $C_{24}H_{12}$ derivatives. Indeed, anions become the dominant charge states at large depths in the cloud. At $A_V = 5$, anions make up 74% , 84% and 88% of the coronene, circumcoronene and circumcircumcoronene derivatives population. In contrast, the PAH anion abundance is only of $1\text{--}2\%$ at the HI to H₂ transition ($A_V \sim 1$) depending on the molecule. However, negatively charged species are already important at an $A_V \sim 2$, especially for the larger species.

While test runs show that the use of different ionization yields does not have an impact on the derived abundances, the adopted dependence of the IPs and EAs on hydrogenation *does* have an effect on our results, but only for the smallest species in our sample. It is important to recall that previous models on PAH abundances in PDRs have not considered negatively charged species, and/or adopt the IP and EA of the parent molecule for all hydrogenation states within a given charge state (Le Page et al. 2001; Le Page et al. 2003; Montillaud et al. 2013; Boschman et al. 2015). Here we find that it is important to use the specific IPs and EAs for each molecule, especially for the smallest species. The large

fraction of negatively charged coronene derivatives results from the adopted EAs of the dehydrogenated states of the molecule, where the EA > 1 eV for $N_H < 8$ molecules (see Figure 3.4). Indeed if we were to adopt the IP and EA of the parent molecule coronene for all de-and-superhydrogenated derivatives, we would obtain that coronene stays neutral in the deepest regions of the cloud (e.g., the electron sticking coefficient is $s_e \sim 10^{-5}$ for an EA = 0.47 eV). The larger molecules on the other hand, are not affected by this, since the EA of the parent molecule is large enough to lead to electron attachment.

We have explored the distribution of hydrogenation states of our three species in a systematic manner over the astrophysical relevant G_0 - $n(H)$ parameter space (Figure 3.9). For these calculations we adopted a gas temperature of 500 K. The results show that coronene is mostly completely dehydrogenated. At a given density, for UV fields $G_0 \gtrsim 0.01 n(H)$, coronene quickly loses hydrogen and becomes fully dehydrogenated. We emphasize that at that point, carbon loss can become important—limiting the lifetime of the pure carbon cluster—but we have not taken that into account. For $G_0 \lesssim 0.05 n(H)$, we can find superhydrogenated coronene molecules contributing at a 10–15% level. However, the greatest contribution in these environments comes from partially dehydrogenated species, with very little contribution from the normally hydrogenated molecule $C_{24}H_{12}$ ($< 10\%$).

Unlike coronene, the larger species are far more difficult to dehydrogenate: for circumcoronene, full dehydrogenation requires G_0 in excess of $\sim 300 n(H)$ at $n(H) = 1 \text{ cm}^{-3}$, and above $5 n(H)$ at $n(H) = 10^3 \text{ cm}^{-3}$. On the other hand, our largest species circumcircumcoronene only dehydrogenates for the highest UV fields and lowest densities ($G_0 > 5 \times 10^4$ and $n(H) < 3 \text{ cm}^{-3}$). Normally hydrogenated species dominate below these limits until superhydrogenation sets in at $G_0 \sim 0.005 n(H)$. For smaller G_0 values, these large PAHs are superhydrogenated. We note that these transitions from fully dehydrogenated to normally hydrogenated, and from normally hydrogenated to superhydrogenated are very sharp (cf. Tielens 2005). From this we take that any PAH is very sensitive to small variations in the hydrogenation parameter over a particular range, specific to that molecule, and for circumcoronene that partly overlaps with the $G_0/n(H)$ range in the NW PDR of NGC 7023 (e.g., the abundance of partially dehydrogenated derivatives of $C_{54}H_{18}$ reaches a value of 20% at $A_V = 1.8$ where $G_0/n(H) = 0.95$ and $G_0 \sim 660$; at $A_V = 2.2$, $G_0/n(H) = 1.35$ and $G_0 \sim 410$, and their contribution decreases to $\sim 10\%$). Inspection of the distribution of $C_{54}H_{18}$ in Figure 3.9 shows that slightly higher $G_0/n(H)$ ratios in this G_0 - $n(H)$ range would have led to complete dehydrogenation of circumcoronene. Given the non-linearity of the multiphoton dissociation processes for $C_{54}H_{18}$, the transition from the normally hydrogenated molecule to the carbon cluster C_{54} does not occur at a constant $G_0/n(H)$ ratio for different G_0 - $n(H)$ values, and thus we do not see more dehydrogenation at $A_V = 2.4$, where $G_0/n(H) \sim 1.43$ and $G_0 \sim 325$.

3.4.2. H₂ Formation

We have included 3 possible dehydrogenation pathways for the PAHs in our study: direct loss of an H atom or an H₂ molecule after photon absorption, and H₂ abstraction described as an Eley-Rideal process from superhydrogenated molecules only. Thus, in our model, H₂ can be formed from the direct loss of 2 duo H-atoms as an H₂ molecule after photon absorption, or from H₂ abstraction after superhydrogenation of the normally hydrogenated molecule.

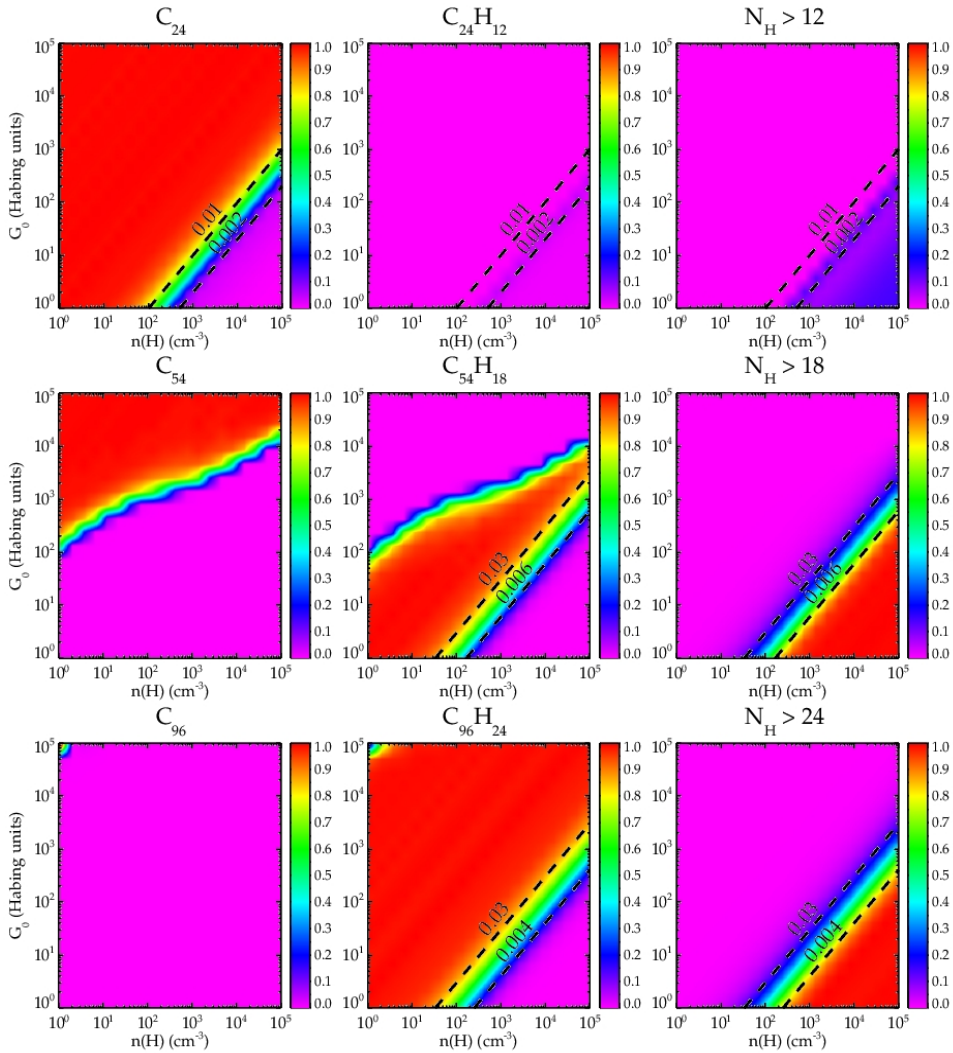


Figure 3.9: Fractional contribution from coronene (*top panels*), circumcoronene (*middle panels*) and circumcircumcoronene (*bottom panels*) derivatives for different G_0 and $n(H)$ values. The contributions include all ionization states. The *left column* shows the contribution from the completely dehydrogenated molecules, C_{24} , C_{54} and C_{96} ; the *middle column* shows the fraction of the normally hydrogenated molecules; and the *right column* shows the distribution of the superhydrogenated species. In all cases, we have assumed a fraction of molecular hydrogen of 0.5, and a carbon abundance of 3.5×10^{-4} relative to hydrogen. Black lines represent constant $G_0/n(H)$ ratios and are given as a reference.

According to our results, direct H-loss is the dominant photodissociation channel for all the molecules in our work. In the case of coronene, complete dehydrogenation is very effective at the surface of the cloud. Direct H_2 -loss rates at $A_V = 0$ are two orders of magnitude lower than the direct H-loss rates for this molecule. For the larger PAHs the trend is similar. While direct H-loss is also dominant over H_2 -loss for circumcoronene and circumcircumcoronene, at some point deep into the cloud ($A_V > 4.5$, $G_0 < 10$) the two rates

become comparable. Inspection of Figure 3.6 shows that H₂-loss can dominate over H-loss in highly shielded environments where $G_0 < 10$. However in such UV-attenuated regions increasing hydrogen densities would tend to superhydrogenate these PAHs, and these, if they were to fragment in any way, would preferentially lose an H atom and not an H₂ molecule.

Regarding H₂ abstraction by H from superhydrogenated PAHs, we find this mechanism not particularly relevant for the conditions in the NW PDR of NGC 7023. Since the formation of H₂ through Eley-Rideal abstraction depends on the gas temperature being sufficient to overcome the addition and abstraction barriers, this mechanism is expected to be important at the surface of the PDR, where also the reservoir of atomic hydrogen is large enough to carry out the addition and abstraction processes. For the smallest molecule in our sample, we obtain that coronene can never reach superhydrogenated states at low A_V values, and hence cannot form H₂ through this mechanism. Boschman et al. (2015) considered H₂ abstraction by H for a wide range of hydrogenation states of coronene ($0 \leq N_H \leq 36$), and also found that this is not a dominant process because this PAH is rapidly stripped off of all its hydrogens.

Since large PAHs are expected to be more stable against dehydrogenation, and also more prone towards superhydrogenation than the smaller species, they are expected to be good candidates for the H₂ formation through Eley-Rideal H₂ abstraction in PDRs. While we do recognize the great stability of large PAHs against dehydrogenation, our results for circumcoronene and circumcircumcoronene show that by the time these molecules are indeed superhydrogenated, it is already at such high extinction values ($A_V > 4.5$), that the gas temperature is too low to lead to high abstraction rates on PAHs.

We have calculated the efficiencies of H₂ formation from PAHs through direct H₂-loss (i.e., photodissociation of PAHs) and H₂ abstraction by H (from superhydrogenated species). The efficiencies, ξ_{H_2} , for a PAH of a given size (i.e., number of C atoms) and ionization state Z , have been defined as the number of H atoms that collide with the PAH molecules, that are converted to H₂:

$$\xi_{H_2}(Z) = \sum_i \frac{2k_{H_2}(Z, i) f(Z, i)}{k_{col}} \quad , \quad (3.11)$$

where the sum is over all hydrogenation states, and k_{col} is a fiducial collision rate of H-atoms with the PAH species, whose expression depends on the PAH charge state under consideration (see Appendix 3.D). In the case of direct H₂-loss, k_{H_2} corresponds to the H₂ photodissociation rate of species with i number of H atoms in a given charge state; and $f(Z, i)$ corresponds to the fraction of PAHs in charge state Z that release H₂ through photodissociation, i.e., normal-to-partially dehydrogenated species with an even number of H atoms greater than the number of solo H atoms. For its part, in the case of H₂ abstraction, k_{H_2} corresponds to the H₂ abstraction rates, k_{er} , in units of 1/s (equation 3.10); and $f(Z, i)$ corresponds to the fraction of PAHs in the respective charge state that go through H₂ abstraction, i.e., superhydrogenated PAHs with i number of H atoms.

Figure 3.10 shows the efficiencies for the 3 PAHs in different environments. The left panel shows the efficiencies of H₂ abstraction from the anion and neutral circumcoronene and circumcircumcoronene molecules. We have plotted these ionization states, since they are the ionization states of superhydrogenated species, whenever they are abundant. The

efficiencies have been calculated for $T_{gas} = 50$ K and 500 K for $G_0/n(H)$ ratios over which superhydrogenated species are present, going from a $\sim 10\%$ abundance at $G_0/n(H) = 0.03$ to a $\sim 100\%$ abundance at $G_0/n(H) = 10^{-4}$ for both, circumcoronene and circumcircumcoronene species. In this same range, the charge state of the population goes from $Z = 0$ and $Z = -1$ states in a 1:3 ratio, to being $Z = -1$ dominated. The resulting efficiencies increase towards lower $G_0/n(H)$ ratios, reaching a plateau once the distribution of species in a given charge state is completely dominated by the PAHs with the largest amount of extra H atoms considered ($f(Z, N_H^0 + 4) \sim 1$). Overall, H_2 formation efficiencies of anions are greater than those of neutral molecules. However, efficiencies are below 1%. The values derived for anionic species are rather independent of PAH size, but depend on temperature given the fiducial collision rate we adopted. On the other hand, the efficiencies derived for neutral PAHs depend on the geometrical cross section of each PAH. At low $G_0/n(H)$ ratios, the efficiencies are independent of the gas temperature. For larger $G_0/n(H)$ ratios, the apparent mild temperature dependence is due to $< 5\%$ differences in the derived fractions of superhydrogenated species within each charge state. In the particular case of NGC 7023, at $A_V \sim 4.8$ the gas temperature is about 50 K and $G_0/n(H) \sim 0.03$. Superhydrogenated circumcoronene and circumcircumcoronene species contribute at a 10% level, anions dominate, and the efficiency of H_2 abstraction is very low (below 1%).

The efficiencies for the direct H_2 -loss from photodissociation have been plotted for neutral coronene at $G_0 = 10$, and $Z > 0$ circumcoronene species at $G_0 = 10^3$. These are the relevant charge states for these molecules in the $G_0/n(H)$ ratios considered. Neutral coronene derivatives contribute in 70–78% to the total abundance of coronene species at $G_0/n(H) = 10^{-4}$ – 10^{-2} , range over which the contribution from normal-to-partially dehydrogenated species goes from 26% to 4%. For $G_0/n(H) > 10^{-2}$ coronene is only found as C_{24} . As for circumcoronene species, $Z = 1$ molecules dominate the distribution at $G_0/n(H)$

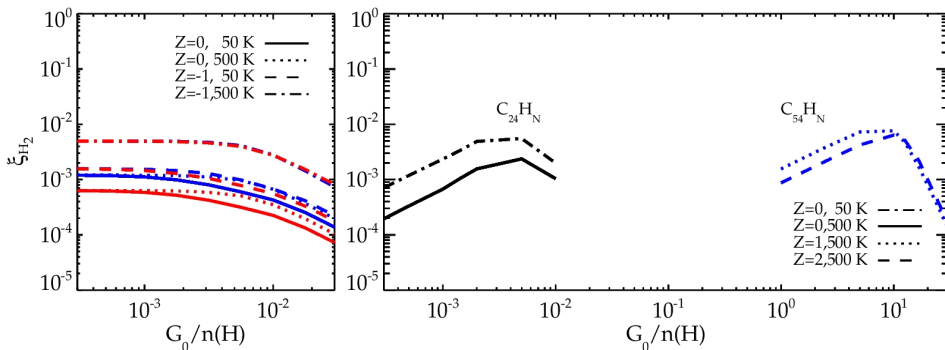


Figure 3.10: Efficiencies of H_2 formation from PAHs. The *left panel* shows the efficiencies of H_2 formation through Eley-Rideal abstraction from superhydrogenated species as a function of $G_0/n(H)$. Estimates for circumcoronene and circumcircumcoronene superhydrogenated species are shown in blue and red, respectively. The efficiencies have been derived for neutrals and anions, since these are the charge states at which superhydrogenated species can be found according to our model. Two gas temperatures have been assumed as a reference. The *right panel* shows the efficiencies of H_2 formation from photodissociation of PAHs. The efficiencies have been derived for neutral coronene at $G_0 = 10$, and $Z > 0$ circumcoronene at $G_0 = 10^3$. We have considered different G_0 values due to the different dehydrogenation behaviour of the species in the G_0 - $n(H)$ parameter space (see Figure 3.9). As it can be derived from the Figure, efficiencies stay below 1% for both mechanisms.

values between 1 and 10, and dications start dominating at $G_0/n(H) > 10$. We have plotted the efficiencies in the $G_0/n(H)$ range over which the relevant hydrogenation states for H₂-loss are present (i.e., normal-to-partially dehydrogenated states with an even number of H atoms above 8). Their contributions go from 51% cations and 14% dications at $G_0/n(H) = 1$, to < 1% at $G_0/n(H)$ greater than 25. At higher $G_0/n(H)$ ratios circumcoronene is found as C₅₄ (Figure 3.9). At $G_0/n(H) < 1$ circumcoronene can be found mainly in its normal hydrogenated neutral state, down to the regime where superhydrogenated species start becoming abundant ($G_0/n(H) < 0.01$). The efficiencies for H₂-loss in these environments are below 10⁻⁴. From the Figure we see that efficiencies of direct H₂-loss are at a similar level as the efficiencies of H₂ abstraction (below 1%). Since the dehydrogenation behaviour is highly PAH size dependent (see left and middle columns of Figure 3.9), different PAHs can be equally efficient in different environments. This depends on where in the $G_0-n(H)$ space, each PAH can be found in the relevant dehydrogenated states for H₂-loss. In the case of NGC 7023, circumcoronene is already found in its normal hydrogenated state, while coronene is completely dehydrogenated. PAHs smaller than N_C = 54 but larger than N_C = 24 could reach efficiencies of 1% at the surface of the NW PDR of NGC 7023.

3.4.3. Spectral Variations

We calculated the emission spectra of C₂₄H₁₂, C₅₄H₁₈ and C₉₆H₂₄ derivatives at different points inside the NW PDR of NGC 7023 from $A_V = 0-2$, considering the distribution of species presented in §4.1 (see Appendix 3.F). The emission spectrum at $A_V = 0-2$ is essentially determined by the dominant ionization state of the PAHs at each point inside the cloud. This is due to the lack of strong variations in the hydrogenation states of the species in our work. In the case of coronene, this molecule is completely dehydrogenated, and only changes in ionization state, being mostly neutral with cationic species varying their abundance from 27% at the surface of the cloud, to 2% at an $A_V = 2$. Recall that we do not consider destruction of the carbon skeleton which may be important for highly dehydrogenated species. The main features we see in the emission spectra of coronene derivatives are the appearance of a complex of bands at around 5 μm (4.95 and 5.12 μm), related to stretching modes of the triple bonds in dehydrogenated species; the strong band at 6.71 μm due to stretching modes of the carbon skeleton; and the bands at 10.13, 10.35 and 20.4 μm due to complex deformation modes of the carbon structure. Among these, the bands at 5.12 and 10.35 μm , although weak, increase in intensity with respect to the 4.95, 6.71, 10.13 and 20.4 μm bands towards more highly ionized environments.

As stated before, circumcoronene *does* present levels of dehydrogenation that vary following the change in the $G_0/n(H)$ ratio. We do not have the intrinsic spectra for most of the partially dehydrogenated species. However, between $A_V = 0$ and 2, partially dehydrogenated species are present only at low A_V ($A_V \sim 0$) where $\sim 34\%$ of the emitting species are partially dehydrogenated. These species correspond to the first partially dehydrogenated molecules (e.g., N_H = 17–12), and so we expect their emission to be similar as that of the parent molecule. Inspection of the emission spectra from circumcoronene derivatives reflect then mainly the change in the ionization state of C₅₄H₁₈. This is apparent from the decrease with A_V in the strength of the 6–9 μm stretching modes relative to the 11–15 μm CH out-of-plane bending modes (Langhoff 1996; Allamandola et al. 1999; Peeters et al. 2002). The signature of positively ionized species is also apparent in the broadening of the 11.25 μm band, which is in fact due to the appearance of the 11.05 μm feature related to CH out-of-plane bending modes in ionized PAHs (Rosenberg et al. 2011; Boersma et al. 2013).

In the case of circumcircumcoronene, as for circumcoronene, the spectrum is also dominated by the changes in the ionization state of the parent molecule. Hence we see the same signatures of ionization as we see for $C_{54}H_{18}$. At the surface of the cloud, circumcircumcoronene molecules are mostly highly positively ionized ($\sim 74\%$). Close to where the HI to H_2 transition occurs, the ratio between neutrals and positively ionized species is close to 1.0. At an $A_V = 1.6$ neutrals still dominate the population with a 73% abundance, while the contribution from anions has increased to 8%, and positively ionized species contribute 19% to the total abundance. At an $A_V = 2$, neutral molecules contribute in 75%, while anions contribute in 15%. We see that this increase in the abundance of anions (and decrease in the abundance of cations) does not have a discernible impact in the emission spectrum.

A comparison between $C_{54}H_{18}$ and $C_{96}H_{24}$ derivatives spectra shows that the 3.28/3.3 and 3.28/11.3 peak intensity ratios are larger for the intermediate size molecule than for circumcircumcoronene (3.28/3.30 = 3.58 and 3.28/11.3 = 0.43 for $C_{54}H_{18}$, against 1.92 and 0.14 respectively for $C_{96}H_{24}$). Both ratios remain relatively constant, which shows that they are not sensitive to the ionization state of the molecules under these conditions. Instead, they do vary with PAH size (Bauschlicher et al. 2008; Ricca et al. 2012; Croiset et al. 2016).

Up to now, we have focused on the behaviour of the PAH bands with depth into the NW PDR of NGC 7023, where physical conditions vary enough to see spectral changes due to ionization but not due to changes in the hydrogenation state of the PAHs. In order to explore the spectral signatures of large variations in the hydrogenation state of our PAHs we have calculated the emission spectra for different $G_0/n(H)$ ratios at $G_0 = 10^3$. These spectra can be found in the Appendix 3.F. Visual inspection of the spectra of coronene species shows that over much of the parameter space, the spectrum of the fully dehydrogenated molecule dominates, and the spectral changes represent the variation in its ionization state (the abundance of $Z > 0$ species varies from 98% at $G_0/n(H) = 100$ to 4.5% at $G_0/n(H) = 0.1$). For $G_0/n(H) \leq 0.01$ partially dehydrogenated derivatives become more relevant. These are mostly anionic and neutral species for which we do not have the IR spectra. The parent molecule is never important (even at a $G_0/n(H) = 0.001$ $C_{24}H_{12}$ contributes at a 1% level only), nor the superhydrogenated species (which barely appear at $G_0/n(H) = 0.001$ contributing at a 5% level).

The spectra of the larger species show instead the clear footprints of hydrogenation. As seen in Figure 3.9, circumcoronene completely dehydrogenates for $G_0/n(H) \gtrsim 100$ at $G_0 = 10^3$. The dominant species at $G_0/n(H) = 100$ is then C_{54}^{+2} in 83% for which we do not have the IR spectrum, but whose emission is expected to be similar to that of C_{54}^+ , except for an even stronger $5\mu\text{m}$ band, as typical from carbon cluster cations. Going to lower $G_0/n(H)$ values we see circumcoronene mostly in its normally hydrogenated state $C_{54}H_{18}$, and thus what we observe are essentially the changes in ionization state, being mostly neutral with an increasing abundance of the anionic molecule (from 7% to 18.5%). This is reflected in the increasing 6.4/11.3 ratio and the red-shift of the bands, intrinsic to anionic species. The contribution from superhydrogenated species in this $G_0/n(H)$ range goes from ~ 3 to 35%, which is clear from the inspection of the $3\mu\text{m}$ region.

Regarding our largest species, circumcircumcoronene stays normally hydrogenated throughout most of the $G_0/n(H)$ space. Therefore down to a $G_0/n(H) = 0.1$ we are basically following the variation in the ionization state of $C_{96}H_{24}$, from being mostly tricationic to

neutral. Going from $G_0/n(H) = 0.1$ to 0.01 the abundance of superhydrogenated species increases to a 19%, which is only clear in the $3\mu\text{m}$ spectral region, although the signal is rather weak. Only at $G_0/n(H) \leq 0.001$ superhydrogenated $Z = -1$ and $Z = 0$ species become the dominant species. Their signal would be noticeable only in the $3\mu\text{m}$ region, since the spectrum of the parent molecule looks fairly similar to that of the first few superhydrogenated derivatives.

The $3\mu\text{m}$ region is particularly sensitive to the superhydrogenation level of PAHs (Bernstein et al. 1996; Sandford et al. 2013). The $3.3\mu\text{m}$ aromatic CH stretch shows the two components expected for the *coronene family*: $3.28\mu\text{m}$ band due to duo hydrogens, and $3.3\mu\text{m}$ band for the solo hydrogens (Ricca et al. 2012). Even though the differences between the spectrum of the parent molecule and those of superhydrogenated derivatives become far more clear with higher degrees of superhydrogenation, the main differences start to show up in the $3\mu\text{m}$ region. With superhydrogenation, new bands appear at longer wavelengths. Zooming in into the $3\mu\text{m}$ region of the intrinsic spectra of superhydrogenated species (see spectra in Appendix 3.F), we can distinguish three main bands at 3.3, 3.41 and $\sim 3.5\mu\text{m}$ (and weaker bands at 3.57 and $3.67\mu\text{m}$). The $3.5\mu\text{m}$ band appears already for a mono superhydrogenated PAH. This band is related to the stretching of each CH_2 complex. The band at $3.4\mu\text{m}$ instead requires two additional H atoms on the ring. This band is related to the stretching modes of the pair of CH_2 groups within the same (duo) ring. Therefore the $3.4\mu\text{m}$ band only appears for hydrogenation states $N_{\text{H}} > N_{\text{H}}^0 + 1$. In fact this pattern is not only seen in the theoretical spectra of these PAHs, but also in that of pyrene, $\text{C}_{16}\text{H}_{10}$, and naphthalene, C_{10}H_8 , derivatives (for which the spectra are provided by the PAHdb). For this last one, there are experimental (argon matrix) spectra of the first superhydrogenated state of the molecule, where they report bands at 3.24 and $3.51\mu\text{m}$, but none at $3.4\mu\text{m}$ (Ricks et al. 2009). Instead both the experimental and theoretical spectrum of $\text{C}_{10}\text{H}_{10}$ (and further superhydrogenated states) *do* show a $3.4\mu\text{m}$ band (Bernstein et al. 1996). Thus the appearance of the $3.4\mu\text{m}$ band appears to be common to PAHs with at least 2 extra H atoms. Once all H-sites on the PAH become superhydrogenated, the $3.3\mu\text{m}$ aromatic CH stretch disappears. We also, stress that the $G_0/n(H)$ value at which these superhydrogenated signatures appear depends on the size of the PAH (c.f., Figure 3.9). Specifically, the superhydrogenated species appear at $G_0/n(H) \lesssim 0.01$ for both circumcoronene and circumcircumcoronene, but their spectral signature would be discernible in the $3\mu\text{m}$ region at $G_0/n(H)$ ten times lower, where superhydrogenated species contribute in more than 30% to the emission.

3.5. Discussion

We found that small PAHs behave quite differently from intermediate and large species. Small PAHs are easily destroyed in most environments; can rarely be found in their normally hydrogenated state; and only for extremely shielded regions (low $G_0/n(H)$ ratios) they can be found in superhydrogenated states. The difference in the abundance distribution between intermediate and large PAHs is related to their dehydrogenation behaviour rather than their superhydrogenation behaviour. The larger the PAH, the more likely it can be found in its normal hydrogenated state. Regarding superhydrogenation of PAHs, intermediate and large PAHs can hardly superhydrogenate in the more diffuse parts of PDRs. These species will lose their extra H atoms very easily, and only in highly shielded environments will reactions with H atoms keep the molecules superhydrogenated. These molecules when dominating the abundance distribution of a given species will be mostly in

$Z = 0$ and $Z = -1$ charge states. Therefore their spectral signature —if observable— would not only be straightforward from the appearance of more bands in the $3\mu\text{m}$ region, but it would also be discernible from a red-shift of the bands (intrinsic to anionic species).

In the particular case of the NW PDR of NGC7023, we find that small PAHs like coronene will remain completely dehydrogenated throughout most of the cloud. Intermediate and large PAH molecules will remain, mainly, normally hydrogenated but highly positively ionized at the surface of the PDR, where the bulk of the PAH emission is observed. Superhydrogenation is only achieved for the larger species in the more shielded regions of the cloud. Recall we have considered a maximum of 4 additional H atoms as the maximum superhydrogenated state of a PAH. Test runs showed PAHs do not superhydrogenate further in the case of the NW PDR of NGC7023. Higher superhydrogenation levels can be achieved in more shielded environments; e.g., considering higher hydrogenated states than $N_{\text{H}}^0 + 4$, circumcoronene derivatives with $N_{\text{H}} > 22$ start appearing at $G_0/n(H)$ below 0.01 at $G_0 = 1000$, increasing their abundance gradually towards more shielded environments, becoming a 50% of the emitting population at $G_0/n(H) \sim 0.002$. Such abundance of highly superhydrogenated molecules would leave a clear footprint in the emission spectra. However, nor the molecular properties nor the energetics involved in the H-addition/H₂-abstraction processes have been studied for such superhydrogenated molecules.

From the observations of the NW PDR of NGC7023 we do see strong emission from the CH modes, and thus, we expect most PAHs to be hydrogenated at some level. Small PAHs like coronene —if present— must contribute at a negligible level to the general population of PAHs in the PDR. Coronene in the NGC7023 NW PDR environment is the epitome of a fully dehydrogenated species. Its spectrum shows the telltale sign of graphene-like flakes with features in the 5 and $10\mu\text{m}$ region. Weak features at 5.25 and $5.75\mu\text{m}$ are routinely detected in sources whose spectra are dominated by the IR emission features (Roche et al. 1996; Boersma et al. 2009). These have been ascribed to weak overtones and combination bands involving the CH in-plane and out-of-plane stretching modes (Boersma et al. 2009; Mackie et al. 2015). As our study illustrates, graphene-like flakes show bands around 4.95, 5.12, and $5.35\mu\text{m}$ due to stretching modes in triple bonds (Bauschlicher & Ricca 2013). Bands are also observed at 10 and $20\mu\text{m}$ due to in-plane stretches of the inner and outer edge C atoms respectively, moving to and outwards the center of the molecule. Hydrogenated PAHs do not show strong bands in the $10\mu\text{m}$ region, but can show bands in the $20\mu\text{m}$ region (Bauschlicher & Ricca 2013).

Besides the caveat mentioned before that small graphene-like flakes are prone to loss of carbon, we should also mention that isomerization of completely dehydrogenated PAHs towards cages or rings may also be important (Berné & Tielens 2012; Zhen et al. 2014a). This is another aspect of the evolution of PAHs in space that was not included in our modelling efforts, as kinetic data on the processes involved are lacking. Further laboratory studies are required to establish the photolysis routes of such species and to assess the origin of the 5, 10, and $20\mu\text{m}$ bands in the interstellar spectra.

It is of interest to compare our model results with observations of PAH band ratios. Combining Spitzer and SOFIA observations, Croiset et al. (2016) derived 3.3/11.3 ratios in NGC7023. This ratio is expected to serve as a proxy for PAH size. Figure 3.11 shows the 3.3/11.3 ratios we obtain from our model for circumcoronene and circumcircumcoronene derivatives in the NW PDR of NGC7023. The 3.3/11.3 ratio varies slightly in our spectra

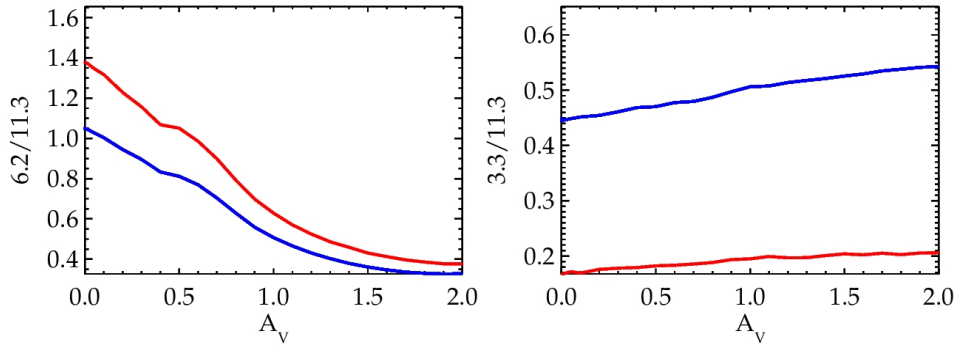


Figure 3.11: PAH band ratios in the NW PDR of NGC 7023. The 6.2/11.3 ratio is usually used as a proxy for the ionization level of the PAH population, while the 3.3/11.3 ratio is expected to trace PAH size. Here we have plotted them for circumcoronene in blue, and circumcircumcoronene in red. The spectra for $C_{96}H_{24}$ derivatives are complete in this A_V range. The spectra for $C_{54}H_{18}$ species are missing only the small contributions from partially dehydrogenated species (read text). Observational studies have derived typical 3.3/11.3 ratios of 0.5 to 0.3 from the surface to the PDR up to distances of about 52 arcsec from the star. As seen in the Figure, intermediate size PAHs could potentially reproduce these values. However, the ionization ratio 6.2/11.3 would then be highly underestimated compared to the observations that predict a value of 2 at the surface of the PDR, decreasing in about 14% to a distance of ~ 55 arcsec from the star.

due to the changes in the ionization state of the molecules. Croiset et al. (2016) report values of 0.5 to 0.3 when going from the surface of the PDR to 52 arcsec away from the star. According to our estimates, PAHs of intermediate size can reproduce such values. We do point out though, that the 3.3/11.3 is a good tracer of PAH size as long as a given ionization state dominates the distribution, e.g., at $G_0/n(H) \sim 30$ the 3.3/11.3 decreases for $C_{96}H_{24}$ species because of the dominant abundance of trications that have a lower 3.3/11.3 ratio. Therefore, beside PAH size, the observed variation in the 3.3/11.3 ratio in the NGC 7023 PDR (Croiset et al. 2016) may also be affected by charge variations.

Figure 3.11 also shows the variation of the 6.2/11.3 ratio in the PDR. We see the 6.2/11.3 ratio decreasing as the dominant ionization state of the PAHs changes from $Z > 0$ dominated to neutral dominated (recall that for both species the spectral variations are essentially tracing the variation in the ionization state of the molecules). From IRS Spitzer observations, Boersma et al. (2014) derived 6.2/11.3 ratios in the range between 1.7 and 2.0, and 7.7/11.3 ratios between 5 and 7. Fleming et al. (2010) also using IRS data reports an average value for the 7.7/11.3 of 6.06 ± 1.74 , with the ratio varying only by 14% from a distance of ~ 40 to 55 arcsec from the star. Our calculated values are lower than the observed ones. Also, our 6.2/11.3 (and 7.7/11.3) band ratios vary by more than 50% from $A_V = 0$ to $A_V = 2$. Assuming $G_0 = 10^3$, we can obtain ratios close to the observed ones ($I_{6.2/11.3} \sim 2$, and $I_{7.7/11.3} \sim 6$) at $G_0/n(H)$ of 1–10, instead of the $G_0/n(H) \sim 0.3$ that we get at $A_V = 0$. In other words, if the density at the surface of the cloud were overestimated by a factor of 10, we could reproduce the observed 6.2/11.3 and 7.7/11.3 ratios with intermediate-to-large PAHs.

3.5.1. Implications on the Origin of the 3.4 μm Feature

Observations of Orion and NGC7023 have both revealed bands at 3.3, 3.4, 3.47, 3.51 and 3.56 μm (Joblin et al. 1996; Pilleri et al. 2015). The origin of these bands has been intensely discussed within the PAH hypothesis. The bands at 3.3 μm have been widely accepted to be due to aromatic CH stretching modes common to the PAH family. The origin of the weaker bands (mainly the 3.4 μm feature) on the other hand, still remains unknown. There are three main candidates for these carriers: 1) the bands may be hot bands of the 3.3 μm CH stretching mode (Barker et al. 1987); 2) the bands may be CH stretching modes of aliphatic side groups attached to the periphery of PAHs, such as methyl groups for example (Duley & Williams 1981; Joblin et al. 1996); and/or 3) the bands may come from superhydrogenated PAHs, where the addition of extra H-atoms disrupts the aromaticity of the molecule creating more bands in the region (Bernstein et al. 1996; Sandford et al. 2013).

In § 3.4.3 (see also Appendix 3.F) we established that, even though the spectrum of the parent molecule looks similar to those of the first 2 superhydrogenated states, the main differences reside in the 3.4 μm band that appears for hydrogenation states greater than ($N_{\text{H}}^0 + 1$). This band is related to stretching modes of the pair of extra H atoms in the same ring. Indeed, the emission spectra from circumcoronene and circumcircumcoronene superhydrogenated species where the extra H atoms are added to only solo positions do not show a 3.4 μm band. The 3.5 μm feature instead seems to be common to the spectra of all superhydrogenated molecules. This band is related to the stretching of each individual CH_2 complex. Note that here we consider superhydrogenated states of up to 4 additional H-atoms. At these superhydrogenation levels, the 3.4 μm band is only observed if the extra H atoms are in duo rings. For higher superhydrogenation states both, the 3.4 and 3.5 μm bands, would also show up for this PAH family, since solo and duo rings would have extra H atoms. However such levels of superhydrogenation are achieved in extremely shielded environments, where the emission from PAHs would come from high density clumps exposed to UV radiation.

From AKARI observations of the NW PDR of NGC7023, aside the main band observed at 3.3 μm there is a secondary band at 3.4 μm , together with what has been defined as a plateau component at 3.45 μm (Pilleri et al. 2015). The 3.4 μm band appears to become less intense as the plateau widens towards more diffuse environments. Our results indicate that intermediate-to-large PAHs can survive in their normally hydrogenated state in regions where $G_0/n(H) = 10\text{--}100$, as it is expected in the more diffuse media of NGC7023 (Berné & Tielens 2012). It is under these conditions that the 3.3 μm is still evident and the 3.4 μm band starts disappearing immersed in the broadening of the 3.45 μm plateau. However these PAHs would not achieve superhydrogenation. Moreover, from what we have seen, the superhydrogenation pattern of PAHs is very similar for circumcoronene and circumcircumcoronene. Thus, unless the parameters in our model are considerably changed, we would not expect $N_{\text{H}} > (N_{\text{H}}^0 + 1)$ species at these $G_0/n(H)$ ratios.

Pilleri et al. (2015) also report 3.4/3.3 band ratios that go from 0.028 to 0.13 from their P1 to P4 positions, where G_0 is expected to vary from 7000 to 150 going from the cavity into the NW PDR. If the 3.4 μm band is solely due to superhydrogenated species with extra H atoms in duo rings, such values could be obtained at $G_0/n(H)$ ratios 2–3 orders of magnitude lower than what we expect in NGC7023 (Figure 3.12). PAHs smaller than $\text{C}_{54}\text{H}_{18}$ could potentially show these ratios at higher $G_0/n(H)$ of few times 10^{-2} at most. Nevertheless as we saw in the case of coronene, these species would probably be completely

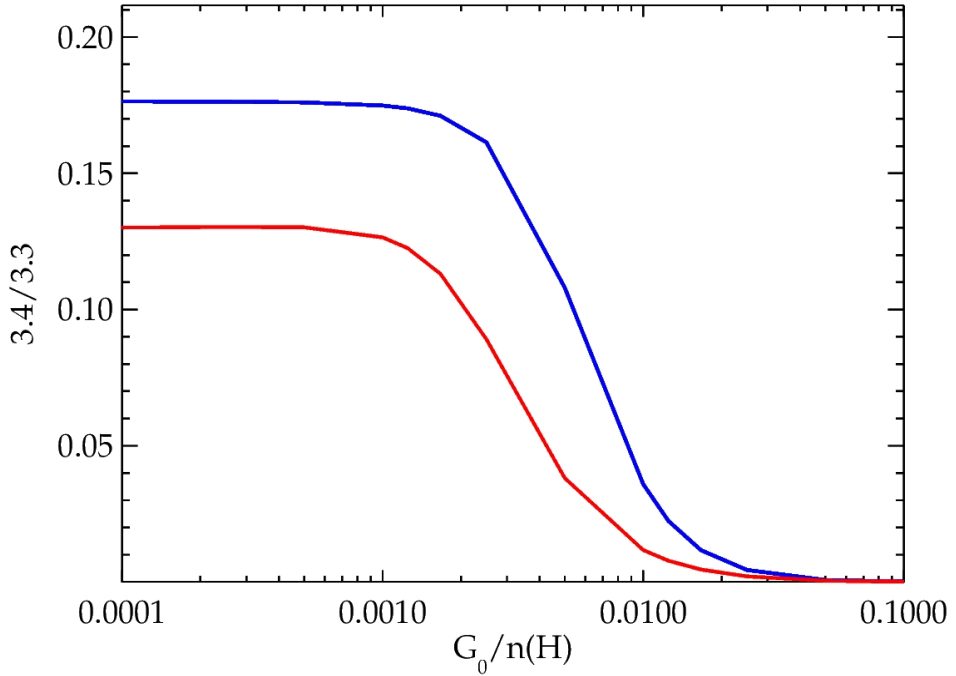


Figure 3.12: Hydrogenation ratio for different $G_0/n(H)$ values. The ratios derived from circumcoronene derivatives are shown in blue, while those from circumcircumcoronene derivatives are shown in red. We have assumed a gas temperature of 50 K, and that the fraction of atomic hydrogen is 10% that of molecular hydrogen, in order to model more shielded environments. The 3.4/3.3 ratio traces the superhydrogenation level of the PAHs as the 3.4 μm band is related to the stretching modes of the pair of CH_2 complexes within the same ring (which are duo rings for the *coronene family*). Observed 3.4/3.3 ratios in NGC7023 range between 0.028 and 0.13, starting from the cavity and going into the NW PDR region, where G_0 is expected to vary from 7 000–150 (Pilleri et al. 2015). We see that these ratios can be achieved with superhydrogenated species but for $G_0/n(H)$ ratios of 0.002–0.006, which is lower than what is expected in the NW PDR of NGC7023.

dehydrogenated, and thus the 3.4 μm band would not be observed. Unless we are underestimating the density in the NW PDR of NGC7023 by a factor of 100, superhydrogenated species cannot explain the observed 3.4/3.3 ratios.

Unfortunately, other signatures of superhydrogenated species are not as clear as the appearance of bands in the 3 μm region. Such species would also show aliphatic CH deformation modes at 6.85 and 7.25 μm . However these modes are intrinsically very weak and would be completely overpowered by the CC modes in PAH cations. Thus, we find that the main noticeable features of superhydrogenation are the 3 μm bands. Longer wavelength features cannot be clearly distinguished from the ones of the parent molecules.

3.5.2. H₂ Formation

As mentioned in § 3.4.2 we have considered two possible ways for PAHs to form H₂ molecules in our model: either through H₂ abstraction by H, or from direct H₂-loss due to photon excitation. It is of some interest then to compare the rates of these processes with those commonly adopted for interstellar dust.

Commonly, H₂ is thought to form on dust grains from physisorbed H-atoms recombining through the Langmuir-Hinshelwood mechanism. The standard formulation of the H₂ formation rate on dust grains is then given by (Hollenbach & McKee 1979; Burke & Hollenbach 1983):

$$R_d(H_2) = \frac{1}{2} S(T, T_d) \eta \sigma_d v_{th} n(H) n_d, \quad (3.12)$$

$$R_d(H_2) \simeq 3 \times 10^{-17} n n(H) S(T, T_d) \eta \text{ cm}^{-3} \text{ s}^{-1},$$

where $S(T, T_d)$ corresponds to the sticking coefficient of H atoms at temperature T colliding with dust grains at temperature T_d ; η is the probability that an adsorbed H atom will meet another H atom on the surface of the grain, attach to it and be released in the form of H₂; v_{th} is the thermal velocity of the colliding H atoms; n is the total density; n_d is the number density of dust grains; and $\sigma_d n_d$ is the total cross section of dust grains. If we take $T = 500$ K and $T_d = 35$ K, the sticking coefficient is estimated to be $S \simeq 0.2$ and the H₂ formation efficiency, η , is close to unity (Hollenbach & McKee 1979; Burke & Hollenbach 1983), resulting in $R_d(H_2) \simeq 6 \times 10^{-18} \text{ cm}^3 \text{ s}^{-1}$. In contrast, experiments on perfect graphite or silicate surfaces measure very low efficiencies (Pirronello et al. 1997; Pirronello et al. 1999; Katz et al. 1999)—as H atoms quickly evaporate before they can recombine—and the inferred H₂ formation rate on such surfaces is negligibly small. The models underpinning the standard dust H₂ formation rate assume therefore the presence of so-called enhanced binding sites for physisorbed H, which allow formation at much higher dust temperatures (Hollenbach & Salpeter 1971; Hollenbach & McKee 1979). However, the presence of enhanced binding sites is not well established and their properties are not well known. Hence, this inferred rate should perhaps more properly be considered as an upper limit.

In our analysis, we can define —analogously— the H₂ formation rate through either direct H₂-loss (i.e., photodissociation of PAHs) or Eley-Rideal H₂ abstractions from PAHs of a given size and charge state Z as:

$$R_{PAH(Z)}(H_2) = \frac{1}{2} \xi_{H_2}(Z) k_{col} n_{PAH(Z)}, \quad (3.13)$$

where $\xi_{H_2}(Z)$ corresponds to our previously defined efficiencies (see § 3.4.2); k_{col} corresponds to the fiducial collision rate dependent on the charge state of the molecule (see Appendix 3.D); and $n_{PAH(Z)}$ corresponds to the number density of PAHs of a given size and charge state. From Figure 3.10 we conclude that the PAHs considered are not able to form H₂ efficiently at the surface of the NW PDR of NGC7023. However, considering a distribution of PAH sizes, there will always be some PAH (e.g., with $30 \lesssim N_C \lesssim 50$) that could be found in the relevant hydrogenation states for H₂-loss and, hence, could form H₂ at efficiencies of $\sim 1\%$ (assuming their molecular properties are similar to those of the *coronene family*). Assuming that 15% of the carbon is locked in PAHs (with a carbon abundance of 3.5×10^{-4} relative to that of hydrogen), and that all PAHs have ~ 40 C atoms, then the H₂ formation rate due to photodissociation would be a few times $10^{-19} \text{ cm}^3/\text{s}$. This is more

than an order of magnitude lower than the standard rate generally adopted for dust grains, and certainly much less than the enhanced rate derived by Habart et al. (2004) for PDRs.

Bron et al. (2014) recognized the issues facing H₂ formation on dust grains in PDRs, and developed a generic model describing H₂ formation through the Eley-Rideal mechanism on chemisorbed H-atoms, on a size distribution of dust grains spanning 5–3000 Å. This is implemented in the Meudon PDR Code and was employed by us to calculate the PDR structure, albeit that we excluded the PAH-sized species in the code (cf., Table 3.1).

First, we recognize that our calculated efficiencies of $\sim 1\%$ are quite comparable to those derived by Bron et al. (2014) ($\simeq 5 \times 10^3$; see their Figure 9) for conditions similar as those of NGC7023 ($n_H = 10^4 \text{ cm}^{-3}$, $G_0 = 1200$). This is however completely fortuitous. In their model H₂ formation is an Eley-Rideal process on chemisorbed H atoms while in our calculations, under these conditions, the Eley-Rideal mechanism is completely unimportant given the high UV radiation field ($\xi_{H_2} \sim \text{few times } 10^{-3}$). In contrast, in our model, H₂ formation is dominated by photolysis. There are some differences in the parameters adopted for the Eley-Rideal mechanism between our model calculations and those of Bron et al. (2014). The main difference is that they use an Eley-Rideal abstraction cross section that is a factor of 100 larger than the value measured for coronene films (Mennella et al. 2012) and adopted by us. Clearly, this cross section is a key factor regulating the ultimate efficiency of the H₂ formation of PAHs, and further experimental studies on free-floating PAHs will be very important to settle this issue.

Second, perusing the results of the Meudon PDR Code in more detail, the formation of H₂ at low A_V in the NW PDR of NGC7023 is due to Eley-Rideal abstractions from dust grains with sizes larger than $\simeq 20 \text{ \AA}$ (Bron et al. 2014). The calculated efficiencies for H₂ formation on dust grains are of $\xi_{H_2, dust} \simeq 0.4$ up to where the HI to H₂ transition occurs. This boils down to an H₂ formation rate about 5 times the standard value of $3 \times 10^{-17} \text{ cm}^3/\text{s}$. This is actually larger than what has been observationally inferred for a warm PDR such as NGC7023 (Habart et al. 2004), which suggests a rate equal to the standard value. Of course, if the abstraction rate for dust grains is a factor 100 lower as experiments on films imply (Mennella et al. 2012), then the Bron et al. (2014) is a gross overestimate. Again, our model predicts that superhydrogenated PAHs are absent at the surface of the NW PDR of NGC7023 and do not contribute to H₂ formation. They only appear deep inside the cloud at $A_V > 4.5$, where the conversion of atomic into molecular hydrogen is essentially complete.

We argue then that at the surfaces of PDRs, PAHs can contribute to the formation of H₂ by means of photodissociation only if PAHs of just the “right” size dominate the PAH population in these regions. Their contribution would be then at the 1–10% level of the standard H₂ formation rate assumed for dust grains. This assumption depends very much on the kinetic parameters that control the branching ratio of H versus H₂ photolysis channels (cf., Figures 3.5 and 3.6), and these have been derived from experiments on the small PAH, pyrene. Further experiments on astrophysically relevant PAHs will be important to make a firm conclusion, but given this caveat, we conclude that PAHs are not the cause of the high inferred H₂ formation rates in PDRs.

3.6. Conclusions

We have developed a kinetic model in order to study the abundance distribution, IR emission, and H_2 formation rate for 3 specific PAHs of different sizes in the NW PDR of NGC7023. The molecules correspond to the first 3 members of the coronene family with PAH sizes between 24 and 96 carbon atoms, which span the astrophysically relevant size range in the ISM. We have chosen to study these species at the molecular specific level, as many of their relevant molecular properties and fragmentation behaviour have been determined.

In order to model the physical conditions inside the cloud we made use of the Meudon PDR Code, and we gave this as input to our kinetic model. We considered the loss of an H atom or an H_2 molecule as multiphoton dissociation processes, and we worked under the premise that PAHs with extra H atoms can form H_2 through an Eley-Rideal abstraction mechanism. We then derived the abundances under the steady state assumption.

In agreement with earlier studies (Le Page et al. 2001; Le Page et al. 2003; Boschman et al. 2012; Montillaud et al. 2013), clear differences emerge in the distribution of species with PAH size. The smallest PAH in our sample, coronene, is found to be a very fragile molecule that is easily destroyed down to its carbon cluster form (assuming no isomerization) for a wide range of $G_0/n(H)$ ratios. Only in highly shielded environments ($G_0/n(H) < 0.01$), would a small fraction of this species be found with extra H atoms.

The larger species on the other hand are more stable against dehydrogenation. In fact, the larger the PAH the more likely it is to find it in its normally hydrogenated state (i.e., 1 H atom per C atom at its periphery). Our largest molecule, circumcircumcoronene, is mostly found in its normal hydrogenated state up to very large $G_0/n(H)$ ratios ($G_0/n(H) \sim 10^5$), while our intermediate size molecule, circumcoronene, starts losing H atoms at $G_0/n(H) \gtrsim 1\text{--}10$ depending on the intensity of the UV field. Regarding the presence of PAHs with extra H atoms, we find that only at $G_0/n(H) < 5 \times 10^{-3}$ intermediate-to-large PAHs with extra H atoms start dominating the abundance distribution, being in their neutral and anionic charge states.

Comparing our findings with observations of the emission in the NW PDR of NGC7023, we find that intermediate size PAHs must be dominating the abundance of the emitting population. Small PAHs like coronene —if present— contribute at a negligible level. Together with this, we agree with previous studies on the fact that the spectral variations observed throughout the PDR in the $5\text{--}20\ \mu\text{m}$ region are mainly related to variations in the ionization state of the PAHs. The footprint of hydrogenation is only discernible in the $3\ \mu\text{m}$ region through the specific appearance of bands at 3.4 and $3.5\ \mu\text{m}$. However this region could be affected by other effects such as anharmonicities or the presence of PAHs with methyl groups attached at their periphery. Based on the available AKARI observations of the NW PDR of NGC7023, we do not expect compact PAHs with extra H atoms to be responsible for the $3.4/3.3$ ratio observed in NGC7023, since superhydrogenated species are only present in more shielded environments where $G_0/n(H)$ is 2–3 orders of magnitude lower than what is derived from observations.

Finally, concerning the role of PAHs in the formation of H_2 in photodissociation regions, we find that PAHs can form H_2 through either Eley-Rideal abstraction of H_2 from superhydrogenated PAHs in highly shielded environments, or through photodissociation

under PDR-like conditions of “normal” or dehydrogenated PAHs. Our results show that, at the surface of PDRs, Eley-Rideal abstraction is never important. Our calculations are in good quantitative agreement with the model results by Bron et al. (2014) if the difference in abstraction cross section is accounted for. We find that photodissociation of PAHs can be a more important source of H₂ in PDR surfaces, but this cannot account for the inferred high rates of H₂ formation in PDRs, unless the kinetic parameters governing the branching ratio between H and H₂ channels for astrophysically relevant PAHs is very different from those measured for small PAHs in the laboratory.

Acknowledgements

Studies of interstellar PAHs at Leiden Observatory are supported through advanced ERC grant 246976 from the European Research Council, through a grant by the Dutch Science Agency, NWO, as part of the Dutch Astrochemistry Network, and through the Spinoza premie from the Dutch Science Agency, NWO. AC acknowledges NWO for a VENI grant (grant number 639.041.543). DFT calculations were performed with the Cartesius Supercomputer facility (grant SH-362-15).

Bibliography

- Aannestad, P. A., & Kenyon, S. J. 1979, *ApJ*, 230, 771
Abouelaziz, H., Gomet, J. C., Pasquerault, D., Rowe, B. R., & Mitchell, J. B. A. 1993, *J. Chem. Phys.*, 99, 237
Alecian, E., Catala, C., Wade, G. A., et al. 2008, *MNRAS*, 385, 391
Allain, T., Leach, S., & Sedlmayr, E. 1996, *A&A*, 305, 602
Allamandola, L. J., Tielens, A. G. G. M., & Barker, J. R. 1989, *ApJS*, 71, 733
Allamandola, L. J., Hudgins, D. M., & Sandford, S. A. 1999, *ApJ*, 511, L115
An, W., Shao, N., Bulusu, S., & Zeng, X. C., *J. Chem. Phys.* 128 (2008) 084301
Andrews, H., Boersma, C., Werner, M. W., et al. 2015, *ApJ*, 807, 99
Bakes E.L.O., Tielens A.G.G.M., Bauschlicher, Jr. C.W., 2001, *ApJ*, 556, 501
Bakes, E. L. O., & Tielens, A. G. G. M. 1994, *ApJ*, 427, 822
Barker, J. R., Allamandola, L. J., & Tielens, A. G. G. M. 1987, *ApJ*, 315, L61
Bauschlicher, C. W. 1998, *ApJ*, 509, L125
Bauschlicher, C. W., Peeters, E., Allamandola, L. J. 2008, *ApJ*, 678, 316
Bauschlicher, C. W., Boersma, C., Ricca, A., et al. 2010, *ApJS*, 189, 341
Bauschlicher, C. W., & Bakes, E. L. O. 2001, *Chem. Phys.*, 274, 11–14
Bauschlicher, C. W., & Ricca, A. 2013, *Chem. Phys. Lett.*, 566, 1
Bauschlicher, C. W., & Ricca, A. 2014, *Theo. Chem. Acc.*, 133, 1454
Becke, A. D. 1993, *J. Chem. Phys.*, 98, 5648
Bernard-Salas, J., Habart, E., Köhler, M., et al. 2015, *A&A*, 574, A97
Berné, O., Joblin, C., Deville, Y., et al. 2007, *A&A*, 469, 575
Berné, O. & Tielens, A. G. G. M. 2012, *Proc. of the National Academy of Science of the United States*, 109, 401
Berné, O., Montillaud, J., Joblin, C. 2015, *A&A*, 577, A133
Bernstein, M. P., Sandford, S. A., & Allamandola, L. J. 1996, *ApJ*, 472, L127
Betts, N. B., Stepanovic, M., Snow, T. P., & Bierbaum, V. M. 2006, *ApJ*, 651, L129
Beyer, T., & Swinehart, D. F. 1973, *Commun. Assoc. Comput. Machin.* 16, 379
Biennier, L., Alsayed-Ali, M., Foutel-Richard, A., et al. 2006, *Discuss. Faraday Soc.*, 133, 289
Boersma, C., Mattioli, A. L., Bauschlicher, C. W., et al. 2009, *ApJ*, 690, 1208
Boersma, C., Rubin, R. H., & Allamandola, L. J. 2012, *ApJ*, 753, 168
Boersma, C., Bregman, J. D., & Allamandola, L. J. 2013, *ApJ*, 769, 117
Boersma C. et al., 2014, *ApJS*, 211, 8
Boersma, C., Bregman, J., & Allamandola, L. J. 2015, *ApJ*, 806, 121
Boschman, L., Reitsma, G., Cazaux, S., Schlathölter, T., Hoekstra, R., Spaans, M., & González-Magaña, O. 2012, *Astrophys. J. Lett.*, 761, L33

- Boschman, L., Cazaux, S., Spaans, M., Hoekstra, R., Schlathölder, T. 2015, A&A, 579, A72
- Bregman, J. D., Allamandola, L. J., Witteborn, F. C., Tielens, A. G. G. M., & Geballe, T. R. 1989, ApJ, 344, 791
- Bron, E., Le Bourlot, J., & Le Petit, F. 2014, A&A, 569, A100
- Burke, J. R., & Hollenbach, D. J. 1983, ApJ, 265, 223
- Cazaux, S., Boschman, L., Rougeau, N., Reitsma, G., Hoekstra, R., Teillet-Billy, D., Morisset, S., Spaans, M., Schlathölder, T. 2016, DOI: 10.1038/srep19835
- Chokshi, A., Tielens, A. G. G. M., Werner, M. W., & Castelaz, M. W. 1988, ApJ, 334, 803
- Croiset, B. A., Candian, A., Berné, O., & Tielens, A.G.G.M. 2016, A&A, DOI: 10.1051/0004-6361/201527714
- Cuppen, H. M., & Herbst, E. 2005, MNRAS, 361, 565
- Dawson, W. R., Kropp, J. L. 1969, J. Phys. Chem., 73, 693–699
- Demarais, N. J., Yang, Z., Martinez, O., Wehres, N., Snow, T. P., & Bierbaum, V. M. 2012, AJ, 746, 32
- Demarais, N. J., Yang, Z., Snow, T. P., & Bierbaum, V. M. 2014, ApJ, 784, 25
- Denifl, S., Ptasíńska, S., Sonnweber, B., et al. 2005, JChPh, 123, 104308
- Draine, B. T., & Sutin, B. 1987, ApJ, 320, 803
- Duley, W. W. 1996, MNRAS, 279, 591
- Duley, W. W., & Williams, D. A. 1981, MNRAS, 196, 269
- Duncan, M. A., Knight, A. M., Negishi, Y., et al. 1999, Chem. Phys. Lett., 309, 49
- Fleming, B., France, K., Lupu, R. E., & McCandliss, S. R. 2010, ApJ, 725, 159
- Frisch, M. J., Trucks, G. W., Schlegel, H. B., et al. 2009, Gaussian 09, Revision D.01, Gaussian, Inc., Pittsburgh PA
- Fuente A., Martín-Pintado J., Rodríguez-Franco A., Moriarty-Schieven G.D., 1998, A&A 339, 575
- Fuente, A., Rodríguez-Franco, A., García-Burillo, S., Martín-Pintado, J., & Black, J. H. 2003, A&A, 406, 899
- Fusaro, M. 2012, Struct. Chem., 23, 237
- Galliano, F., Madden, S. C., Tielens, A. G. G. M., Peeters, E., & Jones, A. P. 2008, ApJ, 679, 310
- Geballe, T., Tielens, A.G.G.M., Allamandola, L. J., Moorhouse, A., Brand, P. W. J. L., 1989, ApJ, 341, 278
- Gry, C., Boulanger, F., Nehmé, C., et al. 2002, A&A, 391, 675
- Habart, E., Boulanger, F., Verstraete, L., et al. 2003, A&A, 397, 623
- Habart, E., Boulanger, F., Verstraete, L., Walmsley, C. M., & Pineau des Forêts, G. 2004, A&A, 414, 531
- Hassouna, M., Le Garrec, J., Rebrion-Rowe, C., Travers, D., & Rowe, B. 2003, *Dissociative Recombination of Molecular Ions with Electrons* ed. Guberman S. L. (Kluwer Academic / Plenum Publishers) p 451–460
- Hollenbach, D., & McKee, C. F. 1979, ApJS, 41, 555
- Hollenbach, D., & Salpeter, E. E. 1971, ApJ, 163, 155
- Joblin, C., Tielens, A. G. G. M., Allamandola, L. J., & Geballe, T. R. 1996, ApJ, 458, 610
- Joblin, C., Pilleri, P., Montillaud, J., et al. 2010, A&A, 521, L25
- Jochims, H. W., Rühl, E., Baumgärtel, H., Tobita, S., & Leach, S. 1994, ApJ, 420, 307
- Jochims, H. W., Rühl, E., Baumgärtel, H., & Leach, S. 1996, A&A, 314, 1003
- Jochims, H. W., Rühl, E., Baumgärtel, H., Tobita, S., & Leach, S. 1997, IJMSI, 167/168, 35
- Jura, M. 1975, ApJ, 197, 575
- Kapinus, V. 2004, Ph.D. thesis, Caltech
- Katz, N., Furman, I., Biham, O., Pirronello, V., & Vidali, G. 1999, ApJ, 522, 305
- Köhler, M., Habart, E., Arab, H., et al. 2014, A&A, 569, 109
- Kropp, J. L., Dawson, W. R. 1967, J. Phys. Chem., 71, 4499
- Kurucz, R. L. 1993, VizieR Online Data Catalog, 6039, 0
- Langhoff, S. R. 1996, J. Phys. Chem., 100, 2819
- Le Bourlot, J., Le Petit, F., Pinto, C., Roue, E., & Roy, F. 2012, A&A, 541, A76
- Le Page, V., Keheyan, Y., Bierbaum, V. M., & Snow, T. P. 1997, JACS, 119, 35
- Le Page, V., Snow, T. P., & Bierbaum, V. M. 2001, ApJSS, 132, 233
- Le Page, V., Snow, T. P., & Bierbaum, V. M. 2003, AJ, 584, 316
- Le Petit, F., Nehmé, C., Le Bourlot, J., & Roueff, E. 2006, ApJSS, 164, 506
- Léger, A. & Puget, J. L. 1984, A&A, 137, L5–L8
- Léger, A., Boissel, P., & d'Hendecourt, L. 1988, Phys. Rev. Lett., 60, 921
- Lemaire, J. L., Field, D., Gerin, M., et al. 1996, A&A, 308, 895
- Ling, Y., Gotkis, Y., & Lifshitz, C. 1995, Eur. J. Mass Spectrom., 1, 41
- Mackie, C. J., Peeters, E., Bauschlicher, C. W., Jr., & Cami, J. 2015, ApJ, 799, 131
- Mallocci, G., Joblin, C., & Mulas, G. 2007, Chem. Phys., 332, 353
- Mallocci, G., Mulas, G., Cecchi-Pestellini, C., & Joblin, C. 2008, A&A, 489, 1183
- Mennella, V., Hornekær, L., Throuwer, J., & Accolla, M. 2012, ApJ, 745, L2

- Montillaud, J., Joblin, C., & Toubanc, D. 2013, *A&A*, 552, A15
- Novotný, O., Sivaraman, B., Rebrion-Rouwe, C., et al. 2005, *J. Chem. Phys.*, 123, 104303
- Paris, C., Alcamí, M., Martín, F., & Díaz-Tendero, S. 2014, *J. Chem. Phys.*, 140, 204307
- Peeters, E., Hony, S., Van Kerkhoven, C., Tielens, A. G. G. M., Allamandola, L. J., Hudgins, D. M., & Bauschlicher, C. W. 2002, *A&A*, 390, 1089
- Pilleri, P., Montillaud, J., Berné, O., & Joblin, C. 2012, *A&A*, 542, A69
- Pilleri, P., Joblin, C., Boulanger, F., & Onaka, T. 2015, *A&A*, 577, A16
- Pino, T., et al., 2011, *EAS Publications Series*, 46, 355
- Pirronello, V., Biham, O., Liu, C., Shen, L., & Vidali, G. 1997, *ApJ*, 483, L131
- Pirronello, V., Liu, C., Roser, J. E., & Vidali, G. 1999, *A&A*, 344, 681
- Press, W. H., Teukolsky, S. A., Vetterling, W. T., & Flannery, B. P. 1992, *Numerical Recipes in Fortran: The Art of Scientific Computing*, 2nd ed. (Cambridge: Cambridge Univ. Press)
- Purcell, E. M. 1976, *ApJ*, 206, 685
- Radziszewski, J. G., Hess, B. A., & Zahradnik, R. 1992, *JChS*, 114, 52
- Rapacioli, M., Joblin, C., & Boissel, P. 2005, *A&A*, 429, 193
- Rauls, E., & Hornekær, L. 2008, *ApJ*, 679, 531
- Rebrion-Rouwe, C., Le Garrec, J., Hassouna, M., Travers, D., & Rowe, B. 2003, *Int. Jour. Mass Spec.*, 223, 236
- Reitsma, G., Boschman, L., Deuzeman, M.J., González-Magaña, O., Hoekstra, S., Cazaux, S., Hoekstra, R., & Schlathöler, T. 2014, *Phys. Rev. Lett.*, 113, 053002
- Ricca, A., Bauschlicher, C. W., Jr., Boersma, C., Tielens, A. G. G. M., & Allamandola, L. J. 2012, *ApJ*, 754, 75
- Ricks, A. M., Douberly, G. E., & Duncan, M. A. 2009, *ApJ*, 702, 301
- Roche, P. F., Lucas, P. W., Hoare, M. G., Aitken, D. K., & Smith, C. H. 1996, *MNRAS*, 280, 924
- Rosenberg, M. J. F., Berné, O., Boersma, C., Allamandola, L. J., & Tielens, A. G. G. M. 2011, *A&A*, 532, A128
- Sandford, S. A., Bernstein, M. P., & Materese, C. K. 2013, *ApJS*, 205, 8
- Schutte, W. A., Tielens, A. G. G. M., & Allamandola, L. J. 1993, *ApJ*, 415, 397
- Sellgren, K., Werner, M. W., Ingalls, J. G., et al. 2010, *ApJ*, 722, L54
- Stein, S. E., & Rabinovitch, B. S., 1973, *J. Phys. Chem.*, 58, 2438
- Stephens, P. J., Devlin, F. J., Chabalowski, C. F., & Frisch, M. J. 1994, *J. Phys. Chem.*, 98, 11623
- Tielens, A. G. G. M. 2005, *The Physics and Chemistry of the Interstellar Medium* (Cambridge: Cambridge Univ. Press)
- Tielens, A. G. G. M. 2008, *ARA&A*, 46, 289
- Throner, J. D., Nilsson, L., Jørgensen, B., et al. 2011, in *PAHs and the Universe*, ed. C. Joblin & A. G. G. M. Tielens (EAS Pub. Ser. 46; Les Ulis: EDP), 453
- Tobita, S., Meinke, M., Illenberger, E., Christophorou, L. G., Baumgärtel, H., & Leach, S. 1992, *Chem. Phys.*, 161, 501
- Tobita, S., Leach, S., Jochims, H. W., Ruehl, E., Illenberger, E., & Baumgärtel, H. 1994, *Canadian J. Physics*, in press
- Verstraete, L., Leger, A., d'Hendecourt, L., Defourneau, D., & Dutuit, O. 1990, *A&A*, 237, 436
- Werner, M. W., Uchida, K. I., Sellgren, K., et al. 2004, *ApJS*, 154, 309
- Witt, A. N., Gordon, K. D., Vijh, U. P., et al. 2006, *ApJ*, 636, 303
- Young Owl, R. C., Meixner, M. M., Fong, D., Haas, M. R., Rudolph, A. L., & Tielens, A. G. G. M. 2002, *ApJ*, 578, 885
- Zhen, J., Castellanos, P., Paardekooper, D. M., Linnartz, H., & Tielens, A. G. G. M. 2014a, *ApJ*, 797, L30
- Zhen, J., Paardekooper, D. M., Candian, A., Linnartz, H., & Tielens, A. G. G. M. 2014b, *CPL*, 592, 211

3.A. Molecular Characteristics

3.A.1. Ionization potentials and electron affinities

Malloci et al. (2008) calculated the IPs for the *even* dehydrogenated states of coronene, i.e., $C_{24}H_{2n}$ where $n = 0-6$. According to their calculations, the IP increases with higher levels of dehydrogenation. This increase is relatively constant, with $\Delta IP \sim 0.1$ eV per dehydrogenation. For coronene, the theoretically calculated energies vary from 7.02 eV for $C_{24}H_{12}$ to 8.25 eV for C_{24} . This last value also agrees with the calculations of An et al. (2008) for C_{24} . The decrease of the IP with hydrogenation has

also been reported for anthracene ($C_{14}H_{10}$) and naphthalene ($C_{10}H_8$) first dehydrogenated and first superhydrogenated states, where ΔIP becomes more constant as the PAH gets larger (Kapinus 2004). Based on this, we decided to adopt this ΔIP with hydrogenation for all molecules and all ionization states.

Table 3.3: Ionization potentials and electron affinities of $C_{24}H_{12}$, $C_{54}H_{18}$ and $C_{96}H_{24}$.

Ionization Potentials			
Molecule		Energy (eV)	References
$C_{24}H_{12}$	IP(1)	7.20	Tobita et al. (1994)
	IP(2)	11.50	Tobita et al. (1994)
$C_{54}H_{18}$	IP(1)	6.14	Mallocci et al. (2007)
	IP(2)	8.91	Mallocci et al. (2007)
	IP(3)	12.94	Bakes & Tielens (1994)
$C_{96}H_{24}$	IP(1)	5.68	Bakes & Tielens (1994)
	IP(2)	8.24	Bakes & Tielens (1994)
	IP(3)	10.80	Bakes & Tielens (1994)
	IP(4)	13.36	Bakes & Tielens (1994)
Electron Affinities			
Molecule		Energy (eV)	References
$C_{24}H_{12}$	EA(1)	0.47	Duncan et al. (1999)
$C_{54}H_{18}$	EA(1)	1.44	Mallocci et al. (2007)
$C_{96}H_{24}$	EA(1)	3.11	Bakes & Tielens (1994)
	EA(2)	0.56	Bakes & Tielens (1994)

3.A.2. IR intrinsic spectra

Tables 3.4–3.6 list the PAHs for which we have the IR intrinsic spectra. The spectra are either taken from the NASA Ames PAH Database (PAHdb) or from our own calculations (C).

Table 3.4: PAH Intrinsic spectra available for coronene $C_{24}H_{12}$ derivatives.

N_H	$Z = -1$	$Z = 0$	$Z = 1$	$Z = 2$
0	...	PAHdb	PAHdb	C
1	...	C	C	C
2	...	C	C	C
3	...	C	C	C
4	C	C
5	C	C
6	C	C
7	C	C
8	C	C
9	C	C
10	C	C
11	C	C
12	PAHdb	PAHdb	PAHdb	PAHdb
13	PAHdb	C	C	C
14	C	C	C	C

Table 3.5: PAH Intrinsic spectra available for circumcoronene $C_{54}H_{18}$ derivatives.

N_H	$Z = -1$	$Z = 0$	$Z = 1$	$Z = 2$	$Z = 3$
0	...	PAHdb	PAHdb
1	C
17	...	C
18	PAHdb	PAHdb	PAHdb	PAHdb	PAHdb
19	PAHdb	C	PAHdb	PAHdb	PAHdb
20	C	C

Table 3.6: PAH Intrinsic spectra available for circumcircumcoronene $C_{96}H_{24}$ derivatives.

N_H	$Z = -2$	$Z = -1$	$Z = 0$	$Z = 1$	$Z = 2$	$Z = 3$	$Z = 4$
0	PAHdb	PAHdb	PAHdb
22	...	PAHdb	PAHdb	PAHdb
24	PAHdb	PAHdb	PAHdb	PAHdb	PAHdb	PAHdb	PAHdb
25	...	PAHdb	PAHdb	PAHdb
26	...	C	C

3.A.3. Electron attachment/recombination with electrons

Tobita et al. (1992) performed low energy electron impact experiments on small neutral PAHs, and reported rate coefficients for electron attachment of 9×10^{-10} and 2×10^{-10} cm³/s for anthracene (C₁₄H₁₀) and pyrene (C₁₆H₁₀), respectively. Deniff et al. (2005) studied the electron attachment to neutral coronene and corannulene (C₂₀H₁₀), and obtained similar trends as observed in the experiments of Tobita et al. (1992). They estimated the electron recombination cross section to be of 3.8×10^{-16} cm² for the formation of the coronene anion. Regarding cations, electron recombination rates have been measured for a few small PAH species using flowing afterglow experiments. These studies have determined rate coefficients of 1×10^{-6} for benzene, 3×10^{-7} for naphthalene, 1.1×10^{-6} for azulene, 5.0×10^{-7} for acenaphthene, 2.4×10^{-6} for anthracene, phenanthrene and fluoranthene, and 4.1×10^{-6} cm³/s for pyrene (Abouelaziz et al. 1993; Hassouna et al. 2003; Rebrion-Rowe et al. 2003; Novotný et al. 2005; Biennier et al. 2006). No studies have been done for the PAHs considered here.

Given the lack of experimental studies on large PAHs, we use collisional rates as described in Bakes & Tielens (1994), which take into account the Coulomb interaction between the particles involved:

$$k_{rec}(Z, N_H) = n(e) s_e(Z, N_H) \left(\frac{8 k_B T_{gas}}{\pi m_e} \right)^{1/2} \pi a^2 \tilde{J}, \quad (3.14)$$

where $n(e)$ is the electron density, k_B is the Boltzmann constant, T_{gas} the gas temperature, m_e the electron mass, $s_e(Z, N_H)$ is the electron sticking coefficient for each molecule, a is the radius of the PAH, and \tilde{J} is a function that depends on the electron charge and the charge of the PAH (see full expression in Draine & Sutin 1987). We calculate the radius of each molecule as $a = 0.9 \times 10^{-8} N_C^{1/2}$ cm, where N_C is the number of carbon atoms of the molecule. Since equation 3.14 is valid for spherical molecules, we use a 0.82 correction factor as derived by Verstraete et al. (1990) for disk-shaped molecules. For positively ionized molecules we assume a sticking coefficient of unity given the attractive interaction between the particles. Sticking coefficients for neutral species are calculated following Allamandola et al. (1989). Polarizabilities are taken from the Cagliari PAH database for the parent molecules C₂₄H₁₂ and C₅₄H₁₈. To determine the polarizability of C₉₆H₂₄, we performed a fit as a function of size to the polarizabilities of all the PAHs compiled in the database (up to sizes of 54 carbon atoms) for a given ionization state, and then extrapolated this to $N_C = 96$. We then used the polarizabilities of the parent molecules for all the respective derivatives. The calculated sticking coefficients increase with EA, reaching unity for EA ≥ 1 eV.

3.B. Photodissociation Rates

Tables 3.7–3.9 present the fit parameters to the H-loss and H₂-loss rates as a function of UV field intensity G_0 for the molecules considered in our work. The fits are of the form $\log_{10}(k_i(G_0)) = \sum_j p_j \log_{10}(G_0)^j$ from $j = 0-4$ for each i process (i.e., H-loss and H₂-loss). The fits are shown for the molecules for which the IR intrinsic spectra were available.

Table 3.7: Fit parameters to H-loss rate, $k_{H,Loss}$, and H₂-loss rate, $k_{H_2,Loss}$, as a function of UV field intensity G_0 for coronene derivatives.

N_H	H-Loss					H ₂ -Loss				
	p_0	p_1	p_2	p_3	p_4	p_0	p_1	p_2	p_3	p_4
Z = -1										
12	-6.131	1.154	-0.153	0.038	-0.001	-8.163	0.909	0.119	-0.047	0.006
13	3.405	0.999	0.001	-0.001	0.000
14	3.448	0.999	0.004	-0.002	0.000
Z = 0										
1	-3.814	1.083	-0.065	0.008	0.002
2	-5.820	1.198	-0.206	0.057	-0.003	-7.870	0.933	0.096	-0.042	0.006
3	-1.850	0.947	0.083	-0.039	0.006
12	-5.800	1.192	-0.198	0.054	-0.003	-7.849	0.925	0.104	-0.043	0.006
13	3.791	1.001	0.004	-0.002	0.000
14	3.693	0.997	0.005	-0.003	0.000
Z = 1										
1	-2.082	1.166	-0.014	-0.019	0.004
2	-3.901	0.960	0.064	-0.031	0.005	-6.494	0.907	0.116	-0.043	0.005
3	-2.359	0.917	0.109	-0.043	0.005
4	-4.356	0.986	0.038	-0.023	0.004	-6.866	0.898	0.136	-0.050	0.006
5	-2.698	0.931	0.096	-0.041	0.005
6	-4.083	1.087	-0.060	0.005	0.001	-6.592	0.892	0.128	-0.045	0.005
7	-3.135	1.076	-0.044	0.000	0.002
8	-5.225	1.143	-0.130	0.028	0.000	-7.481	0.900	0.126	-0.047	0.006
9	-3.540	0.962	0.064	-0.031	0.005
10	-5.728	1.108	-0.088	0.017	0.001	-7.884	0.900	0.139	-0.051	0.006
11	-3.929	1.020	0.030	-0.023	0.004
12	-6.106	1.151	-0.150	0.037	-0.001	-8.155	0.912	0.114	-0.044	0.005
13	3.254	1.047	-0.021	0.004	0.000
14	3.007	0.998	0.004	-0.002	0.000

3.C. Model

Since there are ($N_H^0 + 5$) hydrogenation states for each parent molecule, and N_Z ionization states depending on the molecule, for each species we must solve $(N_H^0 + 5) \times N_Z$ equations of the form:

$$\frac{d[\text{PAH}(Z, N_H)]}{dt} = \sum(\text{Formation}) - \sum(\text{Destruction}),$$

where formation processes (when applicable) include: ionization of PAH ($Z-1, N_H$); electron attachment to PAH ($Z+1, N_H$); loss of an H atom from PAH (Z, N_H+1); loss of H₂ from PAH (Z, N_H+2); H addition to PAH (Z, N_H-1) (or PAH ($Z-1, N_H-1$) in case of associative detachment); and H₂ abstraction from PAH (Z, N_H+1). Destruction processes on the other hand (when applicable) are given by: ionization of PAH (Z, N_H); electron attachment to PAH (Z, N_H); loss of an H atom from PAH (Z, N_H); loss of H₂ from PAH (Z, N_H); H addition to PAH (Z, N_H); and H₂ abstraction from PAH (Z, N_H).

Table 3.8: Fit parameters to H-loss rate, $k_{H,Loss}$, and H₂-loss rate, $k_{H_2,Loss}$, as a function of UV field intensity G_0 for circumcoronene derivatives.

N_H	H-Loss					H ₂ -Loss				
	p_0	p_1	p_2	p_3	p_4	p_0	p_1	p_2	p_3	p_4
Z = -1										
18	-13.972	0.541	0.498	-0.087	0.007	-14.226	1.179	-0.231	0.079	-0.005
19	-2.676	0.973	0.040	-0.017	0.003
20	-2.866	1.275	-0.130	0.019	0.000
Z = 0										
17	-10.438	0.597	0.375	-0.058	0.005
18	-14.148	1.962	-0.031	-0.009	0.003	-13.527	1.051	-0.121	0.060	-0.004
19	-0.624	0.979	0.031	-0.014	0.002
20	-0.982	1.228	-0.115	0.021	-0.001
Z = 1										
1	-10.821	0.825	0.101	0.015	-0.001
18	-13.752	0.537	0.503	-0.089	0.007	-14.036	1.179	-0.230	0.078	-0.005
19	-2.904	0.961	0.058	-0.026	0.004

The system of equations can then be written in matrix form as $M \vec{x} = \vec{0}$, where M represents the kinetic matrix with all the rate constants calculated for a given set of physical conditions T_{gas} , $n(e)$, $n(H)$ and G_0 . For each slab of the PDR this system of equations is solved using the Newton-Raphson Method (Press et al. 1992). This method proved to be fast and reached convergence for every slab considered in our work.

3.D. Fiducial Collision Rates

For neutral species we have considered a fiducial collision rate $k_{col} = \sigma_{col} \times v_{th} \times n(H)$, where σ_{col} corresponds to the geometrical cross section of the parent molecule, and v_{th} corresponds to the thermal velocity of the colliding H atoms. For anions we have considered $k_{col} = 7.8 \times 10^{-10} \times n(H)$, since we consider the H-addition as an associative detachment reaction. For cations on the other hand, the fiducial collision rate adopted is of $k_{col} = 1.4 \times 10^{-10} \times n(H)$. When calculating the efficiency of H₂ formation from direct H₂-loss after photon absorption we multiply the fiducial rates by a 0.5 factor given that each photodissociation event removes 2 H atoms from the molecule.

Table 3.9: Fit parameters to H-loss rate, $k_{H,Loss}$, and H₂-loss rate, $k_{H_2,Loss}$, as a function of UV field intensity G_0 for circumcoronene derivatives.

N_H	H-Loss					H ₂ -Loss				
	p_0	p_1	p_2	p_3	p_4	p_0	p_1	p_2	p_3	p_4
Z = -1										
22	-20.455	1.746	0.265	-0.098	0.012	-19.627	0.667	0.429	-0.068	0.005
24	-20.666	1.769	0.254	-0.096	0.012	-19.841	0.812	0.330	-0.043	0.003
25	-5.927	0.859	0.161	-0.066	0.010
26	-6.042	0.990	0.045	-0.033	0.007
Z = 0										
22	-19.161	1.960	0.050	-0.029	0.007	-18.846	0.693	0.679	-0.167	0.016
24	-19.318	2.106	-0.074	0.005	0.004	-19.040	1.019	0.428	-0.100	0.010
25	-2.764	0.820	0.223	-0.088	0.012
26	-2.819	0.858	0.186	-0.076	0.011
Z = 1										
22	-20.559	1.741	0.236	-0.085	0.011	-19.491	0.420	0.498	-0.075	0.005
24	-20.700	1.802	0.181	-0.066	0.009	-19.818	0.795	0.269	-0.016	0.000
25	-6.489	0.910	0.136	-0.059	0.009

3.E. Relative Abundance Distribution of PAHs in NGC 7023

Figures 3.13–3.15 show the fractional contribution from coronene (black), circumcoronene (blue) and circumcircumcoronene (red) derivatives in the NW PDR of NGC 7023, according to the physical conditions modelled by the Meudon PDR Code. Odd and even hydrogenated states have been depicted in slightly different colors for a better visualization.

Coronene is completely dehydrogenated throughout most of the cloud. Only at an $A_V > 4$ we find traces of the first 4 hydrogenated states. This is driven by a rise in the atomic hydrogen density due to the modelling of the cloud (finite size). In terms of the ionization state of the coronene derivatives, we find that at the surface of the cloud ($A_V = 0$) most molecules are in neutral state, while cations contribute in $\sim 27\%$ to the total PAH abundance. Unlike coronene, circumcoronene derivatives are found in their normally hydrogenated state ($N_H = 18$) with traces of partial dehydrogenation at the surface of the cloud, and at $A_V \sim 1.8$. Regarding ionization, positively ionized species dominate the distribution at the surface of the cloud, contributing in $\sim 59\%$ to the total PAH abundance.

Compared to the smaller molecules, circumcircumcoronene derivatives are mainly found in the normal hydrogenated state ($N_H = 24$). No dehydrogenation is observed. Only minor levels of superhydrogenation appear at high extinction due to the finite cloud size assumption. In terms of ionization, we see a larger contribution from $Z > 0$ species at the surface of the cloud ($\sim 74\%$) compared to coronene and circumcoronene derivatives. There is no significant contribution from $Z = 3$ nor $Z = 4$ species (trications contribute in only 0.9% at $A_V = 0$).

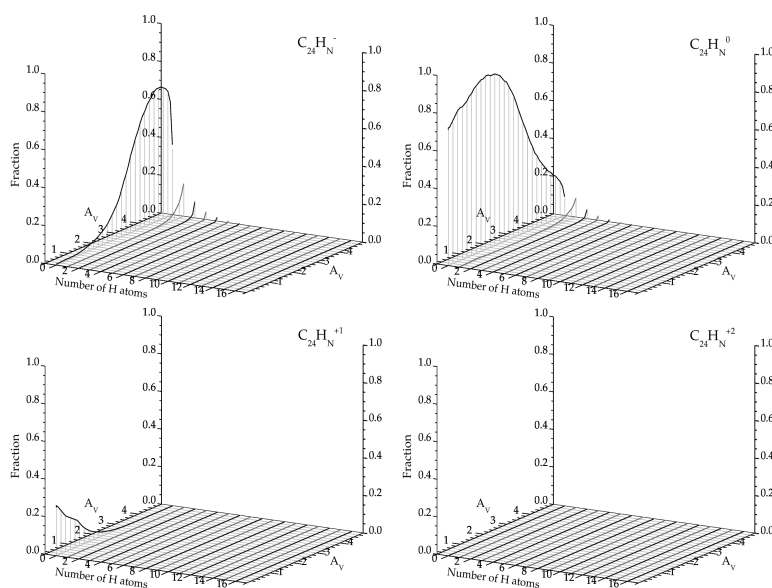


Figure 3.13: Fractional contribution from coronene derivatives in the NW PDR of NGC 7023 according to the physical conditions modelled by the Meudon PDR Code. Coronene is completely dehydrogenated throughout most of the cloud ($N_{\text{H}} = 0$). No contribution from dications is observed.

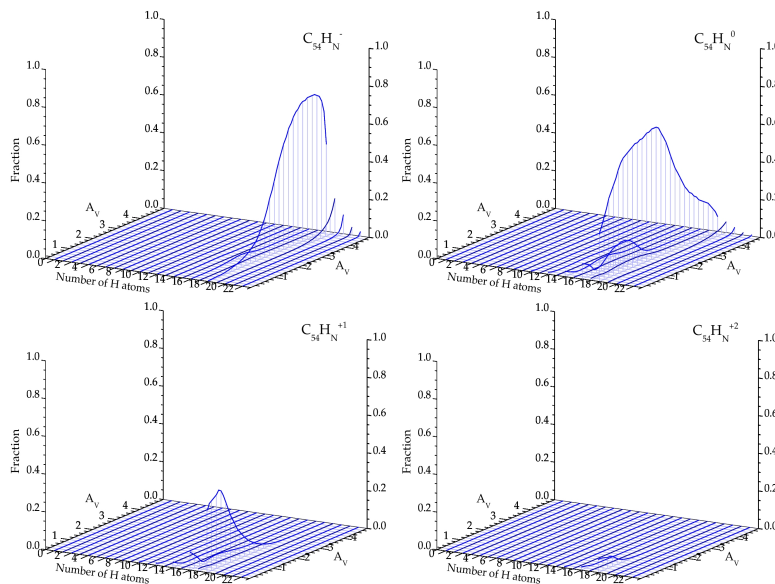


Figure 3.14: Fractional contribution from circumcoronene derivatives in the NW PDR of NGC 7023 according to the physical conditions modelled by the Meudon PDR Code. Unlike coronene, these molecules are found in their normally hydrogenated state ($N_{\text{H}} = 18$) with traces of partial dehydrogenation at the surface of the cloud, and at $A_V \sim 1.8$.

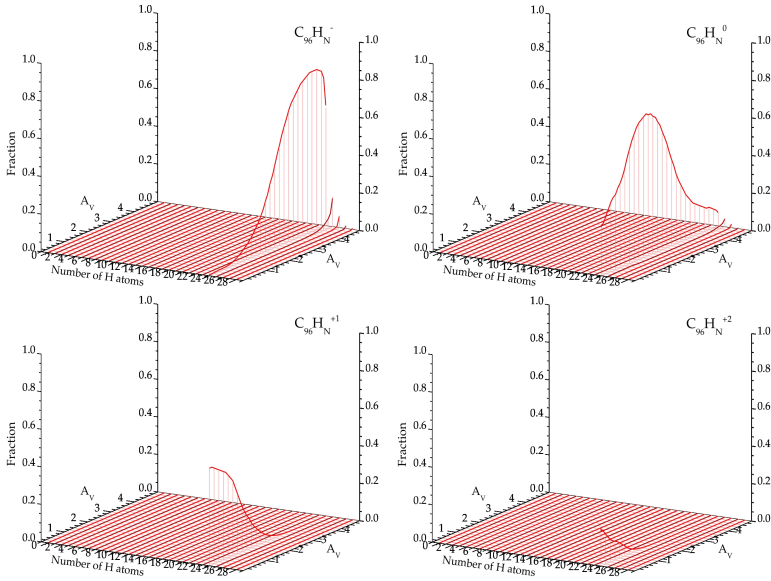


Figure 3.15: Fractional contribution from circumcoronene derivatives in the NW PDR of NGC7023 according to the physical conditions modelled by the Meudon PDR Code. Compared to the smaller species, circumcoronene is mainly found in its normal hydrogenated state ($N_{\text{H}} = 24$). There is no significant contribution from $Z > 2$ species.

3.F. Spectral Variations

3.F.1. PAH emission spectra in the NW PDR of NGC7023

For coronene derivatives, the spectra are dominated by that of the completely dehydrogenated molecule. As listed in Table 3.4, we do not have the intrinsic spectra of the anionic completely dehydrogenated coronene and thus, its contribution is not considered in the spectra shown in Figure 3.16. However we do not expect this to affect the resulting spectrum since the contribution from C_{24}^- increases smoothly from the surface of the cloud up to only a 7.4% at $A_V = 2$. In the case of circumcoronene, $\sim 34\%$ of the emitting species are not considered in the spectrum at $A_V = 0$, where traces of the first partially dehydrogenated molecules are observed (e.g., $N_{\text{H}} = 17\text{--}12$). The spectra at $A_V = 0.4$ to 1.2 on the other hand, are $>85\%$ complete, while at $A_V = 1.6$ and 2.0 the emission is complete to a 80% . Since the contributions from partially dehydrogenated molecules are overall small, and they are not highly dehydrogenated, we expect the spectra to be representative of the actual emission. In the case of our largest species, circumcoronene, all spectra are complete.

3.F.2. PAH emission spectra for different $G_0/n(H)$ ratios at $G_0 = 10^3$

In the case of coronene, the dominant species is the completely dehydrogenated molecule for most $G_0/n(H)$ ratios. Only at $G_0/n(H) \leq 0.01$ partially dehydrogenated derivatives in neutral and anionic form become more relevant. The spectrum at $G_0/n(H) = 0.01$ is missing the contribution from 24% of the emitting species mostly due to C_{24}^- , while the spectrum at $G_0/n(H) = 0.001$ is missing 81.7% due to partially dehydrogenated neutrals and anions. The spectrum of normally hydrogenated coronene is never really important (even at a $G_0/n(H) = 0.001$ $\text{C}_{24}\text{H}_{12}$ contributes at a 1% level only). The same applies for superhydrogenated species, which barely appear at $G_0/n(H) = 0.001$ contributing at

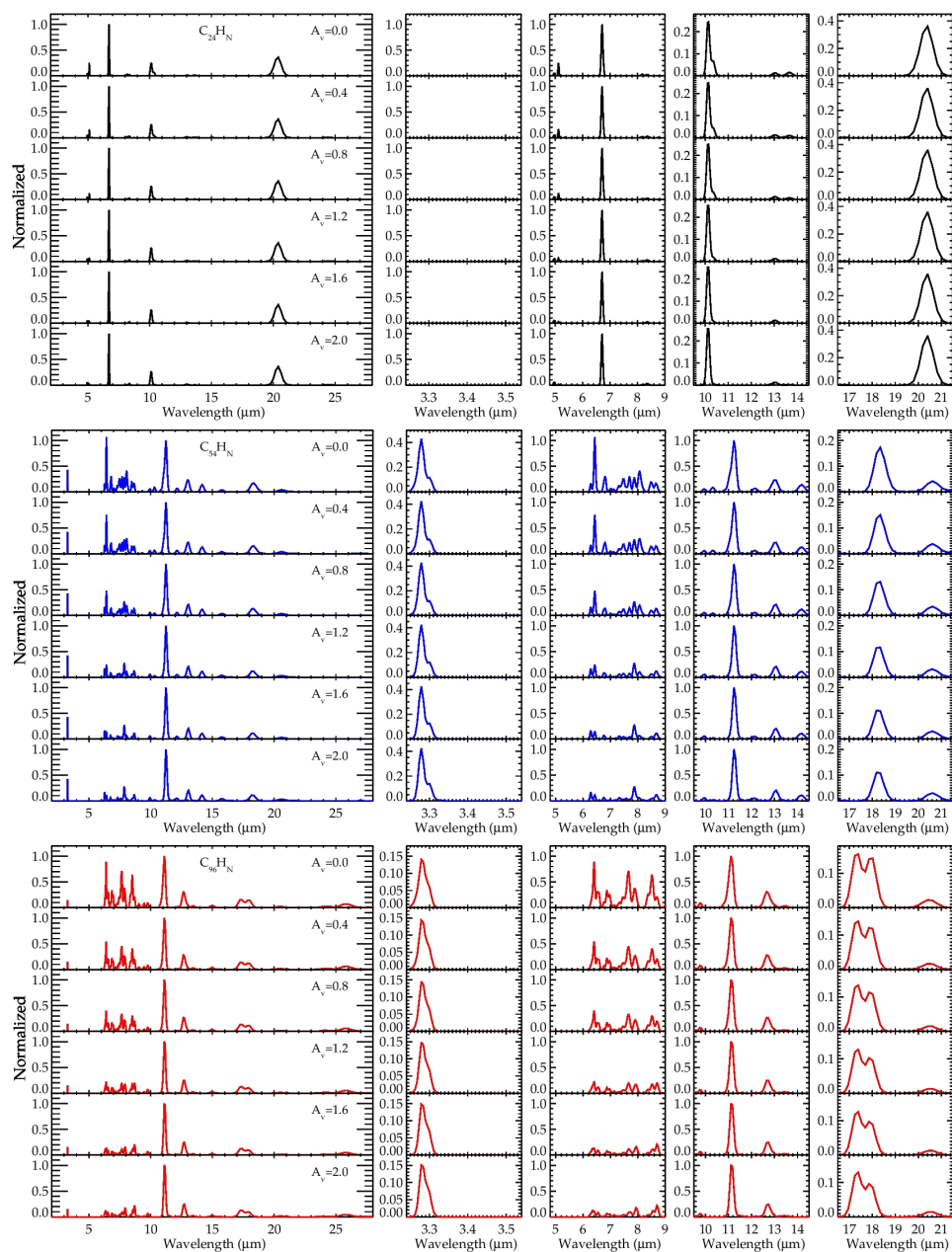


Figure 3.16: PAH emission spectra at different points inside the NW PDR of NGC7023. For each species, the spectra have been derived by adding the contributions of all ionization and hydrogenation states, from the abundances presented in Appendix 3.E. The results for $C_{24}H_{12}$ derivatives are shown in black, while the spectra for $C_{54}H_{18}$ and $C_{96}H_{24}$ species are shown in blue and red, respectively. The spectra have been conveniently normalized to the peak intensity of the $6.7\mu\text{m}$ band for $C_{24}H_{12}$ derivatives, and to the $11.2\mu\text{m}$ band for the larger species.

a 5% level. The spectrum shown in Figure 3.17 is then mainly due to normal-to-superhydrogenated species and not from the partially dehydrogenated molecules, whose contribution would dominate the emission if they were available.

For circumcoronene, the dominant species at $G_0/n(H) = 100$ is C_{54}^{+2} in 83% for which we do not have the IR spectrum. Therefore, the emission shown in Figure 3.17 corresponds mainly to that of C_{54}^+ , that contributes only in 12% to the total abundance, with even smaller traces of $C_{54}H$. Since the spectra of dications is in general similar to that of cations, we expect the actual emission to resemble the one shown in Figure 3.17, except for a stronger $5\mu\text{m}$ band, typical from highly positively ionized completely dehydrogenated PAHs. The spectra at $G_0/n(H) = 10$ is missing the emission from 54% of the species due to partially dehydrogenated molecules in positively ionized states. Going to lower $G_0/n(H)$ values, the spectra at $G_0/n(H) = 0.1$ and 0.01 are 99 and 79% complete respectively. Both dominated by $C_{54}H_{18}$. The contribution from superhydrogenated species in this $G_0/n(H)$ range goes from ~ 3 to 35%, which is clear from the inspection of the $3\mu\text{m}$ region. The spectra at $G_0/n(H) = 0.001$ is missing 97.5% of the emitting species due to the highly superhydrogenated molecules in anionic and neutral states. Thus the emission presented in the Figure corresponds only to the first superhydrogenated molecules for which we have the spectra.

Regarding circumcircumcoronene, the spectra are complete down to a $G_0/n(H) = 0.1$, and show the variation in the ionization state of $C_{96}H_{24}$, from being mostly in $Z = 3$ state to neutral. The spectrum at $G_0/n(H) = 0.01$ is missing 19% of the emitting molecules due to highly superhydrogenated species in $Z = -1$ and $Z = 0$ states, which then become the dominant species at $G_0/n(H) = 0.001$. However these will not have a discernible footprint compared to that of the normally hydrogenated molecule which is still the dominating species: $C_{96}H_{24}$ contributes in 8.8% and $C_{96}H_{24}^0$ in 68% at $G_0/n(H) = 0.1$, and 26% and 21.6% respectively at $G_0/n(H) = 0.01$. Also, going from $G_0/n(H) = 0.1$ to 0.01 the abundance of superhydrogenated species—for which the spectra is considered in Figure 3.17—increases by a factor of 10, which is only clear in the $3\mu\text{m}$ spectral region, although the signal is rather weak.

3.F.3. Intrinsic spectra of different hydrogenation states of neutral coronene, circumcoronene and circumcircumcoronene molecules

Figure 3.18 shows a comparison of the IR spectra of different hydrogenation states of coronene, circumcoronene and circumcircumcoronene in the $3\mu\text{m}$ region. Here we see clearly the aromatic nature of the bands at $3.28\text{--}3.30\mu\text{m}$ that disappear in the completely dehydrogenated molecules, and in the fully superhydrogenated molecule (e.g., $C_{24}H_{24}^0$). We have also checked this for other ionization states. The $3.5\mu\text{m}$ band is common to all superhydrogenated states of these species. This band is due to the CH (symmetric and asymmetric) stretching modes in a single CH_2 group. In the case of $C_{54}H_{19}^0$, the band at $3.5\mu\text{m}$ is very weak: the peak intensity of the $3.28\mu\text{m}$ band is of $12 \times 10^5 \text{ cm}^2/\text{mol}$, whereas the peak intensity of the band at $3.47\mu\text{m}$ is of $0.06 \times 10^5 \text{ cm}^2/\text{mol}$. Thus it cannot be clearly seen with the scale used in this Figure. On the other hand, the band at $3.4\mu\text{m}$ appears from the second hydrogenation on, becoming particularly intense for the fully hydrogenated molecule in the case of coronene ($C_{24}H_{24}$). This band is related to the CH stretches of the CH_2 groups in the same (duo) rings. Superhydrogenated PAHs with extra H atoms in solo positions do not present this band.

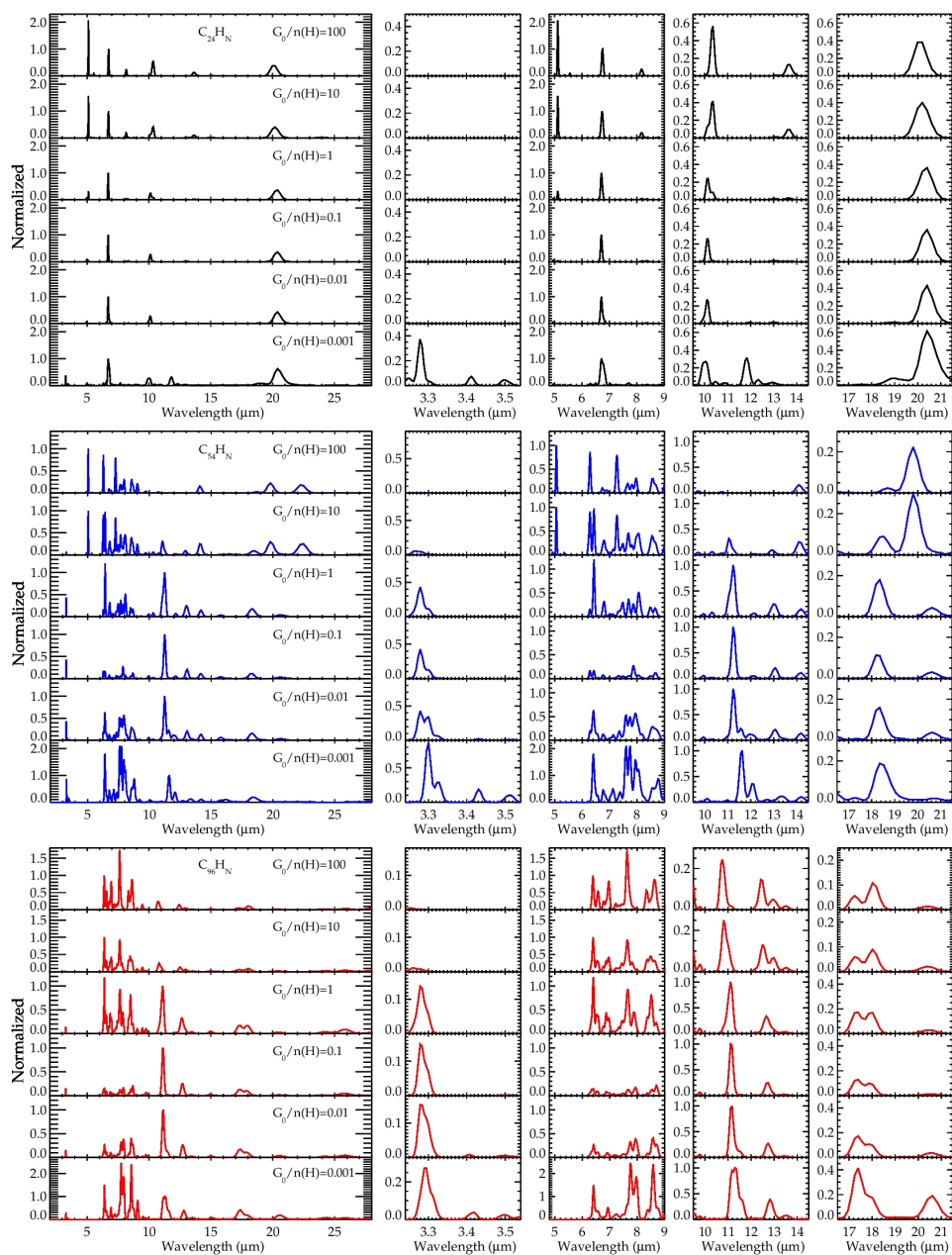


Figure 3.17: Emission spectra for different $G_0/n(H)$ ratios at $G_0 = 10^3$. The results for coronene derivatives are shown in black, while the spectra for $C_{54}H_{18}$ and $C_{96}H_{24}$ derivatives are shown in blue and red, respectively. The spectra have been conveniently normalized for a better comparison between consecutive $G_0/n(H)$ ratios. Given the unavailability of the intrinsic spectra for some of these molecules, the spectra at low $G_0/n(H)$ ratios are not complete due to the increasing abundance of highly superhydrogenated anionic species.

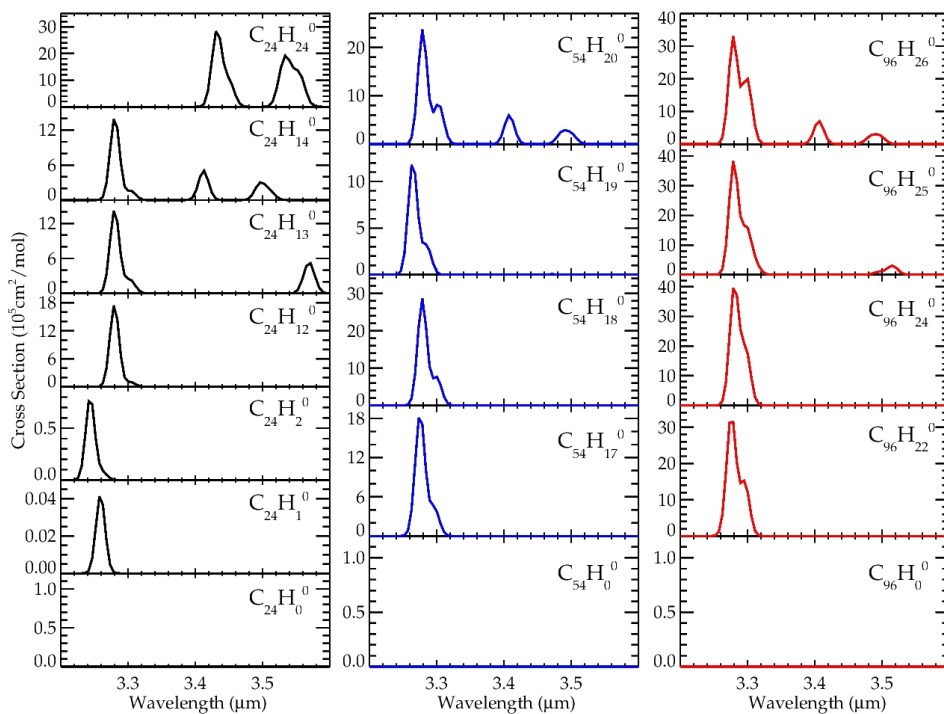


Figure 3.18: Intrinsic spectra of different hydrogenation states of the neutral coronene (*left*), circumcoronene (*middle*) and circumcircumcoronene (*right panel*) molecules. Only the $3\mu\text{m}$ region is presented. This spectral region is the one where differences in the hydrogenation state of PAHs can be clearly observed. Differences in the hydrogenation state (within a given PAH size and ionization state) are clear from the appearance of more features at 3.4 and $3.5\mu\text{m}$.

The Path to PAHDs

We used a kinetic model to analyze the deuteration of PAHs over an astrophysically relevant PAH size range. Our specific goals were to understand how deuterium is locked in PAHs, and if PAHs can contribute to the deuterium fractionation problem at a significant level or not. We expanded the kinetic model of Andrews et al. (2016) to include reactions with deuterated species. The model calculates the abundances of PAHs and its fragments under the influence of photodissociation and atom addition reactions. It uses specific molecular properties for each PAH, based on the latest data available at the present time. It takes into account the small differences in the binding energy between CH and CD bonds which affects the photodissociation rates, as well as the differences in thermal velocity for atomic H and D that affects the addition reaction rate coefficient. Overall we find that deuteration of PAHs largely follows the atomic (D/H) ratio available in the gas phase. Thus the deuterium fractionation in PAHs will be higher if the (D/H) ratio in the ISM is higher. In that sense, the (D/H) ratio in PAHs is sensitive to its local conditions. Our results also show that the deuterium fractionation of PAHs with extra atoms in their edges (creating aliphatic sites) is higher than that of aromatic sites. We have compared our model results with recent observations of deuterated PAHs in photodissociation regions (PDRs). We conclude that the high deuteration observed implies that the gas phase reservoir must be highly fractionated, e.g., possibly because deep in clouds hydrogen is locked up in H₂ while deuterium can still be largely atomic. However, the implied atomic (D/H) fraction in the gas phase is much larger than what PDR models predict. Alternatively, the observed high deuterium fractionation on aromatic sites may reflect chemistry occurring in cold dense molecular cloud cores, that is preserved when (intermediate-to-large) PAHs are transported to the unshielded environment of PDRs. Such a model, can, however, not explain the observed high fractionation of the much more labile, aliphatic groups.

H. Andrews, A. Candian & A. G. G. M. Tielens
A&A, Submitted

4.1. Introduction

It is generally considered that all the deuterium in the universe was formed in the Big Bang (Epstein et al. 1976). The primordial (D/H) ratio is commonly estimated from observations of clouds in the line-of-sight towards distant quasars at high redshift (Adams 1976). Recent (D/H) values derived from observations of damped Lyman- α (DLA) systems, coupled with measurements of the angular power spectrum of the cosmic microwave background (CMB), agree on a cosmic D/H abundance of $\sim 2.5 \times 10^{-5}$ (Srianand et al. 2010; Coc et al. 2015; Cooke & Pettini 2016).

In theory, stars should completely destroy the deuterium in them (Mazzitelli & Moretti 1980), and therefore we expect the (D/H) abundance to decrease steadily as galaxies chemically evolve with time. However *Far-Ultraviolet Spectroscopic Explorer* (FUSE) observations revealed more puzzling results, showing considerable scatter in the (D/H) ratio in the local galactic disk (between $\sim 0.5\text{--}2.2 \times 10^{-5}$; Linsky et al. 2006), with a value of 1.6×10^{-5} within the Local Bubble (Wood et al. 2004).

The values mentioned above cannot be accounted for solely by astration (Tosi 2010). Infall of unprocessed gas in the galaxy (Romano et al. 2006) and deuterium depletion onto dust grains (Draine 2004) have been proposed as important processes to explain the variation of the (D/H) ratio in the local galactic environment. Observationally, correlations of the (D/H) ratio with Fe, Si, and Ti depletions, and with the excitation temperature of molecular hydrogen suggest that deuterium depletion onto dust grains is important (Jura 1982; Draine 2004; Prochaska et al. 2005; Linsky et al. 2006). Theoretically, the slightly higher binding energy of the C-D bond over the C-H bond support the suggestion that carbonaceous grains could preferentially retain the D they acquire in their surface, leading to $(D/H)_{\text{dust}}/(D/H)_{\text{gas}}$ values as high as 5×10^4 (Draine 2006). For this same reason, polycyclic aromatic hydrocarbons (PAHs) may also be important reservoirs of D in space (Tielens 1997; Millar et al. 2000; Draine 2006).

Observational evidence for the presence of deuterated PAHs in the interstellar medium has been reported in few occasions (e.g., Peeters et al. 2004; Onaka et al. 2014; Doney et al. 2016). Given that deuterium is heavier than hydrogen, the PAH vibrational bands are expected to be slightly shifted to longer wavelengths, and –given the plethora of PAH bands at longer wavelengths– the signature of deuterated PAHs is better evaluated in the $4\mu\text{m}$ region (analogue to the $3\mu\text{m}$ region of –hydrogenated– PAHs). More specifically, PAHs with deuterium in them are expected to show bands at $4.4\mu\text{m}$ (D in aromatic groups, analogue to the $3.3\mu\text{m}$) and $4.7\text{--}4.8\mu\text{m}$ (D in aliphatic groups, analogue to the $3.4\text{--}3.5\mu\text{m}$ bands) (Allamandola 1993; Bauschlicher et al. 1997; Hudgins et al. 2004). Peeters et al. (2004), using the *Infrared Space Telescope* (ISO), first reported the signature of deuterated PAHs in Orion. The observations led to $(D/H)_{\text{PAH}}$ ratios 10^4 times larger than the atomic (D/H) ratio found in the gas phase (Peeters et al. 2004; Draine 2006). More recently, Onaka et al. (2014) revisited these detections using the Infrared Camera (IRC) on board AKARI, and also observed the deuterium signature on PAHs, but estimated a $(D/H)_{\text{PAH}}$ lower than previously reported (< 0.03).

Extending this analysis to a larger sample, Doney et al. (2016) looked for the deuterated PAH signature in a sample of 53 HII regions using AKARI, out of which 41 were in the Milky Way. The footprint of deuterium in PAHs was found only in 6 sources, all in our Galaxy. Interestingly, it was found that in the few sources that presented the deuterated

PAH bands, C-D aliphatic bands were stronger than the C-D aromatic bands (contrary to what is observed with the C-H bands), meaning that the little amount of D attached to PAHs is preferably in an aliphatic group, rather than in an aromatic group (see also Peeters et al. 2004). They also observed a wide range of $(D/H)_{\text{PAH}}$ ratios, which points towards a $(D/H)_{\text{PAH}}$ ratio that is very sensitive to local physical conditions.

All these findings pose an interesting chemical question within the framework of interstellar PAHs. What physical conditions favor a high deuterium fractionation of PAHs? How sensitive is the $(D/H)_{\text{PAH}}$ ratio relative to the strength of the UV field and the atomic D and H densities? What fraction of the available D can be indeed locked in PAHs and in which form? In this work we will address these issues within the framework of the PAH kinetic model presented in Andrews et al. (2016). This model includes ionization/electron recombination of PAHs, multiphoton dissociation events, atomic addition reactions, and Eley-Rideal abstraction mechanism of aliphatic groups. We will consider the same PAHs as in Andrews et al. (2016), meaning the first three members of the *coronene family*. For these specific PAHs, many relevant molecular properties have been determined and they span an interesting PAH size range (between 24 and 96 carbon atoms). This will allow us to study how effective PAHs are in retaining the D attached to them.

The present work is organized as follows: section 4.2 presents a general overview of the kinetic model, and how reactions with deuterium are included. The results regarding the deuteration of PAHs, and how the $(D/H)_{\text{PAH}}$ varies with physical conditions for PAHs of different size are presented in section 4.3, and the implications of our results concerning the role of PAHs in the fractionation of D is discussed in section 4.4.

4.2. Method

4.2.1. PAH Structure

We use the PAH kinetic model of Andrews et al. (2016). This model only considered hydrogenation of PAHs. Therefore, modifications had to be made to include the deuteration of PAHs.

We consider 3 PAHs of increasing size within the *coronene family*: coronene $\text{C}_{24}\text{H}_{12}$, circumcoronene $\text{C}_{54}\text{H}_{18}$, and circumcircumcoronene $\text{C}_{96}\text{H}_{24}$. These species span the range of astrophysically relevant PAH sizes (Allamandola et al. 1989), and they are expected to be among the most stable PAHs in the ISM (Ricca et al. 2012). Coronene has a carbon core with 12 H atoms attached in pairs to 6 different rings (i.e., 6 duo rings). Circumcoronene has 12 H atoms attached in pairs to 6 separate rings (6 duo rings), and 6 H atoms attached to other 6 peripheral rings (6 solo rings). Circumcircumcoronene has similarly 6 duo rings and 12 solo rings.

Each PAH is characterized by the total number of edge atoms $N_{\text{edge}} = N_{\text{H}} + N_{\text{D}}$, where N_{H} is the total number of H atoms attached at their periphery, and N_{D} the total number of D atoms attached at their periphery. We refer to homogenic PAHs as those having either only H atoms ($N_{\text{D}} = 0$) or only D atoms ($N_{\text{H}} = 0$). Heterogenic PAHs are those having both H and D atoms in a given ratio (also referred as PAHDs). Those PAHs with all outer edge C atoms occupied are referred to as the normal molecules, i.e., molecules having the

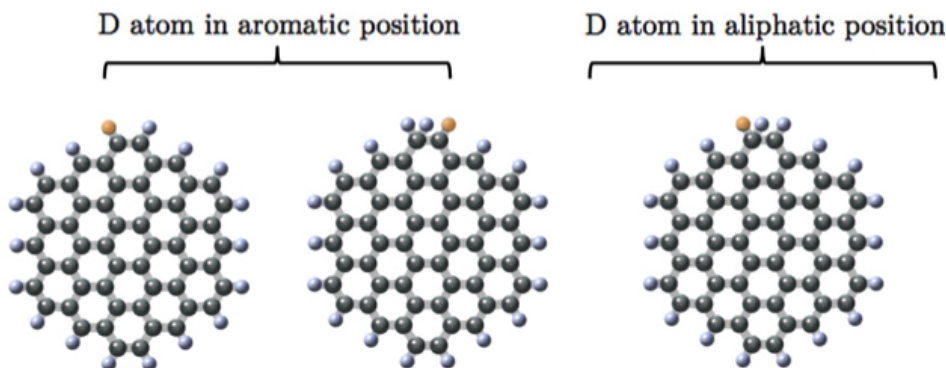


Figure 4.1: Position of a deuterium atom in circumcoronene derivatives. Here we consider molecules with only 1 D atom as an example of heterogenic species. Carbon cores are depicted in grey, H atoms are depicted in white, and D atoms are depicted in orange. From left to right we see $C_{54}H_{17}D$, and two isomers of $C_{54}H_{18}D$. The $C_{54}H_{17}D$ molecule has the D atom in an aromatic position. The heterogenic molecules with $N_{\text{edge}} = 19$ on the other hand, can have an HH aliphatic group while keeping the D atom in an aromatic position; or can have an HD aliphatic group, while having only H atoms in aromatic positions.

total number of edge atoms $N_{\text{edge}} = N_{\text{H}}^0$, where $N_{\text{H}}^0 = 12, 18$ and 24 for coronene, circumcoronene and circumcircumcoronene, respectively. Species with $0 < N_{\text{edge}} < N_{\text{H}}^0$ are called partial species, while those having $N_{\text{edge}} > N_{\text{H}}^0$ are in super states.

For the sake of simplicity, we consider that these PAHs can vary their edge occupation (i.e., total number of edge atoms) from being completely devoid of edge atoms ($N_{\text{H}} = 0$ and $N_{\text{D}} = 0$) to having up to 2 extra edge atoms (i.e., $N_{\text{edge}} = N_{\text{H}}^0 + 2$). We limit ourselves to super states of only +2 as this reduces the number of isomers. Given that the larger molecules are not usually found in highly de-hydrogen/deuterated partial states, we also consider that D atoms can only be attached to the duo rings of the PAHs, that is, all solo rings have only H atoms in them. Thus, the smallest deuterated species for coronene, circumcoronene and circumcircumcoronene are $C_{24}D$, $C_{54}H_6D$ and $C_{96}H_{12}D$, respectively. Both these choices are also supported by the IR studies and neither of these choices has an important impact on our results, but they considerably speed up the computing time.

For the upcoming analysis it is important to keep in mind then that for partial species with $N_{\text{edge}} > N_{\text{solo}}$, deuterium atoms are attached to an aromatic position (see Figure 4.1); while for species in super states deuterium can be attached to either an aromatic position or an aliphatic position (Figure 4.1). Regarding ionization states, we considered anions ($Z = -1$), neutrals ($Z = 0$) and cations ($Z = 1$). Other states are not relevant under the physical conditions we probe.

4.2.2. Molecular Properties

We use the molecular characteristics described in Andrews et al. (2016). Given the lack of specific molecular properties for deuterated species, we decided to use the properties of the homogenic hydrogenated species in Andrews et al. (2016) for all (deuterated and heterogenic) isomers with the same number of edge atoms. This includes the ion-

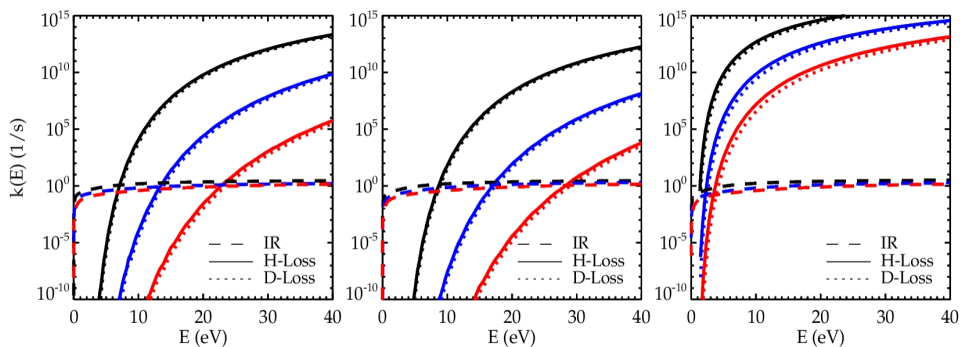


Figure 4.2: Comparison of the IR emission and photodissociation rates for H and D losses as a function of internal energy of the PAHs. The rates determined for coronene, circumcoronene and circumcircumcoronene derivatives are shown in black, blue and red, respectively. The left panel shows the rates for the PAHs in partial states with a total number of edge atoms $N_{\text{edge}} = N_{\text{H}}^0 - 1$, where N_{H}^0 is the number of edge atoms of the PAHs in their normal state (i.e., 12 for coronene, 18 for circumcoronene and 24 for circumcircumcoronene). We have plotted these to exemplify the rates for molecules with an odd number of edge atoms. The middle panel shows the rates for the normal state molecules, exemplifying also the rates for PAHs with an even number of edge atoms. The right panel shows the rates for the first super-state molecules (i.e., with $N_{\text{edge}} = N_{\text{H}}^0 + 1$) to illustrate the rates for super-state PAHs.

ization potentials (IP) and electron affinities (EA) (i.e., the inverse linear relation between these energies and the edge occupation of each PAH), ionization yields, UV absorption cross sections, polarizabilities, IR cross sections and density of states.

4.2.3. Reactions with Deuterium

As mentioned before, Andrews et al. (2016) included ionization and electron recombination of PAHs, (multiphoton) H and H₂ dissociation processes, reactivity with H, and Eley-Rideal abstraction of H₂ from superhydrogenated species. Here, we include PAH reactivity with D, direct D-loss through photodissociation, and Eley-Rideal abstraction of D₂ and HD from species in super states. It is important to mention that we will not consider H₂ photodissociation, since this process will hardly compete against H and D losses in the environments sampled in this work (Andrews et al. 2016).

Photodissociation

Photodissociation rates of H-loss are calculated using the same activation energies and entropies as in Andrews et al. (2016). For species in partial states we then consider activation energies of $E_{\text{act}} = 4.6$ and 4.1 eV, and entropies of $\Delta S = 44.8$ and 55.6 J/K/mol, for species having an even and odd number of edge atoms, respectively (and for all charge states admitted in the model). In order to calculate the photodissociation rate of D-loss from species in partial states, we modified the energies taking into account the different zero-point energies of C-H and C-D bonds (i.e., 0.09 eV). This value comes from a comparison between the ZPE of CH₄ and CD₄ molecules using calculations at the B3LYP/4-31G level. No scaling was applied to the ZPE to account for anharmonicity.

Figure 4.2 shows a comparison of the IR emission and the photodissociation rates as a function of internal energy of hydrogenated PAHs. This illustrates that there are only minor differences in the resulting H and D-loss rates over the relevant energy range.

We consider that the partial species first lose all the edge atoms in duo rings. For PAHs with an even number of edge atoms we include a term in the estimation of the j -loss rate, to account for the number of H and D atoms in each molecule:

$$\tilde{k}_j = \frac{N_{j,duo}}{(N_{edge} - N_{solo})} k_j \quad (4.1)$$

where k_j is the loss rate given by expression (7) in Andrews et al. (2016); and $N_{j,duo}$ corresponds to the total number of j atoms in duo rings that the PAH can lose. For PAHs with an odd number of edge atoms we consider $\tilde{k}_j = k_j$ since the PAH will lose the edge atom left alone in the duo ring. Once all edge atoms in duos are stripped off the PAH, then the molecule starts losing the solo H-atoms with $E_{act} = 4.6$ eV, and change in entropy of $\Delta S = 44.8$ J/K/mol (see more in Andrews et al. 2016).

Regarding PAHs in super states, for the H-loss we adopt the binding energies of an extra H-atom in a duo position, which are of 1.4 eV for the anion, 1.4 eV for the neutral and 1.55 eV for the cation, and an activation entropy of 55.6 J/K/mol (Bauschlicher & Ricca 2014). For the D-loss we again consider the 0.09 eV difference in the activation energy with respect to the values used for the H-loss (Figure 4.2). We assume extra H and D atoms always stick to duo positions for all molecules. For PAHs with an even number of edge atoms we also include a term in the estimation of the photodissociation rate of j -loss, to account for the number of H and D atoms in aliphatic groups:

$$\tilde{k}_j = \frac{N_{j,alip}}{(N_{H,alip} + N_{D,alip})} k_j \quad (4.2)$$

where in this case, $N_{H,alip}$ and $N_{D,alip}$ correspond to the total number of H and D atoms in aliphatic groups, respectively. For PAHs with an odd number of edge atoms we consider $\tilde{k}_H = k_H$ in case the PAH has a H₂ left; $\tilde{k}_D = k_D$ in case the PAH has a D₂ left; and $\tilde{k}_H = 0.5 \times k_H$ and $\tilde{k}_D = 0.5 \times k_D$ in case the PAH has an HD left.

Figure 4.3 shows the variation of the D-loss rates with G_0 for the heterogenic species with $N_D = 1$ and $N_{edge} = N_H^0 - 1$, N_H^0 , and $N_H^0 + 1$. Regarding partial and normal species, we see that for coronene single-photon events dominate, while for the larger PAHs multiphoton events take place. For PAHs in super states on the other hand, due to the low activation energies, single-photon events dominate for all species. These results are very much in line with those obtained for the corresponding H-loss rates, since the energy differences between C-D and C-H bonds are small.

Addition Rates

For positively ionized species we consider the H addition rate derived from the experiments of Le Page et al. (1997) on the hydrogenation of coronene, that is a rate of 1.4×10^{-10} cm³/s (see Andrews et al. 2016). We use this rate for all positively ionized species and for all N_{edge} states. For D addition we divide this rate by a factor of $\sqrt{m_D/m_H} \sim 1.4$ to take into account the slightly larger mass of the D atom, m_D , over that of the H atom, m_H .

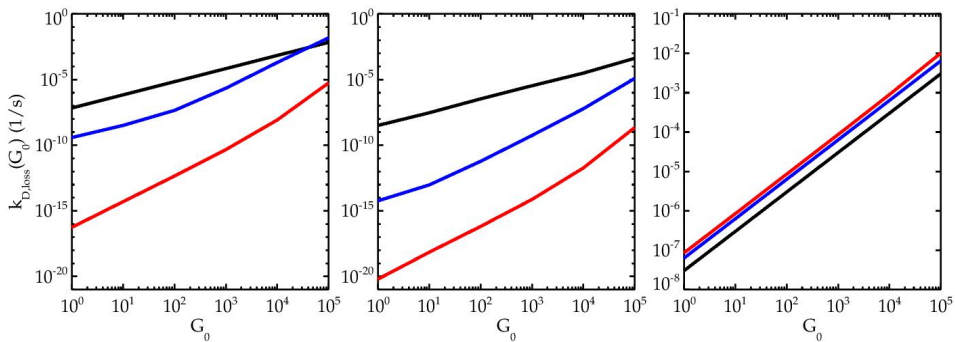


Figure 4.3: Deuterium loss rates through photodissociation as a function of the intensity of the UV field, G_0 . These rates are the resulting one considering also the H-loss and IR emission as relaxation channels. The rates are shown for neutral heterogenic molecules with 1 D atom in their edges. The black curves refer to coronene molecules, while the blue and red curves refer to circumcoronene and circumcircumcoronene molecules respectively. The left panel shows the D-loss rates for the partial-state PAHs $C_{24}H_{10}D$, $C_{54}H_{16}D$ and $C_{96}H_{22}D$, with the D atom alone in a duo ring. As in Figure 4.2 we have plotted these to exemplify the rates for molecules with an odd number of edge atoms. The middle panel shows the rates for the heterogenic normal molecules (i.e., $N_{\text{egde}} = N_{\text{H}}^0$): $C_{24}H_{11}D$, $C_{54}H_{17}D$ and $C_{96}H_{23}D$. The right panel shows the rates for the heterogenic molecules in the first super-state with an HD aliphatic group: $C_{24}H_{12}D$, $C_{54}H_{18}D$ and $C_{96}H_{24}D$. For coronene molecules the rates scale linearly with G_0 , while for the larger species multiphoton events are important for the normal and partial derivatives. The D-loss rate for the super-state molecules on the other hand, changes linearly with G_0 for all species.

For neutral PAHs we use the geometrical cross sections of each molecule, σ_{geom} , together with the energy barriers given by Rauls & Hornekær (2008) for the H addition to neutral coronene:

$$k_{j,\text{add}} = \sigma_{\text{geom}} \sqrt{\frac{8 k_B T_{\text{gas}}}{\pi m_j}} \exp(-E_{\text{barrier}}/k_B/T_{\text{gas}}), \quad (4.3)$$

where k_B is the Boltzmann constant; T_{gas} is the gas temperature; E_{barrier} is the energy barrier for the addition; and m_j is the mass of the j atom reacting with the PAH. For super states we consider the energy barriers from Rauls & Hornekær (2008) for both H and D addition. For the partial species we do not consider any barriers ($E_{\text{barrier}} = 0$), and we adopt a 7% efficiency as found for cations by Demarais et al. (2014). The H and D addition reactions to anionic PAHs on the other hand, is considered as a dissociative attachment process (Demarais et al. 2012). That is, the H addition rate is $7.8 \times 10^{-10} \text{ cm}^3/\text{s}$. Again for the D addition rate we divide by a factor of ~ 1.4 to account for the different atomic masses, which leads to a D addition rate of $5.5 \times 10^{-10} \text{ cm}^3/\text{s}$ for anionic molecules.

It is important to keep in mind that for PAHs in super states, we must consider the edge atoms each PAH has prior to the atom addition, since this determines whether there will be an H_2 , HD or D_2 new aliphatic group in the PAH. To include this, we consider an extra factor in the reaction rate given by $P_j = N_{j,\text{duo}}/(N_{H,\text{duo}} + N_{D,\text{duo}})$, where $N_{H,\text{duo}}$

Table 4.1: Physical conditions used in the model.

Model	G_0 (Habing units)	n (cm ⁻³)	n_D (cm ⁻³)
Diffuse Cloud	1	500	0.016
PDR	1000	10 ⁶	16

and $N_{D,duo}$ correspond to the number of aromatic H and D atoms in duos prior to any additions, respectively. Thus, for example, the PAH $C_aH_bD_c$ with an HD aliphatic group will form from the H addition to the corresponding isomer(s) of the PAH $C_aH_{b-1}D_c$, where the reaction rate is given by $P_D(C_aH_{b-1}D_c) \times k_{H,add}(C_aH_{b-1}D_c)$; and it will form from the D addition to the corresponding isomer(s) of the PAH $C_aH_bD_{c-1}$, where the rate is given by $P_H(C_aH_bD_{c-1}) \times k_{D,add}(C_aH_bD_{c-1})$.

Abstraction Rates

We consider the same parameters for the H_2 abstraction as in Andrews et al. (2016). Given the lack of data, we use the same parameters for the abstraction of H_2 , D_2 and HD. The cross section used comes from experiments on the deuteration of coronene, and corresponds to a value of 0.06 \AA^2 (Mennella et al. 2012). We consider the first abstraction as a barrierless process, and the second abstraction as involving a 0.01 eV barrier (Bauschlicher & Bakes 2001; Rauls & Hornekær 2008). The only difference between the rates comes from the mass of the atom colliding with the PAH.

Just like for the addition processes to PAHs in super states, we include a term of the form $P_j = N_{j,alip}/(N_{H,alip} + N_{D,alip})$, to consider the atom (in an aliphatic group) that the colliding atom is more likely to abstract. When a j atom collides with an HD aliphatic group, we consider it is equally likely to abstract the H as to abstract the D. We assume this since we expect the energy difference to be insignificant.

4.3. Results

We consider two different environments where the total density, n , and the intensity of the UV radiation field, G_0 , are kept fixed, while the density of atomic H, n_H , is varied (see Table 4.1). For the first run we considered $G_0 = 1$ and a total density of 500 cm^{-3} (to simulate a diffuse cloud in the ISM such as ζ Oph), while for the second run we considered a $G_0 = 1000$ and total density of 10^6 cm^{-3} (relevant for a PDR environment). We adopted a $(D/H)_{ISM}$ ratio of 1.6×10^{-5} , and therefore the D density remains fixed at 0.016 cm^{-3} and 16 cm^{-3} for the first and the second runs respectively.

We chose to perform two runs because the edge occupation distribution of PAHs, $f(N_{edge})$, depends on the available H (and D) but also on the ionization balance, which at any given G_0/n_H ratio varies for different values of G_0 and n (this is because our IP and EA values depend on the edge occupation of each molecule).

4.3.1. Relative Abundance Distribution of PAHs

Figure 4.4 shows the total edge occupation distribution of each PAH for the two runs. For the diffuse ISM run ($G_0 = 1$, $n = 500 \text{ cm}^{-3}$) we show the results for the larger molecules (circumcoronene and circumcircumcoronene), while for the PDR model ($G_0 = 1000$, $n = 10^6 \text{ cm}^{-3}$) we show the results for the smaller species (coronene and circumcoronene). As seen from the Figure, PAHs of different sizes show different $f(N_{\text{edge}})$ distributions. At a given G_0/n_H we see the smallest molecule, coronene, stripped off of all edge atoms (black curve), while the larger molecules –as they are more difficult to dissociate– are overall in normal to super states. There is some contribution from partial states for the intermediate PAH, circumcoronene, at $G_0/n_H = 1$ (second run) but is $< 1\%$. For the largest PAH, circumcircumcoronene, there are no partial species.

Comparing top and bottom panels, at higher G_0 and n values the transition from partial to normal and super states occurs at slightly higher G_0/n_H ratio (grey dashed lines). This shift is due to the difference in the $f(Z)$ distribution between the two runs, which is itself given by the $\text{IP}(N_{\text{edge}})$ and $\text{EA}(N_{\text{edge}})$ relations we adopted. At a given G_0/n_H ratio, there is a larger fraction of anions in the second run than in the first one. For example, for circumcoronene at $G_0/n_H = 0.002$ the charge state of PAHs is $f(-1) \simeq 50\%$, $f(0) \simeq 50\%$, and $f(1) \simeq 0.2\%$ in the first run, while in the second run the fractions are $f(-1) \simeq 68\%$, $f(0) \simeq 32\%$, and $f(1) \simeq 0.07\%$. Similarly, at $G_0/n_H = 1$ in the first run, $f(-1) \simeq 69\%$, $f(0) \simeq 30\%$ and $f(1) \simeq 0.1\%$, while in the second run the relative contributions are $f(-1) \simeq 82\%$, $f(0) \simeq 18\%$, and $f(1) \simeq 0.04\%$. Since anions have higher addition rates, the transition from PAHs with less to more edge atoms happens at a higher G_0/n_H in the second run. This is valid for all species. For coronene, the transition from $N_{\text{edge}} = 0$ to partial species occurs at $G_0/n_H \simeq 0.0025$ in the first run, and at $\simeq 0.004$ in the second run; the transition for circumcoronene molecules from (mostly) normal to super states occurs at $G_0/n_H \simeq 0.004$ in the first run, and at $\simeq 0.005$ in the second run; while the transition for the largest PAH occurs at $G_0/n_H \simeq 0.0035$ and $\simeq 0.004$, for the first and second run respectively.

Aside from the shift, the behaviour of the N_{edge} distribution is similar between both runs. Small PAHs are rarely found in normal and super states because they are more prone towards dissociation, and therefore we see coronene as a carbon cluster for a wide range of G_0/n_H ratios. As n_H increases, so does N_{edge} . Up to $N_{\text{edge}} = 8$ the distributions $f(N_{\text{edge}})$ are rather symmetrical with respect to the G_0/n_H given by the grey line in each panel. The distribution of partial species with $N_{\text{edge}} \geq 9$ are different. This is because of the IP/EA dependence on N_{edge} . For coronene, PAHs with less than $N_{\text{edge}} = 8$, have electron sticking coefficients s_{e^-} higher than 0.9, which leads to higher electron recombination rates than for PAHs with more edge atoms. Therefore the PAHs with lower N_{edge} will tend to electron recombine more, and as mentioned before, anions in our models have higher H and D addition rates than neutrals. For $N_{\text{edge}} \geq 9$ electron sticking coefficients are < 0.5 , and therefore the electron recombination rates are severely decreased compared to those of smaller PAHs (e.g., with $s_{e^-} \sim 1$ the electron recombination rates are 2.4 times higher than the rate with $s_{e^-} \sim 0.4$, and $\sim 10^4$ times higher than for normal coronene which has an $s_{e^-} = 7.8 \times 10^{-5}$). Once there are normal molecules, the H and D attachment rates are the same for all Z , since we use the barriers from Rauls & Hornekær (2008). These barriers determine the distribution of the super states where the first addition has a barrier, while the second does not (see $N_{\text{edge}} = 13$ and 14 distributions).

For circumcoronene and circumcircumcoronene, $EA > 1$ eV and thus $s_{e^-} = 1$, leading to the same electron recombination rates for all N_{edge} . Thus, for the larger molecules, the $f(N_{\text{edge}})$ distributions are symmetrical relative to G_0/n_H (grey lines).

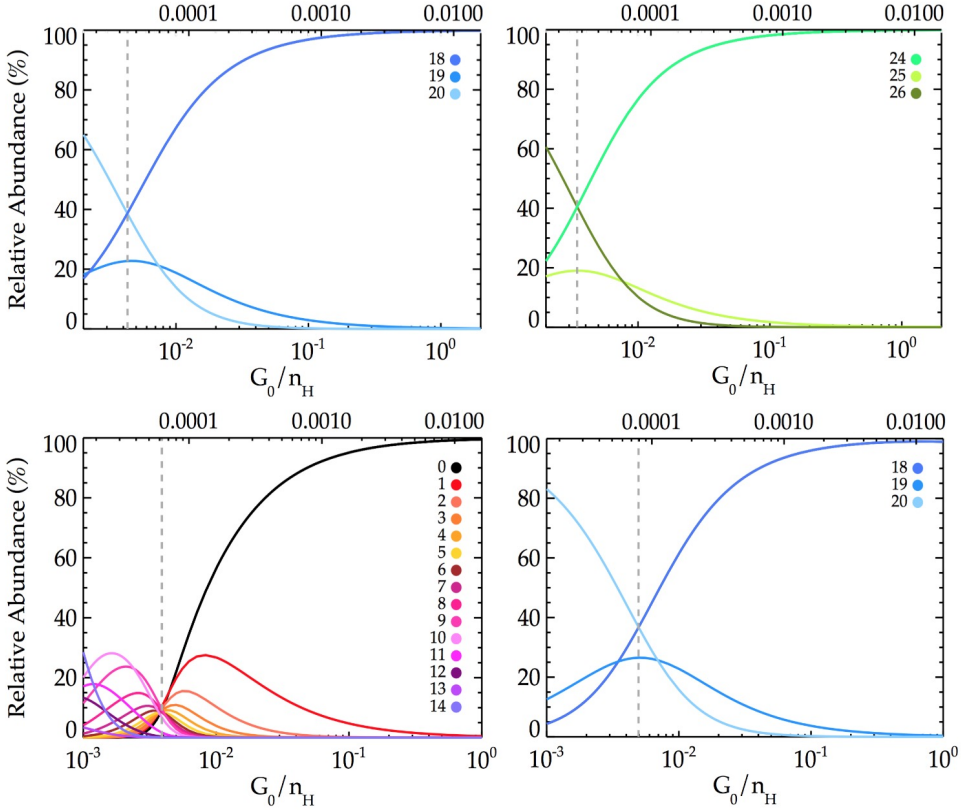


Figure 4.4: Relative abundance of PAHs with a number of edge atoms N_{edge} as a function of G_0/n_H . Each curve considers the sum of the relative abundance of all charge states for each species. The top panels show the distribution $f(N_{\text{edge}})$ for circumcoronene (left) and circumcircumcoronene (right) in the first run, where we considered $G_0 = 1$ and a total density $n = 500 \text{ cm}^{-3}$, illustrating a diffuse ISM type of environment (Table 4.1). The bottom panels show the distribution of coronene (left) and circumcoronene (right) derivatives for the second run, where we considered $G_0 = 1000$ and total density $n = 10^6 \text{ cm}^{-3}$, exemplifying a more PDR-like environment. The grey dashed lines indicate the G_0/n_H at which the large species, circumcoronene and circumcircumcoronene derivatives, change from normal to super states; while coronene derivatives change from being completely devoid of edge atoms (i.e., C_{24} , black curve) to higher occupation states. The top axis shows the atomic n_D/n_H density ratio. In general, results are similar between the two runs (hence we do not show the results for coronene derivatives in the first run, nor for circumcircumcoronene molecules in the second run). The main difference is in the transition points, which occur at slightly higher G_0/n_H in the second run. This shift in the transition points is related to variations in the charge state distribution of the species (read text).

4.3.2. Deuterium Content in PAHs

Regarding the deuteration of PAHs, while coronene can hold only 1 D atom in its edge, the larger PAHs can hold up to 2 (although PAHs with 1 D atom always dominate the heterogenic species). Most of the PAHs will be homogenic, containing only H atoms in their edges. Homogenic species containing only D are only found for coronene as $C_{24}D$. For coronene, more partial species can only survive in highly shielded environments, where the difference between n_H and n_D is large enough to overcome the fact that when dissociating it will be more likely for the PAH to lose an H rather than a D atom (coronene species will have 1 D only). The larger molecules on the other hand, will always be heterogenic.

Figure 4.5 shows the (D/H) ratio for the three PAH species. Coronene derivatives are mostly completely dehydrogenated for most of the G_0/n_H range in both runs: C_{24} represents about 99.8% of the population at $G_0/n_H = 2$ in the first run, and 99.5% of the population at $G_0/n_H = 1$ in the second run. The (D/H) for coronene molecules then is given by $[C_{24}D]/[C_{24}H]$. This ratio is basically determined by the addition rates of atoms to the C_{24} molecule: $k_{D,add}/k_{H,add} \propto (n_D/n_H) \times \sqrt{(m_H/m_D)}$, which is lower than the n_D/n_H available in the medium by a factor of $\sqrt{2} \sim 1.4$ (dashed grey line in Figure 4.5). This relation is valid down to $G_0/n_H \sim 0.005$ – 0.006 , where species with $N_{edge} > 1$ atoms start increasing their abundance $> 40\%$. In this new regime, the (D/H) ratio which is given by $\sum_{n=1}^N [C_{24}H_nD] / \sum_{m=1}^{N+1} (m[C_{24}H_m])$ (where the sum runs over all N_{edge} relevant at a given G_0/n_H ratio) can be approximated by $[C_{24}H_nD] / ((n+1)[C_{24}H_{n+1}])$ where $n+1 = N_{edge}$ that dominates the mixture.

From Figure 4.5 we see there is a dip in the (D/H) ratio for coronene. This dip appears once partial species start dominating the mixture. Even more, we notice that the slope of the dip is steeper when the species with low N_{edge} appear, and becomes flatter as species with higher N_{edge} come into play. This happens because the formation and destruction mechanisms vary for molecules with significantly different N_{edge} . These mechanisms add extra terms to the expressions for the D and H content in coronene species. Since H-only molecules are far more abundant than the heterogenic species, these extra terms become even more relevant for the H-only species, which in turn makes the (D/H) ratio lower than $n_D/(\sqrt{2}n_H)$, which is the factor valid at high G_0/n_H ratios.

We saw that at high G_0/n_H ratios $(D/H) = [C_{24}D]/[C_{24}H]$, where the formation of $C_{24}D$ is given by the D addition to C_{24} , and the formation of $C_{24}H$ by the H addition to the C_{24} molecule (destruction mechanisms are similar for both species). In more shielded environments on the other hand, heterogenic species with 1 D (i.e. $C_{24}H_nD$) are mainly formed by the H addition to the $C_{24}H_{n-1}D$ molecules, and not due to the D addition to H-only PAHs. This is because of the increasing difference between n_H and n_D at lower G_0/n_H ratios (e.g., differences greater than 10^4 at $G_0/n_H < 0.005$ in the second run). Regarding H-only species, coronene molecules with $N_{edge} \leq 4$ are mainly formed by the H addition to anions (and ionization of anions). Partial coronene PAHs with $5 \leq N_{edge} \leq 8$ are formed not only by the H addition to anions, but also from the loss of H atoms from the $N_H + 1$ molecules. Larger species with $N_{edge} = 9$ – 12 , will be formed by those same processes, plus the H addition to neutrals since these molecules do not easily recombine with electrons. Also the destruction rates for these species are slightly lower than for the molecules with lower N_{edge} (which are mainly destroyed by electron recombination). Notice that the decrease in the (D/H) ratio relative to the $n_D/(\sqrt{2}n_H)$ relation in Figure 4.5 (right panel) becomes the largest once species with $N_{edge} = 9$ and 10 atoms become important. This is also the point where the

slope of the dip starts flattening. This happens because for these species, even though we are adding formation processes, such increase is not dramatic because H addition to neutrals is slower than for anions. For the second run, at the lowest G_0/n_H ratio super state species become as relevant as $N_{\text{edge}} = 10$ and 11 species. For these molecules, the destruction rates are higher than for the partial species, but also the formation rates are higher. Therefore as we go to more shielded environments, the change in the (D/H) ratio is not as steep as for high G_0/n_H ratios where PAHs with less N_{edge} atoms dominate the mixture.

For the larger species the situation is different than for coronene. For both circumcoronene and circumcircumcoronene, the distribution of species is dominated by the normal molecule at high G_0/n_H ratio, and by super states in more shielded environments. Hence, we see again the same dip as for coronene, but extending throughout a wider G_0/n_H range, since these molecules are more likely to be found in their normal states rather than in partial states. At high G_0/n_H ratio the (D/H) mainly follows the $[C_{54}H_{17}D]/(18[C_{54}H_{18}])$ ratio in the case of circumcoronene, and $[C_{96}H_{23}D]/(24[C_{96}H_{24}])$ for circumcircumcoronene. As mentioned above, these larger molecules can hold 2 D atoms in them (even 3 but at relative abundances $\sim 10^{-8}\%$), but their contributions will not dominate the (D/H) ratio. At $G_0/n_H = 1$ in the second run, considering circumcoronene molecules with $N_{\text{edge}} = 17-19$, the contribution from $C_{54}H_nD$ species is $\approx 0.3\%$, while $C_{54}H_nD_2$ species are $\approx 6 \times 10^{-4}\%$. Similarly, for circumcircumcoronene, considering PAHs with $N_{\text{edge}} = 24-26$, those with 1 D atom contribute $\approx 0.09\%$, while species with 2 D atoms contribute $\approx 4 \times 10^{-5}\%$. We notice that the contribution from heterogenic species is slightly larger for circumcoronene than for circumcircumcoronene derivatives. This is because the H and D addition processes are dominated by anions for both species (i.e., we do not consider the cross sections of the PAHs for these rates) and because –as mentioned before– there are slightly more neutrals for circumcircumcoronene in normal to super states, which have lower addition rates than the anionic population.

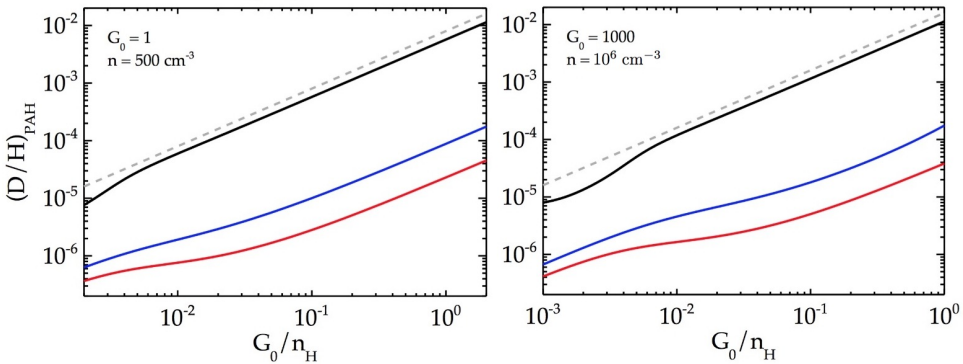


Figure 4.5: Variation of the (D/H) ratio in PAHs as a function of G_0/n_H . Here we use the same color scheme as in Figure 4.2. The left panel shows the results for the first run (diffuse ISM), and the right panel shows the results for the second run (PDR). The dashed grey lines indicate the n_D/n_H variation. As seen from the Figure, the variation of the (D/H) ratio for each PAH is similar between both runs. The difference is in the fact that in the second run we go further down to a $G_0/n_H = 0.001$, and thus, we see the molecules going into the super-state regime.

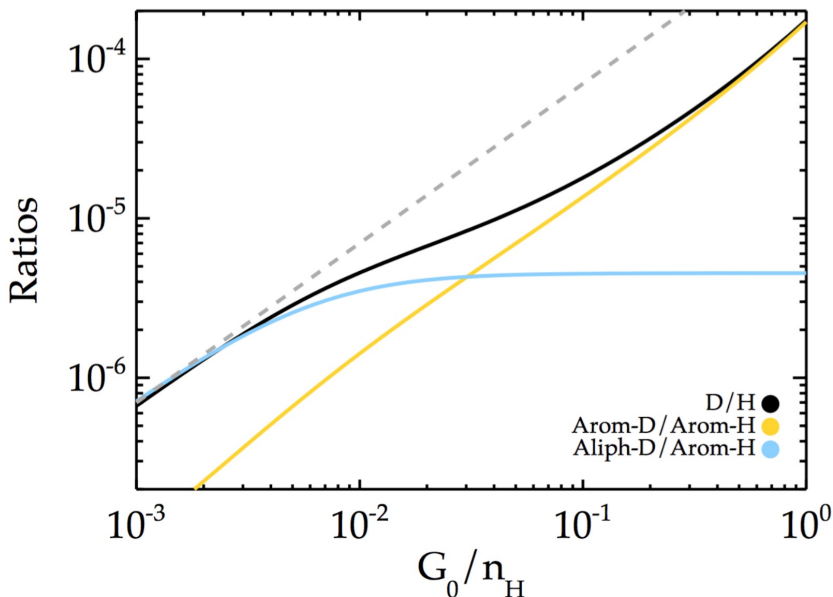


Figure 4.6: Comparison of the aromatic and aliphatic D relative to the aromatic H content of circumcoronene derivatives at $G_0 = 1000$ and $n = 10^6 \text{ cm}^{-3}$. The total (D/H) ratio in circumcoronene molecules is shown in black, while the dashed grey line is the $n_D/(\bar{m} \sqrt{2}n_H)$ relation, with $n_D = 16 \text{ cm}^{-3}$ and $\bar{m} = 16.2$, the weighted average number of aromatic H atoms in circumcoronene derivatives at $n_H = 10^6 \text{ cm}^{-3}$. Here we see the (D/H) ratio in circumcoronene molecules follows the (arom-D/arom-H) relation at high G_0/n_H , while in more dense environments it follows the (aliph-D/arom-H) ratio which is proportional to the $n_D/(\bar{m} \sqrt{2}n_H)$ relation at the lowest G_0/n_H considered.

The formation of circumcoronene and circumcircumcoronene molecules in normal states will be affected not just by the addition processes, but also by the fast dissociation of molecules in super states. The (D/H) ratio then follows the aromatic ratio, (arom-D/arom-H), as long as the normal species dominate the mixture (see Figure 4.6). Once super state molecules become more abundant, the (D/H) ratio starts approaching the aliphatic-D over aromatic-H ratio, (aliph-D/arom-H), which follows $n_D/(\sqrt{2}n_H\bar{m})$, where \bar{m} is the average number of H atoms in aromatic modes in super state molecules weighted by their respective contributions (e.g., at $G_0/n_H = 0.001$ for $G_0 = 1000$, $\bar{m} = 16.2$ and 22.3 for circumcoronene and circumcircumcoronene, respectively). If we were to extend this further to more dense environments, we would see the curve reaching the $n_D/(16\sqrt{2}n_H)$ and $n_D/(22\sqrt{2}n_H)$ limit for circumcoronene and circumcircumcoronene derivatives respectively, as the population would be fully dominated by the maximum N_{edge} adopted in our calculations.

Figure 4.7 shows the variation of the aromatic and aliphatic-D content in super state derivatives of circumcoronene and circumcircumcoronene species. From here we see that heterogenic PAHs in super states have more aliphatic than aromatic D at $G_0/n_H < 0.01$ in a diffuse cloud environment, and at $G_0/n_H < 0.02$ in a PDR-like environment. At high G_0/n_H ratios there is more aromatic D than aliphatic D simply because the normal molecules dominate the population of PAHs (increasing the aromatic D-content).

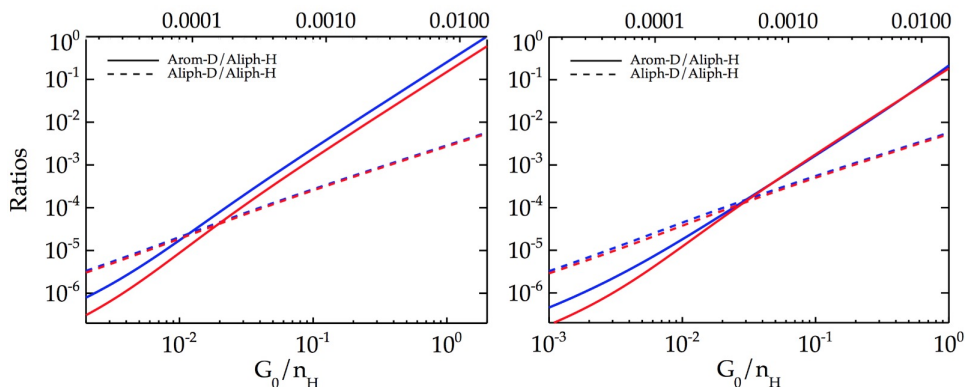


Figure 4.7: Variation of the aromatic and aliphatic D relative to the aliphatic H content in PAHs. Again we use the same color scheme as in Figure 4.5. The left panel shows the results for the first run (diffuse ISM), and the right panel shows the results for the second run (PDR). The top axis shows the atomic n_D/n_H density ratio. PAHs in super states will have the D (mostly 1 D) preferably in an aliphatic mode rather than in an aromatic mode. This happens even when comparing isomers of equal N_{edge} at high G_0/n_H ratios. However at high G_0/n_H ratios, molecules in normal state contribute greatly to the amount of aromatic D. Therefore we see $(\text{arom-D}/\text{aliph-H}) > (\text{aliph-D}/\text{aliph-H})$ down to a G_0/n_H of a few times 0.01. That is the point where addition processes overcome the large dissociation rates adopted for super-state molecules, and species with $N_{\text{edge}} = N_H^0 + 2$ start to appear. The shift in this transition point between both runs is related to the different charge state distributions, as explained for the results of Figure 4.4.

The $(\text{aliph-D}/\text{aliph-H})$ follows the ratio between the D and H addition rates to normal (and super state) molecules. Since we use the same barriers for D and H additions, $(\text{aliph-D}/\text{aliph-H}) \propto n_D/(\bar{m} \sqrt{2} n_H)$ where \bar{m} is the average number of aliphatic H atoms in super-state molecules, weighted by their corresponding abundance (e.g., for circumcoronene $\bar{m} = 2$ at $G_0/n_H = 1$, and $\bar{m} = 3.54$ at $G_0/n_H = 0.001$ in the PDR run). PAHs with aliphatic D (i.e., HD aliphatic group) will be mainly formed by the D addition to H-only normal PAHs. When facing photon absorption at high G_0/n_H ratios, these molecules will preferably lose the H atom (about 3 times more often than the D), retaining the D atom in an aromatic position. However, once addition processes overcome the high dissociation rates for super states (at $G_0/n_H \sim 0.01$; see Figure 4.7), the more likely thing to happen is that the molecules will add another H atom, forming species with HD and HH aliphatic groups.

Heterogenic species with only aliphatic H (i.e., with aromatic D) are mainly formed from the H addition to other heterogenic species. For example, $\text{C}_{54}\text{H}_{18}\text{D}$ with an HH aliphatic group, will be formed from the H addition to the $\text{C}_{54}\text{H}_{17}\text{D}$ molecule. This occurs at a lower rate than the formation of $\text{C}_{54}\text{H}_{18}\text{D}$ with an HD aliphatic group, since H only species (i.e., $\text{C}_{54}\text{H}_{18}$ molecules) are about 300 times more abundant than $\text{C}_{54}\text{H}_{17}\text{D}$ at $G_0/n_H = 1$ in the PDR run. This 300 factor compensates the fact that the H addition rate is about $(n_D/(\sqrt{2} n_H))^{-1} \sim 88$ times greater than the D addition rate, and also the fact that in order to create an HH aliphatic group, the H atom can be added to 11/12 positions (we assume aliphatic groups are in duo rings only). Therefore even though $n_H > n_D$, H only molecules are so abundant, that more aliphatic D will be created after the first addition to the normal PAHs. Once we go into lower G_0/n_H ratios, the more likely thing to happen to the molecules with an HH aliphatic group is to attach another H to the available position, which most of

the times will be another H. Only once in a while the new H will fall on the aromatic D contributing again to the formation of molecules with HH-HD aliphatic groups.

According to our results –and assuming the three PAHs studied here are good representatives of PAHs of different sizes– small species have higher (D/H) ratios than larger ones, even though larger species can hold more than 1 D per molecule, while small PAHs hold only 1 D atom in their edges. This is partly because in larger species there are more edge positions to be occupied by (mostly H) atoms, and partly because, due to the PAH size difference, at a given G_0/n_H ratio larger species are mainly found in their normal (and super) state and therefore having about N_H^0 (mostly H) atoms, while smaller PAHs like coronene are found as completely dehydrogenated with small traces of $N_{\text{edge}} = 1$ molecules.

4.4. Discussion

4.4.1. Deuterium fractionation of PAHs

The largest $(D/H)_{\text{PAH}}$ ratios are attained by coronene molecules. However it should be noted that under the conditions probed here, coronene molecules are mostly C_{24} clusters, which may be rapidly destroyed in the ISM. From that perspective, we ignore coronene in the subsequent discussion (it was mainly included in our calculations to illustrate the trends with PAH size). From Figures 4.5, 4.7 and 4.8, we see that the behaviour of the (D/H) ratio with G_0/n_H is similar between the two runs (diffuse cloud vs the PDR-like environment). The main difference is given by the n_D/n_H ratio, that will shift the curves upwards or downwards depending on the atomic D relative to the atomic H available in the gas phase. As we have adopted a constant elemental abundance ratio of $(D/H)_{\text{ISM}} = 1.6 \times 10^{-5}$, we can take the variation in G_0/n_H as the variation of the H/H₂ ratio in the gas phase. Our results show that the (D/H) ratio in the PAHs reflects the (D/H) ratio in the reservoir. As the reservoir is never very highly fractionated in our calculations, the (D/H) ratio of the PAHs is dominated by the species where one H atom has been replaced by a D.

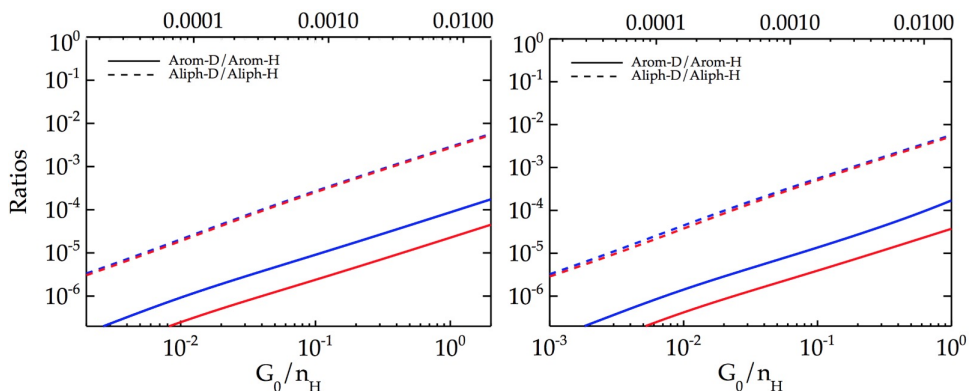


Figure 4.8: Variation of the (arom-D/arom-H) and (aliph-D/aliph-H) ratios for circumcoronene and circumcircumcoronene. Again we use the same color scheme as in Figure 4.5. The left panel shows the results for the first run (diffuse ISM), and the right panel shows the results for the second run (PDR). The top axis shows the atomic n_D/n_H density ratio. Here we see that for both runs and both PAH species, the aliphatic (D/H) ratio is greater than the aromatic (D/H) ratio for all G_0/n_H ratios considered in the model (see more in the discussion).

The atomic (D/H) ratio can be much larger in the diffuse ISM and in PDRs, as H_2 is well protected against photo-destruction through self-shielding, while the photo-destruction of HD is dominated by dust shielding. As a result, photo-destruction of HD is important far deeper into a cloud or PDR than H_2 . This is counteracted by additional HD formation not available to H_2 . As for H_2 , HD can be formed on grain surfaces, but for diffuse clouds –once some H_2 is present– the dominant formation route of HD is $\text{D}^+ + \text{H}_2 \rightarrow \text{H}^+ + \text{HD}$ (Black & Dalgarno 1973; Le Petit et al. 2002). In warm, dense PDRs, HD can also be formed efficiently by the direct reaction, $\text{D} + \text{H}_2 \rightarrow \text{H} + \text{HD}$, which has an activation barrier of 3820 K. Still, models show photo-destruction wins, leading to an enhancement of the atomic (D/H) ratio by up to a factor of 100 (Le Petit et al. 2002). Hence, deuterium fractionation of PAHs is predicted to be modest in diffuse clouds and in PDRs.

Much higher deuterium fractionations of interstellar molecules ($\approx 10^{-2}$) have been observed for molecules such as HCO^+ and HCN inside dark clouds (Lis et al. 2002). Observations of hot Corinos associated with low mass protostars have also revealed deuterium fractionations of the order of ≈ 1 , and even the presence of multiply deuterated species (Ceccarelli et al. 2007). The deuterium fractionation of these species has been ascribed to H and D atoms reacting with CO and other species on grain surfaces, during a cold dense phase of the evolution of the cloud. After evaporation of the ices, these fractionation effects “live on” for some 10^4 yr in the warm gas, before gas phase chemistry “equilibrates” the deuterated species with the local physical conditions (Charnley et al. 1997). The high deuterium fractionation of H_3^+ can reach levels where H_2D^+ , HD_2^+ , and even D_3^+ are more abundant than the parent species when the main destruction agent, CO, depletes in ices in these cores (Roberts et al. 2003). As PAHs are expected to be the last ones to deplete in ices inside dense cores (as their thermal velocity is a factor of ≈ 5 less than for CO), reactions of the type $\text{H}_2\text{D}^+ + \text{PAH} \rightarrow \text{H}_2 + \text{PAHD}^+$ could drive deuterium fractionation of PAHs to very high levels (Tielens 1992). Further deuteration may also occur if PAHs are accreted into ice mantles; e.g., due to photolysis (Sandford et al. 2000).

Once the core dissolves, ices evaporate, and the material finds itself in the PDR surface or in the diffuse ISM, the highly deuterium-enriched PAHs will “equilibrate” with the local physical conditions. The timescale for this depends on the PAH size, the binding energy involved, and the strength of the local radiation field. As Figure 4.3 illustrates, for a 100 C-atom PAH, the aromatic (D/H) ratio acquired in a dense core could survive over the lifetime of a PDR (10^4 yr) for a radiation field of $G_0 < 10^4$. In contrast, a 50 C-atom PAH cannot be exposed to a radiation field stronger than $G_0 \approx 10^2$ without losing its deuterium signature. In the diffuse ISM, both species will retain their high deuterium fractionation in the aromatic modes over relevant timescales (Figure 4.3). Because of the much lower binding energies, aliphatic groups will much more quickly return to the gas phase (steady state) fractionation value. Even for a large PAH, the timescale is ≈ 1 yr in the diffuse ISM.

4.4.2. Observations of interstellar PAHDs

Due to the difference in reduced mass, the C-D vibrational transitions of deuterated PAHs are shifted to longer wavelengths than the corresponding C-H modes. In particular, the aromatic C-D stretching mode (the counterpart of the $3.3\mu\text{m}$ aromatic C-H stretching mode) occurs at $4.4\mu\text{m}$, while aliphatic C-D stretching modes are at $4.6\text{--}4.8\mu\text{m}$ (analogue to the C-H bands at $3.4\text{--}3.5\mu\text{m}$). The $4\text{--}5\mu\text{m}$ region is a relatively clean region of the spectrum with no strong aromatic bands. The longer wavelength in- and out-of-plane bending modes of deuterated bonds also shift but into regions which are crowded with other PAH

bands. Weak bands at 4.4 and 4.6 μm have been detected in a few bright PDRs/HII regions, and have been ascribed to deuterated PAHs (Peeters et al. 2004; Onaka et al. 2014; Doney et al. 2016). It should be noted that these observations are very difficult, as the bands are very weak and –at the limited spectral resolution of these studies– corrections for atomic lines are challenging. The results show that only a small fraction (6 out of 53) of the sources show these bands (Doney et al. 2016). The implied deuterium fractionation for these sources ranges from 0.03¹ up to 0.4 (Doney et al. 2016). In addition, the results show that the aliphatic (D/H) ratio is higher than the aromatic (D/H) ratio, with the aliphatic (D/H) ratio varying from 0.1 to 1 for the detected sources (Doney et al. 2016).

Our calculations show that, in steady state, the deuterium fractionation in PAHs is directly related to the atomic (D/H) ratio in the gas. At an atomic (D/H) ratio of 10^{-2} , the calculated aromatic (D/H) ratio is only 10^{-4} while the aliphatic (D/H) ratio is 10^{-3} (Figure 4.8). In order to reach an aliphatic (D/H) ratio of 0.1 –the lowest value in the observed ratios– a gas phase atomic (D/H) ratio well above 0.1 is needed. Such a high atomic (D/H) ratio in the gas phase is at variance with models for PDRs. In agreement with the observations, our models do predict that PAHs in super states are substantially more deuterated than the purely aromatic molecules. However there is another issue somewhat “hidden” here: the presence of $\approx 10\%$ super-state-PAHs requires a $G_0/n_H \approx 0.03$ (Andrews et al. 2016). If the atomic (D/H) ratio in the gas phase is 0.1, this implies a total density of $n \approx 2 \times 10^5 G_0$ which for a PDR with $G_0 = 10^3$ would imply a density of $2 \times 10^8 \text{ cm}^{-3}$. Thus, the presence of a high abundance of D in super states requires a very dense but moderate UV field environment, and such conditions are untypical for PDRs. We note that this is a direct consequence of the low binding energy of the super states. As emphasized by Andrews et al. (2016), this low binding energy makes the appearance of the 3.4 μm band very unlikely. The current result on deuteration reinforces this point. Methyl groups provide an alternative interpretation for the 3.4 μm band. Now, the aliphatic H in CH_3 groups is bound by $\approx 3.7 \text{ eV}$, and hence this H (or D) is much less labile under irradiation by strong UV fields. The (photo)chemistry of methyl groups is not well understood as the formation of a tropylium structure is involved (Zhen et al. 2016; Rapacioli et al. 2015). Reaction of this structure with atomic H (or D) back to a methyl group may well be inhibited by an activation barrier. We intend to come back to this issue in a future study, once the chemical pathways involved are better characterized.

4.4.3. PAHs and the gas phase abundance of D

The observed variations in the gas phase (D/H) ratio in the solar neighbourhood (10–20 ppm; Draine 2006; Onaka et al. 2014) suggest the presence of a substantial reservoir of deuterium that is not traced by atomic D nor molecular HD. Deuterated PAHs –as well as deuterated dust grains– are expected to be that reservoir (Linsky et al. 2006; Draine 2006). The observed fraction of the elemental C locked up in PAHs is $\approx 10\%$ or 35 ppm. With a typical aromatic (H/C) ratio for PAHs of 1/4–1/3, this implies ≈ 10 and ≈ 20 ppm of aromatic and aliphatic sites, respectively, that could be deuterated. Hence, for PAHs to make a substantial contribution to the missing D reservoir, the D fractionation of PAHs in the diffuse ISM would have to be very high. Focusing again on the astrophysically relevant size range of 50–100 C-atoms, atomic (D/H) ratios in the gas phase would have to be close to unity for this to occur (cf., Fig. 4.5). The IR observations of PDRs and HII regions suggest that the amount of D in PAHs represents 10 ppm of the elemental D (Doney et al. 2016). For the

¹Close to the detection limit of this study

diffuse ISM, we do not have direct, IR observations of the deuterium fractionation of PAHs. However, the atomic (D/H) column density is directly measured by Copernicus and FUSE and is low for the sight-lines investigated by Linsky et al. (2006). Thus, if PAHs are indeed an important contributor to the missing D problem, then this deuterium fractionation must be a relict from an earlier phase of the evolution, where the PAHs were in an environment characterized by a high gas phase (D/H) ratio. As Figure 4.3 illustrates, D fractionation of the aromatic sites can be preserved against photochemical destruction for a timescale ranging from a few million years for 50 C-atom PAHs, to as long as the PAH survives for a 100 C-atom PAH.

As discussed in section 4.4.1, our models do not reproduce the high implied D fractionation of PAHs in PDRs. But then, on a galactic scale, very little of the ISM cycles often through PDRs. PAHs could then acquire a high D fractionation in the shielded environment of cold dense cores (e.g., through either reactions with the deuterated isotopic isomers of H_3^+ in the gas phase), so that the deuterium fractionation observed in PDRs would be derived from this type of environment. Such process could potentially explain the observed substantial variations in the gas phase (D/H) ratio, as different sight-lines might probe different histories of the material.

4.5. Conclusions

We used a kinetic model to analyze the abundance of deuterium in PAHs. We considered 3 PAHs of different size, between 24 and 96 carbon atoms, all within the *coronene* family. We modelled two different environments of fixed total density and intensity of the incident UV radiation field. The two models are expected to represent the diffuse ISM and a PDR-like environment.

Overall we find that deuteration of PAHs is scarce, and its variation with G_0/n_H is similar between the two runs for a PAH of a given size. Clear differences do appear for the different PAH sizes. At a given G_0/n_H , the smallest molecule is stripped off of all edge atoms, while the larger molecules are found in higher degrees of edge occupation (entering to the regime where aliphatic bonds are present). This is what rules the deuteration degree of the PAHs. This also leads to higher (D/H) ratios in small PAHs than in the larger species. However small PAHs are not expected to survive and hence they are not expected to be a relevant reservoir of deuterium.

Regarding the role of PAHs in the deuterium fractionation problem, we find that the (D/H) ratio in PAHs follows the (D/H) ratio available in the reservoir. Given our assumptions, the PAHs studied here cannot reach the fractionation values necessary to account for the observed variations in the (D/H) of the ISM. Our study instead suggests that PAHs between 50 and 100 carbon atoms could eventually reach high fractionation values in more shielded environments (low G_0/n_H), where the available (D/H) might be way larger than what we assumed here. The aromatic (D/H) ratio acquired by a large PAH in a dense core could survive over a time of $\sim 10^4$ yr before losing its deuterium signature when exposed to a more intense UV radiation field in a PDR. In a diffuse ISM-type of environment, even a 50 carbon atom PAH could retain its aromatic deuterium. However, in both cases the aliphatic signature is more easily lost because of the low dissociation energy of an aliphatic CD bond. From this, we also conclude that the deuterated aliphatic signature at 4–5 μm observed in PDRs/HII regions is most likely not due to deuterated PAHs, as modelled in

this work. In view of its larger binding energy, aliphatic D associated with methyl groups might be more resistant against photo-destruction in high UV fields, but the chemistry of such groups in the ISM is not well understood yet. Further laboratory studies will be required to elucidate the molecular structures resulting from their photodissociation and their re-hydrogenation/re-deuteration processes.

Future observations with the upcoming JWST are expected to bring new insights on the deuteration level of PAHs. We recognize that, in PDRs, deuteration might be particularly relevant for deeper, UV-poor environments where excitation of the bands might be less likely. Nevertheless, the expected supreme sensitivity of JWST may make these bands and the chemistry they trace detectable. Of course, high deuteration levels inherited from a cold dense core phase could survive well into the PDR and be readily detected by JWST.

Acknowledgements

Studies of interstellar PAHs at Leiden Observatory are supported through advanced ERC grant 246976 from the European Research Council, through a grant by the Dutch Science Agency, NWO, as part of the Dutch Astrochemistry Network, and through the Spinoza premie from the Dutch Science Agency, NWO. Computing time has been made available by NWO (project SH-362-15) and calculations were performed at the Cartesius supercomputer (SurfSARA, Science Park, Amsterdam NL). A.C. acknowledges NWO for a VENI grant (639.041.543). We also acknowledge the European Union (EU) and Horizon 2020 funding awarded under the Marie Skłodowska-Curie action to the EUROPAH consortium, grant number 722346.

Bibliography

- Adams, T. F. 1976, *A&A*, 50, 461
Allamandola, L. J. 1993, in *Astronomical Society of the Pacific Conference Series*, Vol. 41, *Astronomical Infrared Spectroscopy: Future Observational Directions*, ed. S. Kwok, 197
Allamandola, L. J., Tielens, A. G. G. M., & Barker, J. R. 1989, *ApJS*, 71, 733
Andrews, H., Candian, A., & Tielens, A. G. G. M. 2016, *A&A*, 595A, 23A
Bauschlicher, C. W., & Bakes, E. L. O. 2001, *Chem. Phys.*, 274, 11–14
Bauschlicher, Jr., C. W., Langhoff, S. R., Sandford, S. A., & Hudgins, D. M. 1997, *The Journal of Physical Chemistry A*, 101, 2414
Bauschlicher, C. W., & Ricca, A. 2014, *Theo. Chem. Acc.*, 133, 1454
Black, J. H., & Dalgarno, A. 1973, *ApJ*, 184, L101
Ceccarelli, C., Caselli, P., Herbst, E., Tielens, A. G. G. M., & Caux, E. 2007, *Protostars and Planets V*, 47
Charnley, S. B., Tielens, A. G. G. M., & Rodgers, S. D. 1997, *ApJ*, 482, L203–L207
Coc, A., Petitjean, P., Uzan, J.-P., Vangioni, E., Descouvemont, P., Iliadis, C., & Longland, R. 2015, *Phys. Rev. D*, 92, 123526
Cooke, R., & Pettini, M. 2016, *MNRAS*, 455, 1512–1521
Demarais, N. J., Yang, Z., Martinez, O., Wehres, N., Snow, T. P., & Bierbaum, V. M. 2012, *AJ*, 746, 32
Demarais, N. J., Yang, Z., Snow, T. P., & Bierbaum, V. M. 2014, *ApJ*, 784, 25
Doney, K. D., Candian, A., Mori, T., Onaka, T., & Tielens, A. G. G. M. 2016, *A&A*, 586, A65
Draine, B.T. 2004, in *Origin and Evolution of the Elements*, ed. A. McWilliams & M. Rauch (Cambridge: Cambridge Univ. Press), p. 320
Draine, B. T. 2006, *ASPC*, 348, 58
Epstein, R. I., Lattimer, J. M. & Schramm, D. N. 1976, *Nature*, 263, 198
Hudgins, D. M., Bauschlicher, Jr., C. W., & Sandford, S. A. 2004, *ApJ*, 614, 770
Jura, M. 1982, in *Advances in UV Astronomy: 4 Years of IUE Research*, ed. Y. Kondo, J. M. Mead, & R. D. Chapman (NASA CP 2238: Greenbelt, MD: NSAS), 54
Le Page, V., Keheyan, Y., Bierbaum, V. M., & Snow, T. P. 1997, *JACS*, 119, 35

- Le Petit, F., Roueff, E., & Le Bourlot, J. 2002, *A&A*, 390, 369
- Linsky, J. L., Draine, B. T., Moos, H. W., et al. 2006, *ApJ*, 647, 1106
- Lis, D. C., Gerin, M., Phillips, T. G., & Motte, F. 2002, *ApJ*, 569, 322
- Mazzitelli, I. & Moretti, M. 1980, *ApJ*, 235, 955
- Mennella, V., Hornekær, L., Throuer, J., & Accolla, M. 2012, *ApJ*, 745, L2
- Millar, T. J., Roberts, H., Markwick, A. J., & Charnley, S. B. 2000, *Philos. Trans. R. Soc. London A*, 358, 2535
- Onaka, T., Mori, T. I., Sakon, I., et al. 2014, *ApJ*, 780, 114
- Peeters, E., Allamandola, L. J., Bauschlicher, Jr., C. W., et al. 2004, *ApJ*, 604, 252
- Prochaska, J. X., Tripp, T. M., & Howk, J. C. 2005, *ApJ*, 620, L39
- Rapacioli, M., Simon, A., Marshall, C.C.M., Cuny, J., Kokkin, D., Spiegelman, F., & Joblin, C. 2015, *J. Phys. Chem. A*, 119, 12845–12854
- Rauls, E., & Hornekær, L. 2008, *ApJ*, 679, 531
- Ricca, A., Bauschlicher, C. W., Jr., Boersma, C., Tielens, A. G. G. M., & Allamandola, L. J. 2012, *ApJ*, 754, 75
- Roberts, H., Herbst, E., & Millar, T. J. 2003, *ApJ*, 591, L41
- Romano, D., Tosi, M., Chiappini, C., & Matteucci, F. 2006, *MNRAS*, 369, 295
- Sandford, S. A., Bernstein, M. P., Allamandola, L. J., Gillette, J. S., & Zare, R. N. 2000, *ApJ*, 538, 691
- Srianand, R., Gupta, N., Petitjean, P., Noterdaeme, P. & Ledoux, C. 2010, *MNRAS*, 405, 1888
- Tielens, A. G. G. M. 1992, in *IAU Symposium*, Vol. 150, *Astrochemistry of Cosmic Phenomena*, ed. P. D. Singh, 91
- Tielens, A. G. G. M. 1997, in *AIP Conf. Proc.* 402, *Astrophysical Implications of the Laboratory Study of Presolar Materials*, ed. T. H. Bernatowicz & E. K. Zinner (New York: AIP), 523
- Tosi, M. 2010, in *Proc. IAU Symp.* 268, *Light Elements in the Universe*, ed. C. Charbonnel, M. Tosi, F. Primas & C. Chiappini (Cambridge: Cambridge Univ. Press), 153
- Verstraete, L., Puget, J. L., Falgarone, E., et al. 1996, *A&A*, 315, L337
- Wood, B. E., Linsky, J. L., Hébrard, G., Williger, G. M., Moos, H. W., & Blair, W. P. 2004, *ApJ*, 609, 838
- Junfeng, Z., Castellanos, P., Linnartz, H. & Tielens, A. G. G. M. 2016, *Molecular Astrophysics*, 5, 1–8

Whipping IC63/IC59

IC63 and IC59 are a pair of cometary-shaped nebulae in the vicinity of the star γ Cas (also known as *Tsih*, "the Whip"). Both nebulae have very different optical appearances, despite the fact that both objects lie at similar projected distances from the star: IC63 shows bright rims and filaments, while IC59 looks more homogeneous and faint. In this work, we aim to perform a general description of the two nebulae from an observational standpoint, in order to study the physical conditions at the UV-illuminated surfaces of these objects. We used the available data on both nebulae taken with Spitzer and Herschel, to study the infrared emission at the tip of both clouds, and derive the intensity of the UV radiation field. Using PACS line spectroscopy we obtained the intensity of the cooling lines [CII] $158\mu\text{m}$ and [OI] $63\mu\text{m}$, and we used these to estimate the density in these regions. Excitation diagrams of molecular hydrogen were obtained to derive the gas temperature. We also used [CII] $158\mu\text{m}$ velocity maps of IC59 taken with GREAT on board SOFIA, to explore the gas dynamics in this nebula. We find that [the IR emission from polycyclic aromatic hydrocarbons \(PAHs\) is very similar at the tip of both nebulae](#). Even though it varies in intensity between the two, the derived PAH band ratios are remarkably similar. These ratios are similar to those found in the more shielded regions of other nebulae such as NGC7023 and NGC2023. Regarding the physical conditions, we get that while in IC63 the intensity of the UV field, G_0 , is a factor of ~ 10 higher than in IC59, the density n at the tip of IC59 is lower than in IC63 by a similar factor. For both objects we derive G_0 values significantly lower than what previous works have so far assumed. Comparison with other reflection nebulae PDRs and known correlations support our claim that [both IC63 and IC59 are low-UV irradiated environments](#). We conclude that the tips of IC63 and IC59 are about 3 and 5 times farther away from the star than their respective projected distances. The similarity of the mid-infrared emission between the two nebulae is consistent not only with both objects being overdensities within the same region around γ Cas, but it is also consistent with the [similar \$G_0/n\$ ratio and ionization parameters, which altogether rule the evolution of the hydrogenation and ionization level of the emitting population of PAHs](#). Finally, regarding the kinematics of the material in IC59, we find evidence of photo-evaporation due to the incident radiation from γ Cas.

H. Andrews, E. Peeters & A. G. G. M. Tielens
In progress

5.1. Introduction

Polycyclic Aromatic Hydrocarbons (PAHs) are presumed to be the most abundant organic molecules in space, with abundances of the order of 10^{-7} to that of hydrogen. They are a set of very stable planar molecules disposed in a carbon core with hydrogen atoms attached to their periphery (Léger & Puget 1984; Allamandola et al. 1985). After the absorption of high energy (< 13.6 eV) photons, these molecules relax through their vibrational modes emitting copiously in the IR, and producing strong emission bands at 3.3, 6.2, 7.7, 11.3 and $12.6\ \mu\text{m}$ together with weaker bands. Therefore, their emission is the brightest in regions illuminated by UV radiation, such as photon-dominated regions (PDRs).

PDRs can generally be described as the regions of the interstellar medium (ISM) where the photo-chemistry is dominated by UV radiation (Hollenbach & Tielens 1997, 1999). In the clouds around young hot stars, the PDRs correspond to the transition zones between the ionized (mostly atomic) material, and the cold molecular clouds. They are regions of (mostly neutral) gas and dust, where we see the transition from atomic H to molecular H_2 (and from CII to C to CO). These interface regions are thus ubiquitous in space. Hence, understanding the mechanisms that rule their evolution is of great importance, as these regions are where the exchange of energy between the stars and the ISM occurs.

The physical conditions within a PDR mainly depend on two parameters: the intensity of the UV field G_0 , and the total density n . The main heating mechanisms within a PDR are the photoelectric effect on PAHs and small dust grains, and the FUV pumping of H_2 molecules. Being the smallest particles in the dust grain distribution, PAHs are particularly efficient in heating the gas through the photoelectric effect (D'Hendecourt & Léger 1987; Lepp & Dalgarno 1988; Bakes & Tielens 1994). Deeper in the cloud other heating mechanisms become more relevant, such as photoionization of elements, cosmic ray ionization and gas-grain collisions, among others (Tielens & Hollenbach 1985; Hollenbach & Tielens 1999). On the other hand, the main cooling mechanism in PDRs is due to radiative line cooling of forbidden transitions, such as [CII] $157\ \mu\text{m}$ and [OI] $63\ \mu\text{m}$.

PDRs are then bright in IR emission due to the emission from vibrational modes of PAHs, rotational and vibrational lines of H_2 , fine structure lines (e.g. [CII], [OI]), rotational lines of CO, and dust continuum emission. Observations of the near, mid and far-IR emission of PDRs obtained with the Spitzer Space Telescope (Werner et al. 2004) and Herschel Space Observatory (Pilbratt et al. 2010) allow us to derive the physical conditions in these regions. In this work, we use photometric and spectroscopic data from Spitzer and Herschel to study the physical conditions in the pair of nebulae IC 63 and IC 59, both in the vicinity of the star γ Cas. We also include velocity maps from the Stratospheric Observatory For Infrared Astronomy (SOFIA; Young et al. 2012) to study the dynamics of the material in IC 59.

IC 63 and IC 59 are a pair of nebulae in the constellation of Cassiopeia (IC 59 J2000.0 coordinates: $00^{\text{h}}57^{\text{m}}34^{\text{s}}$, $+61^{\text{d}}06^{\text{m}}15^{\text{s}}$; IC 63 J2000.0 coordinates: $00^{\text{h}}59^{\text{m}}00^{\text{s}}$, $+60^{\text{d}}53^{\text{m}}14^{\text{s}}$). Both objects are illuminated by the B0 IV star γ Cas (also referred to as HD 5394 or *Tsih*, "the Whip"). The projected distance between IC 63 and γ Cas is about 20 arcmin or ~ 1.3 pc, while the projected distance between IC 59 and the star is about 1.5 pc. Observations in $\text{H}\alpha$ show the system is embedded in a larger diffuse cloud of about 2 degrees surrounding γ Cas (Karr et al. 2005).

The PDR of IC63 has been extensively studied both theoretically and observationally. In particular, the works of Jansen et al. (1994, 1995, 1996) have positioned IC63 as a warm and high-density PDR, with molecular abundances similar to those found in dark clouds, and with a very low gas-phase carbon abundance (only 13% that of the solar abundance). Excitation diagrams of H_2 obtained with ISO data showed two components in IC63 of 106 and 685 K and column densities of $5.9 \times 10^{21} \text{ cm}^{-2}$ and $1.2 \times 10^{19} \text{ cm}^{-2}$ respectively (Thi et al. 2009). Physical conditions including H_2 column density and G_0/n_H as well as the gas temperature, have been found to vary only slightly at the tip of IC63 (Karr et al. 2005; Thi et al. 2009; Fleming et al. 2010).

IC59 on the other hand has been less studied. Physical conditions derived from ISO data reveal a slightly cooler and less dense object than IC63, but also show H_2 fluorescence and PAH emission just like in IC63 (Karr et al. 2005). This suggests that, although both nebulae appear to be at a similar projected distance to the star, they are actually at very different real distances, where IC59 is probably the farthest object away from γ Cas.

Regarding PAH emission, 5.5–17.0 μm ISOCAM CVF spectra of both nebulae suggest similar PAH populations at the tip of both objects (Karr et al. 2005). Fleming et al. (2010) focused on the PAH emission at the tip of IC63 only, and using the low resolution Spitzer spectra, they found that the PAH and H_2 emissions, appear to come from the same parts of the nebula. They also found that the dehydrogenation ratio (as measured from the intensity ratio between the PAH features at 12.7 and 11.3 μm) remains rather constant throughout most of the studied region, decreasing only slightly near the starward edge of the PDR. No PAH emission study from Spitzer spectral data has been published so far on IC59.

The goal of this paper is to analyze the PAH emission and the physical conditions in both IC63 and IC59 from an observational perspective, using data from the Spitzer, Herschel and SOFIA observatories. Section 5.2 presents the Spitzer, Herschel and SOFIA data. Section 5.3 shows first the analysis of the PAH emission, followed by the determination of the physical conditions in both nebulae. In section 5.4, we analyze what the physical conditions imply about the PAH emission, and their role in the heating of the gas in these two nebulae. We also discuss the dynamics in IC59 based on the SOFIA [CII] 157 μm velocity maps obtained for this cloud. Finally, section 5.5 presents the conclusions of this work.

5.2. Data

5.2.1. Spitzer Data

IRAC and MIPS Photometry

We used photometric data on both nebulae taken with the Infrared Array Camera (IRAC; Fazio et al. 2004) and the Multiband Imaging Photometer for Spitzer (MIPS; Rieke et al. 2004). The data were retrieved from the Spitzer Heritage Archive as part of the program ID 202 for IC63 (PI: G. Fazio) and ID 3512 for IC59 (PI: C. Joblin). The raw data products of the IRAC images at 3.6, 4.5, 5.8 and 8.0 μm , and MIPS images at 24 μm were processed with the Spitzer Science Centre (SSC) pipeline. Corrections for extended emission, zodiacal light and background subtraction were performed on all images. The IRAC and MIPS photometry are accurate to 10%. The full-width-at-half-maximum (FWHM) of the point-spread function (PSF) of the IRAC images is of 1.6", 1.6", 1.8" and 1.9" at 3.6, 4.5, 5.8, and 8.0 μm , while that of MIPS 24 μm is of 6".

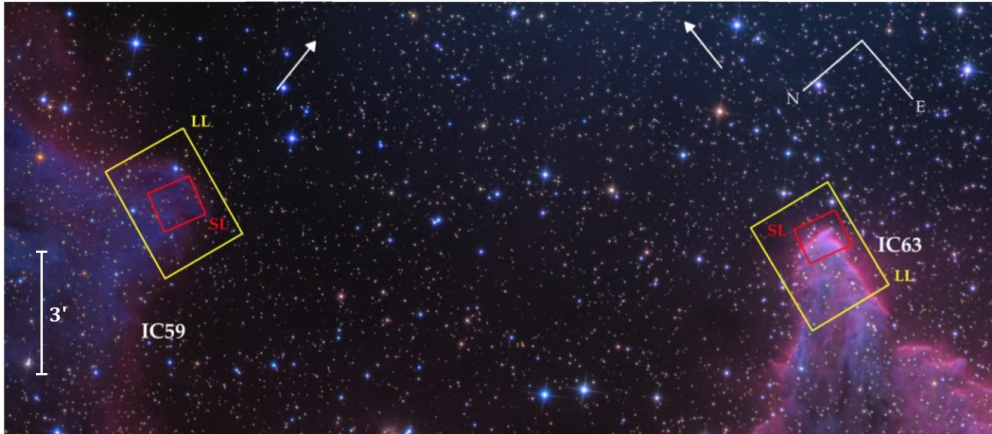


Figure 5.1: Spitzer IRS data at the tip of both IC63 and IC59. SL datasets are shown in red rectangles, and LL datasets are depicted in yellow. IC59 data were acquired on the same day, and with the same instrument and settings as the IC63 data. The background samples were chosen by checking for non-negative pixels in the background-subtracted regions in IC63 as well as in IC59, in order to isolate the mid-IR emission coming from both nebulae. The image of both nebulae has been taken from the Astronomy Picture of the Day archive (<http://apod.nasa.gov/apod/ap111103.html>; image credit Ken Crawford). The white arrow points towards the star γ Cas, which is about 20 arcmin from the tip of IC63.

IRS Spectra

We retrieved the spectroscopic data for both IC63 and IC59 from the Spitzer Heritage Archive. The Basic Calibrated Data (BCD) set is part of the SPECPRD program (ID: 3512, PI: C. Joblin), and was obtained with the Infrared Spectrograph instrument (IRS; Houck et al. 2004) in spectral mapping mode. We used the short and long wavelength (SL, 5.2–14.5 μm ; LL, 14.0–38.0 μm) low resolution modules ($R \sim 60$ –130).

Data cubes were built using CUBISM (Smith et al. 2007). We performed background subtraction by using off-source data, that were taken simultaneously with on-source data (see Figure 5.1). These background samples were chosen by comparing the spectra of different regions throughout the field, and by checking for non-negative pixels in order to isolate the mid-IR emission coming from IC63 and IC59. The background samples were combined using the Average + Min/Max Trim option. Differences between the resulting sky spectra using the different background datasets are $\lesssim 0.5$ MJy/sr. Edge effects were also removed using CUBISM. The rest of bad pixels were removed using the automated-bad-pixel routine, as well as by interactive inspection of the spectra.

Once the data cubes were built, they were aligned spatially, and resampled to the SL scale ($1.8''/\text{pixel}$). We retrieved the 1D spectra of each pixel from each data cube. Consecutive orders were averaged in the regions of overlap, i.e., 7.5–7.6 μm between SL2 and SL1 orders, 14.2–14.7 μm between SL1 and LL2 orders, and 20.5–21.0 μm between LL2 and LL1 orders. No scaling was necessary after performing the background subtraction. The spectra were finally re-binned in a 2×2 pixel step.

In order to derive PAH band ratios, we decomposed the spectra using spline functions to distinguish the emission from emission lines (e.g., [Ne II], H₂) and PAH bands, with respect to the emission from the underlying plateaus at 5–10, 10–15 and 15–18 μm (e.g., Boersma et al. 2012, Peeters et al. 2017). The specifications of the method have been described in Andrews et al. (2015). Here we summarize it as follows: first we remove the continuum underneath the plateaus and PAH bands by fitting a spline function, using as anchor points the local minima at 5.5, 10.3, 10.5, 15.0 and 19.6 μm . After this, we distinguish the emission from the broad plateaus from that of the narrower PAH bands and emission lines, by using anchor points at around 5.5, 6.6, 7.2, 8.1, 8.4, 8.8, 9.4, 9.9 and 10.3 μm for the features rising above the first plateau between 5–10 μm ; at 10.3, 10.5, 11.8, 12.2, 13.2, 14.5 and 15.0 μm for the features of the second plateau at 10–15 μm ; and at 15.0, 15.6, 16.2, 16.7, 17.5, 18.0, 19.4 and 19.6 μm for the third plateau at 15–20 μm . These local anchor points proved to properly isolate the PAH bands. The integrated intensities were obtained by fitting multi-gaussian profiles to the remaining flux using the least square curve fitting routine MPFITFUN on IDL (Markwardt 2009). Finally the narrow emission lines were subtracted, in order to isolate the emission coming from the PAH features and plateaus.

We also analyzed the spectra using the PAHFIT routine from Smith et al. (2007), which fits the spectra assuming the plateaus are an inherent part of the PAH bands (Sellgren et al. 2007, Smith et al. 2007). We did this to check the correlations between the observed PAH band ratios, as general trends have been found to be the same irrespective of the decomposition method used (Galliano et al. 2008). In the following we only present the spline decomposition results, unless stated otherwise.

5.2.2. Herschel

PACS Photometry

The datasets were downloaded from the Herschel Science Archive (HSA). We retrieved data taken with the Photodetector Array Camera and Spectrometer (PACS) at 70 and 160 μm (Poglitsch et al. 2010), and the Spectral and Photometric Imaging Receiver (SPIRE) at 250, 350 and 500 μm (Griffin et al. 2010). The photometric data was reduced with the Herschel Interactive Processing Environment (HIPE) version 14.0 with the recommended pipeline for the reduction of observations of extended sources. The PACS data was obtained in scan map observation mode, and it was treated with the MADmap pipeline (Cantalupo et al. 2010). The SPIRE maps were obtained with the Naive Scan Mapper task. We considered flux calibration errors to be of 15% for PACS and 7% for SPIRE data (Griffin et al. 2010; Swinyard et al. 2010). The PSF FWHM is of 5.2" and 12" for the 70 and 160 μm images, while for the SPIRE data is of 18", 25", and 37" at 250, 350 and 500 μm respectively.

PACS Line Spectroscopy

For both nebulae, spectroscopic observations of the [C II] 157 μm and [O I] 63 μm cooling lines were obtained with PACS and retrieved from the HSA. The observations are centered on the tip of each nebulae, coinciding with the IRS SL fields (see Figure 5.1). The observations were carried out using the unchopped spectroscopy mode. Background observations were also obtained. The data was reduced with the unchopped line scan pipeline for transient correction (Fadda et al. 2016). The beam FWHM varies from about 9" to 13" between the spectral range covered by PACS (55 and 180 μm). The spectral resolution at 63 and 157 μm correspond to $R \sim 3400$ and 1500, respectively. The line fluxes were extracted by

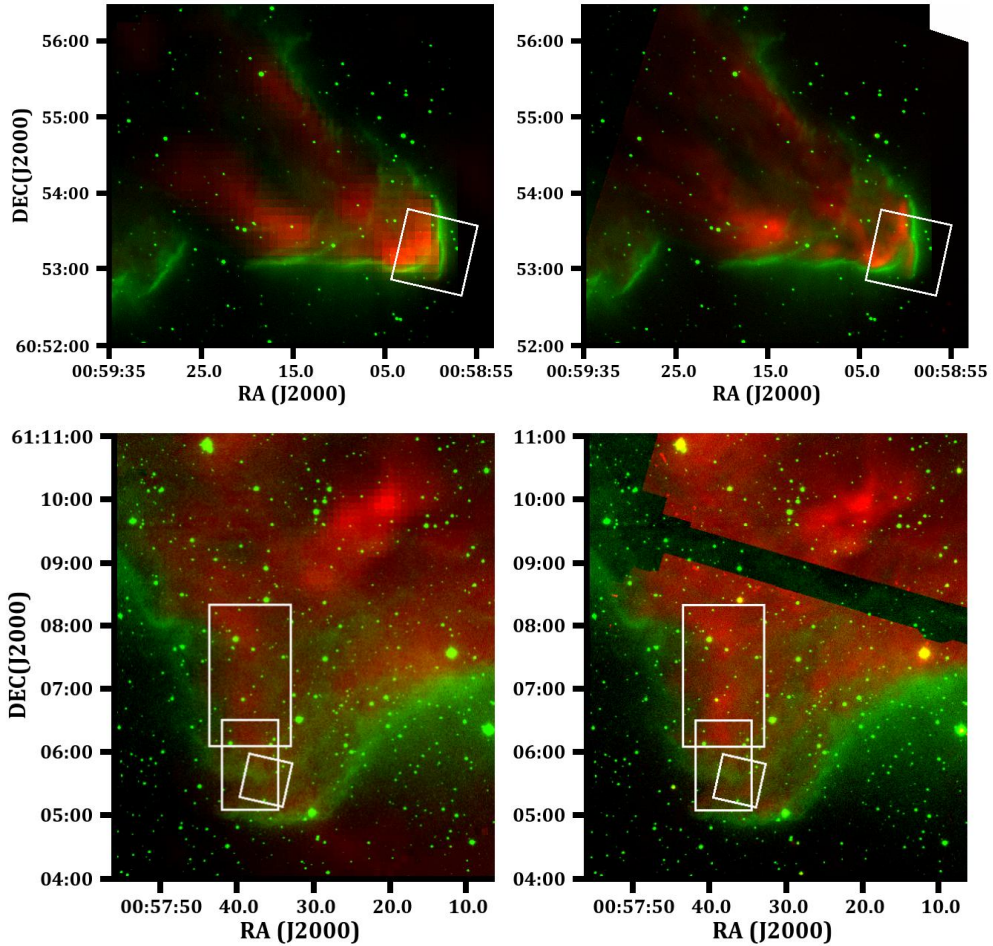


Figure 5.2: Two-colour images of IC 63 (top panels) and IC 59 (bottom panels). The figures show a comparison between the H α emission (in green) from the INT/WFC Photometric H α Survey of the Northern Galactic Plane (IPHAS; Drew et al. 2005; Barentsen et al. 2014), and the IRAC 8 μ m image taken with Spitzer (in red, right column), and the PACS 160 μ m image taken with Herschel (in red, left column). The regions covered by IRS spectral data are shown for both nebulae. For IC 59 we have also added the fields observed with SOFIA in the two runs (white rectangles aligned parallel to the declination axis).

Table 5.1: PAH band ratios at the tip of IC63 and IC59.

Ratio	Spline		PAHFIT	
	IC63	IC59	IC63	IC59
6.2/11.3	1.04±0.008	1.01±0.014	0.94±0.007	0.93±0.013
7.7/11.3	1.39±0.055	1.77±0.046	1.86±0.021	2.20±0.040
8.6/11.3	0.18±0.005	0.22±0.007	0.35±0.005	0.35±0.008
12.7/11.3	0.18±0.006	0.24±0.008	0.48±0.004	0.49±0.006
16.4/11.3	0.02±0.001	0.03±0.001	0.03±0.001	0.02±0.001
(5–10)/11.3	4.41±0.029	4.48±0.050
(10–15)/11.3	2.09±0.013	1.59±0.016
(15–18)/11.3	0.28±0.002	0.27±0.003

fitting a local continua and a Gaussian line profile to the data. Intensity maps of the integrated flux were then created using HIPE. The final integrated maps are about $120'' \times 120''$ centered on the tips of each nebulae.

5.2.3. SOFIA Velocity Maps

We obtained velocity maps of the [CII] $157 \mu\text{m}$ line for IC59 with the German Receiver for Astronomy at Terahertz frequencies (GREAT) spectrometer on board of SOFIA (Heyminck et al. 2012; Young et al. 2012; Temi et al. 2014). The observations were performed in two runs: one in May 2014 and the other in January 2015 (program ID: 02_0090, PI: E. Peeters). The observations were carried out in on-the-fly mapping mode, in combination with position switching mode. Data reduction was done with the CLASS software (Pety et al. 2005), and the spatial resampling and further analysis was done with IDL. The final field of the May 2014 run is about $65'' \times 110''$ at the tip of the nebula, while that of the January 2015 run is about $75'' \times 130''$, northeast of the tip (see Figure 5.2). The spectral resolution is 0.12 km/s for the May 2014 run, and 0.48 km/s for the January 2015 run.

5.3. Results

5.3.1. PAH Emission

Figure 5.3 shows the average mid-IR spectra of the tip of the nebulae. For IC63 we have considered the region where the PAH emission is the brightest (white square in Figure 5.4). For IC59 on the other hand, we have considered the average of the entire SL-IRS field (see Figure 5.2), as these spectra have low S/N ratios.

In general, both spectra are similar in shape but differ greatly in intensity, as the emission from the tip of IC63 is brighter than that of IC59 (e.g., the intensity at $11.3 \mu\text{m}$ in IC63 spectrum is ~ 130 MJy/sr, while in IC59 spectrum is ~ 9 MJy/sr for the applied apertures). Both spectra present the same PAH bands, as well as H_2 lines and the [Ne II] $12.8 \mu\text{m}$ ionization line (the [SIII] $18.7 \mu\text{m}$ line can be seen in some spectra in IC63 but is not discernible in

Table 5.2: Correlation coefficients for IC63 PAH band ratio plots shown in Figure 5.5.

x -Ratio vs y -Ratio	A	B	Corr. Coef.
6.2/11.3 vs 7.7/11.3	0.491	0.868	0.41
6.2/12.7 vs 7.7/12.7	1.065	1.323	0.86
6.2/(15–18) vs 7.7/(15–18)	1.191	0.520	0.91
(5–10)/(15–18) vs. (10–15)/(15–18)	0.453	0.070	0.94
11.3/12.7 vs (15–18)/12.7	0.233	0.298	0.57
12.7/11.3 vs 16.4/11.3	0.142	0.003	0.40
6.2/11.3 vs 12.7/11.3	-0.045	0.254	-0.14

The A and B coefficients correspond to the parameters derived from a linear fit of the form $y = A \times x + B$. The correlation coefficients correspond to the weighted Pearson correlation coefficients between x and y data points.

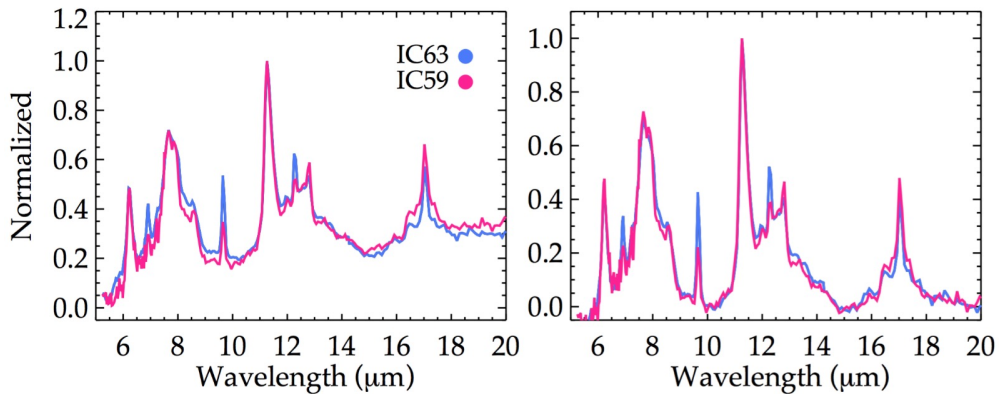


Figure 5.3: Mid-IR spectra of IC63 and IC59 observed with the IRS instrument on board Spitzer. The spectra correspond to the SL and LL modules. For IC63, we have chosen a $15'' \times 15''$ region at the tip of the nebula, along the second front seen in Figure 5.4 where the PAH emission is the brightest. However, inspection of the entire data cube shows only small variations in the PAH band ratios throughout the tip of the nebula ($\lesssim 40\%$). For IC59, we took the average spectrum over a $25'' \times 25''$ region at the tip of the nebula (see Figure 5.2). The left panel shows both spectra normalized to the peak intensity of the $11.3\mu\text{m}$ feature (132.14 MJy/sr for IC63 and 9.34 MJy/sr for IC59). The right panel shows the spectra normalized to the peak intensity of the $11.3\mu\text{m}$ feature, after the subtraction of the continuum between 5 and $20\mu\text{m}$.

IC 59). Also both spectra present similar PAH band ratios (see Table 5.1). No C_{60} emission was detected at $18.9\mu\text{m}$.

Looking at the spatial distribution of PAH emission at the tip of IC 63 (Figure 5.4), we can distinguish a first front sticking out in the western part of the cloud (closest in projection to the star), and a second one with two bright regions where the PAH emission is more intense. The spatial distribution of the 6.2 , 7.7 , 11.3 and $12.7\mu\text{m}$ bands follow each other, as well as the spatial distribution of the $5\text{--}10$ and $10\text{--}15\mu\text{m}$ plateaus. In contrast, the spatial distribution of the $15\text{--}18\mu\text{m}$ plateau is different from what is observed from the other PAH bands (e.g., the first front is not as clear as in the other bands). In the case of IC 59, the poor signal of the spectra does not allow an analysis of the spatial distribution of PAH emission on a pixel-to-pixel basis.

From Figure 5.5 we find that contrary to most studies in the literature (e.g., Hony et al. 2001, Peeters et al. 2002), IC 63 does not show a clear correlation between the $6.2/11.3$ and $7.7/11.3$ ratios. We claim the correlation cannot be observed because these ratios remain relatively constant throughout the studied region. Indeed, comparing all the available spectra at the tip of IC 63 (with enough S/N ratio) normalized to the peak of the $11.3\mu\text{m}$ band, we get that the spectra vary $<40\%$ throughout the studied region. Thus, we find that the PAH emission at the tip of IC 63 is remarkably steady, and overall it also agrees with the average PAH emission observed at the tip of IC 59.

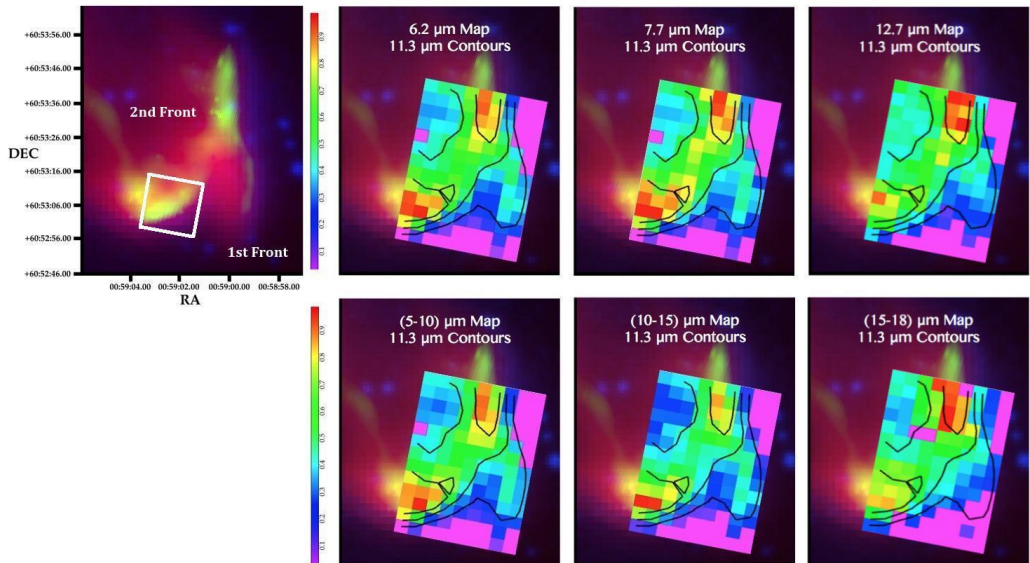


Figure 5.4: Surface brightness maps of PAH emission at the tip of IC 63. The maps are 13×9 pixels ($3.6''/\text{pixel}$) in size. They have been overlaid on top of a three-color image made from DSS (blue), IRAC $8.0\mu\text{m}$ (green) and PACS $160\mu\text{m}$ images (red). The star γCas is located ~ 20 arcmin to the southwest of the tip (see also Figure 5.1). The maps have been normalized to their maximum peak value, and we have overplotted the contours of the $11.3\mu\text{m}$ band spatial distribution for comparison. The white square in the first map indicates the region (along the second front) where the PAH emission is the brightest, and whose average spectrum is shown in Figure 5.3.

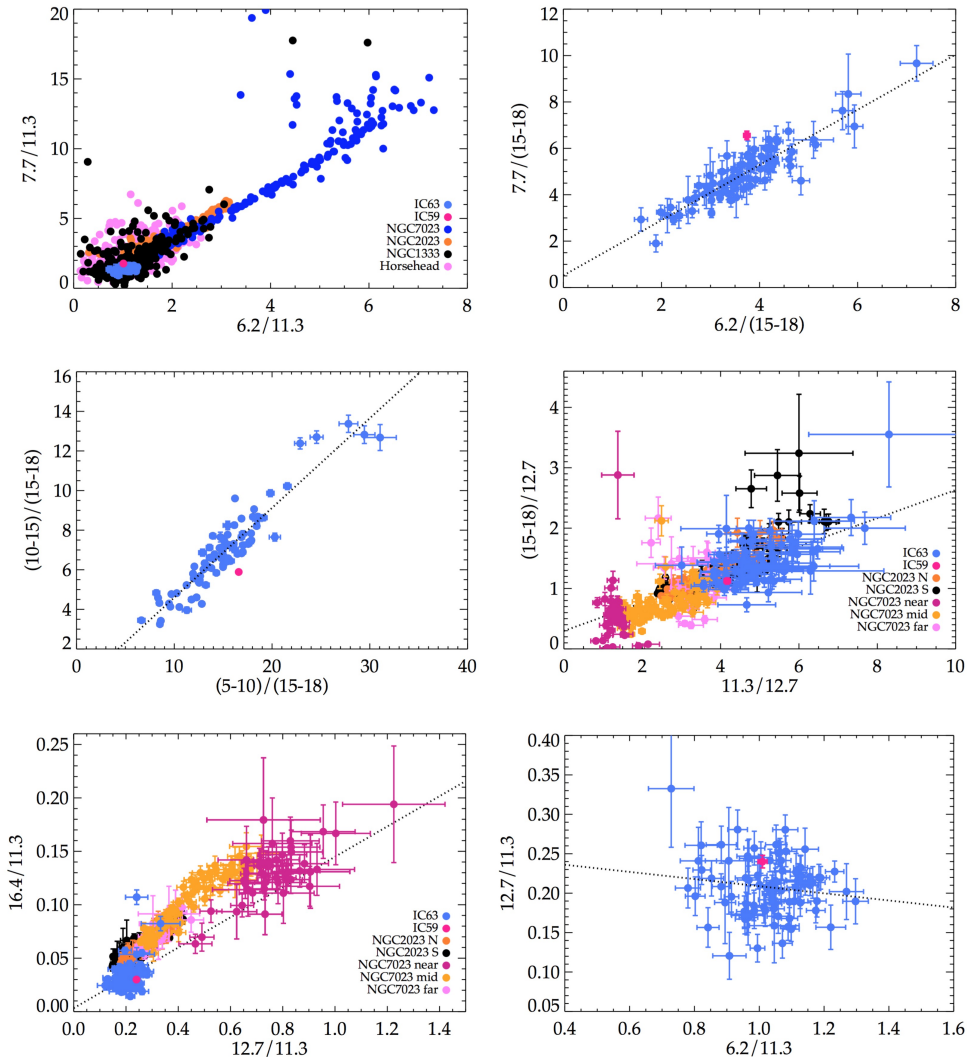


Figure 5.5: Correlations between PAH band ratios observed at the tip of IC63. We also show the PAH band ratios obtained from the average spectrum of IC59 shown in Figure 5.3 (also plotted in the same color as in Figure 5.3). We have plotted the data published in Stock et al. (2016) in the 6.2/11.3 versus 7.7/11.3 correlation plot. Note the ratios published in their work are obtained using different anchor points than ours. However for building this plot, we have plotted their data derived from a spectral decomposition consistent with our method. The data of NGC2023 north (N) and south (S) regions, as well as the data for NGC7023 ("near", "mid" and "far") have been taken from Shannon et al. (2015). The different regions in NGC7023 are at different distances from the star and trace the cavity ("near" region), the PDR front ("mid" region), and the cloud ("far" region). The dotted lines correspond to the linear fits derived from the data points (see also Table 5.2).

Even though we do not see a correlation between the 6.2 and 7.7 μm bands when normalizing by the 11.3 μm band, we do see a tentative correlation when normalizing by the 15–18 μm plateau ($P = 0.91$). The fact that we do find a correlation when normalizing by the

15–18 μm plateau might be pointing towards a different origin of this plateau compared to the 6.2 and 7.7 μm bands, associated to PAH species. This is also pointed out when comparing the strength of the plateaus. The only correlation we see is between the (5–10)/(15–18) and the (10–15)/(15–18) ratios, showing that at the tip of IC 63, the behaviour of the emission of the (15–18) plateau seems to be unrelated to the shorter wavelength features.

Compared to PAH band ratios of other nebulae such as NGC 2023 and NGC 7023, it is clear that IC 63 (and IC 59) PAH ratios span only a small range in values (see Figure 5.5), which is the origin of the lack of correlations seen in the PAH band ratios. Shannon et al. (2015) found a correlation between the 11.3/12.7 and the (15–18)/12.7 ratios. Even though we do not see this correlation in our data alone ($P = 0.57$; see Figure 5.5), the data points of IC 63 (and IC 59) follow the correlation found for NGC 2023 and NGC 7023. In addition, three different regions are indicated for NGC 7023 at different distances from the star, and trace the cavity ("near" region), the PDR front ("mid" region), and the cloud ("far" region). As can be seen in the 11.3/12.7 and the (15–18)/12.7 correlation plot, these three regions occupy different sectors in the plot, i.e., the PAH ratios of the "near" region have the smallest ratios, the "mid" region (where the PAH emission is the brightest) has intermediate values, and the PAH ratios from the "far" region (the more shielded region) are the largest ones. When compared to IC 63 (and IC 59) PAH ratios, we see these are more extreme than those from the "far" region in NGC 7023 (i.e., are at higher 11.3/12.7 and (15–18)/12.7 ratios).

This sort of sequence is also observed for the correlation between the 12.7/11.3 and 16.4/11.3 ratios shown in Figure 5.5. Also, visual comparison with the data published in Boersma et al. (2014) for the north-western PDR of NGC 7023 shows a similar trend in the 6.2/11.3 versus 12.7/11.3 plot. Comparing IC 63 (IC 59) PAH band ratios to those derived for NGC 2023 or NGC 7023, we notice again that our ratios do not vary as much as for the other objects (Boersma et al. 2014; Shannon et al. 2015). For the 12.7/11.3 versus 16.4/11.3 correlation plot, we also notice the same sequence: the smaller ratios for NGC 7023 are from regions farther away from the star, with IC 63 (and IC 59) exhibiting the smallest PAH band ratios. This suggests that the population of PAHs emitting in IC 63 (and IC 59) are most likely less ionized than the emitting PAHs in the more shielded parts of NGC 7023 and NGC 2023.

5.3.2. Physical Conditions

Dust Temperature

From the PACS 70 and 160 μm images we determined color dust temperatures, assuming a modified blackbody for the dust with a spectral emissivity index $\beta = 1.8$ (Dupac et al. 2003). Figure 5.6 shows the dust temperature maps for both nebulae, compared to the $\text{H}\alpha$ images from IPHAS. The dust temperatures span similar ranges between both objects. Considering other β values between 1 and 2 do not change the spatial distributions, nor the derived values significantly ($\Delta T_{\text{dust}} \sim 2$ K). Overall for IC 63, the dust temperature distribution is rather homogeneous: at the position of the spectrum shown in Figure 5.3 the dust temperature is about 30 K, similar to the value derived for the region centered on position (RA, DEC) = (00:59:15, +60:53:15) which appears to be another region where the PAH emission is as bright as in the tip (see Figure 5.2).

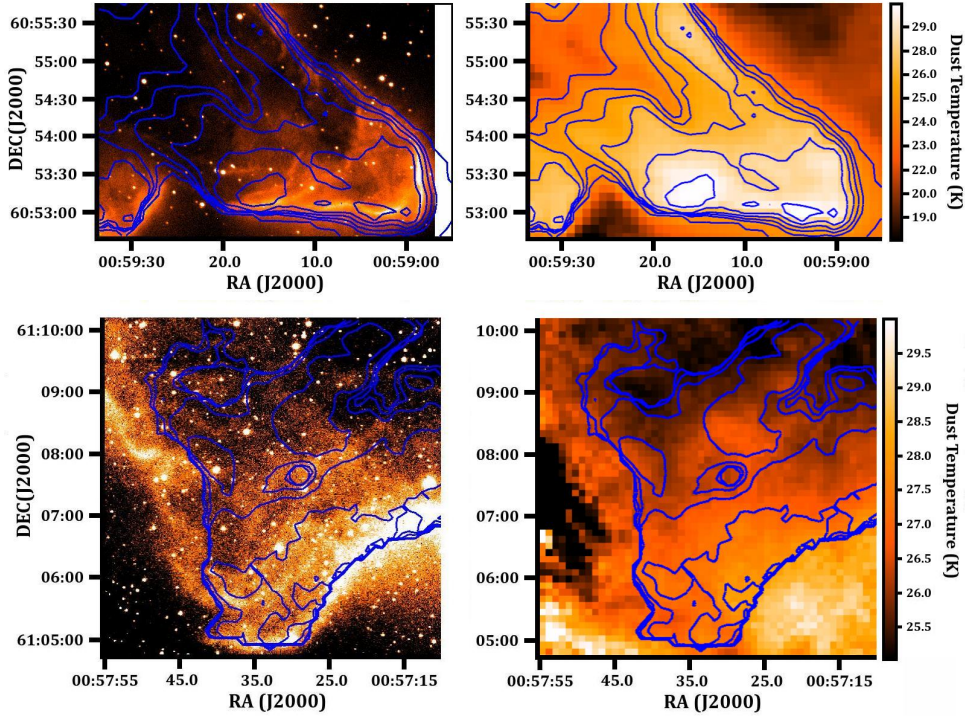


Figure 5.6: Dust temperature maps (right panels) and its comparison to the $H\alpha$ emission from IPHAS (left panels) for both, IC63 (top panels) and IC59 (bottom panels). The blue contours correspond to the contours of the dust temperature maps considering intensities above a 4σ cut. We have plotted these contours for visual guidance, as they delineate well the emission at 70 and $160\mu\text{m}$.

In the case of IC59, the region covered by the IRS-SL data (the tip) is not where the radiation of the star is directly heating the dust. This appears to happen instead at the western side of the cloud, in the concave part at around position (RA, DEC) = (00:57:15, +61:06:00). This region is in fact in the radial direction to the star (see white arrow in Figure 5.1). The temperature there is about 29.5 K , while at the tip of the nebula the temperature is slightly lower, $T_{\text{dust}} \sim 27\text{ K}$.

UV Radiation Field Incident on IC63/IC59

We derive the intensity of the UV radiation field G_0 at the tip of IC63 and IC59 directly from integrating the spectral energy distributions (SEDs). The SEDs of IC63 and IC59 were built from convolving all photometric images to match the SPIRE $500\mu\text{m}$ image resolution, using the kernels of Gordon et al. (2008)¹ for each specific filter: IRAC 3.6, 4.5, 5.8 and $8.0\mu\text{m}$, MIPS $24\mu\text{m}$, PACS 70 and $160\mu\text{m}$, and SPIRE 250, 350 and $500\mu\text{m}$ (see Table 5.3). Assuming a spectral emissivity index $\beta = 1.8$, we fit the far IR spectral region of the SEDs with one component modified blackbody model where the flux density is described as $S_\lambda \propto \lambda^{-\beta} B_\lambda(T_{\text{dust}})$ leaving as free parameters the dust opacity at $160\mu\text{m}$ and the dust temperature T_{dust} . The results of the fit lead to opacities and dust temperatures of $\tau_{160} =$

¹http://dirty.as.arizona.edu/~kgordon/mips/conv_psf/conv_psf.html

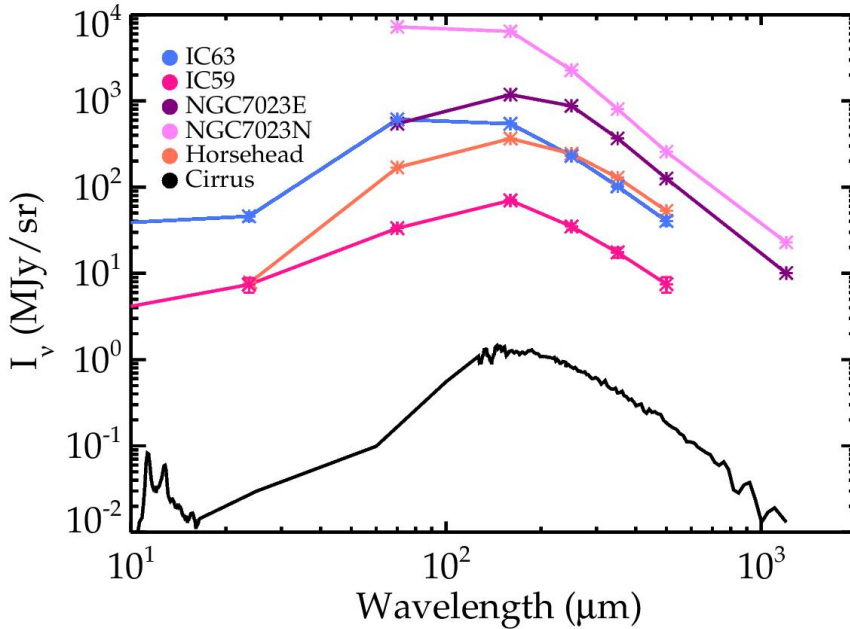


Figure 5.7: Far IR spectral energy distribution of IC63 and IC59 compared to that of the Horsehead PDR ($G_0 = 100$ and $T_{dust} = 23.3$ K for a spectral index $\beta = 0.99$; Ochsendorf & Tielens 2015), and NGC7023 eastern (E) and north (N) PDRs ($G_0 = 250$ and 2600 , and $T_{dust} \sim 20$ and 30 K, respectively assuming $\beta = 2$; Köhler et al. 2014). Also shown is the SED derived for the cirrus cloud in the diffuse ISM (Compiègne et al. 2010). For IC63 we found $G_0 = 150$ and $T_{dust} \sim 30$ K, while for IC59 we derive values of $G_0 = 25$ and $T_{dust} = 27$ K.

8×10^{-4} and $T_{dust} \sim 30$ K for IC63, and $\tau_{160} = 2 \times 10^{-4}$ and $T_{dust} = 27$ K for IC59. The resulting intensities of the UV field were estimated following Meixner et al. (1992). Assuming that all the UV radiation incident on the tip of the nebulae is re-emitted and observable at IR wavelengths, and considering the geometrical factor equal to 1 (assumed for spherical geometries) we obtain a $G_0 \sim 150$ at the tip of IC63, and a $G_0 \sim 25$ at the tip of IC59.

The values obtained are several times lower than what has been adopted in previous studies. Most studies on IC63 have assumed an incident UV radiation field of 650 Draine field units at the tip of IC63 based on the work of Janssen et al. (1994). In that study they derived the emission from γ Cas based on spectrophotometric measurements (Code & Meade 1979) and broad band flux at 950 \AA (Troy et al. 1975). According to this, they estimated an extinction corrected flux at 1000 \AA of $F_{IC63} = 2.2 \times 10^{-5}$ photons/s/cm²/Hz, assuming the projected distance between IC63 and the star (1.3 pc) as the actual distance between the sources. This is equivalent to ~ 650 Draine field units, 1100 Habing field units and 900 Mathis field units at 1000 \AA . Later on, France et al. (2005) directly measured the UV emission of γ Cas using a flux calibrated FUSE spectrum. Assuming again the projected distance of 1.3 pc as the actual distance between the star and the nebula, these authors found that, the UV radiation field incident on IC63 is a bit lower than what Janssen et al. (1994) predicted: assuming the distance from Earth to γ Cas is 230 pc (Vakili et al. 1984) then the UV radiation incident on IC63 is $F_{IC63} = 1.9 \times 10^{-5}$ photons/s/cm²/Hz at 1000 \AA , which at $d_{IC63} = 1.3$ pc is equivalent to 950 Habing field units approximately.

Table 5.3: Photometric Intensities at the tip of IC63 and IC59.

λ (μm)	IC63		IC59	
	I_ν (MJy/sr)	δI_ν	I_ν (MJy/sr)	δI_ν
3.6	2.8	0.3	0.4	0.1
4.5	1.2	0.1	0.2	0.1
5.7	11.2	1.6	2.4	0.8
7.9	37.3	3.6	3.5	1.1
23.7	46.0	5.2	7.4	1.4
70.0	611.0	6.4	33.4	2.4
160.0	543.3	5.6	70.2	3.1
250.0	230.7	5.6	35.2	2.9
350.0	102.9	4.4	17.5	2.3
500.0	40.6	4.6	7.6	1.5

We acknowledge that the estimates derived from the SEDs are strongly subjected to the geometry assumed for each system. In contrast with previous studies, our derived values would imply that IC63 is at least 3 times farther away than the projected distance to the star. Similarly, the tip of IC59 is even farther away than IC63, at least 5 times its projected distance to γ Cas (1.5 pc). Just recently, studies on the polarization of light through IC63 and IC59 have suggested this as a possible scenario (Andersson et al. 2013; Soam et al 2017). Analyzing a narrow band emission image of the $2.12\mu\text{m}$ H_2 line, Andersson et al. (2013) found "streamers" that are oriented at a steeper position angle than the projected radius between the star and IC63. Based on this, they estimated an actual distance of 2 pc instead of 1.3 pc. Soam et al. (2017) on their study of the magnetic field in IC63 and IC59 observed that the radiation from γ Cas hits the concave part of the M shape of IC59 (around position (RA, DEC) = (00:57:15, +61:06:00) in Figure 5.2), and therefore the tip of IC59 (where IRS SL data was taken) is probably farther away from the star than the concave part (see Figure 5.2).

Figure 5.7 shows a direct comparison of the SEDs of IC63 and IC59 with those of other well-known objects such as the Horsehead PDR and NGC7023 taken from the literature (Köhler et al. 2014; Ochsendorf & Tielens 2015). Compared to other PDRs we see that IC63 and IC59 have SEDs similar to those of regions of moderate-to-low G_0 values, such as NGC7023 E ($G_0 = 250$, $T_{dust} = 20$ K; Pilleri et al. 2012; Köhler et al. 2014) and the Horsehead PDR ($G_0 = 100$, $T_{dust} = 23$ K; Ochsendorf & Tielens 2015). The prototypical and well-studied NGC7023 N PDR on the other hand is at a higher $G_0 \sim 2600$ (Pilleri et al. 2012; Okada et al. 2013; Köhler et al. 2014). We notice both IC63 and NGC7023 N peak at similar wavelengths ($\lambda_{peak} \sim 100\mu\text{m}$, $T_{dust} \sim 3000/\lambda_{peak}$). However the surface brightness of IC63 is more than an order of magnitude less than that of NGC7023 N. Thus we suspect the irradiated surface is either much smaller than what we assume (i.e., the geometrical factor is much less than 1), or IC63 is a clumpy medium with a surface filling factor less than 0.1 (and thus most of the UV radiation can escape through the cloud).

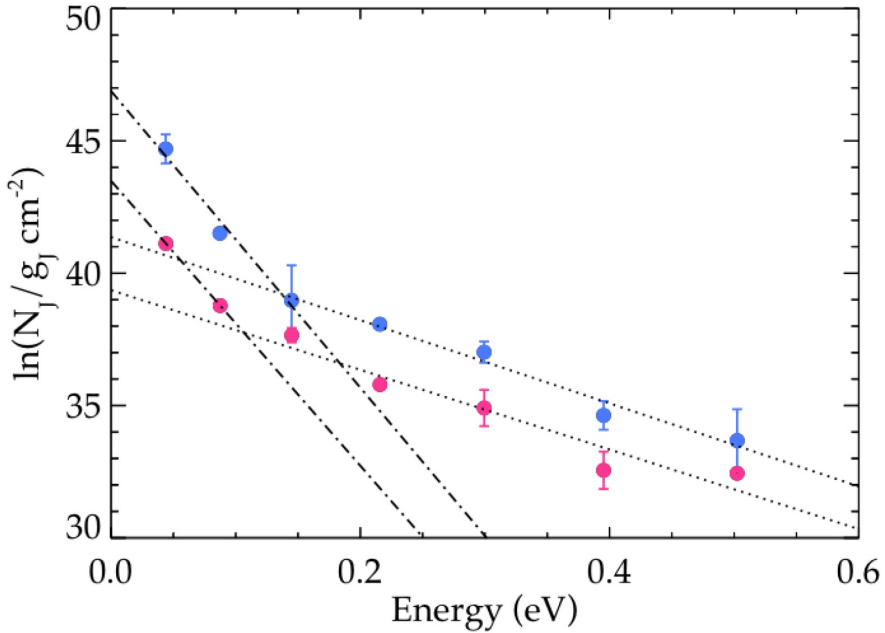


Figure 5.8: H₂ Excitation Diagrams for IC63 (blue) and IC59 (red). Two temperature fits have been applied for both nebulae. For IC63 we find that the high column density gas ($2.3 \times 10^{20} \text{ cm}^{-2}$) is at $T = 207 \pm 30 \text{ K}$ (dashed lined), while the low column density gas ($9.3 \times 10^{17} \text{ cm}^{-2}$) is at $T = 740 \pm 47 \text{ K}$ (dotted line). For IC59 on the other hand, we find slightly cooler temperatures: the high column density gas ($1.2 \times 10^{20} \text{ cm}^{-2}$) is at $T = 150 \pm 34 \text{ K}$ (dashed line), while the low column density gas ($1.8 \times 10^{17} \text{ cm}^{-2}$) is at $T = 675 \pm 49 \text{ K}$ (dotted line).

Gas Temperature

We built excitation diagrams of H₂ to derive the excitation temperature of the molecular hydrogen gas (see Figure 5.8). We assume that the lines are optically thin, and we adopt an ortho-to-para ratio of 3. The properties of each level (upper level energies and Einstein coefficients) have been taken from Rosenthal et al. (2000). We find two temperature components for both nebulae. For IC63 we find the cooler component has a temperature of $T = 207 \pm 30 \text{ K}$ and a high column density of $2.3 \times 10^{20} \text{ cm}^{-2}$. The warmer component is at $T = 740 \pm 47 \text{ K}$ and has a lower column density of $9.3 \times 10^{17} \text{ cm}^{-2}$. For IC59 we find slightly cooler temperatures and lower densities, although agreeing within errors to those derived for the tip of IC63: the cooler component is at $T = 150 \pm 34 \text{ K}$ and has a high column density gas of $1.2 \times 10^{20} \text{ cm}^{-2}$, while the low column density gas ($1.8 \times 10^{17} \text{ cm}^{-2}$) is at $T = 675 \pm 49 \text{ K}$. These estimates appear to be in good agreement with the values determined for IC63 from Thi et al. (2009) using ISO data.

Density

From the diagnostic diagrams of Kaufman et al. (1999, 2006) we can constrain the density of the gas based on the intensity ratios of the cooling lines. For IC63, we find $([\text{OI}] 63/[\text{CII}] 157) = 2.04 \pm 0.52$ and $([\text{CII}] 157 + [\text{OI}] 63)/I_{FIR} = 0.016$ at the tip of the nebula (with $I_{FIR} = 3.6 \times 10^{-2} \text{ erg/s/cm}^2/\text{sr}$ considering the factor of 2 that takes into account that the cool-

Table 5.4: Fine structure line intensities for IC63 and IC59.

Line	IC63		IC59	
	I	δI	I	δI
[CII] 157	2.01×10^{-7}	3.22×10^{-8}	6.20×10^{-8}	9.86×10^{-9}
[OI] 63	4.10×10^{-7}	8.26×10^{-8}	5.56×10^{-8}	2.78×10^{-8}

*All intensities are given in $W/m^2/sr$.

ing lines are optically thick, while the dust emits in all directions). These values constrain the mean density to $1.2 \times 10^4 \text{ cm}^{-3}$ assuming a $G_0 = 150$. It is important to mention that the derived ratios fall in a region of the Kaufman diagrams where the density is relatively independent of G_0 . For IC59 on the other hand, we get a lower density estimate of $2 \times 10^3 \text{ cm}^{-3}$ for a $G_0 = 25$ ($([OI] 63/[CII]157) = 0.90 \pm 0.47$ and $([CII] 157 + [OI]63)/I_{FIR} = 0.019$, $I_{FIR} = 6.5 \times 10^{-3} \text{ erg/s/cm}^2/sr$).

The fact that we find a lower density for IC59 is consistent with the results presented in Figure 5.8, since from the excitation diagrams it follows that in IC63, levels 2 to 4 (S(0) to S(2)) are in local-thermodynamic-equilibrium (LTE), while in the excitation diagram of IC59 we see that levels from 4 on arise from UV fluorescence.

5.3.3. [CII] Velocity Map of IC59

Figure 5.9 shows the [CII] $157 \mu m$ emission line velocity map obtained with SOFIA. The [CII] emission is more intense in the north part of the cloud (farther away from the star in terms of projected distance). There is very little emission at the tip of the nebula, where the SL-IRS data was taken. The velocity map shows a redshifted component that crosses the map in the southeast to northwest direction (see position (RA, DEC) = (00:57:40.0, +61:06:20)). This component lies almost perpendicular to the radial direction to the star, behind the delineated region where the dust temperature increases (see Figure 5.6). This component is probably related to the movement of the material in the PDR. The redshift of the line reaches velocities of up to $+0.03 \text{ km/s}$, compared to the largest blueshifts observed in the northwest part of the map and at the tip (blueshifts of up -0.74 km/s). Some blueshifted lines at -0.67 km/s might show a second component, but the data is not clear enough to distinguish them quantitatively. Overall the FWHM of the [CII] line appears to be rather narrow ($\sim 1.75 \text{ km/s}$), becoming broader only in the eastern and northern area of the map, where it reaches values of 3.3 km/s at position (RA,DEC) = (00:57:34, +61:07:53).

We also notice the [CII] $157 \mu m$ emission follows the clumps observed in the IRAC 8 and MIPS $24 \mu m$ images, which show where the FUV radiation is dominating the environment. From this it appears that the cometary shape of IC59 is more of a projection effect, where the clump at the north of the map (that is farther from the star in projection) would be actually closer to the γCas .

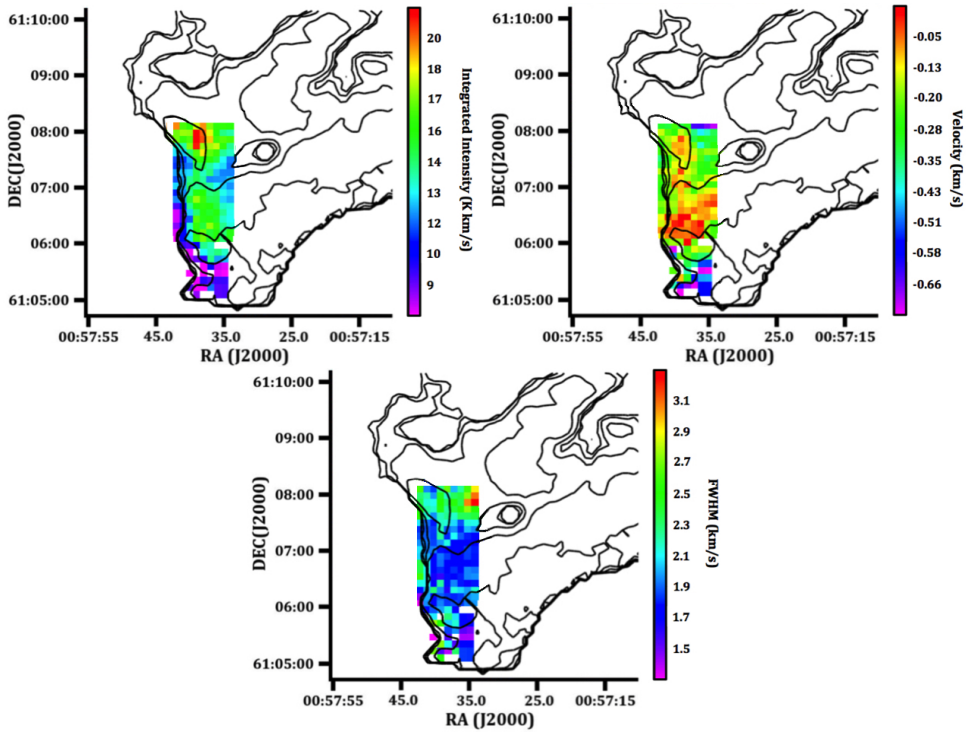


Figure 5.9: SOFIA results on the [CII] $157\ \mu\text{m}$ line emission in IC59. The panels show the maps of the central velocity of the line, the FWHM of the [CII] lines after a Gaussian line profile fit, and the integrated line intensity. The black contours correspond to the contours of the dust temperature shown in Figure 5.6, and are plotted for visual guidance purposes only.

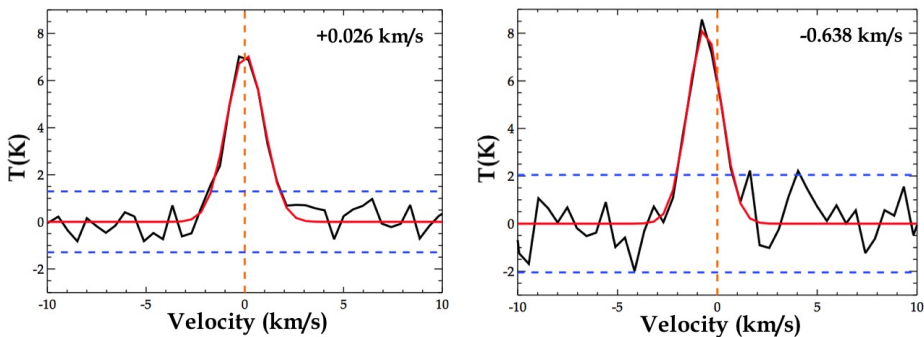


Figure 5.10: Example spectra of the [CII] $157\ \mu\text{m}$ line for two different positions in IC59. The data is shown in black, while the Gaussian line profile fit is shown in red. The blue dashed lines indicate $\pm 2\sigma$ of the continuum level. The right panel shows the spectrum at the position (RA, DEC) = (00:57:37, +61:08:07) at the northern part of the map shown in Figure 5.9, while the left panel corresponds to a position in the southern part of the map, at (RA, DEC) = (00:57:39, +61:06:28).

[b]

Table 5.5: Summary of Physical Conditions at the tip of IC63 and IC59.

Property	IC63	IC59
G_0	150	25
n (cm ⁻³)	1.3×10^4	2×10^3
T_{gas} (K)	207	150
T_{dust} (K)	30.0	27.0
ϵ_{gas}	0.016	0.018
G_0/n	0.012	0.013
γ	1079	995

5.4. Discussion

In section 5.3.1, we found that the PAH emission is rather uniform at the tip of IC63, and its derived PAH band ratios are similar to those found in the average spectrum of IC59. Even though both clouds are illuminated by the same star—and hence, we expect them to be composed of similar initial interstellar material—the similarity in their emission is still puzzling, as physical conditions may vary considerably between the two studied regions.

When comparing the PAH band ratios at the tip of IC63 (and IC59) to those found in other reflection nebulae like NGC 7023 and NGC 2023, we find two interesting results. First, as mentioned above, PAH band ratios do not vary much within the tip of IC63 (and IC59). In fact, the range of PAH band ratios seen in IC63 and IC59 is considerably smaller than that observed in other objects, such as NGC 7023. In this source, large variations have been found throughout a region of about $45'' \times 40''$, which at a distance of about 430 pc, corresponds to a projected region of $\sim 0.09 \times 0.08$ pc² (Boersma et al. 2014). The region at the tip of IC63 on the other hand, correspond to a projected area of about 0.05×0.03 pc² ($47'' \times 32''$), assuming that IC63 is at the same distance from Earth as γ Cas (~ 230 pc).

The second interesting result is that, taking under consideration the differences between our spectral decomposition methods, IC63 PAH band ratios (and IC59) are close to those from "zone 5" of NGC 7023 in Boersma et al. (2014), as inferred from a visual inspection of the correlation plots. This zone corresponds to a region farther away from the star, already in the dense cloud where the PAH emission is weaker. The PAH band ratios in this zone alone do not vary much, i.e., greater variations in the PAH band ratios are observed across all zones in NGC 7023, as such region is extended enough to trace variations in the physical conditions.

The similarity of IC63 (and IC59) PAH band ratios with those from "zone 5" of NGC 7023 refers to the sequence mentioned in section 5.3.1 (see also Figure 5.5). The PAH band ratios found for IC63 (and IC59) compared to other sources then, resemble (or are even more extreme than) the ratios found in the more shielded parts of other reflection nebulae such as NGC 7023 and NGC 2023.

5.4.1. Variability of PAH Emission

The observed variations in relative intensities of the main PAH bands are mainly controlled by the PAH charge balance. This in turn is set by the competition between the ionization and recombination rates, and is thus defined by the so-called ionization parameter $\gamma \equiv G_0 \sqrt{T_{gas}}/n_e$, where n_e is the electron density. We have estimated γ at the tip of IC 63 and IC 59 assuming that, as expected in PDRs, the electrons come from the ionization of neutral carbon atoms, and thus we adopt a carbon abundance of 1.6×10^{-4} (Sofia et al. 2004). The derived values are listed in Table 5.5. Based on the physical conditions we derived for IC 63 and IC 59, we find that the ionization parameter, as well as G_0/n are similar for these two regions. The similarity between their PAH emission is thus not surprising.

The ionization parameter is an indicator of the ionization degree of the emitting PAHs (Bregman & Temi 2005; Galliano et al. 2008; Stock et al. 2016). Galliano et al. (2008) studied several Galactic regions for which the physical conditions were known, and for which the IR spectra were observed with either ISO or Spitzer telescopes. Based on this data set, they obtained an empirical relation between the ionization parameter and the 6.2/11.3 PAH band ratio (see Figure 5.11). The data points for IC 63 and IC 59 agree with the relation found by Galliano et al. (2008) within 3σ , and lie close to the data points of HII regions and other reflection nebulae such as NGC 2023 (Stock et al. 2016). In fact we again see that the

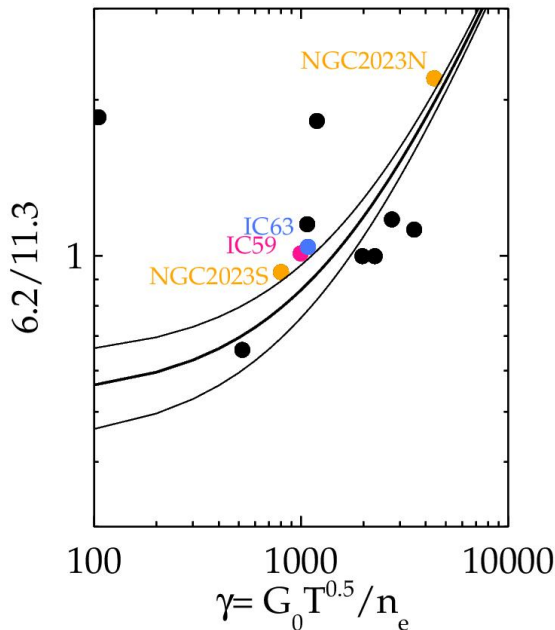


Figure 5.11: Ionization parameter γ versus the 6.2/11.3 PAH band ratio. The data points for IC 63 and IC 59 are shown in blue and red respectively. The black points are taken from Stock et al. (2016), while the lines correspond to the fit and its 1σ deviations derived from the systematic study of PAH emission in galactic regions done by Galliano et al. (2008). We have highlighted the data points for NGC 2023 N (north) and NGC 2023 S (south), since these are PDRs in the reflection nebula NGC 2023, which is a relatively benign environment comparable to IC 63 and IC 59.

6.2/11.3 ratios of IC63 and IC59 are close to that of NGC2023 south (S), which is denser than the northern PDR, NGC2023 N.

5.4.2. Heating Efficiency

As seen from the relation depicted in Figure 5.11, the higher the ionization parameter, the greater the 6.2/11.3 PAH ratio, which is expected to trace the ionization degree of the emitting PAHs. The charge state of PAHs is important in determining the efficiency of the photoelectric effect (Bakes & Tielens 1994). The heating efficiency of the gas ϵ_{gas} can be obtained by comparing the emissions of the cooling lines with the dust continuum emission. Assuming that all of the cooling of the gas in the PDR is done through the [CII] 157 and [OI] 63 μm fine structure lines, we can approximate ϵ_{gas} as the ratio $([\text{CII}] + [\text{OI}])/I_{FIR}$. The results are shown in Figure 5.12 as well as in Table 5.5. The derived heating efficiencies ϵ_{gas} for IC63 and IC59 appear to be consistent with an inverse relation between ϵ_{gas} and γ , as the more ionized the PAHs, the less effective is the photoelectric heating of the gas.

The efficiencies found at the tip of IC63 and IC59 are comparable to those found in the relatively low-UV excited PDRs of the Horsehead Nebula ($\epsilon_{gas} \sim 2\%$, $G_0 \sim 100$; Goicoechea et al. 2009). Our observational estimates of ϵ_{gas} also agree with the theoretical predictions from Bakes & Tielens (1994), where the theoretical efficiencies are expected to be $\sim 2\%$ for both IC63 and IC59 considering the γ values listed in Table 5.5 (see equation 40 in Bakes & Tielens 1994).

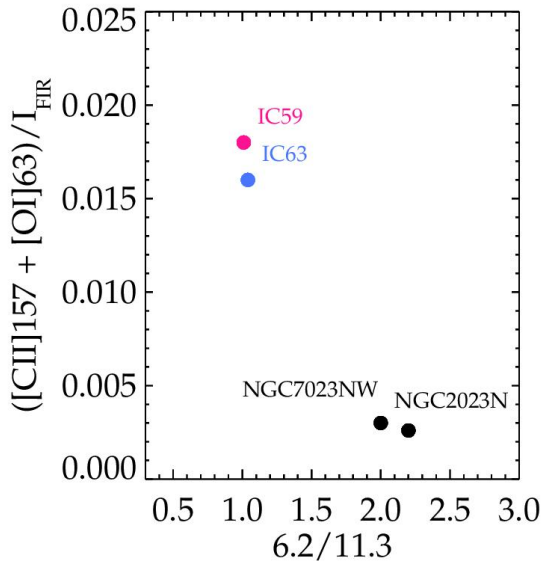


Figure 5.12: Comparison between the 6.2/11.3 PAH band ratio and the heating efficiency approximated by the $([\text{CII}]157 + [\text{OI}]63)/I_{FIR}$ ratio. The data points for IC63 and IC59 are shown in the same colors as in the previous figures. The data points for the northwestern PDR of NGC 7023 (Boersma et al. 2014; Bernard-Salas et al. 2015) and the north PDR of NGC 2023 (Stock et al. 2015; Peeters et al. 2017) are shown in black for comparison.

5.4.3. Other Correlations

Stock & Peeters (2017) found an empirical relation between the intensity ratio of the two components of the $7.7\ \mu\text{m}$ PAH band, and the UV radiation field given in Habing field units. As their sample consisted mostly on high- G_0 PDRs, it is of great interest to plot IC63 and IC59 data points to sample the low- G_0 end of the relation. We therefore decomposed the $7\text{--}9\ \mu\text{m}$ region following Stock & Peeters (2017). The $7.7\ \mu\text{m}$ PAH band is fitted with two Gaussian components at 7.55 and $7.87\ \mu\text{m}$, with fixed peak wavelength and FWHM. The results are shown in Figure 5.13. Since the $7.8\ \mu\text{m}$ band has been associated to PAHs with irregular structures, while the $7.6\ \mu\text{m}$ component has been ascribed to more compact (and thus stable) species (Peeters et al. 2017), the inverse relation between the $7.8/7.6$ and G_0 might be tentatively reflecting the destruction of irregular-shaped (less stable) PAHs in high-UV irradiated environments. In addition to structural changes, it is hypothesized that the $7.8\ \mu\text{m}$ component originates in larger species, and thus this ratio may also reflect changes in the size distribution of its carriers (Peeters et al. 2017). Given the derived G_0 values for IC63 and IC59, it is clear that they agree with the relations found by Stock & Peeters (2017) in the low- G_0 limit. Interestingly enough, our derived $7.8/7.6$ ratios fall close to the value found in the Horsehead PDR, and differ greatly from the higher- G_0 PDRs of NGC2023 and NGC7023 NW, in consistency with Figures 5.7, 5.11 and 5.12.

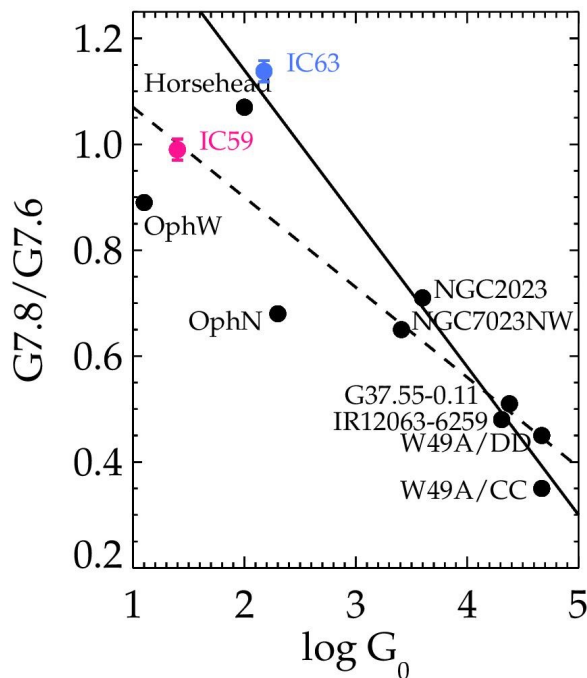


Figure 5.13: Intensity ratio of the two components of the $7.7\ \mu\text{m}$ PAH band versus the intensity of the UV radiation field G_0 . Again the data points for IC63 and IC59 are shown in the same colors as in the previous figures. The black points are taken from Stock & Peeters (2017). The dashed line corresponds to the fit to all black data points, while the solid line corresponds to the fit excluding the data points in the Ophiuchus diffuse cloud (Stock & Peeters 2017).

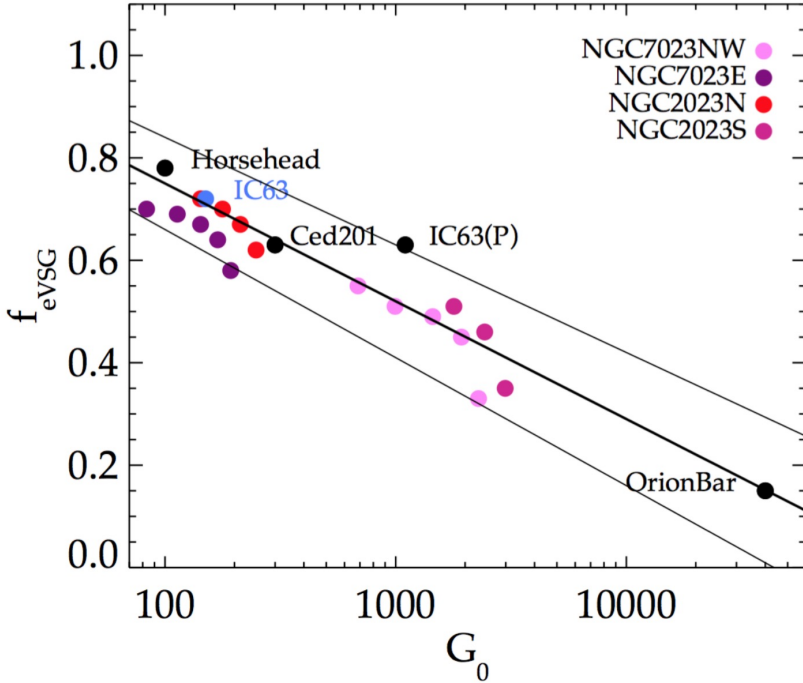


Figure 5.14: Fraction of carbon atoms locked in eVSGs relative to the carbon in the PAHs, f_{eVSG} , versus UV field intensity, G_0 . Data points and the correlation have been taken from Pilleri et al. (2012). We have highlighted the data points for the PDRs in the reflection nebulae NGC7023 and NGC2023 for comparison purposes with IC63. The data point IC63(P) corresponds to the estimate obtained by Pilleri et al. (2012), which assumed a $G_0 = 1100$ corresponding to the 650 Draine fields published in Janssen et al. (1994).

Likewise, Pilleri et al. (2012) reported an inverse correlation between G_0 and the fraction of carbon atoms locked in the so-called evaporating very small grains (eVSGs) relative to the carbon in the PAHs, f_{eVSG} . This was interpreted as PAHs being released into space by the photo-evaporation of VSGs in high-UV radiation environments, in agreement with previous observational studies (Rapacioli et al. 2005; Berné et al. 2007). The fraction of eVSGs was determined by using the fitting tool PAHTAT (PAH Toulouse Astronomical Templates; Pilleri et al. 2012) which yields the relative contributions of different dust emission components for a given IR spectrum, i.e., positively ionized PAHs, neutral PAHs and the eVSG component. We applied PAHTAT to the average spectra of IC63 and IC59. For IC63, we found $f_{eVSG} = 0.72$, which is consistent with the estimate published by Pilleri et al. (2012), who found $f_{eVSG} = 0.63$ (data point labeled IC63(P) in Figure 5.14). This, together with our new estimate of G_0 , situates IC63 in the upper left corner of the G_0 versus f_{eVSG} diagram, also in good agreement with their published relation (see Figure 5.14).

For IC59, we found a $f_{eVSG} = 0.60$ which does not appear to be consistent with the observed relation (Figure 5.14), unless we are underestimating G_0 by a factor greater than ~ 100 , which seems unlikely, at least at the tip of the nebula. Note that Pilleri et al. (2012) explicitly stated the relation is applicable for $10^2 \lesssim G_0 \lesssim 10^4$ and densities in the range $10^2\text{--}10^5 \text{ cm}^{-3}$ as observations and modelling are difficult outside these ranges.

5.4.4. Morphology of IC59

Figure 5.2 shows the general structure of IC63 and IC59 as seen in different wavelengths. Bright $H\alpha$ rims delineate the IRAC $8.0\mu\text{m}$ and PACS $160\mu\text{m}$ emission for both nebulae. In addition to the bright $H\alpha$ rims in IC63, faint extended $H\alpha$ emission is also seen at the tip of the nebula (where the IRS spectra have been taken). This is also what we see at the tip of IC59. Only farther away from the star, clear bright clumps are seen in the IRAC $8.0\mu\text{m}$ image (around position (RA, DEC) = (00:57:20,+61:10:00)). In this sense, for both nebulae we find that the regions where the PAH emission is the brightest are not where the IRS SL-LL datasets have been observed.

In particular, for IC59 the tip of the nebula (as seen from optical images) is not the region most intensely hit by the stellar radiation (see Figures 5.2 and 5.6). This instead happens to the western concave side of the nebula, which lies facing the radial direction to the star. This explains why the PAH and [CII] emission at the tip is weak compared to the northern region. The G_0 value found from the SED indicates the tip is indeed farther away from the star, and thus it is mostly a projection effect. We encourage then follow up studies to focus on the northwestern region of IC59 rather than the tip.

A comparison of the velocity of [CII] $157\mu\text{m}$ with that of the ionized gas and molecular gas can tell us whether the material in the cloud is being evaporated due to the incident stellar radiation, as [CII] is an important tracer of PDRs. Previous studies on the kinematics of the entire nebula of IC59 report that the molecular gas (as traced by $^{12}\text{CO}(J = 1-0)$) shows velocities between $+1.03$ to $+2.65$ km/s, peaking at about 2 km/s (Karr et al. 2005). Such peak velocity is observed in an unresolved clump of molecular material observed farther north from the tip of IC59. The position of this clump corresponds to the brightest in the IR bands shown in Figure 5.2 (IRAC $8\mu\text{m}$ and PACS $160\mu\text{m}$ images). We suspect that this is the material behind the ionization front produced by γCas that is hitting the western concave part of IC59 (and that this material is closer to the star than the tip where the IRS-SL data was taken).

Our [CII] $157\mu\text{m}$ velocity map shows velocities between -0.74 to $+0.33$ km/s. Previous measurements on neutral gas, as traced by the 21 cm emission, show velocities of about 1 km/s (Blouin et al. 1997, Karr et al. 2005). Fich et al. (1990) determined a velocity for the ionized gas of -2 km/s for IC63. Assuming this to be valid also for IC59, the data would be suggesting an overall velocity gradient between the different components, consistent with an interface being photo-evaporated due to the radiation from γCas . The material lying almost perpendicular to the radial direction to the star (where the [CII] velocity map shows a redshifted component that crosses the map in the southeast to northwest direction) appears to be "dragged" by the incident radiation of the star (Figure 5.9). Adopting an estimate of the mass of the cloud of IC59 equal to $m_c = 0.7 M_\odot$ (Blouin et al. 1997) we can obtain the evaporation timescale of the cloud t_{pe} , considering the mass loss rate $dm_c/dt \sim A_c \times \rho_{PDR} \times c_{PDR}$, where A_c corresponds to the area facing the ionization front produced by the radiation of γCas ; ρ_{PDR} corresponds to the mass density of the heated gas; and c_{PDR} is the isothermal sound speed in the PDR gas. Considering a kinetic temperature of 650 K, we obtain a speed of 2 km/s. Assuming a facing area $\sim \pi r_c^2$, with the radius $r_c \sim 0.3$ pc, and a density $\sim 10^{-22}$ gr/cm³, we obtain a rough estimate for the mass loss rate of $\sim 10^{-6} M_\odot/\text{yr}$. This would imply a time scale of ~ 1 Myr for the evaporation of the available reservoir of gas in the nebula.

5.5. Conclusion

We re-visit the pair of nebulae IC 63 and IC 59, both being cometary-shaped clouds in the vicinity of a single star, γ Cas. Using Herschel and Spitzer photometry and spectroscopy, and high resolution velocity maps from SOFIA, we studied the PAH emission at the tip of both nebulae, and we make an assessment of the general physical conditions under which they emit.

We found that the PAH emission, as quantitatively measured in terms of PAH band ratios, is remarkably homogeneous throughout the tip of IC 63. The ratios found are also quite similar to the PAH band ratios derived from the average spectrum of the tip of IC 59. This we claim to be due to a similar G_0/n ratio and ionization parameter in the two objects, as derived from the photometric data and cooling line ratios.

Comparison to other well-studied nebulae, the PAH band ratios found for IC 63 and IC 59 ratios are similar to those found in the more shielded regions of other nebulae, such as NGC 7023 and NGC 2023. Considering the physical conditions derived in this work, we get that the PAH emission observed in IC 63 and IC 59 consistently situates these nebulae as low- G_0 PDRs, contrary to what has been predicted in previous studies.

Using SOFIA data we obtained [CII] $157\ \mu\text{m}$ velocity maps for IC 59. Given the cometary shape of IC 59 and the velocity gradient between the molecular gas, HI and [CII] components, we claim that the cloud is being photo-evaporated due to the influence of the star. The difference in the morphology of IC 59 observed in the optical compared to the IR wavelengths, suggests that the tip (as seen in optical images) of IC 59 is quite likely to be farther away from the star than the rest of the cloud, and that the cometary shape of IC 59 is mostly the result of projection effects.

Acknowledgements

Based [in part] on observations made with the NASA/DLR Stratospheric Observatory for Infrared Astronomy (SOFIA). SOFIA is jointly operated by the Universities Space Research Association, Inc. (USRA), under NASA contract NAS2-97001, and the Deutsches SOFIA Institut (DSI) under DLR contract 50 OK 0901 to the University of Stuttgart. E.P. acknowledge support from an NSERC Discovery Grant. Studies of interstellar PAHs at Leiden Observatory are supported through advanced ERC grant 246976 from the European Research Council, through a grant by the Dutch Science Agency, NWO, as part of the Dutch Astrochemistry Network, and through the Spinoza premie from the Dutch Science Agency, NWO.

Bibliography

- Allamandola, L. J., Tielens, A. G. G. M., & Barker, J. R. 1985, *ApJL*, 290, L25
 Andersson, B.-G., Piirola, V., De Buizer, J., Clemens, D. P., Uomoto, A., Charcos-Llorens, M., Geballe, T. R., Lazarian, A., Hoang, T., & Vornanen, T. 2013, *ApJ*, 775, 84
 Andreus, H., Boersma, C., Werner, M. W., et al. 2015, *ApJ*, 807, 99
 Bakes, E. L. O., & Tielens, A. G. G. M. 1994, *ApJ*, 427, 822
 Barentsen, G., Farnhill, H. J., Drew, J. E., González-Solares, E. A., Greimel, R., Irwin, M. J., Miszalski, B., Ruhland, C., Groot, P., et al. 2014, *MNRAS*, 444, 3230
 Bernard-Salas, J., Habart, E., Köhler, M., et al. 2015, *A&A*, 574, A97

- Berné, O., Joblin, C., Deville, Y., et al. 2007, *A&A*, 469, 575
- Blouin, D., McCutcheon, W. H., Dewdney, P. E., et al. 1997, *MNRAS*, 287, 455
- Boersma, C., Rubin, R. H., & Allamandola, L. J. 2012, *ApJ*, 753, 168
- Boersma C. et al., 2014, *ApJS*, 211, 8
- Bregman, J., & Temi, P. 2005, *ApJ*, 621, 831
- Cantalupo, C. M., Borrill, J. D., Jaffe, A. H., Kisner, T. S., & Stompor, R. 2010, *ApJS*, 187, 212
- Code, A. D., & Meade, M. R. 1979, *ApJS*, 39, 195
- Compiègne, M., Flagey, N., Noriega-Crespo, A., Martin, P. G., Bernard, J.-P., Paladini, R., & Molinari, S. 2010, *ApJ*, 724, L44
- Drew, J. E., et al. 2005, *MNRAS*, 362, 753
- Dupac, X., Bernard, J., Boudet, N., et al. 2003, *A&A*, 404, L11
- D'Hendecourt, L. B., Léger, A. 1987, *A&A*, 180, 9
- Fadda, D., Jacobson, J. D., & Appleton, P. N. 2016, *A&A*, 594, 90
- Fazio, G. G., et al. 2004, *ApJS*, 154, 39
- Fich, Michel, Dahl, Geoff P., & Treffers, R. 1990, *AJ*, 99, 622
- Fleming, B., France, K., Lupu, R. E., & McCandliss, S. R. 2010, *ApJ*, 725, 159
- France, K., Andersson, B.-G., McCandliss, S. R., & Feldman, P. D. 2005, *ApJ*, 628, 750
- Galliano, F., Madden, S. C., Tielens, A. G. G. M., Peeters, E., & Jones, A. P. 2008, *ApJ*, 679, 310
- Goicoechea, J. R., Compiègne, M., & Habart, E. 2009, *ApJ*, 699, L165
- Gordon, K. D., Engelbracht, C. W., Rieke, G. H., et al. 2008, *ApJ*, 682, 336
- Griffin, M. J., Abergel, A., Abreu, A., et al. 2010, *A&A*, 518, L3
- Hegminck, S., Graf, U. U., Güsten, R., et al. 2012, *A&A*, 542, L1
- Hollenbach, D. J., & Tielens, A. G. G. M. 1999, *RvMP*, 71, 173
- Hollenbach, D. J., & Tielens, A. G. G. M. 1997, *ARAA*, 35, 179
- Hony, S., et al. 2001, *A&A*, 370, 1030
- Houck, J. R., Roellig, T. L., van Cleve, J., et al. 2004, *ApJS*, 154, 18
- Jansen, D. J., van Dishoeck, E. F., & Black, J. H. 1994, *A&A*, 282, 605
- Jansen, D. J., van Dishoeck, E. F., Black, J. H., Spaans, M., & Sosin C. 1995, *A&A*, 302, 223
- Jansen, D. J., van Dishoeck, E. F., Keene, J., Boreiko, R. T., & Betz, A. L. 1996, *A&A*, 309, 899
- Karr, J. L., Noriega-Crespo, A., & Martin, P. G. 2005, *AJ*, 129, 954
- Kaufman, M. J., Wolfire, M. G., Hollenbach, D. J., & Luhman, M. L. 1999, *ApJ*, 527, 795
- Kaufman, M. J., Wolfire, M. G., & Hollenbach, D. J. 2006, *ApJ*, 644, 283
- Köhler, M., Habart, E., Arab, H., et al. 2014, *A&A*, 569, A109
- Léger, A., & Puget, J. L. 1984, *A&A*, 137, L5–L8
- Lepp, S., & Dalgarno, A. 1988, *ApJ*, 335, 769
- Markwardt, C. B. 2009, in *ASP Conf. Ser. 411, Astronomical Data Analysis Software and Systems XVIII*, ed. D. A. Bohlender, D. Durand, & P. Dowler (San Francisco, CA: ASP), 251
- Meixner, M., Haas, M. R., Tielens, A. G. G. M., Erickson, E. F., & Werner, M. 1992, *ApJ*, 390, 499
- Ochsendorf, B. B., & Tielens, A. G. G. M. 2015, *A&A*, 576, 2
- Okada, Y., Pilleri, P., Berné, O., et al. 2013, *A&A*, 553, A2
- Peeters, E., Hony, S., Van Kerkhoven, C., Tielens, A. G. G. M., Allamandola, L. J., Hudgins, D. M., & Bauschlicher, C. W. 2002, *A&A*, 390, 1089
- Peeters, E., Bauschlicher, C. W., Allamandola, L. J., Tielens, A. G. G. M., Ricca, A., & Wolfire, M. G. 2017, *ApJ*, 836, 198
- Pety, J. 2005, *Semaine de l'Astrophysique Française*, ed. F. Casoli et al., EDP Sciences, p. 721
- Pilbratt, G. L., Riedinger, J. R., Passvogel, T., et al. 2010, *A&A*, 518, L1
- Pilléri, P., Montillaud, J., Berné, O., & Joblin, C. 2012, *A&A*, 542, A69
- Poglitsch, A., Waelkens, C., Geis, N., et al. 2010, *A&A*, 518, L2
- Rapacioli, M., Joblin, C., & Boissel, P. 2005, *A&A*, 429, 193
- Rieke, G. H., et al. 2004, *ApJS*, 154, 25
- Rosenthal, D., Bertoldi, F., & Drapatz, S. 2000, *A&A*, 356, 705
- Sellgren, K., Uchida, K. I., & Werner, M. W. 2007, *ApJ*, 659, 1338
- Shannon, M. J., Stock, D. J., & Peeters, E. 2015, *ApJ*, 811, 153
- Smith, J. D. T., Draine, B. T., Dale, D. A., Moustakas, J., Kennicutt, R. C. Jr, et al. 2007, *ApJ*, 656, 770
- Soam, A., Maheswar, G., Lee, C. W., Neha, S., & Andersson, B.-G. 2017, *MNRAS*, 465, 559
- Sofia, U. J., Lauroesch, J. T., Meyer, D. M., & Cartledge, S. I. B. 2004, *ApJ*, 605, 272
- Stock, D. J., Wolfire, M. G., Peeters, E., Tielens, A. G. G. M., Vandenbussche, B., Boersma, C., & Cami, J. 2015, *A&A*, 579, 67
- Stock, D. J., Choi, W. D.-Y., Moya, L. G. V., Otaguro, J. N., Sorkhou, S., Allamandola, L. J., Tielens, A. G. G. M., & Peeters, E. 2016, *ApJ*, 819, 65
- Stock, D. J., & Peeters, E. 2017, *ApJ*, 837, 129
- Swinyard, B. M., Ade, P., Baluteau, J.-P., et al. 2010, *A&A*, 518, L4

- Temi, P., Marcum, P. M., Young, E., et al. 2014, *ApJS*, 212, 24
Thi, W.-F., van Dishoeck, E. F., Bell, T., Viti, S., & Black, J. 2009, *MNRAS*, 400, 622
Tielens, A. G. G. M., & Hollenbach, D. 1985, *ApJ*, 291, 747
Troy, B. E., Jr., Johnson, C. Y., Young, J. M., & Holmes, J. C. 1975, *ApJ*, 195, 643
Vakili, F., Granes, P., Bonneau, D., Noguchi, M., & Hirata, R. 1984, *PASJ*, 36, 231
Werner, M. W., Uchida, K. I., Sellgren, K., et al. 2004, *ApJS*, 154, 309
Young, E. T., Becklin, E. E., Marcum, P. M., et al. 2012, *ApJ*, 749, L17

Nederlandse Samenvatting

Sterren worden gevormd in koude wolken van stof en gas door gravitatie-instorting en uiteindelijk de ontsteking van het materiaal initiëren, waarbij waterstofatomen tot helium fuseert. Naarmate sterren evolueren, blijven ze lichtere elementen fuseren tot zwaardere elementen, waardoor ongelooflijke hoeveelheden energie in de ruimte worden vrijgegeven. Afhankelijk van hun massa, zullen sterren op een zeker punt in hun leven stoppen met kernfusie van elementen. Sterren, zoals de zon, kunnen koolstof synthetiseren, maar het grootste deel van het totale koolstofbudget in het interstellair medium is afkomstig van sterren die massiever zijn dan de zon. Koele heldere sterren die verder geëvolueerd zijn, zoals de zogenaamde Asymptotische Reuzentak sterren (AGB) sterren, kunnen tijdens hun leven zelfs veel zwaardere elementen vormen. Op deze manier kunnen sterren, terwijl ze evolueren, massa in de ruimte brengen, alsook de chemie en de fysica van hun omgeving beïnvloeden door hun sterke straling. Als sterren hun brandstofvoorraad hebben uitgeput, waarbij ze ofwel kunnen exploderen als een supernova of een minder tragische dood sterven, zullen de overblijfselen van de ster het interstellair medium verrijken en zodoende de ingrediënten leveren voor de geboorte van toekomstige generaties sterren. Dit is de levenscyclus van materie in het interstellair medium en het vormt de machinerie waarmee de 'gewone' baryonische materie steeds opnieuw wordt gerecycled.

Deze interactie tussen straling en materie (die in de sterren zelf worden gevormd of de resten van de vorige generaties sterren zijn) bepaalt het type van complexere verbindingen die we in het interstellair medium vinden. Tegenwoordig weten we dat het interstellair medium veel meer complex materiaal bevat, waaronder koolstofhoudende moleculen, zoals benzeen, methanol, zelfs aminozuren en polycyclische aromatische koolwaterstoffen. Dit proefschrift is met name gericht op het laatste element uit deze opsomming, namelijk: de polycyclische aromatische koolwaterstoffen, kortweg aangeduid als PAH's.

PAH's zijn naar verwachting de meest voorkomende organische moleculen in de ruimte. Hun relevantie in interstellair wolken is significant (zie hoofdstuk 1) en ze worden zelfs verwacht een rol te spelen in de vorming van het leven, zoals we het op de Aarde kennen. Hoe deze koolstofhoudende verbindingen in/rondom sterren zijn samengesteld, wordt nog niet goed begrepen en is uiterst uitdagend. We kunnen echter bestuderen hoe deze familie van moleculen onder astrofysische omstandigheden evolueert om aanwijzingen te krijgen over hun rol in de ruimte.

De emissie van PAH's wordt waargenomen in het mid-infrarode spectrum van een uiteenlopend type astronomische bronnen, die onderworpen zijn aan hoog energetische (ultraviolette) stellair straling. Daarom is hun emissie gemakkelijk te zien in wat we fotodissociatie-gebieden (PDR's) noemen. Dit zijn de regio's rond de sterren waar de foto-

chemie wordt bepaald door ultraviolette straling, en die zodoende corresponderen met de overgangslagen waar het materiaal verandert van, daar het meestal atomair en geïoniseerd is (dichter bij de ster), naar voornamelijk moleculair (verder weg van de ster, in de meer afgeschermd gebied). In dit proefschrift richten we ons op de studie van de emissie van PAH's in de PDR's rond sterren, om te begrijpen hoe deze familie van moleculen evolueert met variaties in de fysische condities.

Wij verwijzen naar PAH's als een familie van moleculen, en niet als individuele moleculen. Na het absorberen van fotonen met een hoge energie raken de PAH's in een aangeslagen toestand, gaan door verschillende interne processen en kunnen ze uiteindelijk terug vallen in een lagere energietoestand door hun trillingen modi, die detecteerbaar zijn in het mid-infrarode deel van het spectrum van astronomische bronnen. Aangezien dergelijke vibraties gemeenschappelijk zijn bij PAH's als een familie, kan de identificatie niet één op één worden uitgevoerd. Op een bepaalde manier kunnen we dit zien als mensen op Aarde. We hebben allemaal dezelfde fysieke structuur en we lopen, rennen en springen op een soortgelijke manier. We hebben echter individuele vingerafdrukken, die elk van ons uniek maken. In tegenstelling tot onszelf hebben we nog geen vingerafdrukken van individuele PAH's kunnen detecteren en daarom kunnen we ze niet afzonderlijk onderscheiden. We kunnen ze alleen als een geheel bestuderen, zoals aliens ons zouden bestuderen als mensen, en niet als onafhankelijke individuen.

PAH's worden vervolgens op statistische wijze bestudeerd. Vanwege de veeleisende experimentele opstellingen en tijdrovende berekeningen die nodig zijn om de moleculaire eigenschappen van individuele PAH's te bestuderen, is het meeste onderzoek vanuit een vrij algemeen standpunt uitgevoerd, waarbij algemene eigenschappen worden toegewezen aan een klasse van moleculen die overeenkomen met de waarnemingen. Tegengoedig kunnen we dankzij de succesvolle ontwikkeling van experimenten en berekeningen (zie hoofdstuk 1) nog een stap verder gaan en PAH's bestuderen vanuit een moleculaire basis. Dat wil zeggen, we kunnen de fysieke eigenschappen van specifieke PAH's met verschillende kenmerken verkrijgen, hun gedrag onder astrofysische omstandigheden modifieren en op deze manier zulke specifieke moleculen als toepasselijke vertegenwoordigers van PAH's van verschillende klassen gebruiken. Dit is precies het idee achter de projecten die in dit proefschrift worden gepresenteerd. Hierbij is de uitgebreide actuele kennis die beschikbaar is over specifieke PAH's (geen gebruik makend van algemene eigenschappen) in astrofysische contexten geplaatst om enkele sleutelvragen in het onderzoeksgebied van PAH's aan te pakken.

Dit proefschrift

In hoofdstuk 2 gebruiken we de beschikbare gegevens over honderden individuele PAH's die zijn samengesteld in de NASA Ames PAH IR Spectroscopische Database om het bestaan van de zogenaamde grandPAH's op de helderste mid-infrarood spots in PDR's te onderzoeken. De grandPAH's zijn voorgesteld om een set van de stabielste PAH-moleculen te vertegenwoordigen, die de intense processen in het interstellair medium kunnen overleven en domineren derhalve de PAH-populatie in de ruimte. De vraag of een unieke mix van PAH's in de helderste plaatsen van PDR's uitstraalt, vloeit voort uit de observaties zelf: de mid-infrarood-emissie op de helderste plek in de PDR's rond drie verschillende hete sterren is verrassend vergelijkbaar. We hebben de emissie van de PAH's in de database gemodelleerd en we hebben de waarnemingen gemonteerd om de emitterende PAH-populatie te

karacteriseren. We hebben vernomen dat subtiele variaties in de emissie-eigenschappen van individuele PAH's kunnen leiden tot waarneembare verschillen in de resulterende spectra. We hebben dus bewijs gevonden dat de PAH-populaties vanuit verschillende gezichtslijnen opvallend vergelijkbaar moeten zijn en zodoende het concept van grandPAH's mogelijk zou kunnen worden toegepast. Deze unieke mix van PAH's zou het resultaat zijn van intensieve verwerking bij de grenslijm tussen de PDR en de moleculaire wolk. In het hypothetische scenario waar de grandPAH's geïdentificeerd kunnen worden, zouden ze een beginpunt zijn voor het opsporen van de wijze waarop het koolstofhoudende materiaal rond sterren op een hoopt en wordt vernietigd.

In hoofdstuk 3 gebruiken we een nog specifiekere aanpak, waar we drie goed (theoretisch en experimenteel) gebestudeerde individuele PAH's overwegen om te zien hoe ze uiteindelijk met verschillende fysische condities in een prototypische PDR evolueren. We hebben een kinetisch model gebouwd, waarbij rekening wordt gehouden met de meest relevante foto/chemische reacties, met behulp van de nieuwste gegevens die beschikbaar zijn voor elk molecuul. De drie individuele moleculen hebben astrofysisch-relevante groottes en zullen naar verwachting uit een familie van PAH's komen, die vrij stabiel zijn tegen straling. In het algemeen hebben we de verschillen in de verdeling van de soorten vergeleken met PAH-grootte. We hebben geconstateerd dat de variaties in de emissie worden gedomineerd door de variatie in de ionisatie-toestand van de dominante hydrogeneringstoestand van elke soort. Gezien elke PAH hier als een vertegenwoordiger van PAH's van verschillende afmetingen is bestudeerd, verwachten we dat het moeilijk is om het effect van dehydrogenering in de emitterende PAH-spectra te begrijpen, gezien dat voor iedere fysische conditie alleen PAH's binnen een klein gebied vatbaar zijn voor dehydrogenering, doordat ze snel ontdaan worden van alle H-atomen (en wellicht kunnen isomeriseren tot andere structuren zoals kooi structuren of fullerenen). Afgezien van het onderzoeken hoe PAH-emissie is gekoppeld aan de variaties in de fysische omstandigheden binnen een PDR, tackelen we ook enkele van de huidige vragen op het gebied, zoals of PAH's met extra H atomen de dragers van de $3.4\ \mu\text{m}$ band kunnen zijn en de rol van PAH's in de hoge moleculaire waterstofvormingsgraden waargenomen in PDR's. Voor de eerste vraag zien we dat PAH's met extra H-atomen waarschijnlijk niet de enige dragers zijn van de $3.4\ \mu\text{m}$ band, omdat deze soorten alleen in zeer gunstige omgevingen worden gevonden die tegengesteld zijn aan het astronomische bewijs. Wat de H_2 -vorming in PDR's betreft, zien we dat H_2 -ontvreemding van PAH's met extra H-atomen een inefficiënt proces is in vergelijking met H_2 -vorming op stofdeeltjes. We vinden echter dat foto-dissociatie van PAH's van kleine tot middelmatige afmetingen kan bijdragen aan de vorming van H_2 in PDR-oppervlakken, maar dat ze niet verantwoordelijk zijn voor de hoge H_2 -vormingssnelheden die zijn afgeleid van waarnemingen.

In hoofdstuk 4 wordt nagegaan of het deuteriumgehalte in PAH's de waargenomen variatie van de deuterium overvloed in het lokale interstellair medium kan verklaren (zie hoofdstuk 1). We hebben deze vraag opnieuw vanuit een moleculair standpunt gebaseerd op het model dat in hoofdstuk 3 is gepresenteerd. We beschouwden dezelfde drie PAH's en we hebben het kinetische model dienovereenkomstig gewijzigd om rekening te houden met reacties waarbij deuterium-atomen betrokken zijn. We vinden dat deuteratie van PAH's grotendeels volgt op de atoom (D/H) verhouding die in de gasfase beschikbaar is. Met andere woorden, de deuterium fractionering in PAH's zal hoger zijn als de (D/H) verhouding in het interstellair medium hoger is. Zo concluderen we met de recente waarnemingen van deuterate PAH's in PDR's dat de hoge deuteratie waargenomen in PDR's impliceert

dat het gasfase-reservoir ook zeer gefractioneerd moet zijn. De impliciete atoom (D/H) fractie in de gasfase is echter veel groter dan wat PDR-modellen voorspellen. Om dit te doen overeenstemmen stellen wij voor dat de hoge deuterium-fractie in PAH's de chemie kan afspiegelen die voorkomt in de koude dichte moleculaire wolken, die behouden blijft wanneer (middelgrote-tot-grote) PAH's naar de meer niet afgeschermden delen van PDR's gaan. Dit is een aannemelijke verklaring voor de deuterium fractionering met betrekking tot aromatische plaatsen, maar het kan de geobserveerde hoge fractionering van de alifatische groepen (PAH's met extra atomen, die gemakkelijk verloren gaan wanneer PAH's blootgesteld zijn aan UV-straling) niet verklaren.

Ten laatste in hoofdstuk 5 karakteriseren we PAH-emissie vanuit een nauwgezet observatie-kader. Alle vorige hoofdstukken hebben PDR's overwogen, aangezien dit de beste laboratoria zijn om PAH-uitstoot te bestuderen. In dit laatste hoofdstuk richten we ons op de PDR's van het beroemde paar nevels IC63-IC59 in de buurt van de ster γ Cas. Beide nevels hebben zeer verschillende optische verschijningen, ondanks het feit dat beide voorwerpen op soortgelijke geprojecteerde afstanden van de ster liggen. De waarnemingen bij de optische tip van deze objecten tonen aan dat de IR-uitstoot van PAH's zeer vergelijkbaar is. Deze gelijkheid is niet alleen in overeenstemming met dat beide objecten hoge dichtheidsobjecten zijn in dezelfde omgeving als de omgeving rond γ Cas, maar het is ook consistent met vergelijkbare fysische parameters, die de evolutie van het hydrogenerings- en ioniseringsniveau van de emitterende PAH-populatie bepalen. Vergeleken met andere PDR's van weerspiegelings-niveau en bekende correlaties tussen PAH's en astrofysische parameters blijkt dat zowel IC63 als IC59 tamelijk lage UV-bestraalde gebieden zijn.

Curriculum Vitae

I was born on May 1986, in a small town (that no longer exists) situated in the middle of the beautiful and dry Atacama desert: Chuquicamata, Chile. When I was about a year old, my family (and *natuurlijk* myself) moved to the sea side, to Antofagasta; a well known city by astronomers, as this is where people first arrive to go to the Very Large Telescope (VLT). Living in Antofagasta (a city with strict light pollution policies due to the astronomical activity) was lovely. Not only because of the people and its nice temperate climate, but also because the sky there is so clear that you always get to see weird things falling from it. I guess that is when —without being really aware of it— I set my eyes on astronomy.

By the time I was 14 years old, we moved to the capital of the country, Santiago. There, aside from encountering a very different life-rhythm than in the north, I was inspired by my school teachers to develop my mathematics and physics studies. In 2004 I entered to study astrophysics at Pontificia Universidad Católica de Chile (PUC). Early on, I started to work as a teaching assistant of several physics courses to engineers, civil constructors, medicine students and physicists. I really enjoyed that experience, although grading the exams of 150 students not so much...

For my bachelor's thesis I worked under the supervision of Prof. Luis Felipe Barrientos from my university, and Prof. Sebastián López from Universidad de Chile (U. Chile). With them, I entered into the world of extragalactic astronomy, and I started what would later become my master's thesis on galaxy clusters in the line of light to background quasars. This project was carried out within the Quasars Behind Clusters group (QbC), which gathered astronomers from both universities. In fact, my master's thesis was the first one being shared between both universities, and personally, it was a great opportunity for me to experience working with scientists from different institutes. It also gave me the amazing opportunity to spend several nights observing at Gemini South telescope at Cerro Pachón, and at the Magellan Telescopes at Las Campanas Observatory (LCO).

During my master's program, I also worked on other projects with Prof. Andrés Meza (from Universidad Andrés Bello, Chile) on the cosmological perturbations after the Big Bang; Prof. Marcio Catelán (PUC) on analyzing light curves for the Vista Variable in the Vía Láctea (VVV) survey; and with Prof. Paulina Lira (U. Chile) on active galactic nuclei, which also took me to spend some amazing time in Florianópolis (Brazil) to work under the supervision of Prof. Roberto Cid Fernandes at Universidade Federal de Santa Catarina (UFSC). All this experience gave me a broad view about the different fields in astronomy.

In late 2011, I decided to pursue a PhD in Leiden to work under the supervision of Prof. A. G. G. M. Tielens on polycyclic aromatic hydrocarbons (PAHs) in space. Motivated by the curiosity towards integrating astronomy to other sciences, here I entered into the world of the local interstellar medium, and the astrochemistry of it. I was part of the Dutch Astrochemistry Network (DAN), which periodically organized meetings involving not only astronomy, but also biology and chemistry. This was a great opportunity to understand more how different scientific branches can overlap and contribute with one another. I had the amazing opportunity to visit NASA Ames Research Center in Mountain View California, to present my research and work together with Prof. Louis Allamandola and Dr. Christiaan Boersma. I also got to meet amazing people who work on very exciting research regarding the role of PAHs in astrobiology. I attended several workshops and schools in the Netherlands (as part of the DAN) and I also had the possibility to go abroad to learn and present my work. I also had the opportunity to work with Prof. Els Peeters using SOFIA, which is the largest airborne observatory in the world. Besides my work on research, during my years at the Sterrewacht, I was also in charge of assessing the colloquia of master students, I was involved in the editing of the annual reports, and I organized the always fun friday social gatherings, the *borrels*.

Acknowledgments

I might not be able to find the right words to express precisely what I would like to say in this section, but let's give it a try...

Natuurlijk I would like to start by thanking Xander for his nice spirit, all the lovely and funny meetings we always had, and of course, thank you for your guidance and all the amazing input you gave me during all these years. You are not only a Santa Claus for all the kids who see you in restaurants, but you are a Santa to all the PhDs from the observatory (just ask around!). I would also like to thank my colleagues specially Alessandra, Els, Lou and Christiaan, for all your input in the different projects we carried out together. Working with you taught me a lot and helped me to push the work forward.

I would also like to thank the supporting staff of the Sterrewacht. In particular Evelijn, Anita, Liesbeth and Yvonne. Thank you for arranging with such a nice disposition all necessary procedures. Thank you also to the computer guys: Erik, Aart, David and Leonardo, thank you for always fixing my computer-related problems, which I must say there were so many!

Throughout these years, an important part of my daily routine were the conversations with my nice officemates! Sascha, Isabel, Maria, Alessandra, Mher, Cameron, Ingrid, Anemieke, Corentin and Tao. Thank you for all the nice conversations and jokes we have shared all this time. Sascha (and of course Gilles!), Isabel and Maria: I really enjoyed releasing all our emotions together and thank you for all the moral support you have given me!

Now, being in the office right next to Xander's, implied most of my officemates were also from my research group: the ISM group. With this, I would like to thank the current members, and of course the ones who were here when I first arrived. Lynn, Marcelo, Bram, Sebastiaan, Koen, Silvia, Kirstin, Raymond, Carmen, Jungfeng, Cornelia, Claudia, Kim, Ainil. Thank you for all your nice input and the good moments we shared together, either in meetings, conferences and/or schools. In particular, thank you Lynn and Ainil! I will always remember you guys and I wish you the best!

My generation fellows, specially Andra, Marco, Alex South and Monica. We helped each other, specially when we first arrived, when we were all a bit lost trying to understand the dutch culture, and their language. I will never forget Marco, Monica and Alex(s) all our dutch sessions/burger-king/eazie-evenings together with Bernard and Shuo. How we 'prepared' before each lesson in the Kayser Lounge, and how we desperately tried to survive the gatentekst part of each class. I have had so much fun with all of you. I think in one way or another we bonded really well, and I will always remember you!

When looking back to my first years, I cannot forget to mention the previous generations, Irene, Matteo, Silvia, Thanja, Gleb, Berenice. I saw you struggle and now I understand why (haha). Thank you for all the nice times we shared together! I would also like to thank all my colleagues at the Sterrewacht throughout these years: Daniel P., Daniel H., Emanuele, Niels, Ann Sofie, Eva, Mike, Andrew, Eleonora, Chris, Gabriela, David, Henriette, Christian, Jeroen, Stephanie, Ricardo, Luis, Viviani, Sierk, Edwin, Tommaso, Allison, Mieke, Luke, Ayush, Carmen, Noel, Mariam, Ali, Max, Nienke, Catherine, Alan, Anton. I enjoyed meeting you and talking to you at the borrels, coffee breaks, memorable dinners and parties, etc. We complained about the weather, the health system, the biking, the coffee in the Kayser Lounge, did I say the weather? if not, the weather, etc. etc. You made this place a pleasant one, and I am thankful to all of you for that!

I would also like to thank all the housemates I had (some of which I have already mentioned above) specially Marlinda for being such a good friend, who always listened to all my ridiculous work and non-work related stories.

Oh my goodness, it is time to thank my community. So many awesome memories I would like to thank you about, but I would need at least another 4 years to write them all! Thank you Vicho, los Marianos, Cristi, Claudio, Yanett, Max, Cristóbal, Dani, Camila, Andrea, Lizette, Marta, Lina, Diana, Jorge, Santiago, Paula, Pedro, Francisca, Carlitos, Seba, Javi, Nico, Wijnand, Francisco, Pablo! All the late lunches, the coffee breaks, the barbecues, the parties, the borrels, the after-borrels, the after-after-borrels, etc. etc. You made this place feel like home in one way or another. The thought of leaving this place brings me to tears because of you. Son muy buena onda todos y la verdad es que los extrañaré mucho. Cada uno a su manera contribuyó con mi paso por estas frías y lluviosas tierras. Y a cada uno me lo llevo en el corazón. En especial Seba, Javi, Nico, Wijnand...ya nos encontraremos en alguna junta anual o algo así. Lo importante es que los recuerdos estén siempre presentes, y que nuestra amistad no se pierda nunca. Fran! Aunque llegaste hace poco, yo creo que por acá va la nueva presidenta. ¡Gracias por apañar en todo! Y al fin tener a alguien para compartir datos no-astrónomicos (¡atroooo gaya!). Pedro ¡Ministro! Tienes que seguir desarrollando tus cualidades administrativas y cocinísticas (sí, cocinísticas...hablo mal el español y ¡qué!). La comunidad ahora dependerá de ti! Pablo, gracias por ser un gran apoyo moral, por siempre dejarme hablar todo el rato (de verdad todo el rato), y sobretodo, por enseñarme todos los modismos y expresiones chilenas desconocidas para mí hasta ahora. Créeme que todo ese conocimiento lo he digerido (haha). Francisco, gracias por ser mi apoyo y por ser tan good listener también (bueno, es que hablo mucho, lo sé haha). Pucha mi querida comunidad, se les echará de menos...¡hay que decirlo! ¡Los quiero a todos! ¡Atrooooooooooooo!

At last but most importantly, of course even though far away, my family is the most important support I have. Mom and dad, well the thesis is dedicated to you. Son lo más importante en mi vida y donde voy, los llevo conmigo siempre. La verdad es que no puedo estar más agradecida por todo lo que me han dado, y la suerte que he tenido de que sean mis padres. A mis hermanos...Broooo gracias por siempre hacerme reír. Me siento muy agradecida de poder contar contigo always. Maureen y Christian, gracias por el apoyo y por esos dos hermosos cosetos checos que ahora tengo de sobrinos, y que me sacan una sonrisa con cada minúscula cosa que hacen. Querida familia: ¡los adoro always!